

**ELECTRONIC STRUCTURE AND
RELATED PROPERTIES OF $A_2M_{1-x}M'_xTO_6$
DOUBLE PEROVSKITES**



A THESIS SUBMITTED TO THE
CENTRAL DEPARTMENT OF PHYSICS
INSTITUTE OF SCIENCE AND TECHNOLOGY
TRIBHUVAN UNIVERSITY
NEPAL

FOR THE AWARD OF
DOCTOR OF PHILOSOPHY
IN PHYSICS

BY
SHALIKA RAM BHANDARI

MAY 2022

**ELECTRONIC STRUCTURE AND
RELATED PROPERTIES OF $A_2M_{1-x}M'_xTO_6$
DOUBLE PEROVSKITES**



A THESIS SUBMITTED TO THE
CENTRAL DEPARTMENT OF PHYSICS
INSTITUTE OF SCIENCE AND TECHNOLOGY
TRIBHUVAN UNIVERSITY
NEPAL

FOR THE AWARD OF
DOCTOR OF PHILOSOPHY
IN PHYSICS

BY
SHALIKA RAM BHANDARI
MAY 2022

DECLARATION

This thesis entitled **ELECTRONIC STRUCTURE AND RELATED PROPERTIES OF $A_2M_{1-x}M'_xTO_6$ DOUBLE PEROVSKITES** which is being submitted to the Central Department of Physics, Institute of Science and Technology (IOST), Tribhuvan University, Nepal, for the award of the degree of Doctor of Philosophy (Ph.D.), is a research work carried out by me under the supervision of Associate Prof. Dr. Gopi Chandra Kaphle, Central Department of Physics, Tribhuvan University, Kirtipur, Nepal and co-supervision of Associate Prof. Dr. Madhav Prashad Ghimire, Central Department of Physics, Tribhuvan University, Kirtipur, Nepal and PD Dr. Manuel Richter, Leibniz Institute for Solid State and Materials Research, IFW-Dresden, Germany.

This research is original and has not been submitted earlier in part or full in this or any other form to any university or institute, here or elsewhere, for the award of any degree.

SHALIKA RAM BHANDARI

RECOMMENDATION

This is to recommend that **Mr. SHALIKA RAM BHANDARI** has carried out research work entitled "**ELECTRONIC STRUCTURE AND RELATED PROPERTIES OF $A_2M_{1-x}M'_xTO_6$ DOUBLE PEROVSKITES**" for the award of Doctor of Philosophy (Ph.D.) in **PHYSICS** under our supervision and guidance.

To our knowledge, this work has not been submitted for any other degree. He has fulfilled all the requirements laid down by the Institute of Science and Technology (IOST), Tribhuvan University, Kirtipur, Nepal, hence we recommend for the submission of the thesis for the award of Ph.D. degree.

.....

Supervisor

Dr.Gopi Chandra Kaphle

Associate Professor

Central Department of Physics

Tribhuvan University, Kirtipur, Kathmandu, Nepal

.....


Co-Supervisor

Dr. Madhav Prasad Ghimire

Associate Professor

Central Department of Physics

Tribhuvan University, Kirtipur, Kathmandu, Nepal



Co-Supervisor

PD Dr. Manuel Richter

Leibniz Institute for Solid State and Materials Research

IFW-Dresden, Germany

MAY 2022

LETTER OF APPROVAL

Date:

On the recommendation of Assoc. Prof. Dr. **Gopi Chandra Kaphle**, Central Department of Physics, Tribhuvan University, Kirtipur, Kathmandu, Nepal, Assoc. Prof. Dr. **Madhav Prasad Ghimire**, Central Department of Physics, Tribhuvan, University, Kirtipur, Kathmandu, Nepal, and PD. Dr. **Manuel Richter**, Leibniz Institute for Solid State and Materials Research, IFW-Dresden and DCMS, Dresden, Germany, this Ph.D. thesis submitted by **Shalika Ram Bhandari**, entitled "**ELECTRONIC STRUCTURE AND RELATED PROPERTIES OF $A_2M_{1-x}M'_xTO_6$ DOUBLE PEROVSKITES**" is forwarded by Central Department Research Committee (CDRC) to the Dean, Institute of Science and Technology (IOST), Tribhuvan University (TU).

.....

Dr. Om Prakash Niraula

Professor and Head

Central Department of Physics

Tribhuvan University, Kirtipur

Kathmandu, Nepal

Date:

ACKNOWLEDGMENT

First of all, I would like to express my sincere appreciation to my advisors Assoc. Prof. Dr. Gopi Chandra Kaphle, Assoc. Prof. Dr. Madhav Prasad Ghimire, Central Department of Physics (CDP), Tribhuvan University (TU), Kirtipur, Kathmandu, Nepal and PD. Dr. Manuel Richter, Leibniz Institute for Solid State and Materials Research, IFW-Dresden and DCMS, Dresden, Germany for their supervision, guidance, constant inspiration and incredible assistance throughout my research.

I would like to thank Prof. Dr. Om Prakash Niraula, Head, Central Department of Physics (CDP), TU, who helped me from his side. I would like to acknowledge Prof. Dr. Binil Aryal, Dean, IOST for his valuable suggestions and encouragement throughout the Ph.D. work, CDRC members, Professors, and the staffs of CDP, TU for support and interaction during this period. I specially thank Leibniz Institute for Solid State and Materials Research, IFW-Dresden, Germany for providing me a good platform to work there for three months as a research scholar with full financial support and providing a scientific environment throughout. I would like to thank Prof. Dr. Jeroen van den Brink, Leibniz Institute for Solid State and Materials Research, IFW-Dresden, Germany for his suggestions and Mrs. Ulrike Nitzsche, IFW-Dresden, Germany for technical assistance through out my research. I am thankful also to my collaborators from USA, India, Germany and Sweden, co-authors and all members of Advanced Material Research Laboratory (AMRL), CDP, TU for technical and scientific support. Thanks goes to Condensed Matter Physics Research Center (CMPRC-Butwal), Rupan-dehi, Nepal and AMRL for providing the computational and technical support and Bhairahawa Multiple Campus for supporting role.

Finally, I would like to acknowledge National Academy of Science and Technology (NAST), Nepal for three years Ph.D. fellowship through the grant number PhD/074-75. Last but not the least, I would also like to thank my lovely wife Mrs. Shikha Sharma Pandey Bhandari for her love and constant support, for my late nights and early mornings. I have no words to express my thankfulness to my family members particularly my father Mr. Krishna Prasad Bhandari, mother Mrs. Radha Devi Bhandari. I would like to dedicate this thesis to my lovely sons Mr. Sharthak Bhandari and Mr. Shiryan Bhandari. The continuous support, encouragement and motivation that I

got from family, friends are immense in completing this thesis and is the driving force that making me to move in right direction throughout my life.

SHALIKA RAM BHANDARI

MAY 2022

ABSTRACT

From density functional computations, we investigated several properties of double perovskites in $A_2M_{1-x}M'_xTO_6$. We start with Ca-based double perovskites Ca_2CrOsO_6 as a parent material and studied electronic and magnetic properties by doping with different transition metals. Ca_2CrOsO_6 is a newly manufactured double perovskite material which has been discovered with ferrimagnetic (FiM) ground state. This material shows insulating character with energy gap of 0.59 eV and net magnetic moment of $0.23 \mu_B$. We further explore the thermoelectric and optical properties of Ca_2CrOsO_6 . In our calculation, Ca_2CrOsO_6 doesnot show promising for transport and optical applications. With substitution of one Ni atom to the Cr-site on parent material, $Ca_2Cr_{0.5}Ni_{0.5}OsO_6$ is found to be half metal that is desirable for spintronics. Likewise, we investigated other two new materials with double perovskite configuration Ca_2CrIrO_6 and Ca_2FeIrO_6 by substituting Fe and Ir at Cr and Os site, respectively, with the same occupancy ratio as in parent materials. The calculation of formation and cohesive energies on both the materials give negative values which suggests that both the material are thermodynamically stable and are possible to synthesize. Spin orbit coupling (SOC) plays a significant role in the calculation of electronic and magnetic properties. Both the materials Ca_2CrIrO_6 and Ca_2FeIrO_6 are found to have ferrimagnetic ground state and are stable with semiconducting energy gap of 0.25 eV and 0.13 eV, respectively. This has been found by taking up the electron-electron correlation (U) and SOC effect. In addition, we also calculated the spin exchange coupling parameters of different atoms. Various properties as Curie temperature (T_C) of different materials have been computed by using these exchange parameters. The estimation of T_C has been done as per Heisenberg model of the Mean Field Approximation (MFA). Our calculated transition temperature T_C value are 906 K and 827 K for Ca_2CrIrO_6 and Ca_2FeIrO_6 , respectively, which are in a valid T_c trends of other double perovskites. Similarly, Cr and Os sites are substituted by Ni and Ir in Ca_2CrOsO_6 to obtain Ca_2NiIrO_6 and found that this doped structures exhibit FiM ground state and is stable with semiconducting band gap of 0.08 eV which persist even with strong effect of SOC. The T_C calculated for this material by MFA is found to have 272 K. We further explored the properties of Ca_2MnIrO_6 which is also found to have FiM ground state with half-metallic nature.

Focusing on Sr-based double perovskites, we carried out our research on a newly synthesized materials $SrLaMM'O_6$ ($M= Ni, Fe; M'= Os, Ru$). The strong electron-

correlation effect (U) were considered for the M and M'-sites. We found the antiferromagnetic (AFM) ground state for SrLaNiOsO₆, SrLaFeOsO₆ and SrLaNiRuO₆ with their magnetic easy axis along [001]-direction. Electronic behavior in these compounds are found to be insulating. Upon inclusion of SOC in Os-5d site leads to the opening of the very small band gap (0.03 eV) which dictates the significant influence of SOC in SrLaFeOsO₆. Other two compounds SrLaNiOsO₆ and SrLaNiRuO₆ also shows Mott-insulating characteristics having 0.33 eV and 0.58 eV energy gap, with dominant contributions from Os-5d and Ru-4d bands around the Fermi level. Our results agrees fairly with the experimental finding for these systems. Charge ordering is found to be prominent in these compounds i.e. a symmetry reduction by different charges on structurally (originally) identical sites.

Moving on to lanthanide based double perovskites, we have explored the Tb₂FeCrO₆ which is synthesized by our collaborators using the neutron powder diffractometer. We perform DFT calculation on this DPs. The material shows AFM ground state with insulating character. The energy gap is calculated as 0.12 (2.4) eV in GGA (GGA+ U). We further computed the spin exchange coupling parameters and used in calculating Neel temperature (T_N). The calculated T_N is 853 K for Tb₂FeCrO₆.

LIST OF ACRONYMS AND ABBREVIATIONS

APW	:	Augmented Plane Wave
FM	:	Ferromagnetic
AFM	:	Antiferromagnetic
FiM	:	Ferrimagnetic
FP-LAPW	:	Full-Potential Linearized Augmented Plane Wave
HM	:	Half Metals
LO	:	Local Orbital
MT	:	Muffin-Tin
BO	:	Born-Oppenheimer
BZ	:	Brillouin Zone
CB	:	Conduction Band
DPs	:	Double Perovskites
DFT	:	Density Functional Theory
HK	:	Hohenberg Kohn
KS	:	Kohn Sham
DOS	:	Density of States
PDOS	:	Partial Density of States
GGA	:	Generalized Gradient Approximation
LDA	:	Local Density Approximation
PBE	:	Perdue, Burke, and Ernzerhof
SCF	:	Self Consistent Field
SWE	:	Schrodinger Wave Equation
TF	:	Thomas Fermi
VB	:	Valence Band
eV	:	Electron Volt
Ry	:	Rydberg
XC	:	Exchange Correlation
SOC	:	Spin-Orbit Coupling
DPs	:	Double Perovskite
U	:	Coulomb Interaction

LIST OF TABLES

		Page No.
Table: 1	Muffin-tin radii for Calcium containing compounds	30
Table: 2	Muffin-tin radii for osmium containing compounds	31
Table: 3	Muffin-tin radii for ruthenium containing compound	31
Table: 4	Muffin-tin radii for terbium containing compounds	31
Table: 5	Computed effective and individual magnetic moments (μ_B) and band gap 'E _g ' (eV) for Ca ₂ CrOsO ₆ compound.	37
Table: 6	For the Ca ₂ CrOsO ₆ compound, calculated optical parameters at the major peak value	40
Table: 7	Computed effective, individual and orbital moments (μ_B) and band gap 'E _g ' (eV) for Ca ₂ Cr _{0.5} Ni _{0.5} OsO ₆ compound.	44
Table: 8	Computed spin and orbital moments (in μ_B) and band gap 'E _g ' (eV) for Ca ₂ CrIrO ₆ compound.	48
Table: 9	Calculated magnetic exchange coupling parameters (meV) for DPs Ca ₂ MIrO ₆	51
Table: 10	Calculated effective and individual moments (μ_B) and energy gap 'E _g ' (eV) for Ca ₂ FeIrO ₆ compound.	55
Table: 11	Computed spin exchange coupling parameters (in meV) for DPs Ca ₂ FeIrO ₆	58
Table: 12	Calculated effective and individual moments (μ_B) and energy gap 'E _g ' (eV) for Ca ₂ NiIrO ₆ compound.	60
Table: 13	Calculated effective and individual moments (μ_B) and energy gap 'E _g ' (eV) for Ca ₂ MnIrO ₆ compound.	65
Table: 14	Computed effective, individual and orbital magnetic moments (μ_B) and energy gap 'E _g ' (eV) for SrLaNiOsO ₆ compound. . .	70
Table: 15	Computed effective, individual and orbital moments (μ_B) and energy gap 'E _g ' (eV) for SrLaFeOsO ₆ compound.	78

Table: 16	Computed effective, individual and orbital moments (μ_B) and energy gap 'E _g ' (eV) for SrLaNiRuO ₆ compound.	85
Table: 17	Calculated effective and individual moments (μ_B) and energy gap 'E _g ' (eV) for Tb ₂ FeCrO ₆ compound.	91
Table: 18	Computed spin exchange coupling parameters (in meV) for DPs Tb ₂ FeCrO ₆ (Pnma) with $U_{Tb} = 6$ eV, $U_{Fe} = 5$ eV and $U_{Cr} = 3$ eV, M =Cr or Fe.	95

LIST OF FIGURES

		Page No.
Figure: 1	Crystal structure of CaTiO_3 perovskites (Moreira <i>et al.</i> , 2009).	2
Figure: 2	Crystal structure of double perovskites structure: $\text{Ca}_2\text{CrIrO}_6$.	4
Figure: 3	Self-consistency flow chart showing working procedure in KS formalism (Kohn & Sham, 1965).	19
Figure: 4	(a) Partition of the unit cell into atomic spheres (I) and an interstitial region (II), (b) Mufin-tin potential model (Pashov <i>et al.</i> , 2020).	22
Figure: 5	Selection of k path for monoclinic structures in first Brillouin zone (Actyawan & Curtarola, 2010).	25
Figure: 6	The directional properties of five d orbitals (Miessler & Tarr, 1996).	26
Figure: 7	The energy ranges of e_g and t_{2g} orbitals (Legendre <i>et al.</i> , 2021).	27
Figure: 8	Self consistent flow chart for organisation of calculation (Blaha <i>et al.</i> , 2001).	28
Figure: 9	Crystal structure of double perovskites $\text{Ca}_2\text{CrOsO}_6$	34
Figure: 10	(a) Density of states and (b) band structure of $\text{Ca}_2\text{CrOsO}_6$ with GGA functional.	34
Figure: 11	(a) Density of states and (b) band structure of $\text{Ca}_2\text{CrOsO}_6$ with GGA+ U functional.	35
Figure: 12	(a) Density of states and (b) band structure of $\text{Ca}_2\text{CrOsO}_6$ with GGA+ U +SOC.	36
Figure: 13	Isosurface of spin magnetization density at $\pm 0.21e/\text{\AA}^3$ of (left) $\text{Ca}_2\text{CrOsO}_6$ and (right) $\text{Ca}_2\text{Cr}_{0.5}\text{Ni}_{0.5}\text{OsO}_6$	36
Figure: 14	(left) Seebeck coefficient, (middle) electrical conductivity, and (right) power factor as a function of temperature for CCOO.	38

Figure: 15	(a) The real and imaginary part of the dielectric function $\epsilon(\omega)$, (b) Electron energy loss function $L(\omega)$, vs photon energy and (c) optical conductivity $\sigma(\omega)$ for CCOO.	39
Figure: 16	Total DOS of $\text{Ca}_2\text{Cr}_{0.5}\text{Ni}_{0.5}\text{OsO}_6$ with (a) GGA and (b) GGA+ U functional.	42
Figure: 17	Band structure of $\text{Ca}_2\text{Cr}_{0.5}\text{Ni}_{0.5}\text{OsO}_6$ with (a) GGA and (b) GGA+ U functional.	42
Figure: 18	(a) The density of states and (b) band structures of CCNOO under GGA+ U +SOC.	43
Figure: 19	Isosurface of spin magnetization density at $\pm 0.21e/\text{\AA}^3$ for $\text{Ca}_2\text{CrOsO}_6$ (left) and $\text{Ca}_2\text{Cr}_{0.5}\text{Ni}_{0.5}\text{OsO}_6$ (right).	43
Figure: 20	Crystal structure of $\text{Ca}_2\text{BB}'\text{O}_6$ double perovskites.	45
Figure: 21	The total and partial DOS of $\text{Ca}_2\text{CrIrO}_6$ within (a) GGA and (b) GGA+ U functional, respectively.	46
Figure: 22	(a) The density of states and (b) band structure of $\text{Ca}_2\text{CrIrO}_6$ under GGA+ U +SOC.	47
Figure: 23	Isosurface of spin magnetization density at $\pm 0.23 e/ A^3$ for $\text{Ca}_2\text{FeIrO}_6$ (left) and $\text{Ca}_2\text{CrIrO}_6$ (right), respectively.	49
Figure: 24	Calculated spin exchange interactions in DPs $\text{Ca}_2\text{CrIrO}_6$	49
Figure: 25	Calculated versus measured Curie temperatures for different double perovskites.	51
Figure: 26	The total and partial DOS of $\text{Ca}_2\text{FeIrO}_6$ within (a) GGA and (b) GGA+ U functional, respectively.	53
Figure: 27	(a) The total and partial DOS and (b) band structures of $\text{Ca}_2\text{FeIrO}_6$ under GGA+ U +SOC.	54
Figure: 28	Spin magnetization density at $\pm 0.23 e/ A^3$ for $\text{Ca}_2\text{FeIrO}_6$ (left) and $\text{Ca}_2\text{CrIrO}_6$ (right), respectively.	55
Figure: 29	Calculated magnetic exchange interactons in the DPs configurtion $\text{Ca}_2\text{CrIrO}_6$ and $\text{Ca}_2\text{FeIrO}_6$	57
Figure: 30	Crystal structure of $\text{Ca}_2\text{NiIrO}_6$ (colors in sky blue, blue, grey and red spheres corresponds to Ca, Ni, Ir and O atoms, respectively).	58
Figure: 31	(a) The DOS and (b) band structures of $\text{Ca}_2\text{NiIrO}_6$ under GGA+ U +SOC.	59
Figure: 32	Spin exchange interactions paths in DPs configuration $\text{Ca}_2\text{NiIrO}_6$	61
Figure: 33	Crystal structure of $\text{Ca}_2\text{MnIrO}_6$ DPs.	62

Figure: 34	Total and partial DOS of $\text{Ca}_2\text{MnIrO}_6$ under (a) GGA and (b) GGA+ U functional.	63
Figure: 35	(a) Total and partial DOS and (b) band structures of $\text{Ca}_2\text{MnIrO}_6$ under GGA+ U +SOC.	64
Figure: 36	Computed magnetic exchange interactions in DPs configuration $\text{Ca}_2\text{MnIrO}_6$	66
Figure: 37	Crystal structure of double perovskites $\text{SrLaBB}'\text{O}_6$ (where grey, blue, green, and red spheres correspond to Sr(La), B, B' and O sites).	67
Figure: 38	Schematic representation of the super-exchange interactions between Ni and Os with d^3 - d^5 electronic configurations.	67
Figure: 39	Total and partial DOS for SrLaNiOsO_6	68
Figure: 40	Partial DOS within LDA+ U and LDA+ U +SOC functional for SrLaNiOsO_6	69
Figure: 41	Band structures of SrLaNiOsO_6 within LDA functional.	71
Figure: 42	Band structures of SrLaNiOsO_6 within LDA+ U functional.	72
Figure: 43	Band structures of SrLaNiOsO_6 within LDA+ U +SOC functional.	73
Figure: 44	Fat band structures on Ni-3d of SrLaNiOsO_6 within LDA+ U +SOC functional.	73
Figure: 45	Fat band structures Os1-5d on SrLaNiOsO_6 within LDA+ U +SOC functional.	74
Figure: 46	Schematic representation of the super-exchange interactions between Fe and Os with d^3 - d^5 electronic configurations.	75
Figure: 47	Total and partial DOS for SrLaFeOsO_6	76
Figure: 48	Partial DOS for SrLaFeOsO_6	77
Figure: 49	Band structures of SrLaFeOsO_6 within LDA functional.	79
Figure: 50	Band structures of SrLaFeOsO_6 within LDA+ U functional.	80
Figure: 51	Band structures of SrLaFeOsO_6 within LDA+ U +SOC functional.	80
Figure: 52	Schematic representation of the super-exchange interactions between Ni and Ru with d^3 - d^4 electronic configurations.	82
Figure: 53	Total and partial density of states for SrLaNiRuO_6	83
Figure: 54	Partial density of states for SrLaNiRuO_6	84
Figure: 55	Band structures of SrLaNiRuO_6 within LDA functional.	86
Figure: 56	Band structures of SrLaNiRuO_6 within LDA+ U functional.	87
Figure: 57	Band structures of SrLaNiRuO_6 within LDA+ U +SOC functional.	88

Figure: 58	Fat band structures of SrLaNiRuO ₆ within LDA+ <i>U</i> +SOC functional.	88
Figure: 59	Fat band structures of SrLaNiRuO ₆ within LDA+ <i>U</i> +SOC functional.	89
Figure: 60	Schematic representation of the super-exchange interactions between Fe and Cr with d ⁵ -d ³ electronic configurations.	90
Figure: 61	Total and partial DOS of Tb ₂ FeCrO ₆ with GGA functional. The vertical dotted line indicates E_F	91
Figure: 62	Bands of Tb ₂ FeCrO ₆ within GGA. The horizontal dotted line indicates $E_F=0$	92
Figure: 63	Total and partial DOS of DPs Tb ₂ FeCrO ₆ under GGA+ <i>U</i> functional.	93
Figure: 64	Band structure of Tb ₂ FeCrO ₆ DPs within GGA+ <i>U</i> functional. . .	93
Figure: 65	Exchange paths between transitional elements Cr–Cr, Fe–Fe and Cr–Fe. Spins are assigned in [010] direction.	94

TABLE OF CONTENTS

	Page No.
Declaration	i
Recommendation	ii
Letter of approval	iii
Acknowledgment	iv
Abstract	vi
List of Acronyms and Abbreviations	viii
List of Tables	ix
List of Figures	xi
CHAPTER 1	1
1 INTRODUCTION	1
1.1 General Introduction	1
1.1.1 Perovskites	2
1.1.2 Double Perovskites	3
1.1.3 Half-Metals	4
1.2 Rational of the Study	5
1.3 Objectives of the Study	6
1.3.1 General Objectives	6
1.3.2 Specific Objectives	6
1.4 Organization of the Thesis	6

CHAPTER 2	8
2 LITERATURE REVIEW	8
2.1 Experimental based literature review:	8
2.2 Theoretical/ Computational based literature review:	9
2.3 Research Gap	11
CHAPTER 3	12
3 MATERIALS AND METHODS	12
3.1 Theoretical Background	12
3.2 Theoretical Details	12
3.2.1 The Many-Body System and Born-Oppenheimer (BO) Approximation	12
3.2.2 Hartree-Fock Approximation	14
3.2.3 Density Functional Theory	14
3.2.4 Thomas-Fermi-Dirac Approximation	15
3.2.5 Hohenberg-Kohn Theorem	16
3.2.6 First Hohenberg-Kohn (HK) Theorem	16
3.2.7 Second Hohenberg-Kohn (HK) Theorem	17
3.2.8 Kohn-Sham Theorem	18
3.2.9 Exchange-Correlation Functional	20
3.2.10 Local Density Approximation (LDA)	20
3.2.11 Generalized Gradient Approximation (GGA)	21
3.3 Methods of Electronic Structure Calculation	21
3.3.1 The Full Potential Augmented Plane Wave (APW) Methods	22
3.3.2 Band Structure	24
3.3.3 Density of States (DOS)	25
3.3.4 Crystal Field Theory	26
3.4 Computational Details	27
3.4.1 FP-LAPW+LO	28
3.5 Crystal Structures and Computational Details	30
CHAPTER 4	32
4 RESULTS AND DISCUSSION	32

4.1	Introduction	32
4.2	Ca-Based Double Perovskites:	
	Parent Material: $\text{Ca}_2\text{CrOsO}_6$	33
4.2.1	Electronic and Magnetic Properties	33
4.2.2	Thermoelectric Properties	37
4.2.3	Optical Properties	39
4.3	Ni Doped at Cr Site on Parent Material:	
	$\text{Ca}_2\text{Cr}_{0.5}\text{Ni}_{0.5}\text{OsO}_6$	41
4.3.1	Electronic and Magnetic Properties	41
4.4	Ir Doped at Os Site on Parent Material: $\text{Ca}_2\text{CrIrO}_6$	44
4.4.1	Stability of the Structure	45
4.4.2	Electronic and Magnetic Properties	45
4.4.3	Magnetic Ordering Temperature and Exchange Coupling Constant	48
4.5	Fe and Ir Doped at Cr and Os Site on Parent Material: $\text{Ca}_2\text{FeIrO}_6$	52
4.5.1	Stability of the Structure	52
4.5.2	Electronic and Magnetic Properties	53
4.5.3	Magnetic Ordering Temperature and Exchange Coupling Constant	56
4.6	Ni and Ir Doped at Cr and Os Site on Parent Material: $\text{Ca}_2\text{NiIrO}_6$	58
4.6.1	Electronic and Magnetic Properties	59
4.6.2	Magnetic Ordering Temperature and Exchange Coupling Constant	61
4.7	Mn and Ir Doped at Cr and Os Site on Parent Material: $\text{Ca}_2\text{MnIrO}_6$	61
4.7.1	Electronic and Magnetic Properties	62
4.7.2	Magnetic Ordering Temperature and Exchange Coupling Constant	65
4.8	Sr-Based Double Perovskites:	
	Parent Material: SrLaNiOsO_6	66
4.8.1	Electronic and Magnetic Properties	67
4.9	Fe Doped at Ni Site on Parent Material: SrLaFeOsO_6	75
4.9.1	Electronic and Magnetic Properties	75
4.10	Ru doped at Os Site on parent material: SrLaNiRuO_6	82
4.10.1	Electronic and Magnetic Properties	82
4.11	Tb-Based Double Perovskites: $\text{Tb}_2\text{FeCrO}_6$	90
4.11.1	Electronic and Magnetic Properties	90
4.11.2	Evaluation of Exchange Coupling Constant	93

CHAPTER 5	96
5 CONCLUSION AND RECOMMENDATIONS	96
5.1 Conclusion	96
5.2 Recommendations for Future Work	98
CHAPTER 6	99
6 SUMMARY	99
REFERENCES	101
APPENDIX	110

CHAPTER 1

INTRODUCTION

1.1 General Introduction

The study of all the materials that we use every day like metals, insulators, glass, ceramics, polymers or composite of these has been ongoing for as long as the existence of human being. Study deals with how materials work, designed and can we created for new application as technology. From the early age of human existence, humans started to use stones as materials for tools to improve their lives. The invention of materials have crucial role in forming and improving the society that we have today. Materials have direct interaction to the environment and the impact of any materials in environment is always interesting. Since, people are focusing to design of new material by various means such as by chemical doping, strain, temperature etc. The electrical band structures are wrealed to reveal the features of innovative materials which helps to predict several properties such as band gap, magnetic behavior, transport properties, etc which have large application in invention new modern devices to improve the quality of life. In the realm of solid state physics, the perovskite structure is very prevalent and technologically significant among the many materials, such as Huesler alloys, iridates, and rhodates. Oxides of the perovskite kind are crucial for fundamental research and applications such as lithium ion conductors and proton conductors, among others. It is also used to generate laser light, light-emitting diode (LED). The properties of perovskite i.e. superconductivity, magnetoresistance, ionic conductivity etc are great important in microelectronics and telecommunication. Advanced materials depending on the structural topology are noted to show interesting behaviour like Hall effects, Dirac or Weyl Fermions, flat band, etc that are relevant for quantum computing and advanced technology.

In present day, people demand smart devices and technology with portable size, high speed and greater accuracy. To fulfill such demand, study of Material Science and engineering is necessary. Computation simulation is the technique with which one can explore the novel properties of the materials by means of density functional theory.

1.1.1 Perovskites

Initially, Gustav Rose found the perovskite structure in the Russian Ural mountain in 1839. Perovskite is named in honor of scientist Lev Perovski. CaTiO_3 was the first found material in this structure. Thousands of examples of this kind of structure are now known.

Perovskite compounds have the chemical formula ABX_3 , with A and B being cations and X being an anion. The B-site cations are smaller and more electro-negative and A-site cations are often larger electro-positive metals. The A-site ions are usually alkaline earth or rare earth ion for example, Pb^{2+} , Bi^{3+} , Sr^{2+} , Ca^{2+} , La^{3+} . B-site ion might be 3d, 4d and 5d transition elements such as Cr^{3+} , Ru^{4+} , Os^{3+} , respectively. X-site ions are O^{2-} , F^- , Cl^- , Br^- , N^{3-} and S^{2-} . The co-ordination number of A and B-sites are 12 and 6, respectively.

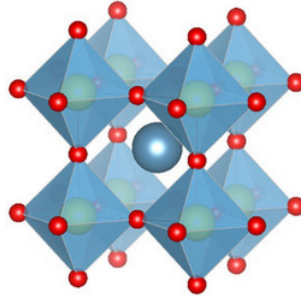


Figure 1: Crystal structure of CaTiO_3 perovskites (Moreira *et al.*, 2009).

The ideal perovskites have cubic symmetry. They are in the space group $Pm-3m$. Deformation of the ideal structure can lead to a variety of structural variants. Oxides of the perovskite kind are crucial for fundamental research and applications such as lithium ion conductors and proton conductors, among others. It is also used to generate laser light, light-emitting diode (LED). The properties of perovskite i.e. superconductivity, magnetoresistance, ionic conductivity etc are great important in microelectronics and telecommunication.

1.1.2 Double Perovskites

It is understood that there are many compounds with the perovskite structure since either of its three sites can undergo chemical replacement. Both cations and anions can be substituted in a variety of ways. In the perovskite either A-site or B-site multiple cations are used, these could be arranged in a random or systematic way. The two cation's different sizes and charges are often what determine the ordering. Both A and B-site cations are recognized to place orders, although the ways they do so varies greatly. The most frequent type of ordering in a rock-salt ordering that is prevalent in a 1:1 ratio is B-site cations. This would result in perovskite with the composition $A_2BB'X_6$. There is another type of perovskite $AA'BB'O_6$, This displays the A and A' cations ordered stacked and the B and B' cations ordered according to rock salt (Anderson *et al.*, 1993; Bidault *et al.*, 1995; Viana *et al.*, 1994; Trepakov *et al.*, 1995; Salce *et al.*, 1994). Tolerance factor (t) gives a relation between different cations and anions in DPs (Correa *et al.* 2010) which is given as,

$$t = \frac{r_A + r_O}{\sqrt{2}\left(\frac{r_B}{2} + \frac{r_{B'}}{2} + r_O\right)} \quad (1.1)$$

where r_A , r_B , $r_{B'}$ represent different radii of ions and r_O represents radius of oxygen. The DPs having structure $A_2BB'O_6$ are found by doping one of the ion at B sites with another B' ion. These types of compound are well studied experimentally and theoretically because of their unusual and alluring characteristics. Some of the DPs with structure $A_2BB'O_6$ have huge application in the field of spintronics due to their novel properties (Ishida *et al.*, 1995). Spintronic devices not only use the charge of the electron but spin of the electron is also used. The devices thus obtained are more efficient in memory devices in modern technology (Sadoc *et al.*, 2007; Fert 2008). Numerous research on the magnetic characteristics, crystal structure, and crystal development of 5d DPs oxides had been conducted experimentally. The finding of room-temperature CMR and half metallicity in Sr_2FeMoO_6 and Sr_2FeReO_6 (Wolf *et al.*, 2001; Kobayashi *et al.*, 1998; Sarma *et al.*, 2000; Tokura, 2006), multi ferroicity in Bi_2NiMnO_6 (Shimakawa *et al.*, 2011), magneto dielectricity in La_2NiMnO_6 (Rogado *et al.*, 2005), results to intensive research in DPs. Recent studies are focused to understand the different behaviour of 3d-4d (5d) containing DPs that are found with huge spin polarisability (Meetei *et al.*, 2013; Erten *et al.*, 2013; Feng *et al.*, 2014; Ghimire and Hu 2014, 2016).

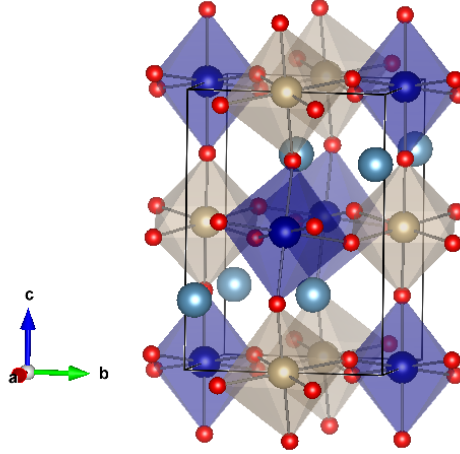


Figure 2: Crystal structure of double perovskites structure: $\text{Ca}_2\text{CrIrO}_6$.

$\text{AA}'\text{BB}'\text{O}_6$ perovskites may become unstable if the A-site cations have a significant size imbalance. The rock-salt arrangement sequence in $\text{A}_2\text{BB}'\text{O}_6$ perovskite can allow significant size mismatches among the cations which was discovered by Ward *et al.* in 1961 (Ward *et al.*, 1961). The A and A' layers must have identical lateral dimensions. The DPs structure has double of unit cell than perovskite structure. It has 12 co-ordinate A- site and 6 co-ordinate B-sites. The unique properties of these DPs arise from the combination of an electronically more localized 3d ions with a more delocalized 4d or 5d ions.

1.1.3 Half-Metals

Half metals (HM) have one spin channel metallic and enters a gap in the opposite spins channel. HM are the severe form of strong ferromagnets (or saturated Hubbard ferromagnets), wherein not only 3d electrons but also additional (s, p) down-spin bands can be completely polarized without crossing the E_F . On the other hand, a ferrimagnetic HM is one that has population of atoms with opposite magnetic moments as a result of anti-parallel alignment of two magnetic atoms that are not equal, as in anti-ferromagnets. HM antiferromagnetism on the otherhand has anti-parallel alignment of equivalent spins, as a result the total magnetization in the materials is zero. Due to either charge doping or distortion, the spin polarization at the Fermi level while its total moment remains zero. For their technical uses in spin electronics, read heads, magnetic RAM, nanoparticles, etc., all three forms of HM compounds have generated interest. Quantitative degree of half metallicity is defined by means of the spin polarizability

(P) which is given as:

$$P = \frac{\rho \uparrow (E_F) - \rho \downarrow (E_F)}{\rho \uparrow (E_F) + \rho \downarrow (E_F)} \quad (1.2)$$

where $\rho \uparrow (E_F)$ and $\rho \downarrow (E_F)$ represent density of states at Fermi level. The \uparrow and \downarrow represent the up and down spin states, respectively. Due to this, half metals can produce spin-polarized currents without use of external magnetic field, hence are useful for spintronic devices. Many substances having DPs structures have been suggested as potential candidates for half metallic ferromagnets (HMF) (Ghimire *et al.*, 2018; Hu *et al.*, 2014), half metallic ferrimagnets (HMF_iM) and HM antiferromagnets (HMAFMs) (Ghimire *et al.*, 2016).

1.2 Rational of the Study

At present, study on $A_2M_{1-x}M'_xTO_6$, is limited and few experimental systems are discovered despite of its attracting features suitable for significant uses of technology in spin electronics, Read Head, magnetic RAM, nano-particles etc. Recent studies on this class of material shows novel properties in DPs such as discovery of room-temperature CMR and half metallic behaviour in Sr_2FeMoO_6 and Sr_2FeReO_6 (Kobayashi *et al.*, 1998; Sarma *et al.*, 2000), multi ferroicity in Bi_2NiMnO_6 (Shimakawa *et al.*, 2011), magneto dielectricity in La_2NiMnO_6 (Rogado *et al.*, 2005), increases the need for DPs materials research. Recent studies have focused on understanding the electrical and magnetic characteristics in 3d-4d (5d) containing DPs that gives high spin polarization which is necessary for device applications at room temperature. In this context, the proposed project has a large scope in terms of spintronic which is relevant and necessary to extend scientific research in Nepal and abroad. This study is expected to be a resource program of studies for those who are interested in the field. Hence, study of $A_2M_{1-x}M'_xTO_6$ with the proposed full potential linear augmented plane wave method (FPLAPW) which enlightened the basic properties of the systems such as electronic, magnetic and optical properties. From the band structure and density of state calculations, one can have the idea about the nature of the solids i.e. either it is an insulator or metal or semiconductor. Most favorable conformal is found from the ground state (GS) energy calculation.

1.3 Objectives of the Study

1.3.1 General Objectives

The present work will mainly focus on the study of structural, electronic and magnetic properties (DOS and band structures) near E_F of the proposed material $A_2M_{1-x}M'_xTO_6$, (where $A = Ca, Sr, Tb$, M and $M' = Cr, Fe, Ni, Mn, Co$, $T = Os$ and Ir with substitution ratio $x = 0, 0.5, 1$), M , M' and T are transition metals.

1.3.2 Specific Objectives

- (a) Study of electronic and magnetic properties of Ca-based double perovskites, Sr-based double perovskites and Tb-based double perovskites.
- (b) Study of thermoelectric and optical properties of Ca-based parent material.

The obtained results will be communicated in conferences and will be published in the referred journals.

For the computation, full potential DFT-package with Wien2k code (Blaha *et al.*, 2001) will be used in addition to full-potential local-orbital (FPLO) code (Koepernik and Eschrig, 1999) and other codes as necessary. These code requires a LINUX based operating system (CentoS, Ubuntu, Mint, Fedora, Minderva, Puppy Linux, etc.) with FORTRAN compilers.

1.4 Organization of the Thesis

The organization of this thesis is done as follows:

- **Chapter 1:** We shall discuss about the introduction of the materials, rational and objectives of the study.
- **Chapter 2:** We shall discuss the available literature related to the present work. The chapter is named as Literature Review, which aims to prepare the required background and justify the objectives of the study.
- **Chapter 3:** We present the theoretical background, formulas and algorithm that we have used during the entire work in Materials and Methods. Basic introduction of density-functional theory with some special features including

about computational details and the systems under study are discussed in the chapter.

- **Chapter 4:** Here, we present Results and discussion of main findings of the present work.
- **Chapter 5:** The conclusions and possible extension of the present work are discussed. The chapter is named as Conclusions and Recommendations.
- **Chapter 6:** We discuss about the Summary of our findings and work before the list of references.

CHAPTER 2

LITERATURE REVIEW

2.1 Experimental based literature review:

Numerous research on 3d-4d(5d) DPs oxides' crystal structure, magnetic properties, and crystal formation have been conducted experimentally. Anderson *et al.* (1993) studied that due to its intriguing features that are advantageous for spintronic applications, DPs oxides have found many applications. These materials exhibit a range of electrical and magnetic characteristics, including metallicity, half-metallicity, insulator status, ferromagnetism, ferrimagnetism, and antiferromagnetism. Kobayashi *et al.*, (1998); Tokura *et al.*, (2006) investigated that room temperature CMR and HM character in $\text{Sr}_2\text{FeMoO}_6$ and $\text{Sr}_2\text{FeReO}_6$. Likewise, multiferrocity in $\text{Bi}_2\text{NiMnO}_6$ (Shi *et al.*, 2013) magneto dielectricity in $\text{La}_2\text{NiMnO}_6$ (Rogado *et al.*, 2005) has been reported. Among the DPs, magnetic insulating state in Sr_2MOsO_6 ($M = \text{Cu}, \text{Ni}$) (Tian *et al.*, 2011) has been found experimentally. In the Ba based double perovskites Ba_2XReO_6 ($X = \text{Mn}, \text{Fe}, \text{Co}, \text{Ni}$), only $\text{Ba}_2\text{FeReO}_6$ is metallic ferrimagnet, whereas $M = \text{Mn}, \text{Ni}$ compounds are found to be ferrimagnetic semiconductors (Sleight *et al.*, 1972). Similarly, Sleight *et al.* (1962) and Ramesha *et al.* (2000) studied A_2CrMoO_6 , A_2CrReO_6 and ALaMnReO_6 ($A = \text{Ca}, \text{Sr}, \text{Ba}$) and reported that materials are stable with semi-conducting behaviour. Kobayashi *et al.* (1998) reported that $\text{Sr}_2\text{FeReO}_6$ shows metallic and ferrimagnetic characteristics and huge tunneling magneto-resistance beyond 400 K. Comparable information on metallic magnetism was provided by Gopalakrishnan *et al.* (2000) in $\text{Ba}_2\text{FeReO}_6$. Besides its application in spintronic, $\text{A}_2\text{BB}'\text{O}_6$ has potential uses in photocatalysts, fluorescent, and microwave dielectric ceramic (Iwakuwa *et al.*, 2011; Bugarish *et al.*, 2003). Osmate oxides which have been recently synthesized are drawing a lot of interest and they are resulting in a variety of unusual phases. Transi-

tion from a metal to an insulator induced by magnetism is investigated in $\text{Cd}_2\text{Os}_2\text{O}_7$ (Yamaura *et al.*, 2012) and NaOsO_3 (Calder *et al.*, 2012). Transitional structure of the ferroelectric type is found in metallic LiOsO_3 (Shi *et al.*, 2013). Ferromagnetism with a Curie temperature of 458 K has been recorded in $\text{Sr}_2\text{FeMoO}_6$ and thin films of Sr_2CrWO_6 (Kobayashi *et al.*, 1998). It has been discovered that Fe-based DPs A_2FeBO_6 (A = Ca, Ba, Sr; B = Mo, Re) exhibits HM behavior and has a high $T_{\text{extrm}C}$ value (Telling *et al.*, 2008; Ritter *et al.*, 2000; Alonso *et al.*, 2000; Kato *et al.*, 2000). They have reported that $\text{Ca}_2\text{FeReO}_6$ stands out because it exhibits a metal-insulator transition. Similarly, Yuan *et al.* (2015) synthesized osmium DPs oxides B_2MgOsO_6 (B= Ca, Sr) that has a single magnetic element per formula unit, and examined the crystal structures and magnetic characteristics of these. Using first-principles DFT theory and the experimental results, they concluded that B_2MgOsO_6 (B= Ca, Sr) are nearly to be antiferromagnetic Mott-insulator. Its energy gap is significantly influenced by both the crystal field and electronic correlations U of 1.8-3 eV. The indirect band gap is investigated as 0.25 eV and 0.15 eV respectively, which is in close agreement with the experiment. No energy gap ever develops at E_F in the absence of " U ."

2.2 Theoretical/ Computational based literature review:

Recent investigations by Sarma *et al.* (2000); Meetei *et al.* (2013) and Erten *et al.* (2013) have focused on characterizing the electronic and magnetic characteristics of 3d-4d(5d) DPs, which display significant spin polarizability required for technological applications at ambient temperature. Among DPs structure Mott-insulating ferromagnetic state in $\text{Ba}_2\text{NaOsO}_6$ (Xiang *et al.*, 2007), and half semi-metallic AFM in $\text{Sr}_2\text{CrOsO}_6$ (Lee *et al.*, 2008) are some of the reported cases. Numerous DPs explored from first-principle calculation reported with half metallic ground state (HM GS) (Fang *et al.*, 2001; Hua *et al.*, 2001). Recent research has focused on Sr-based $\text{Sr}_2\text{BB}'\text{O}_6$ with B = Mo, Re, W and Te because of their high magneto resistance (Zhao *et al.*, 2005; Azad *et al.*, 2002; Tian *et al.*, 2006). Most generally few of the $\text{A}_2\text{BB}'\text{O}_6$ show both metallic and magnetic properties, and several of them are semiconductor with ferromagnetic GS. Chattopadhyay *et al.* (2001) stated that as A switches from Ba to Sr to Ca, the shift from metal to insulator occurs in $\text{A}_2\text{Fe}(\text{Re}/\text{Mo})\text{O}_6$. Rai *et al.* (2015) examined the electronic, magnetic and optical characteristics of A_2FeReO_6 (A= Sr, Ba) and revealed HM characteristics on it. On the group of iridate perovskites, Ghimire

et al. (2016) investigated the $\text{Pr}_2\text{MgIrO}_6$ and observed that on hole doping (Sr) to Pr site, insulator metal transition was observed. It was found that upon 50% Pr replacement with Sr, HMAFM was discovered despite of strong spin-orbit coupling due to Pr and Ir ions. Substantial interest has been generated by recent progress in synthesizing osmium oxides, which has led to the formation of several unusual phases. For instance, $\text{A}_2\text{Os}_2\text{O}_7$ (A = Cs, Rb and K) exhibits anomalous superconductivity (Hiroi *et al.*, 2012). On the family of newly synthesized osmium double perovskites, $\text{Ca}_2\text{FeOsO}_6$ shows interesting features (Feng *et al.*, (2014); Ghimire & Hu (2014, 2016). This material is found to be a ferrimagnetic Mott insulator having effective moment $\mu_{tot} = 4 \mu_B$ /unit cell in agreement with experimental finding of Feng (2013). This material was found interesting from first-principles investigation because contribution around Fermi level was only by Os-5d electrons in spin down state and Fe-3d state have no contribution there. Furthermore, one may get exquisite controlling over charge and spin by substituting Fe with 3d elements larger than five valence electrons. Specially, the replacement of iron atom by the nickel atom was considered to identify the half-metallic antiferromagnetism and half-metallic ferrimagnetism which is desirable in spintronics. There are many orthochromites and orthoferrites studied in past. TbCrO_3 had shown the spontaneous magnetization (Gordan *et al.*, 1976). The mixture of orthoferrites and orthochromites compound, $\text{Bi}_2\text{FeCrO}_6$, has a very large polarization and magnetization, therefore shows the multiferroic property. This multiferroic material can be used to develop spintronic devices (Baettig *et al.*, 2005). The multiferroicity of this material can enhance the development of nanostructure material because it can be used as the magnetic and the electric component simultaneously (Nechache *et al.*, 2012) and photovoltaics material (Nechache *et al.*, 2015). $\text{TbFe}_{0.5}\text{Cr}_{0.5}\text{O}_3$ and $\text{DyFe}_{0.5}\text{Cr}_{0.5}\text{O}_3$ show the spin reorientation transition property, in which the spin of the magnetic atoms rotate around c-axis (Bolletta *et al.*, 2019). A significant size disparity among the cations might cause instability on $\text{AA}'\text{BB}'\text{O}_6$ perovskites. In $\text{A}_2\text{BB}'\text{O}_6$ perovskite the rock-salt ordering can accommodated asignificant extent of size disparity among the cations, which was discovered by Ward *et al.*,(1961).

From the above literature survey, it is found that $\text{A}_2\text{MM}'\text{O}_6$ is still in initial phase of study both experimentally and theoretically despite of enormous properties it has shown recently (Feng *et al.*, 2014; Ghimire *et al.*, 2014). From these survey, it can be concluded that new material invention as half metals related to research into the magnetic and electronic characteristics in $\text{A}_2\text{M}_{1-x}\text{M}'_x\text{TO}_6$ compounds are possible and

might be robust to work on or above room temperature.

2.3 Research Gap

- $A_2M_{1-x}M'_xTO_6$ is still in initial phase of study both experimentally and theoretically
- New material invention/prediction with substitution of different 3d-4d (5d) transition metals could be possible
- DPs with FiM GS exhibit high spin polarization essential for modern device applications however limited work has been done
- Study of thermoelectric and optical properties on DPs is limited: need to be explored

CHAPTER 3

MATERIALS AND METHODS

3.1 Theoretical Background

In this chapter, we discuss about the basic theory upon which our calculations are based like DFT and methods of electronic structure calculation. Hartree-Fock approach considers the the asymmetric product of single electron wave function. It explains the correlation brought on by identical-spin electrons, but the motion with the opposite spin is not associated (Grosso *et al.*, 2000; Agrawal *et al.*, 2010). The approaches that deal with the phenomena connected to the many electron system beyond Hartree-Fock indicate electron correlation methods. The first-principle method which takes account of electron correlation is DFT. The electronic orbitals are solution to a Schrodinger equation which relies on the electron density in DFT. In the theory, the electronic states are addressed for self-consistency using the Hartree-Fock model. The exchange correlation is stated like functional of electron density. The exchange-correlation potential contains both dynamic correlation effect caused by the Coulomb repulsion between the electrons and the exchange-interaction resulting from wave function's asymmetry.

3.2 Theoretical Details

3.2.1 The Many-Body System and Born-Oppenheimer (BO) Approximation

The Hamiltonian for many body system with nuclei and electrons can be written as:

$$H = - \sum_I \frac{\hbar^2}{2M_I} \nabla_{R_I}^2 - \sum_i \frac{\hbar^2}{2m_e} \nabla_{r_i}^2 + \frac{1}{2} \sum_{I,J \neq J} \frac{Z_I Z_J e^2}{|R_I - R_J|} + \frac{1}{2} \sum_{i,j,i \neq j} \frac{e^2}{|r_i - r_j|} - \sum_{I,i} \frac{Z_I e^2}{|R_I - r_i|} \quad (3.1)$$

Where, The indices I, J , and i, j represent nuclei and electrons, R_I and M_I are locations and masses of the nuclei, r_i and m_e for the electrons and Z_I the atomic number of nucleus. The Ist and IInd term represents the kinetic energy (K.E.) of the nuclei and electron, respectively.

The IIIrd, IVth and Vth term represents the potential energy (P.E.) of the Coulomb interaction between the nuclei, between the electrons and Coulomb interaction between the nuclei and electrons, respectively.

The time independent Schrodinger equation for the system:

$$H_{tot}\psi\{(R_I), (r_i)\} = E\psi\{(R_I), (r_i)\} \quad (3.2)$$

Where, $\psi\{(R_I), (r_i)\}$ represents total wave function of the system.

Everything about the system is known if the above mentioned Schrodinger equation can be solved. But there is no practical way to resolve it. Thus, Born and Oppenheimer created the Born-Oppenheimer approximation (1927). The mass of a proton is approximately 1836 times that of an electron, making nuclei substantially heavier than electrons. As a result, nuclei travel more slowly than electrons by roughly two orders of magnitude. As a result, we can distinguish between the motion of nuclei and electrons.

Then the total wave function can be written as,

$$\psi\{(R_I), (r_i)\} = \Theta\{(R_I)\}, \phi\{(r_i); (R_I)\} \quad (3.3)$$

Where, $\Theta\{(R_I)\}$ and $\phi\{(r_i); (R_I)\}$ describe the nuclei and electrons respectively. By using the BO approximation above equation can be divided into two separate S.E.,

$$H_e\phi\{(r_i), (R_I)\} = V\{(R_I)\}\phi\{(r_i); (R_I)\} \quad (3.4)$$

where,

$$H_e = -\sum_i \frac{\hbar^2}{2m_e} \nabla_{r_i}^2 + \frac{1}{2} \sum_{I, J, I \neq J} \frac{Z_I Z_J e^2}{|R_I - R_J|} + \frac{1}{2} \sum_{i, j, i \neq j} \frac{e^2}{|r_i - r_j|} - \sum_{I, i} \frac{Z_I e^2}{|R_I - r_i|} \quad (3.5)$$

and

$$\left[-\sum_I \frac{\hbar^2}{2M_I} \nabla_{R_I}^2 + V\{R_I\} \right] \Theta\{R_I\} = E' \Theta\{R_I\} \quad (3.6)$$

After the solution of equation (3.4), $V\{R_I\}$ is obtained and application on equation (3.6), which has no electronic degree of freedom, the motion of the nuclei is obtained. The importance of BO approximation is to distinguish the motion of electrons and nuclei.

3.2.2 Hartree-Fock Approximation

Hartree methods were introduced by Hartree and later Hartree-Fock (HF) was developed by Slater, Fock and others in the late 1920. These approximations are mainly used to study the electronic structure of atoms with more than one electron. The characteristics of atoms, molecules, and solids are often computed using these HF approaches. It is also used for the determination of the wave function and the energy of quantum many body system (i.e. N-body). The two fundamental approximations used in this method are that the atomic nuclei are infinitely heavy and, as a result, fixed in space at their equilibrium positions. Another one is the many electron wave functions are a product of a single electron wave function that is fully antisymmetrized because electrons are fermions and must adhere to the Pauli exclusion principle. The difference of the exact non-relativistic ground state energy of the system and HF energy with the infinite basis set is called the correlation (Blinder *et al.*, 1965) or the error in HF approximation is known as correlation. For large Z value, Hartree and exchange dominates over correlation but when Z is order of one, correlation becomes important. The N electron anti-symmetric product of N single particle spin-orbitals is conveniently written as a determinant, known as the Slater determinant named after John Slater,

$$\psi(1, 2, \dots, N) = \frac{1}{\sqrt{N!}} \begin{vmatrix} \phi_1(1) & \dots & \phi_1(N) \\ \dots & \dots & \dots \\ \phi_N(1) & \dots & \phi_N(N) \end{vmatrix}$$

If two exchange particles are identical to the exchange of two column, then the determinant sign has changed. Pauli's exclusion principle, which states that two or more identical fermions cannot have the same state, is demonstrated when two rows have equal determinants, which equal to zero.

3.2.3 Density Functional Theory

DFT is the system which finds the ground state properties without dealing directly with the many electron state. Old DFT is Thomas-Fermi theory in 1926. In addition to proposing LDA and Gradient Expansion Approximation (GEA) in 1965, Kohn-Sham equations are foundation of modern DFT. The Nobel Prize in Chemistry was then given to Walter Kohn in 1998 for creating DFT. Currently DFT is assumed to be best method to calculate the electronic structure. It may be applied with different compounds in both quantum and conventional materials. It is a computational quantum mechanical approach utilized in the fields of material sciences, physics, and chemistry. It is one of the most well-known and useful techniques used in computational physics, condensed matter physics, and computational chemistry. Computational cost is also low as compared to traditional methods i.e. Hartree-Fock method and other methods.

In DFT the wave function ψ is substituted with electron density. DFT's basic principle is to use a system's particle density rather than its many-body wave function to characterize a many-body system. Because of its particle density, it has the potential to decrease the $3N$ degrees of freedom to only three spatial coordinates. The original DFT is expanded to cover a broad area of circumstances.

The electron density is the most essential parameter in DFT. The possibility of getting anyone of the N electrons in the volume $d\mathbf{r}$ is given by,

$$n(r) = N \int \dots \int |\psi(x_1, x_2, \dots, x_N)|^2 dx_1 dx_2 \dots dx_N \quad (3.7)$$

where, $n(\mathbf{r})$ represents non-negative function of only the 3 spatial variable that disappears at infinity and integrates to the total no. of electrons:

$$\begin{aligned} n(r) &\leq 0 \\ n(r \rightarrow \infty) &= 0 \\ \int n(r) dr &= N \end{aligned}$$

The $n(r)$ might be measured empirically, for instance, via X-ray diffraction.

3.2.4 Thomas-Fermi-Dirac Approximation

Thomas-Fermi (TF) model which is familiar as old DFT was proposed by Llewellyn Thomas and Enrico Fermi in 1927. Instead of the wave function, they employed the electron density $n(\mathbf{r})$ as the fundamental variable in their approach. The external potential $V_{ext}(\mathbf{r})$ can be expressed as a function of the electron density $n(\mathbf{r})$ like,

$$E_{TF}[n(\mathbf{r})] = A_1 \int \{n(\mathbf{r})\}^{5/3} d\mathbf{r} + \int n(\mathbf{r}) V_{ext}(\mathbf{r}) d\mathbf{r} + \frac{1}{2} \int \int \frac{n(\mathbf{r})n(\mathbf{r}')}{|\mathbf{r} - \mathbf{r}'|} d\mathbf{r} d\mathbf{r}' \quad (3.8)$$

where, the first term is K.E. of the non interacting electrons in a homogeneous electron gas (HEG) with $A_1 = \frac{3}{10}(3\pi^2)^{2/3}$ in atomic units. Second and third terms are nuclear-electron and electron-electron interactions respectively. In the main TF approach, the exchange and correlation among electrons was not taken into account. In 1928, this model was improved by Dirac by adding exchange term, $A_2 \int n(\mathbf{r})^{4/3} d\mathbf{r}$ to equation (3.8) with $A_2 = -\frac{3}{4}(3/\pi)^{1/3}$. With the inclusion of this term, Thomas Fermi Dirac (TFD) equation becomes,

$$E_{TFD}[n(\mathbf{r})] = A_1 \int \{n(\mathbf{r})\}^{5/3} d\mathbf{r} + \int n(\mathbf{r}) V_{ext}(\mathbf{r}) d\mathbf{r} + \frac{1}{2} \int \int \frac{n(\mathbf{r})n(\mathbf{r}')}{|\mathbf{r} - \mathbf{r}'|} d\mathbf{r} d\mathbf{r}' + A_2 \int \{n(\mathbf{r})\}^{4/3} dr \quad (3.9)$$

By minimizing TFD equation, one may determine the GS density and energy. By using the technique of Lagrangian multipliers, then TFD equation becomes,

$$\frac{5}{3}\{n(\mathbf{r})\}^{2/3} + V_{ext}(\mathbf{r}) + \int \frac{n(\mathbf{r}')}{|\mathbf{r} - \mathbf{r}'|} d\mathbf{r}' + \frac{4}{3}A_2\{n(\mathbf{r})\}^{1/3} - \mu = 0 \quad (3.10)$$

Since this theory does not explain atomic bonding, molecules and solids cannot exist according to it (Teller, 1962). Though it falls short of adequately describing electrons in matter, the idea of using electron density as the fundamental variable serves to demonstrate how DFT operates.

3.2.5 Hohenberg-Kohn Theorem

This theorems published by the P. Hohenberg and W. Kohn in 1964 called as Hohenberg-Kohn (HK) theorems (Hohenberg & Kohn, 1964). HK theorem is applicable if a particle is moving in an external field of potential $V(\mathbf{r})$. According to this, the wave function of non-degenerate case is unique functional of the particle GS density $n_0(\mathbf{r})$ (Kohn & Sham, 1965). It is mainly divided into two theorem as follows:

3.2.6 First Hohenberg-Kohn (HK) Theorem

According to this theorem, the external potential $V_{ext}(\mathbf{r})$ is a unique function of particle GS density $\rho(\mathbf{r})$. Then we have to show that two distinct GS wave functions cannot have the identical GS density.

Let two different system with GS wave functions ψ_0 and ψ'_0 . The K.E. operator for the N-electron system is ' T ', the operator that describe interaction is ' W ' and $V = \sum v(\mathbf{r}_i)$ are the external potential of the two systems. If we consider,

$$V(\mathbf{r}) \neq V'(\mathbf{r}) + c$$

where, c is constant. This assumes that GS PE of one system $V(\mathbf{r})$ is not equal with GS PE of the system with another wave function.

Then,

$$H\psi_0 = (T + W + V)\psi_0 = E_0\psi_0 \quad (3.11)$$

$$H'\psi'_0 = (T + W + V)\psi'_0 = E'_0\psi'_0 \quad (3.12)$$

Starting with the two system described by equation (3.11) and (3.12),

$$H = H' + V - V'$$

The ground of system 1 is,

$$E_0 = \langle \psi_0 | H | \psi_0 \rangle$$

From the variational theorem this must be less than expectation value, $\langle \psi_0 | H | \psi_0 \rangle$ because the wave function, ψ'_0 is not the lowest eigenstate of H , i.e. ψ'_0 can not the correctly explain the GS energy of system 1.

Therefore,

$$E_0 < \langle \psi'_0 | H | \psi'_0 \rangle$$

$$E_0 < \langle \psi'_0 | H' + V - V' | \psi'_0 \rangle$$

$$E_0 < \langle \psi'_0 | H' | \psi'_0 \rangle + \langle \psi'_0 | v - v' | \psi'_0 \rangle$$

$$E_0 < E'_0 + \int n'_0(\mathbf{r})[V(\mathbf{r}) - V'(\mathbf{r})]d\mathbf{r} \quad (3.13)$$

where, $\langle \psi'_0 | H | \psi'_0 \rangle = \int n'_0(\mathbf{r})V(\mathbf{r})d\mathbf{r}$ $n_0(\mathbf{r}) = \int |\psi(\mathbf{r}_1, \mathbf{r}_2, \dots, \mathbf{r}_N)|^2 d\mathbf{r}_1 d\mathbf{r}_2 \dots d\mathbf{r}_N$

Similarly, from the variational theorem, we are aware that the GS energy E'_0 of the system 2 must be less than the expectation value of $\langle \psi'_0 | H' | \psi'_0 \rangle$,

$$\therefore E'_0 < E_0 + \int n_0(\mathbf{r})[V'(\mathbf{r}) - V(\mathbf{r})]d\mathbf{r} \quad (3.14)$$

If we assume, ψ_0 and ψ'_0 can have the same GS density then we can write $n_0(\mathbf{r}) = n'_0(\mathbf{r})$.

Then,

$$E_0 + E'_0 < E'_0 + E_0$$

Therefore, two distinct GS wave functions can not have the same GS density.

3.2.7 Second Hohenberg-Kohn (HK) Theorem

This theorem states that, two distinct potentials can not produce the identical GS wave function.

If the two systems described by different potentials, V and V' have identical GS wave function $\psi_0 = \psi'_0$ then,

$$(V - V')\psi_0 = (E_0 - E'_0)\psi_0$$

Then, clear contraction to the requirement that the potential be different,

$$(V - V') = (E_0 - E'_0)$$

Thus, if the GS wave function of two system are the same, the potential that describe those systems can only differ by a constant.

Thus, two distinct potential can not produce the identical GS wave function.

3.2.8 Kohn-Sham Theorem

Kohn-Sham equation (KS) takes into account of orbital effect and makes DFT practicable. It decompose the GS density $n(\mathbf{r})$ of interacting electron system into the sum of N independent orbital contributions. (Kohn & Sham, 1965). It is much easier to solve than the coupled Schrodinger equation. The great advantage of the KS equation over Thomas-Fermi theory is that almost all the K.E. (T_S) is treated exactly.

The GS energy of the system,

$$E_0 = \min_{n \rightarrow N} \left[E(n) + \int n(\mathbf{r}) V_{Ne} d\mathbf{r} \right] \quad (3.15)$$

where, $E(n)$ represents universal function containing K.E., the classical Coloumb interaction and non clasical part,

$$E(n) = T(n) + J(n) + E_{ncl}(n) \quad (3.16)$$

Here, only $J(n)$ is well recognized. The major challenge is finding the $T(n)$ and $E_{ncl}(n)$. KS developed the strategy shown below in 1965 to address this issue. To determine the precise K.E. of a reference system that doesn't interact but has the same density,

$$T_s = -\frac{1}{2} \sum_i^N \langle \psi_i | \nabla^2 | \psi_i \rangle$$

$$n_s(\mathbf{r}) = \sum_i^N \sum_s |\psi_i(\mathbf{r}, s)|^2 = n(\mathbf{r}) \quad (3.17)$$

where, ψ_i = orbital of the independent system.

T_s does not represents the real K.E. of the system. Kohn and Sham resolved this by considering the separation of the functional as $E(n)$,

$$E[n] = T_s(n) + J(n) + E_{XC}(n) \quad (3.18)$$

where, E_{XC} = Exchange corelation energy

$$E_{XC} = (T(n) - T_s(n) + (E_{ee}(n) - J(n))) \quad (3.19)$$

Equation (3.18) can be written as,

$$E[n] = T_s(n) + J(n) + E_{XC}(n) + E_{Ne} \quad (3.20)$$

$$E[n] = T_s(n) + \frac{1}{2} \iint \frac{n(\mathbf{r}_1)n(\mathbf{r}_2)}{r_{12}} d\mathbf{r}_1 d\mathbf{r}_2 + E_{XC}(n) + \int V_{Ne} n(\mathbf{r}) d(\mathbf{r}) \quad (3.21)$$

$$E(n) = -\frac{1}{2} \sum_{i=1}^N \langle \psi_i | \nabla^2 | \psi_i \rangle + \frac{1}{2} \sum_i^N \sum_i^N \int \int |\psi_i(\mathbf{r}_1)|^2 \frac{1}{|\mathbf{r}_1 - \mathbf{r}_2|} |\psi_j(\mathbf{r}_2)|^2 d(\mathbf{r}_1) d(\mathbf{r}_2) + E_{XC}(n) - \sum_i^N \int \sum_A^M \frac{Z_A}{|\mathbf{r}_1 - \mathbf{R}_{1A}|} |\psi_i(\mathbf{r}_1)|^2 d\mathbf{r}_1 \quad (3.22)$$

The term that cannot have an explicit form is E_{XC} . The resulting equations are KS equations,

$$\left(-\frac{1}{2} \nabla^2 + \int \frac{\rho(\mathbf{r}_2)}{|\mathbf{r}_1 - \mathbf{r}_2|} d\mathbf{r}_2 + V_{xc}(\mathbf{r}_1) - \sum_A^M \frac{Z_A}{|\mathbf{r}_1 - \mathbf{R}_{1A}|} \right) \psi_i = \left(-\frac{1}{2} \nabla^2 + V_s(\mathbf{r}_1) \right) \psi_i = \epsilon_i \psi_i \quad (3.23)$$

$$V_s(\mathbf{r}_1) = \int \frac{n(\mathbf{r}_2)}{|\mathbf{r}_1 - \mathbf{r}_2|} d\mathbf{r}_2 + V_{xc}(\mathbf{r}_1) - \sum_A^M \frac{Z_A}{|\mathbf{r}_1 - \mathbf{R}_{1A}|} \quad (3.24)$$

where, $V_{XC} = \frac{\delta E_{XC}}{\delta n}$

It is crucial to understand that the KS technique would provide the correct energy if the precise form of E_{XC} and V_{XC} were known.

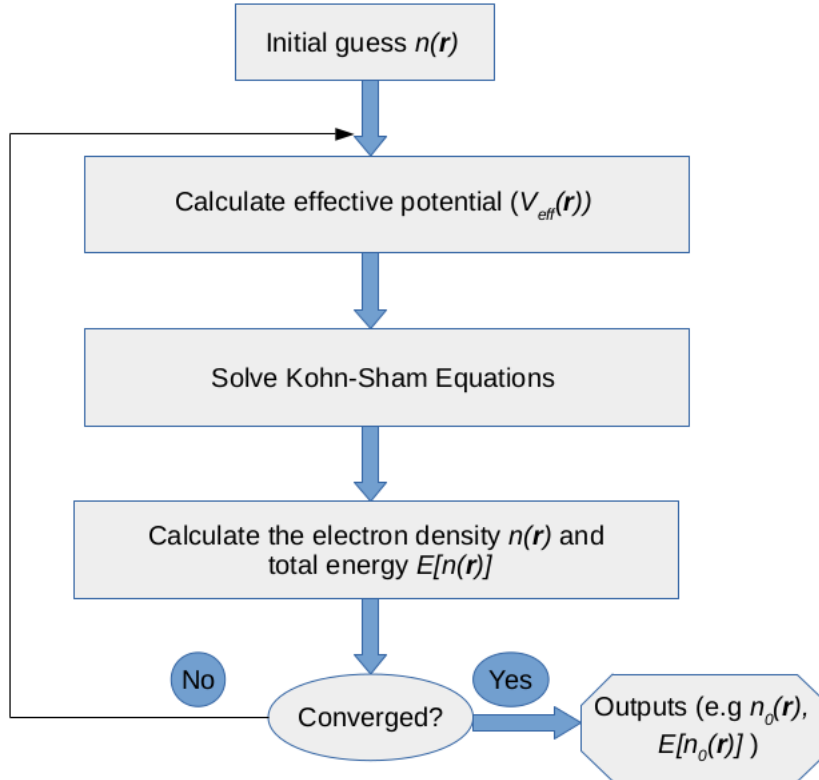


Figure 3: Self-consistency flow chart showing working procedure in KS formalism (Kohn & Sham, 1965).

3.2.9 Exchange-Correlation Functional

The main problem with the Kohn-Sham procedure described above is the introduction of an unknown exchange-correlation functional. As long as there is no expression for this term, it is impossible to solve the KS equations. The main objective of contemporary DFT is to investigate improved approximation for these two values. Therefore, in search of explicit form of these functional, many approximations have been developed. The most popular approaches in material science are the local density approximation (LDA) and the generalized gradient approximation (GGA).

3.2.10 Local Density Approximation (LDA)

The Kohn-Sham strategy accounts for a viable technique to apply density functional theory. It provides a realistic and manageably simple approximation for the exchange-correlation energy E_{xc} . Local density theories based on the HK theorem have been applied to atoms and molecules. The precise functionals for exchange and correlation are unknown which is the main issue with DFT except in an approximation for the interacting uniform electron gas. For the later, numerical data are available from Quantum Monte Carlo (QMC) calculations (Ceperley & Alder, 1984). But, some approximation exists like LDA, which is most widely used approximation. The approximation makes it possible to calculate several physical quantities with great accuracy.

All approximation exchange-correlation functionals are built on the LDA. The concept of a uniform electron gas lies at the core of this paradigm. The foundation of LDA is the premise that we may express E_{xc} as below,

$$E_{xc}^{LDA}[n] = \int n(\mathbf{r})\epsilon_{xc}(n(\mathbf{r}))d\mathbf{r} \quad (3.25)$$

Here, $\epsilon_{xc}(n(\mathbf{r}))$ is exchange-correlation energy per particle of an uniform electron gas of density $\rho(\mathbf{r})$. Taking the functional derivative of E_{xc}^{LDA} , we find exchange-correlation potential as

$$v_{xc}^{LDA} = \frac{\delta E_{xc}^{LDA}}{\delta n} = \epsilon_{xc}[n(\mathbf{r})] + n(\mathbf{r})\frac{\partial \epsilon_{xc}[n]}{\partial n} \quad (3.26)$$

The exchange-correlation energy per particle $\epsilon_{xc}(n(\mathbf{r}))$ can be decomposed into exchange and correlation terms linearly,

$$\epsilon_{xc}(n(\mathbf{r})) = \epsilon_x(n(\mathbf{r})) + \epsilon_c(n(\mathbf{r})) \quad (3.27)$$

Now, equation (3.24) can be written as

$$E_{xc}^{LDA}[n] = \int n(\mathbf{r})[\epsilon_x(n(\mathbf{r})) + \epsilon_c(n(\mathbf{r}))] = E_x[n(\mathbf{r})] + E_c[n(\mathbf{r})] \quad (3.28)$$

For spin polarized systems,

$$E_{xc}^{LSDA}[n_{\uparrow}(\mathbf{r}), n_{\downarrow}(\mathbf{r})] = \int n(\mathbf{r})\epsilon_{xc}[n_{\uparrow}(\mathbf{r}), n_{\downarrow}(\mathbf{r})]d\mathbf{r} = \int n(\mathbf{r})[\epsilon_x[n_{\uparrow}(\mathbf{r}), n_{\downarrow}(\mathbf{r})] + \epsilon_c[n_{\uparrow}(\mathbf{r}), n_{\downarrow}(\mathbf{r})]]d\mathbf{r} \quad (3.29)$$

The exchange term $\epsilon_x[n]$ is first derived originally by Bloch and Dirac which is given by atomic units as,

$$\epsilon_x[n] = -\frac{0.458}{r_s} \quad (3.30)$$

Where, r_s represents the radius of a sphere containing single electron and is given by, $(4\pi/3)r_s^3 = n^{-1}$. The correlated part is first estimated by Wigner (1934) and is given as

$$\epsilon_c[n] = -\frac{0.44}{r_s + 7.8} \quad (3.31)$$

The accuracy of LDA is often considered satisfactory in condensed matter system, but it is much less so in atomic and molecular physics, for which highly accurate experimental data are available. For the case of cohesive energy and bond strengths in molecules and solids LDA overestimates, so this problem is corrected by introducing gradient corrections, i.e. GGA.

3.2.11 Generalized Gradient Approximation (GGA)

GGA is also most widely used approximation in solid state physics (Perdew, 1996). It gives a more reliable result for the main type of chemical bonds such as covalent, ionic, metallic, and hydrogen bridge. So, GGA is considered as an improved approximation over LDA. In GGA, gradient correlation are added.

The exchange-correlation energy in terms of GGA,

$$E_{XC}^{GGA} = \int \epsilon_{xc}(n(\mathbf{r})|\nabla n(\mathbf{r})|, \dots)d\mathbf{r} \quad (3.32)$$

Potentially meta-GGA is more accurate than the GGA Functionals. Meta-GGA DFT is based on second derivatives of the electron density. Whereas, GGA has only the first derivative and density.

3.3 Methods of Electronic Structure Calculation

The most precise tool for solid-state electronic structure computation is the WIEN2k code that depends on linearized augmented plane wave (LAPW) (Blaha *et al.*, 2001). Relativistic treatment is given to core energy levels, whereas semi-relativistic treatment or the second variational technique with SOC is given to valence levels. A plane wave expansion is employed

for the operations in other places. Every plane wave is elevated with atomic function in atomic sphere. Using the linear variation approach, the KS equation solution is enlarged in the coupled basis set of LAPWs. Additional basis functions known as local orbitals (LO) can be introduced to enhance linearization and to enable an uniform handling of semicore and valence state in same energy window. Since, it makes no use of shape approximations, hence it is commonly referred to as a full potential method (FP-LAPW).

3.3.1 The Full Potential Augmented Plane Wave (APW) Methods

The Linearized Augmented Plane Wave (LAPW) Method

Among many approach, the most popular technique for calculating the electrical structure of crystals is the linearized augmented plane wave (LAPW) approach. For the consideration of exchange and correlation, it is based on DFT and employs techniques like LSDA. The literature has many types of LSDA potentials, but more recent enhancements utilizing the generalized gradient approximation (GGA) are also accessible. Relativistic effects is applied for valence states using a scalar relativistic treatment with SOC. The Core states receive complete relativistic treatment. Every detail of LAPW method is explained by Singh, (2001). However, the basic ideas of energy-band methods, the LAPW technique is used for getting solution of KS equations for the GS density, total energy, and KS eigen values. The main steps tailored to the problem is described as follows:



Figure 4: (a) Partition of the unit cell into atomic spheres (I) and an interstitial region (II), (b) Mufin-tin potential model (Pashov *et al.*, 2020).

From Fig. 4, the unit cell is divided into non-conjoining atomic spheres that are centered at the atomic sites and an area known as the interstitial region. For the different types of basis sets are used:

1.) Inside atomic sphere with the radius ‘R’, a linear combination of radial functions times spherical harmonics $Y_{lm}(\vec{r})$ is used

$\Phi_{k_n} = \sum_{lm} [A_{lm,k_n} u_l(r, E_l) + B_{lm,k_n} v_l(r, E_l)] Y_{lm}(\vec{r})$ where, $u_l(r, E_l)$ represent regular solution of the radial SE for energy E_l and the spherical portion of the potential of the sphere $u_l(r, E_l)$

represents energy derivative of u_l examined at the same energy E_l . The coefficients A_{lm} and B_{lm} are functions of k_n determine the required that the each plane wave's associated basis function for the interstitial area is matched by the basis function.

2.) In interstitial region plane wave expansion is employed

$$\phi_{k_n} = \frac{1}{\sqrt{w}} e^{ik_n \cdot r}$$

where, $k_n = k + k_n$ represent the reciprocal lattice vectors. Every atomic sphere has an atomic-like function that enhances each plane wave.

The results obtained by solving the KS equations are extended in basis set of LAPW's as per linear variation approach

$$\psi_k = \sum_n c_n \phi_{k_n}$$

Here, coefficients c_n are investigated using the Rayleigh-Ritz variational principle.

Various basis functions could be introduced to enhance the linearization and provide a consistent handling of semi-core and valence levels within one energy region. These are referred to as local orbitals (LO), and are expressed as:

$$\phi_{lm}^{LO} = [A_{lm,k_n} u_l(r, E_l) + B_{lm,k_n} u_l(r, E_l)] Y_{lm}(\vec{r})$$

A_{lm} , B_{lm} and C_{lm} are found by normalising ϕ^{LO} .

Full Potential Local Orbital (FPLO) Code

Among the computational codes based on DFT for electronic structure calculation, FPLO is a code that is easy for handling, has high accuracy, and gives the stability of the numerics. This code is based within a framework of KS and Kohn-Sham-Dirac equation. FPLO features a non-relativistic version of calculation (Koepernik & Eschrig, 1999). In non-relativistic FPLO, extended states are a linear combination of LO that in turn gives a solution like SE with a spherically average potential. In this version, orbitals are classified as core state and valence state. Non overlapping states from different sites are considered to be core states while overlapping states are treated as valence states. It contains three modes of relativistic calculations: scalar relativistic [2 category] and full relativistic. So, as a whole there are four different variants of relativistic calculations are available in FPLO. For exchange-correlation potential it has two functionals: GGA of the Perdew-Burke-Ernzerhof functional and Local Spin Density Approximation (LSDA). For highly correlated systems, LSDA+ U and GGA+ U are implemented (Eschrig *et al.*, 2003). Atomic position optimization can be performed via force calculation which is implemented in non-relativistic and for scalar relativistic modes. While performing the calculation in FPLO, we should be familiar with different features available within this computation code. These are explained below:

1] FEDIT

- It is input file editor.

- It generate input file as =.in
- Latest version used in our calculation is fedit18.00–52–x86 64.

2] XFPLO

- It is used for the visualization of structures and Fermi surfaces and the Brillouin zone
- Splitting of structure, generation of supercell, structure, and symmetry manipulation.
- It reads the cif file, imports it and converts into executable =.in file.
- It provides automatic path construction with automatic point labels for all sym metries in the Fermi surface mode.

3] FPLO

- Performs Kohn-sham calculation.
- Latest version used in our calculation is fplo18.00–52–x86 64.
- Final output provides information on the system such as energy, charge state, magnetic moment, energy band gap, etc.

3] FOPTICS

- Tool for optical properties calculation.
- It calculate dielectric function, optical conductivity and loss function.
- Latest version used in our calculation is foptics18.00–52–x86 64.

4] XFBP

- Graph plotting tool.
- Helps to plot graph of different calculations such as: band structure, DOS, dielectric function, optical conductivity, loss function etc.

3.3.2 Band Structure

When a solid is produced, the energy levels in the atoms and molecules can split into a nearly continuous range of levels, which is known as a band (Ashcroft & Mermin, 1976). Atomic orbitals divide if multiple atoms are packed closely together to form a molecule. As a result, there are as many molecular orbitals as proportional to atoms. The orbitals increases significantly many of atoms are packed together to create a solid. As a result, the energy

disparity between them gets quite minimal. Unlike the discrete energy levels of individual atoms, the energy levels of electrons in solids create continuous bands of energy. When the atomic and molecular orbitals of more than one symmetry type exists, different bands are formed the overlap of different types of orbitals (Kittel, 1996).

In crystals, electrons are grouped in energy levels. The study of band structure helps to classify the solids into conductor, insulator and semiconductor. The band gaps existing in insulator and semi-conductors are the area where no energy orbitals exist. The crystal will be an insulator if valence electrons completely occupy the bands while rest bands are vacant. A crystal behaves like a magnetic insulator if the number of outermost electrons are with even integer (Kittel, 1996). Given that each primitive cell has a single valence electron, the alkaline metals and new metals must be metals.

Out of different methods available for the structure calculation, we employed the FP-LAPW technique. Studying the first Brillouin zone is adequate due to symmetry as the behaviors of the complete solid may be used to define its solution. Here, we focus only on first Brillouin zone. The first Brillouin zone of monoclinic structure alongwith high symmetry points is shown in Fig. 5.

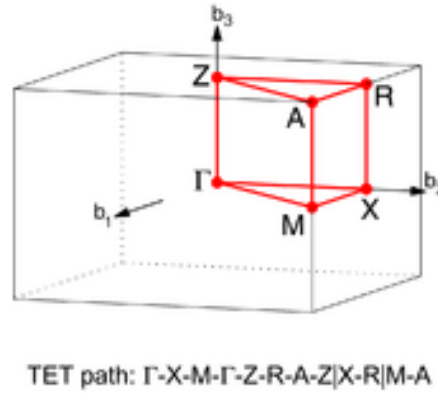


Figure 5: Selection of kpath for monoclinic structures in first Brillouin zone (Actyawan & Curtarola, 2010).

3.3.3 Density of States (DOS)

The number of states per unit of energy at each energy level that may be inhabited is known as the DOS. Additionally, it is explained as the quantity of permitted quantum states per unit of energy range. In order to determine the likelihood that a Fermion would occupy a certain quantum state in a system at thermal equilibrium, the Fermi-Dirac probability distribution function is utilized. Particles that adhere to the Pauli exclusion principle are called fermions.

3.3.4 Crystal Field Theory

To know more about the characteristics of transition metal complexes, a model which is based upon electrostatic interactions has been created. This model, known as the crystal field theory (CFT), provides insight into the many characteristics of transition metals. In coordination complexes, CFT emphasizes the non-bonding electrons on the central metal ion rather than the metal-ligand links. Similar to valence bond theory, CFT only partially explains how complexes behave. Moreover, it clarifies that the valence band theory. Every covalent connection involving ligands and metal ions is disregarded by CFT in its purest form. The ligand and the metal are both seen as extremely tiny point charges.

Since electron carry negative charges, the supplied electrons from the ligands will repel the center metal's electrons. Let's think about how the electrons in an octahedral complex behave in their nonbonding d orbitals. The five d orbitals are distributed in space as shown in Fig. 6 and are made up of lobe-like areas. The six ligands in an octahedral compound cooperate along the axes.

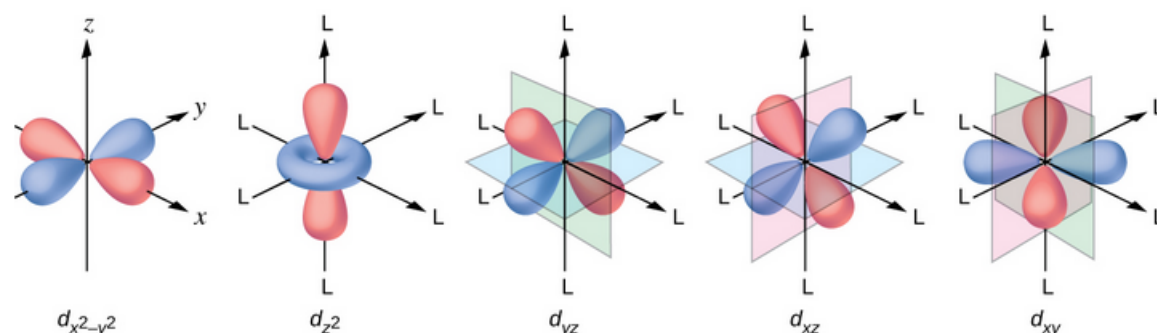


Figure 6: The directional properties of five d orbitals (Miessler & Tarr, 1996).

The electrons are dispersed amongst five d orbitals in an uncomplicated metal ion in gaseous phase so that each orbital has the equal amount of energy. Nevertheless, the affinities of the d orbitals change when ligands connect to a metal ion. Out of five d energy levels, the d_{z^2} and $d_{x^2-y^2}$ orbitals which are directed in the direction of ligands are named as e_g orbitals (Fig. 6). Another three energy levels, d_{xy} , d_{xz} , and d_{yz} orbitals are named as t_{2g} orbitals. The point charge of the six ligands oppose the electrons in metal ion as they move toward in the directional axes of the octahedron. Consequently, there is a stronger attraction among ligands and the electrons in the e_g orbitals than among the ligands and t_{2g} orbitals. Whereas the lobes of the t_{2g} energy levels point between the ligands, those of the e_g energy levels point straight towards the ligands. As a result, the PE of the electrons which are in the e_g orbitals are larger than the electrons that lie in t_{2g} subshells. As seen in Fig. 7, energy difference between the orbitals may be depicted.

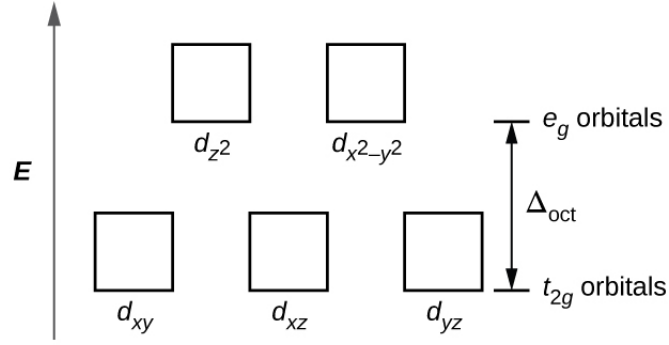


Figure 7: The energy ranges of e_g and t_{2g} orbitals (Legendre *et al.*, 2021).

The term "crystal field splitting" refers to the energy variation between the e_g and the t_{2g} orbitals, and it is represented by the symbol Δ_{oct} .

The type of the six ligands surrounding the core metal ion, the charge on the metal, or even if the metal is using d orbitals are just a few of the variables that affect the amplitude of the Δ_{oct} . Various ligands result in various splittings of the crystal field.

3.4 Computational Details

Computational physics demands all the details of simulation to reproduce the same data independently in another lab. By details we mean all the approximations, error limits, thresholds, softwares and finally system specific parameters and codes used to prepare corresponding input files. In this chapter, the procedure for the band structure and DOS calculation is discussed. The computations were performed using full potential linearized augmented plane wave plus local orbitals (FP-LAPW+LO) techniques applied on WIEN2k code. Which is dependent on first principle DFT at 0 K temperature.

Initialization of the Calculation (`init_lapw`)

After the basic structure file given by experiments to initialize the calculation and basic input files are created. In this step large number of individual steps are necessary to initialize the calculation. For initialization, we have two ways by command line and graphics (`w2web`) methods. Initialization command all of the inputs for the SCF calculation will be created by `init_lapw` using certain default settings. After the initialization, run SCF calculation using script `run_lapw` with the desired options. Also we can select charge and energy criterion by adding `-cc` and `-ec` respectively on command line with proper values. Spin polarized computations are applicable to magnetic systems. As a result, the identical procedure is made separately for spin-up and spin-down electrons.

Orbital Potentials

In WIEN2k, by going beyond normal GGA/LDA for inclusion of orbital dependent potential, methods like GGA+ U /LDA+ U , which are excellent for strongly correlated systems has been used. Usually for d-orbitals of late transition metal atoms and 4f/5f atoms. For the calculation of coulomb potential we required two additional input files `case.indm` and `case.inorb` (for LAPWDM and ORB). In which we can select proper value of U and J for atoms and then add `-dm -orb` on command line. The density matrix will be computed in `lapw2`, after being blended, orbital dependent potentials will be computed on the `orb`.

Spin-Orbit Interaction

The second variational technique uses spin-orbit interaction (SO), which uses scalar-relativistic orbitals as its foundation. The number of eigen values will quadruple when LAPWSO is applied after applying the spin-interaction because SO combines the spin up and down states, making them indistinguishable. To initialize using `initso_lapw` script for SO calculation, we add `run_lapw -so` to the terminal. SO may be quickly implemented in non-spin polarized conditions. This would also utilize the complex LAPW2 version.

In contrast, the SO in spin-polarized scenario may alter the symmetry dependent on the magnetization direction. For this we need to use script `initso_lapw` together with `symmetso` creates the appropriate symmetry. Perform the SCF calculation first, store the result, initialize SO, and then run another SCF cycle with `-so` on the command line to include SO in the computation. For spin-polarized systems, we can add `-dm` for orbital magnetic moments.

Here are some executable commands that run WIEN2k package, to calculate self-consistent field as,

1. LDA(GGA)
 - `init_lapw`: to initialize calculation with the structure data
 - `run_lapw`: run the SCF calculations for non-spin polarized case
 - `runsp_lapw`: run the SCF calculations for spin polarized case
2. LDA(GGA)+ U
 - `runsp_lapw -dm -orb`: run the SCF for Coulomb interaction
3. LDA(GGA)+ U +SOC
 - `initso_lapw`: to initialize calculation for the SOC case
 - `runsp_lapw -dm -orb -so`: run the SCF for SOC

3.5 Crystal Structures and Computational Details

The electronic and magnetic characteristics are found with FP-LAPW method as accomplished in WIEN2k code (Blaha *et al.*, 2001) and FPLO code (Koepernik and Eschrig, 1999). In case Ca-based and Tb-based materials, the standard generalized gradient approximation (PBE-GGA) (Perdew *et al.*, 1996) have been applied with correlation energy U of 4 eV and 1.5 eV for chromium (nickel) and osmium, respectively. In case of Sr-based materials, For the exchange-correlation potential LDA (Anisimov *et al.*, 1993) was chosen for the self-consistent calculations as this funtional is sufficient to address the results similar to GGA. In Sr based materials, results given by LDA was more comparable with experimental results than the results obtained with GGA. So we have reported the results by LDA. The MAE is measured by self consistent calculations with SOC applied in five different direction of the magnetization. The R_{MT} of the atoms are measured to be 2.14, 1.94, 1.99, 2.01 and 1.64 Bohr for calcium, chromium, nickel, osmium and oxygen, respectively. 500 k -points within full Brillouin zone is applied that gives to 8 x 8 x 6 k -mesh. For various magnetic configurations, the high symmetry structure is split to most stable space group $P1$, with the lowest symmetry which is primitive and most stable symmetry. That produces 20 in-equivalent atoms out of which 3 types of oxygens are found which forms octahedra with Cr or Fe and Ir, respectively. The non-overlapping muffin-tin sphere radii (R_{MT}) for various elements like Sr, La, Ni, Fe, Os, Ru, Tb, Cr, and O are presented in tables (1), (2), (3) and (4).

Table 1: Muffin-tin radii for Calcium containing compounds

Atoms	Ca	Cr	Ni	Os	O
Muffin Tin Radius (Bohr)	2.14	1.94	1.99	2.01	1.64

Table 2: Muffin-tin radii for osmium containing compounds

Atoms	Sr	La	Ni	Fe	Os	O
Muffin Tin Radius (Bohr)	2.31	2.49	2.04	2.04	2.02	1.65

Table 3: Muffin-tin radii for ruthenium containing compound

Atoms	Sr	La	Ni	Ru	O
Muffin Tin Radius (Bohr)	2.31	2.48	2.05	1.97	1.69

Table 4: Muffin-tin radii for terbium containing compounds

Atoms	Tb	Fe	Cr	O
Muffin Tin Radius (Bohr)	2.35	2.0	1.96	1.72

CHAPTER 4

RESULTS AND DISCUSSION

4.1 Introduction

In this chapter, we present, discuss, and analyze the main findings of our present work. We have investigated the electronic and associated characteristics of many DPs $A_2M_{1-x}M'_xTO_6$, (where A= Ca, Sr,Tb, M and $M' =$ Cr, Fe, Ni, Mn, Co, T= Ru, Os, Ir, with substitution ratio $x= 0, 0.5, 1$), M, M' and T are transition metals using full potential linear augmented plan wave (FP-LAPW) method developed by Blaha *et al.* (2001). The FP-LAPW method is more accurate and efficient technique to study electronic properties. Density functional theory has been used in the computations considering LDA and further modification in it as GGA functional. Electron correlation (U) and SOC has also been considered in deriving the results. Using full potential DFT-package such as with WIEN2k code (Blaha *et al.*, 2001) and FPLO code (Koepernik & Escrig, 1999), the electronic and magnetic characteristics were computed. Using the experimental parameters, we have calculated the total energies by creating a super cell with different magnetic alignments. For the U -values of 3d and 4d/5d atoms, we vary the values from 3-6 eV and 0.5-2.5 eV, respectively. Also, the second variational method SOC was applied to examine the effect of spin quantization along magnetic axis [100], [010], [001], [110] and [111]-directions. By analyzing the band structure, the contributions of each and every atoms and orbitals have been studied, specifically the transition metals and their d-orbitals. Likewise, Density of States (DOS), spin and orbital magnetic moments for the above mentioned compounds have been studied. In self consistent field (SCF) calculations, we have used the energy and charge convergence criteria in the order of 10^{-6} Rydberg and 10^{-4} electrons.

4.2 Ca-Based Double Perovskites:

Parent Material: $\text{Ca}_2\text{CrOsO}_6$

We have considered $\text{Ca}_2\text{CrOsO}_6$ (CCOO) as a parent material for the Ca-based double perovskites which has been recently synthesized experimentally by Morrow *et al.* (2016) in which Curie temperature (T_C) has been reported with 489.8 K. In this material the occupancy ratio of two TM chromium and osmium cations, are in 76% and 24% dictating the signatures of antisite disorder in the system. The crystalline structure of CCOO has monoclinic structure with space group $P2_1/n$ that belongs to number 14, which have been maintained by CrO_6 and OsO_6 octahedra [Fig. 9]. We have carried out the related calculations by taking experimental lattice parameters which are $a=5.351 \text{ \AA}$, $b=5.456 \text{ \AA}$, and $c=7.620 \text{ \AA}$, with $\beta=90.09^\circ$, respectively. The typical Cr-O and Os-O bond lengths for inter-octahedral Cr-O-Os are 1.97 \AA and 1.95 \AA , respectively, also with bond angles produced being 153.2° , 152.7° and 153.8° .

In this material, we are interested to study the electronic, magnetic and other characteristics of $\text{Ca}_2\text{CrOsO}_6$ because of (i) high critical temperature (T_C), (ii) the FiM ground state with insulating character, and (iii) small net magnetic moment. With substitution by different transition metals, the material is assumed to show different novel properties like HM by closing the band gap in one spin-channel, reducing the total magnetic moments; and increasing in (T_C) (Gepreg *et al.*, 2006). These features is expected to provide new spintronic device in DPs that works at room temperature.

First, we made DFT calculations and investigated that CCOO has FiM ground state (GS) with insulating behaviour with net magnetic moment, $\mu_{tot} = 0.23 \mu_B$ per unit cell. The optical study in CCOO which reveals that optical interband transition between Cr-3d and Os-5d bands in plateau like area. Transport propertis of the parent material is also calculated where we find Seebeck coefficient, thermal conductivity and power factor of CCOO. The proposed values and the results of optical and thermoelecric properties obtained from parent materials shows that these materials are not so suitable for optical and thermoelectric properties. So we limited study of these properties only in parent materials.

4.2.1 Electronic and Magnetic Properties

First, the crystal's symmetry is lowered by creating a supercell structure to lowest and most stable symmetry that has space group $P1$, which is primitive that also contains a total of 20 inequivalent atoms and produces 3 different types of oxygen. Five different types of magnetic configurations and one non-magnetic state were taken into consideration to determine the magnetic GS. Frequently checked different magnetic configuration are FM- $\uparrow\uparrow\uparrow$, AFM1- $\uparrow\downarrow\uparrow\downarrow$,

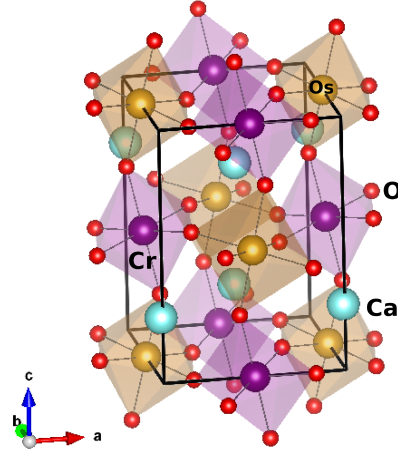


Figure 9: Crystal structure of double perovskites $\text{Ca}_2\text{CrOsO}_6$.

AFM2- $\uparrow\downarrow\uparrow$, FiM1- $\uparrow\uparrow\downarrow\downarrow$ and FiM2- $\uparrow\uparrow\downarrow$, respectively. While comparing the energy of different magnetic configurations, we found that the material is stable with lowest energy in FiM1 configuration (see in appendix). On this basis, we extended all further calculation by taking structure of FiM state. The spin orbit coupling (SOC) is considered for spin quantisation along [100], [010], [001], [110] and [111] directions. Magnetic easy axis is found in [001] direction and the magnetic anisotropic energy (MAE) is found to be 12.76 meV/unit cell.

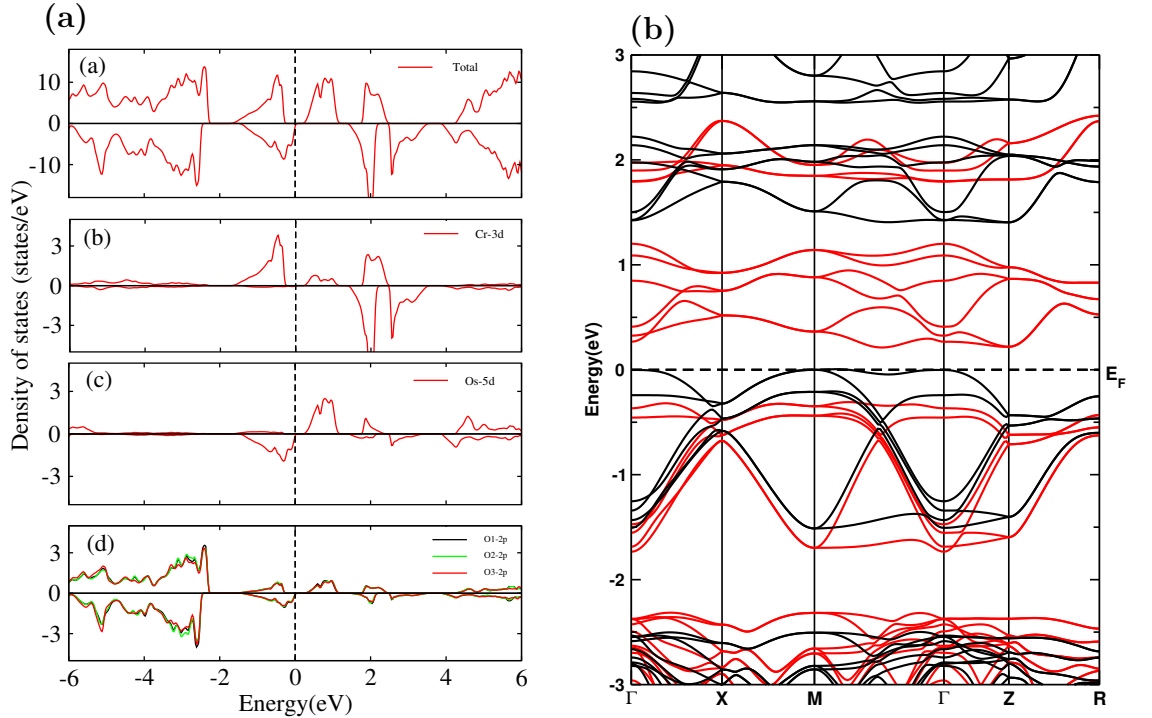


Figure 10: (a) Density of states and (b) band structure of $\text{Ca}_2\text{CrOsO}_6$ with GGA functional.

The electronic total, partial DOS and band structure of $\text{Ca}_2\text{CrOsO}_6$ under GGA, GGA+ U and GGA+ U +SOC are demonstrated in Fig. 10, Fig. 11 and Fig. 12, respectively. From the DOS and band plot, we can see that Cr-3d and Os-5d orbitals as well as hybridized O-2p orbitals are responsible for a significant portion of the contribution near to the E_F . In CCOO, Cr is found to have charge state +3 with $3d^3$ configuration. Three electrons move to t_{2g} states in up state and e_g states remain vacant which can be seen in DOS plot. Due to half filled state, t_{2g} lies on valence area while e_g states are found in conduction region due to its empty state. For spin down cases, both t_{2g} and e_g states are un-occupied hence these move to conduction region. While Os has charge state +5 with $5d^3$ structure. These 3 electrons from Os move to t_{2g} states in spin-down channel. Here, in $\text{Ca}_2\text{CrOsO}_6$, the energy gap is discovered to be ~ 0.59 eV (Fig. 14 and Fig. 15 (left)) confirming insulating state in CCOO. The results obtained from our DFT calculation are consistent with experimental reports (Morrow *et al.*, 2016).

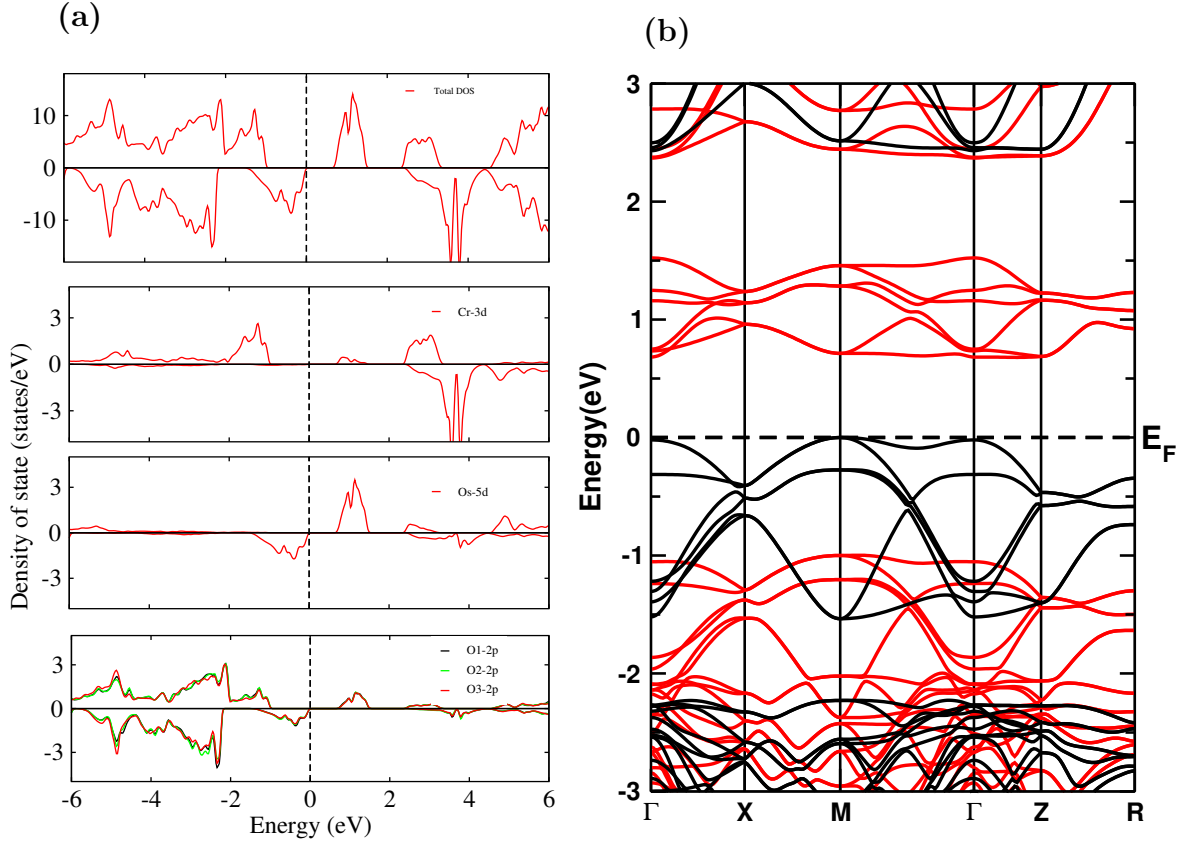


Figure 11: (a) Density of states and (b) band structure of $\text{Ca}_2\text{CrOsO}_6$ with GGA+ U functional.

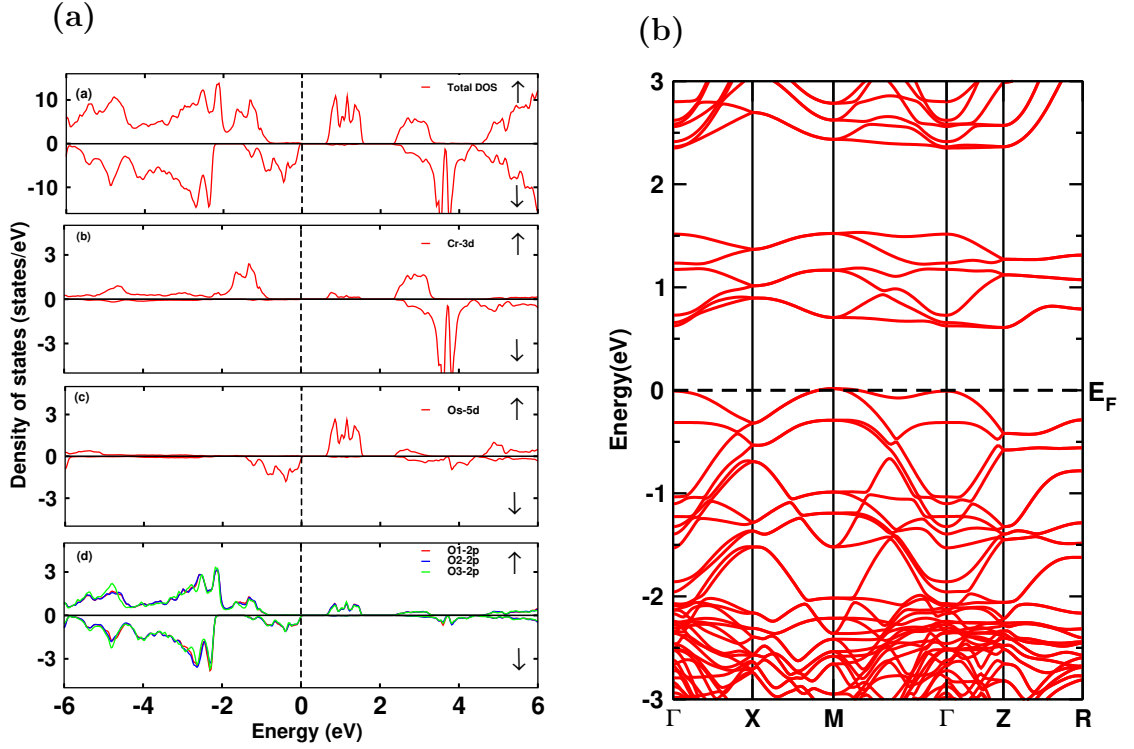


Figure 12: (a) Density of states and (b) band structure of $\text{Ca}_2\text{CrOsO}_6$ with GGA+ U +SOC.

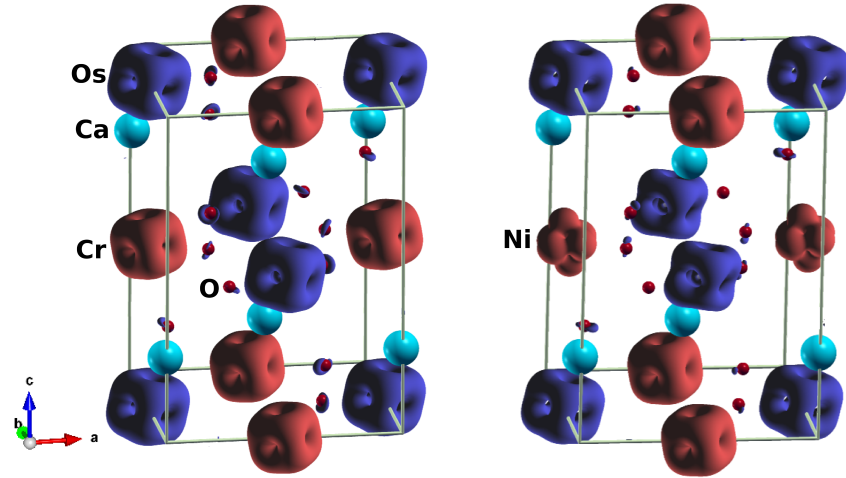


Figure 13: Isosurface of spin magnetization density at $\pm 0.21e/\text{\AA}^3$ of (left) $\text{Ca}_2\text{CrOsO}_6$ and (right) $\text{Ca}_2\text{Cr}_{0.5}\text{Ni}_{0.5}\text{OsO}_6$.

The magnetic moments on chromium and osmium are 2.5 and $1.6 \mu_B$, respectively, and total moment is $0.23 \mu_B$ per unit cell, as shown in table 5. Oxygen also gets small magnetic moment of magnitude of $0.07 \mu_B$ because of the effect of partial charge transfer from 3d and 5d transition metals that helps to increase the total magnetic moment. This picture of charge transfer effects between different atoms can be seen and understand based on the spin density

Table 5: Computed effective and individual magnetic moments (μ_B) and band gap ‘ E_g ’ (eV) for $\text{Ca}_2\text{CrOsO}_6$ compound.

$\text{Ca}_2\text{CrOsO}_6$				
site	GGA	GGA+ U	GGA+ U +SOC	Expt.
Cr	2.20	2.52	2.52/0.05	2.5
Os	- 1.45	- 1.66	- 1.59/0.14	1.26
O1	- 0.10	- 0.11	- 0.10	-
O2	- 0.09	- 0.10	- 0.10	-
O3	- 0.09	-0.10	- 0.10	-
Net.	0	0	0.23	0.2
E_g	0.53	0.65	0.59	-

plot as in Fig. 13.

The spin moment in osmium is decreased because of intense Os-O hybridization. Orbital moment is produced after the application of SOC. The orbital moment of Cr and spin magnetic moment are in parallel direction which clarifies that 3d orbital is might be half filled or more than half filled. While in Os, direction of orbital moment and spin magnetic moment are in antiparallel which confirms 5d orbitals are less than half filled that resembles with Hund’s third rule (Jeng *et al.*, 1987). As a result, the orbital magnetic moments of chromium and osmium lie in same direction that increase the total magnetic moments in CCOO.

4.2.2 Thermoelectric Properties

The study of thermoelectric properties in oxide materials have been found to be environmental friendly, toxicless, nice stability, cost saving, good thermoelectric behaviour and with other interesting properties (Roy *et al.*, 2016; Saxena *et al.*, 2017; Sugahara *et al.*, 2006). While discussing electric and magnetic properties, we found insulating behaviour with some flat band in our parent material $\text{Ca}_2\text{CrOsO}_6$, so we planned to study thermoelectric properties in it.

As we found with many literature that good performance of thermoelectric device is provided by figure of merit $ZT = S^2\sigma T/\kappa$, where S , σ and κ represents the Seebeck coefficient, electrical conductivity, and thermal conductivity, respectively (Boona *et al.*, 2017; Tan *et al.*, 2017). Within rigid band approximations (RBA) and constant relaxation time technique (CRTA), we have calculated the electrical transport coefficients S , σ , and $S^2\sigma$, using the

Boltztrap algorithm. This presumes that S doesnot depends on relaxation time (τ). These two approaches are found to be appropriate in the theoretical finding of new thermoelectric materials as reported earlier (Madsen *et al.*, 2008; Lee *et al.*, 2016; Zeeshan *et al.*, 2018).

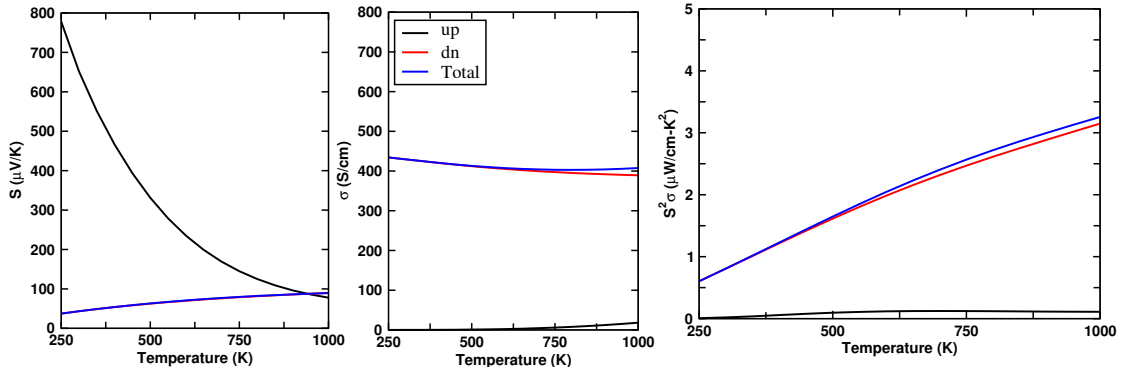


Figure 14: (left) Seebeck coefficient, (middle) electrical conductivity, and (right) power factor as a function of temperature for CCOO.

Fig. 14 reveals that S , σ and PF for CCOO for both spin state, and the overall contribution with regard to τ , as a function of temperature. The parameters that were looked at for both spin channels using the two current model where the σ and S are provided as,

$$\sigma = \sigma(\uparrow) + \sigma(\downarrow) \quad (4.1)$$

$$S = \frac{S(\uparrow)\sigma(\uparrow) + S(\downarrow)\sigma(\downarrow)}{\sigma(\uparrow) + \sigma(\downarrow)} \quad (4.2)$$

where (\uparrow) and (\downarrow) represents the coefficients for up and down spin, respectively. The total Seebeck coefficient calculated is growing with the range 300 K to 1000 K as presented in Fig. 14. The positive value calculated range from 43 to 83 $\mu\text{V/K}$ that indicates p -type charge carriers. Nonetheless, comparing to standard values (150 $\mu\text{V/K}$), the Seebeck coefficient values calculated are not very significant (Tritt, 2014). For calculating the σ and PF, relaxation time need to be used which is not inconsequential to find. We tried to find on the basis of prior theoretical investigations. It has been found that a relaxation time of 5×10^{-15} s is used to investigate the transport properties in such similar materials (Parrey *et al.*, 2018). We did the same, which led to the right application of total electrical conductivity, which ranges from 429 to 404 S/cm in the range of 300 to 1000 K. Values that could be allocated to the more DOS at valence band maximum (VBM) due to the reprobate bands. The reprobate bands produce more DOS that causes large number of charge carriers. When relate to the conduction band minimum, the large number of DOS at valence band maximum

around Fermi level suggests that hole doping may be appropriate to enhance the transport characteristics (Zeeshan *et al.*, 2018).

The calculated value of PF lies in the range of $0.08 \mu\text{W}/\text{cm}\cdot\text{K}^2\text{-s}$ at 300 K to $3\mu\text{W}/\text{cm}\cdot\text{K}^2\text{-s}$ at 1000 K. Using the same relaxation time, i.e., $\tau = 5 \times 10^{-15}$ s, the greatest PF found is $15 \mu\text{W}/\text{cm}\cdot\text{K}^2$ at 1000 K. Even if the obtained value is not substantial, it could be substantially enhanced by using the right dopants and synthesis method, prompting for more experimental research. Hence, we have limited our study for thermoelectric properties only in parent material.

4.2.3 Optical Properties

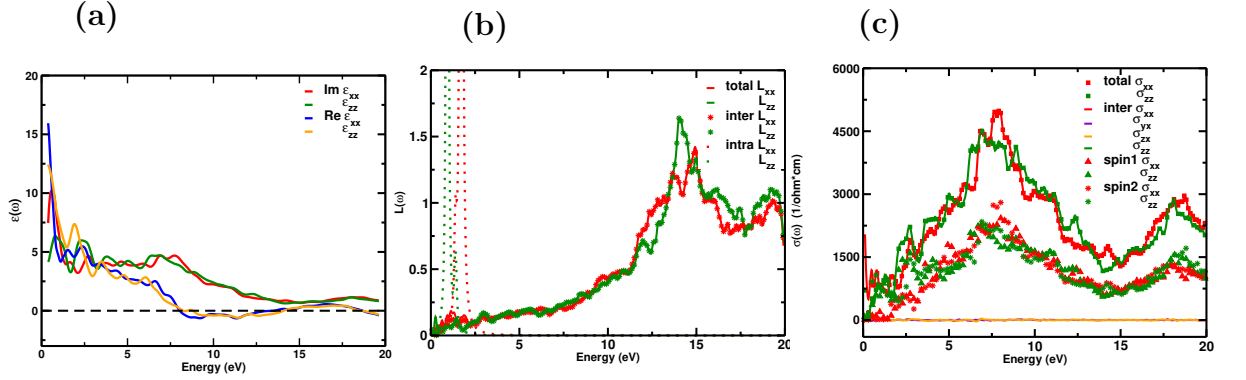


Figure 15: (a) The real and imaginary part of the dielectric function $\epsilon(\omega)$, (b) Electron energy loss function $L(\omega)$, vs photon energy and (c) optical conductivity $\sigma(\omega)$ for CCOO.

We studied the optical properties of our parent DPs $\text{Ca}_2\text{CrOsO}_6$, taking both the polarization directions E_{xx} and E_{zz} being $E_{xx} = E_{yy}$ because they have symmetric tetragonality. $j_a = \sigma_{ab} E_b$ is the photonic current created by electric field E_b . The properties of a compound under incoming light are given by the complex dielectric function ($\epsilon(w)$),

$$\epsilon(w) = \epsilon_1(w) + i\epsilon_2(w) \quad (4.3)$$

where $\epsilon_1(w)$, $\epsilon_2(w)$ are the real and imaginary components of the dielectric function, respectively. Through the joint DOS and momentum matrix elements between filled and unoccupied states, the imaginary part $\epsilon_2(w)$ is determined from the electronic structure:

$$\epsilon_2(w) = \frac{Ve^2}{2\pi\hbar m^2 w^2} \int d^3k \sum |kn|p|kn'|^2 f(kn)[1 - f(kn')]\delta(E_{kn} - E_{kn'} - \hbar w) \quad (4.4)$$

where p represents momentum operator, kn denotes the eigen function with the eigenvalue E_{kn} . The term $f(kn)$ denotes the Fermi distribution function. The Kramers Kronig dispersion

relations (Toll, 1956) supply the real component of the dielectric function ϵ_1 .

$$\epsilon_1(\omega) = 1 + \frac{2}{\pi} \int \frac{\epsilon_2(\omega')\omega'}{\omega'^2 - \omega^2} d\omega' \quad (4.5)$$

The dielectric function given below is intimately related to other optical characteristics such as optical conductivity $\sigma(\omega)$ and electron loss function $L(\omega)$.

$$\sigma(\omega) = \frac{-i\omega(\epsilon_2(\omega) - 1)}{4\pi} \quad (4.6)$$

$$L(\omega) = \frac{\epsilon_2}{\epsilon_1^2(\omega) + \epsilon_2^2(\omega)} \quad (4.7)$$

The electronic polarizability of materials due to incident photon is given by the $\epsilon_1(\omega)$. The fluctuation of the $\epsilon_1(\omega)$ as a function of photon energy is shown in Fig. 15 (a). x and z polarizations ($\epsilon_1^{xx}(0)$, $\epsilon_1^{zz}(0)$) have computed static dielectric constants of 15.94 eV and 12.43 eV, respectively. Both ϵ_1^{xx} and ϵ_1^{zz} decline first and then rapidly increases when energy of incident light increases up to 1.055 eV. In comparison to ϵ_1^{xx} , ϵ_1^{zz} goes deeper with a tiny rise in energy of incident photon above 0.0 eV, then increases again. Both ϵ_1^{xx} and ϵ_1^{zz} have a maximum peak at a specific energy when ϵ_1^{xx} outnumbers ϵ_1^{zz} by a factor of two. The plot also shows that optical anisotropy exists up to ~ 14 eV, after which it become nearly optically isotropic. At ~ 7.6 eV, both ϵ_1^{xx} and ϵ_1^{zz} reach zero, indicating the occurrence of plasmonic type oscillation. The $\epsilon_2(\omega)$ is known to be connected to optical absorption. Figure 15 depicts the dependency of $\epsilon_2(\omega)$ on photon energy.

Table 6: For the $\text{Ca}_2\text{CrOsO}_6$ compound, calculated optical parameters at the major peak value

Optical parameters	$\epsilon_1^{xx}(0)$	$\epsilon_1^{zz}(0)$	$L(\omega)$	$\sigma_1^{xx}(\omega)$	$\sigma_1^{zz}(\omega)$
eV	15.9	12.4	14.1	7.8	7.3

It can be seen that $\epsilon_2(\omega)$ increased rapidly above the threshold energy. This represents the estimated energy gap, and reached a peak value at 1.0-1.5 eV. Following this significant oscillations $\epsilon_2(\omega)$ becomes small. Within the energy limit of 3.0 eV to 10.0 eV, a large plateau-like region is produced. The optical conduction map, that shows active absorption of energy of incident light because of direct electron transitions, also confirms this. Figure 15 (middle)

shows the variation of $L(\omega)$ versus energy of incident radiation. The energy loss caused by a fast electron scattering while travelling through a material is described by $L(\omega)$. In the case of an intra-band transition, electron loss is extremely high in the area of small energy. $L(\omega)$, on the other hand, gradually increases up to 12.0 eV before suddenly increasing after 13.0 to 14.0 eV for inter-band transitions. The inverse relationship between $L(\omega)$ to $\epsilon_2(\omega)$ accounts for the small energy loss spectra. The sharp peak in the $L(\omega)$ spectra between 13.0 and 14.0 eV correlates to the Plasmon frequency ω_p between 13.0 and 14.0 eV. As illustrated in Fig. 15 (c), the optical conductivity $\sigma(\omega)$ has also been computed. In CCOO, $\sigma_{xx}(\omega)$, $\sigma_{zz}(\omega)$, $\sigma_{yx}(\omega)$, and $\sigma_{zx}(\omega)$ are the only independent components of $\sigma(\omega)$ in which $\sigma_{yx}(\omega)$ and $\sigma_{zx}(\omega)$ components are zero. Between (3-12) eV, the optical conductivity of $\text{Ca}_2\text{CrOsO}_6$ displays a plateau-like feature instead of a pronounced peak-like pattern. This demonstrates a strong optical interband transition between the 3d orbitals of chromium and 5d orbitals of osmium bands in that area.

4.3 Ni Doped at Cr Site on Parent Material:



$\text{Ca}_2\text{Cr}_{0.5}\text{Ni}_{0.5}\text{OsO}_6$ (CCNOO) is obtained by substituting Ni to the Cr-site partially (50%) in recently synthesized material $\text{Ca}_2\text{CrOsO}_6$. Doping of Ni at Cr site adds additional 5 electrons to the system. Ni has the charge state +2 with $3d^8$ configurations. Like in $\text{Ca}_2\text{CrOsO}_6$, we started our calculation by considering five magnetic configurations and one non magnetic state. Frequently checked different configurations are FM- $\uparrow\uparrow\uparrow\uparrow$, AFM1- $\uparrow\downarrow\uparrow\downarrow$, AFM2- $\uparrow\downarrow\downarrow\uparrow$, FiM1- $\uparrow\uparrow\downarrow\downarrow$ and FiM2- $\uparrow\uparrow\uparrow\downarrow$, respectively, and found that FiM1 is stable with lowest energy. So, we extended all other further calculation by taking FiM1 configurations. The spin orbit coupling is considered for spin quantisation along [100], [010], [001], [110] and [111] directions.

4.3.1 Electronic and Magnetic Properties

The electronic total and partial DOS as well as band structure of CCNOO under GGA, GGA+ U and GGA+ U +SOC are depicted in Fig. 16, Fig. 17 and Fig. 18, respectively. From the DOS and band plot we can see that substantial contribution around E_F is due to Cr-3d, Ni-3d and Os-5d orbitals hybridizes significantly with O-2p orbitals.

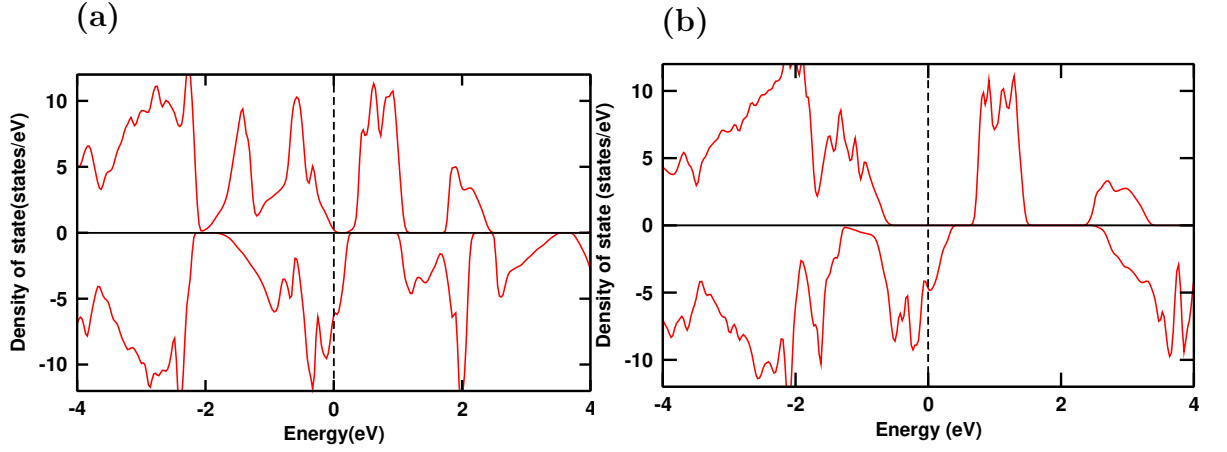


Figure 16: Total DOS of $\text{Ca}_2\text{Cr}_{0.5}\text{Ni}_{0.5}\text{OsO}_6$ with (a) GGA and (b) GGA+ U functional.

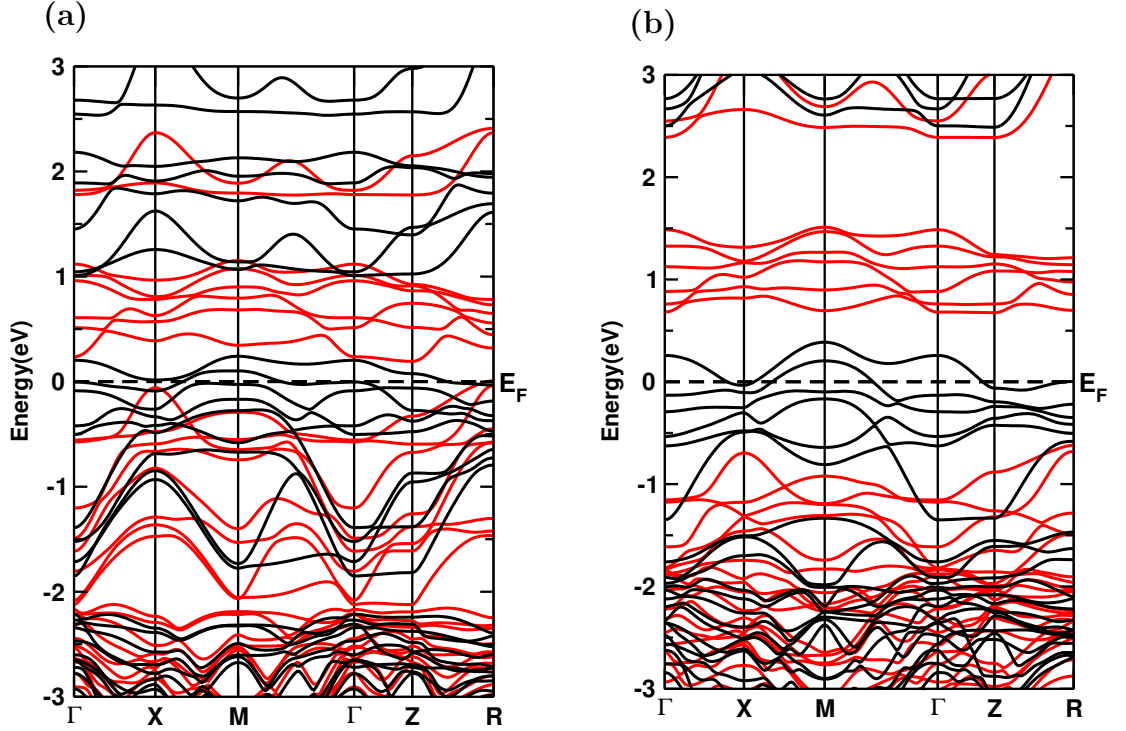


Figure 17: Band structure of $\text{Ca}_2\text{Cr}_{0.5}\text{Ni}_{0.5}\text{OsO}_6$ with (a) GGA and (b) GGA+ U functional.

With Ni substitution, five extra electrons are added to the system, out of them three electron go to t_{2g} state for spin down channel and two electrons go to e_g states in spin up as Ni interacts ferrimagnetically with Os. The 3 electrons of Ni in down channel now produces repelling force to Os- t_{2g} bands that were already there. Due to this repulsive effect, Os bands moves to conduction region from occupied region crossing Fermi level in spin down channel (Fig. 18 (b)). For spin down, that results in a metallic condition and spin up remains insulating. Hence, with insulating state, spin up channel acts as insulator and spin down as

a metallic, the material CCNOO is found to be a half metallic. It's noteworthy to observe that the HM state is still stable for U_{Os} up to 4 eV.

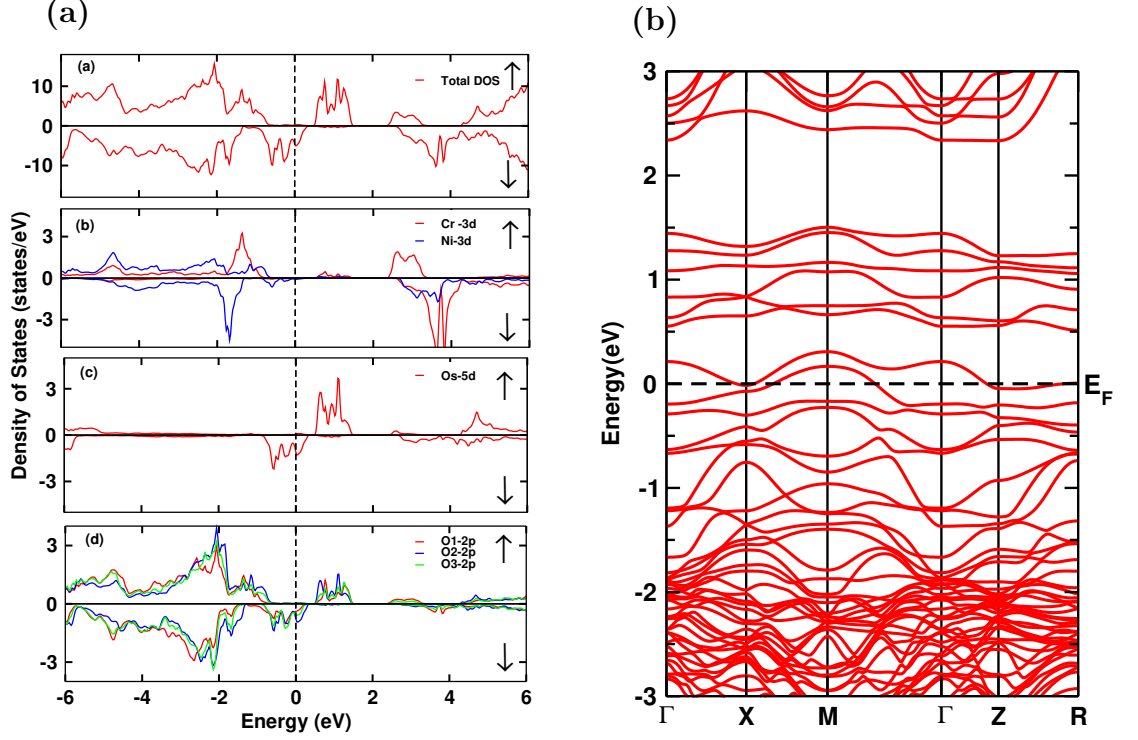


Figure 18: (a) The density of states and (b) band structures of CCNOO under GGA+ U +SOC.

The magnetic moments of chromium, nickel and osmium atoms are found to be $2.52 \mu_B$, $1.64 \mu_B$ and $1.42 \mu_B$ respectively. The effective moment of the material is computed to be $0.21 \mu_B$ per unit cell. As a result of the partial charge transfer from chromium, nickel and osmium atoms to oxygen, these ions acquire spin polarization in same direction to osmium ions and a modest moment of $0.07 \mu_B$, which is similar to the spin density diagram in Fig. 19.

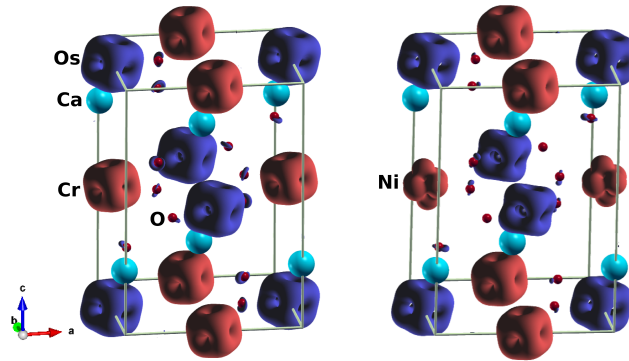


Figure 19: Isosurface of spin magnetization density at $\pm 0.21 e/\text{\AA}^3$ for $\text{Ca}_2\text{CrOsO}_6$ (left) and $\text{Ca}_2\text{Cr}_{0.5}\text{Ni}_{0.5}\text{OsO}_6$ (right).

Table 7: Computed effective, individual and orbital moments (μ_B) and band gap ‘ E_g ’ (eV) for $\text{Ca}_2\text{Cr}_{0.5}\text{Ni}_{0.5}\text{OsO}_6$ compound.

$\text{Ca}_2\text{Cr}_{0.5}\text{Ni}_{0.5}\text{OsO}_6$			
site	GGA	GGA+ U	GGA+ U +SOC
Cr	2.19	2.52	2.52/0.05
Ni	1.32	1.65	1.64/0.14
Os	- 1.28	-1.48	- 1.42/0.16
O1	- 0.08	- 0.09	- 0.08
O2	-0.03	-0.05	- 0.05
O3	- 0.05	- 0.07	- 0.07
Net	0.0	0	0.21
E_g	Metallic	Metallic	HM

The structure of spin density considerably alters when one of the chromium atoms is substituted with nickel(Fig. 19 (right)). In reality, nickel has charge state +2 with $3d^8$ structure. Five electrons from Ni goes to up state and completely filled in up spin and another three electrons go to down in t_{2g} states. Hence, only remaining observable state is the e_g state, that can be seen in the charge density plot of nickel atoms (Fig. 19 (right)).

4.4 Ir Doped at Os Site on Parent Material: $\text{Ca}_2\text{CrIrO}_6$

The material $\text{Ca}_2\text{CrIrO}_6$ (CCIO) is obtained by substituting Ir in place of Os in recently synthesised material $\text{Ca}_2\text{CrOsO}_6$ (Morrow *et al.*, 2016). The detail information (experimental or theoretical) regarding different properties of $\text{Ca}_2\text{CrIrO}_6$ are not available in the literature yet.

Fig. 20 depicts the crystal structure of $\text{Ca}_2\text{CrIrO}_6$ has space group $P2_1/n$ and its monoclinic structure is maintained by BO_6 and IrO_6 octahedra. The experimental lattice parameters opted are $a=5.351 \text{ \AA}$, $b=5.456 \text{ \AA}$, $c=7.620 \text{ \AA}$, $\beta=90.092^\circ$.

4.4.1 Stability of the Structure

For the stability of the doped materials, we have checked the cohesive and formation energy of the material as,

$$E_{for} = E_{Ca_2B'IrO_6}^{tot} - [2E_{Ca}^{bulk} + E_B^{bulk} + E_{Ir}^{bulk} + 6E_O^{bulk}] \quad (4.8)$$

$$E_{coh} = E_{Ca_2B'IrO_6}^{tot} - [2E_{Ca}^{iso} + E_B^{iso} + E_{Ir}^{iso} + 6E_O^{iso}] \quad (4.9)$$

Where, B= Cr, $E_{Ca_2B'IrO_6}^{tot}$ is the total energy and E_{Ca}^{bulk} , E_B^{bulk} , E_{Ir}^{bulk} , E_O^{bulk} being energy of Ca, Cr, Ir and O elements and E_{Ca}^{iso} , E_B^{iso} , E_{Ir}^{iso} , E_O^{iso} being energy of isolated calcium, chromium, iridium and oxygen, respectively. From the calculation, we got the the formation and cohesive energies for the compound CCIO to be -2.84 eV/atom, and -2.66 eV/atom, respectively. The results thus obtained for both cohesive and formation energies suggest that the material Ca_2CrIrO_6 is thermodynamically stable structure and can be synthesized experimentally.

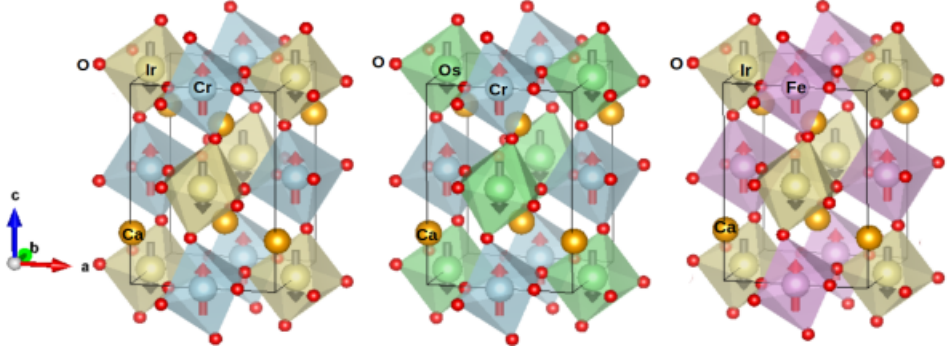


Figure 20: Crystal structure of $Ca_2BB'O_6$ double perovskites.

4.4.2 Electronic and Magnetic Properties

We start by talking about the magnetic lowest energy. Four different magnetic configurations, one FM, two AFM, and one FiM have been taken into consideration for this. This is done after taking into account the fact that the crystal's NM state was discovered to have the most unstable condition with maximum energy. The FiM magnetic state is found to have lowest energy of all other magnetic state for the materials indicating its ground state. The SOC calculations were performed to examine the effect of spin quantisation along $[100]$, $[010]$, $[001]$, $[110]$ and $[111]$ directions. Based on it, the MAE was found along $[010]$ for Ca_2CrIrO_6

direction. Furthermore, we also checked its ground state by fixed spin moment calculation (FSM) with different magnetic moment. This FSM calculation confirmed that the materials have lowest energy with FiM configuration.

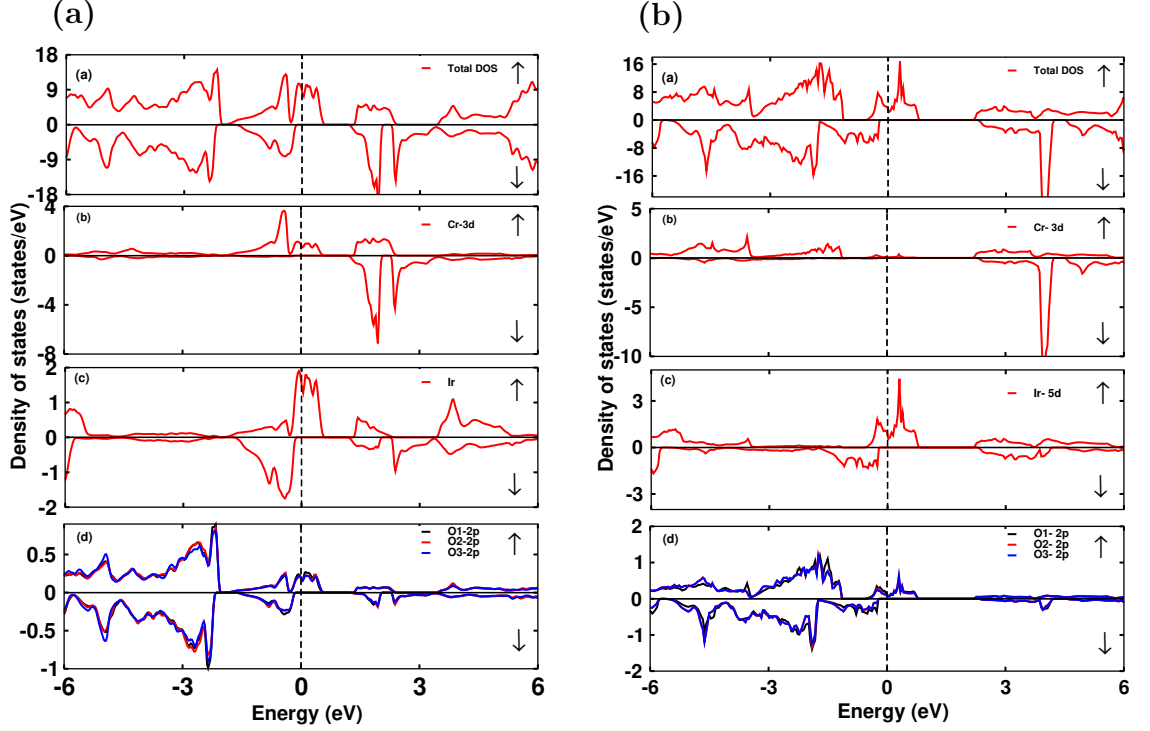


Figure 21: The total and partial DOS of $\text{Ca}_2\text{CrIrO}_6$ within (a) GGA and (b) GGA+ U functional, respectively.

In $\text{Ca}_2\text{CrIrO}_6$, the 3d transition metal Cr has charge state +3 with $3d^3$ configuration. Chromium interacts ferrimagnetically with iridium. Three electrons of chromium move to t_{2g} states for spin up cases. The e_g state is found to be non occupied in both channel and remains in conduction area. Likewise, iridium has charge +5 state with d^3 configuration. Three electrons goes to spin down in t_{2g} state and are found near to Fermi level in valence region and e_g state lie in conduction region as seen in Fig. 22.

Due to 3d transition elements present in the material, we extended our calculation with DFT+ U approximation. As the material contains Ir-5d element, we further extended our calculation to consider GGA+ U +SOC. SOC has been applied in five different directions [100], [010], [001], [110], [111] and investigated that SOC has a significant effect on the magnetic as well as electronic properties, specifically it opens the gap of 0.25 eV in $\text{Ca}_2\text{CrIrO}_6$. Hence, presence of gap on the material confirms that the material is semiconductor.

The DOS and band structure of the material with GGA, GGA+ U is presented in Fig. 21.

The prime contribution to the total DOS near to E_F is contributed by Cr-3d, Ir-5d, and O-2p states.

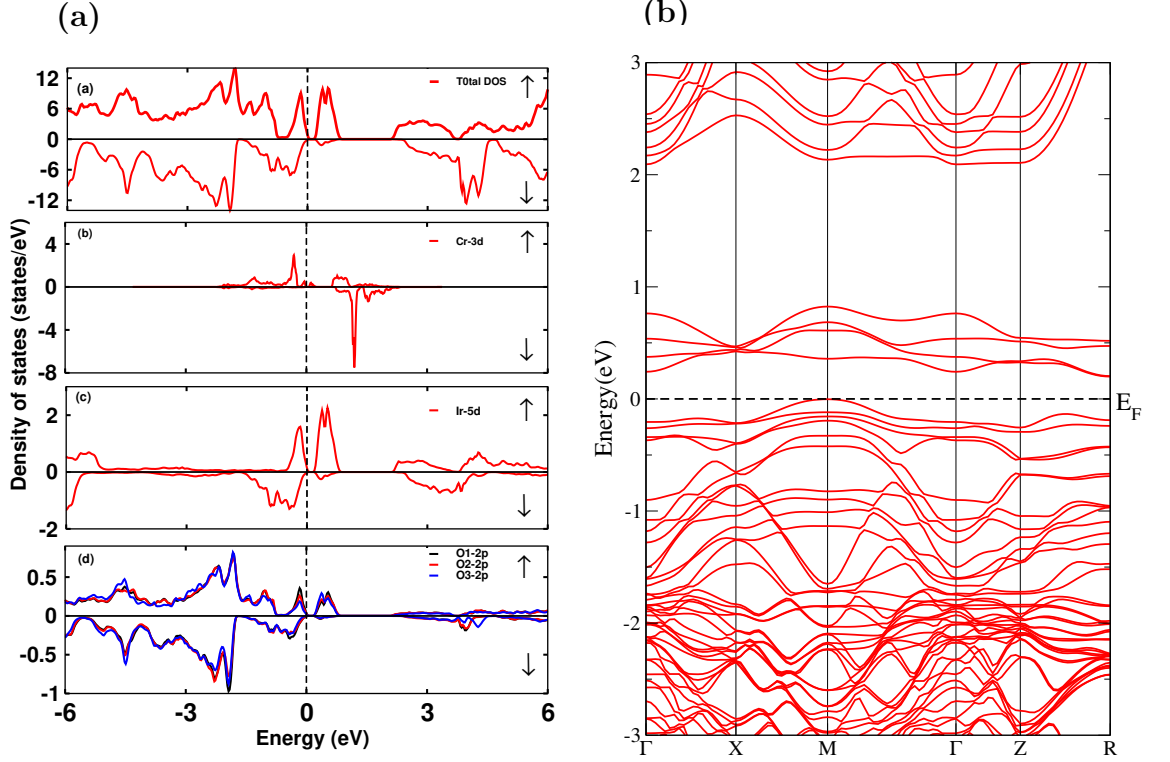


Figure 22: (a) The density of states and (b) band structure of Ca₂CrIrO₆ under GGA+*U*+SOC.

Oxygen-2p states are hybridized with iridium-5d states near E_F . From DOS plot, it is seen that Ir- t_{2g} (i.e., d_{xy} , d_{xz} , d_{yz}) states lie in valence region for spin down cases. This clarifies that Ir- t_{2g} states have filled orbitals for spin down channel. For spin up channel, both states lie in conduction region showing their empty state. With the ionic picture, this picture is determined to be consistent. Due to intense hybridization, the charge transfer effect is noticeable between the iridium-5d and oxygen-2p states. This produce small moments in oxygen atoms that polarised in same direction with Ir atoms.

The spin and orbital moment for chromium is computed as $2.54 \mu_B$ and $-0.073 \mu_B$. These moments are found to align in opposite direction indicating that 3d orbital are less or greater than half occupied Ca₂CrIrO₆. As in table 8, the spin moment in iridium is decreased because of the strong Ir-O hybridization. SOC produces the orbital moment that causes the small decrease in spin magnetic moment. In case of Ir-5d, orbital moment is obtained to be $-0.28 \mu_B$. This moment is in same direction with orbital magnetic moment of Cr that contribute to rise the effective moment to be $2.59 \mu_B$.

Table 8: Computed spin and orbital moments (in μ_B) and band gap ‘ E_g ’ (eV) for $\text{Ca}_2\text{CrIrO}_6$ compound.

$\text{Ca}_2\text{CrIrO}_6$			
site	GGA	GGA+ U	GGA+ U +SOC
B	2.12	2.55	2.54/−0.073
B′	−0.72	−0.96	−0.82/−0.284
O1	−0.08	−0.10	−0.078
O2	−0.076	−0.11	−0.083
O3	−0.072	−0.10	−0.085
Net	2.0	2.0	2.59
E_g	Metallic	Metallic	0.25

Hybridization of transition metals with oxygen produces polarisation in 2p orbitals as in Fig. 23 and this effect increases the resultant magnetic moment. Moment in oxygen site is found to be $0.078 \mu_B$ in same direction of Ir, which suggests that the stronger Ir-O covalency than Cr-O in $\text{Ca}_2\text{CrIrO}_6$. The charge density of Cr-3d states are not spherical due to only up channel are occupied in t_{2g} state and e_g state remains empty in both channel. So the contribution of charge distribution is only by t_{2g} state. Similarly, for Ir, charge distribution is in t_{2g} states for spin down channel that are clearly shown in Fig. 23.

4.4.3 Magnetic Ordering Temperature and Exchange Coupling Constant

Magnetic ordering temperature of the proposed material is also estimated by calculating the spin exchange parameters within DFT. We have used the exchange parameters for calculating the Curie temperature which is based upon Heisenberg model of the mean field approximation (MFA).

It is possible to express the Hamiltonian for spin interactions as

$$\hat{H} = - \sum_{i < j} J_{ij} \hat{S}_i \hat{S}_j \quad (4.10)$$

(J_{ij}) is coupling constant between spin at sites i and j . These i and j specify atomic sites in the crystal ($S_{Fe} = \frac{5}{2}$, $S_{Cr} = \frac{3}{2}$, $S_{Ir} = \frac{3}{2}$), As shown in the figure 24, J_1 for J_{Cr-Cr} (on-plane), J_2 for J_{Fe-Fe} (on-plane), J_3 for J_{Cr-Fe} (out-of-plane) having closest neighbors of 6, 12 and 12, respectively are considered for our calculations.

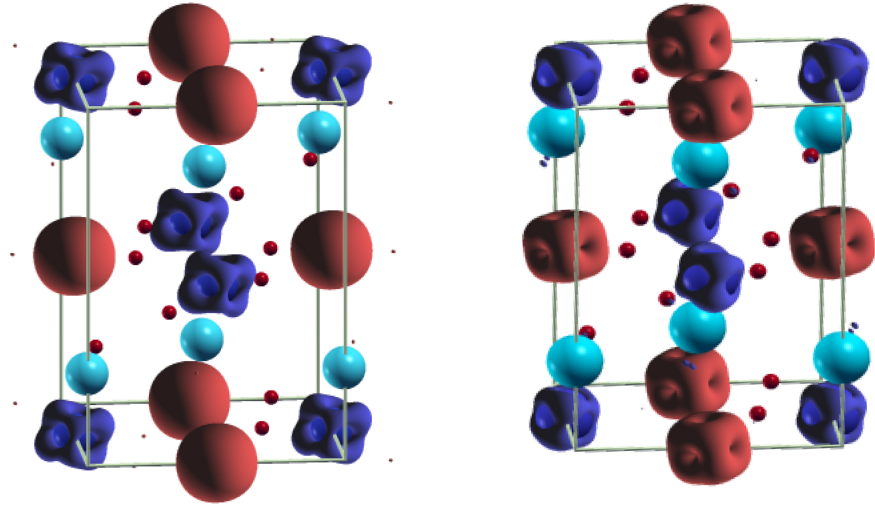


Figure 23: Isosurface of spin magnetization density at $\pm 0.23 e/ \text{Å}^3$ for $\text{Ca}_2\text{FeIrO}_6$ (left) and $\text{Ca}_2\text{CrIrO}_6$ (right), respectively.

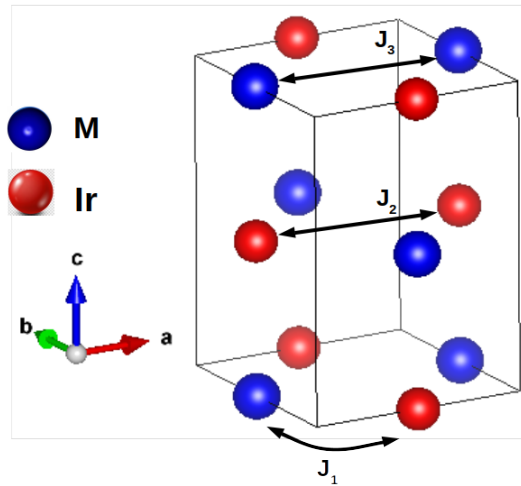


Figure 24: Calculated spin exchange interactions in DPs $\text{Ca}_2\text{CrIrO}_6$.

we used the energies of four spin configurations converged using on-site potential $+U$ and drafted following equations on the basis of spin Heisenberg hamiltonian.

$$E_{FM} = E_o + \frac{15}{4}(-6J_1) + \frac{9}{4}(-12J_2) + \frac{25}{4}(-12J_3) \quad (4.11)$$

$$E_{FIM} = E_o + \frac{15}{4}(+6J_1) + \frac{9}{4}(-12J_2) + \frac{25}{4}(-12J_3) \quad (4.12)$$

$$E_{AF1} = E_o + \frac{15}{4}(+2J_1) + \frac{9}{4}(+4J_2) + \frac{25}{4}(+4J_3) \quad (4.13)$$

$$E_{AF2} = E_o + \frac{15}{4}(+2J_1) + \frac{9}{4}(-12J_2) + \frac{25}{4}(+4J_3) \quad (4.14)$$

Solving process for J values in $\text{Ca}_2\text{CrIrO}_6$:

1. $E_{FM} - E_{uudd}$

$$0.011745033800253 = -27J_1 \quad (4.15)$$

$$J_1 = -0.000435001251861(\text{Hartree}) \quad (4.16)$$

$$J_1 = -1.89647495773932 \times 10^{-21}(\text{Joule}) \quad (4.17)$$

2. $E_{FM} - E_{uddd}$

$$9.4114599050954 \times 10^{-5} = -18J_1 - 36J_3 \quad (4.18)$$

$$-36J_3 = -0.007735907934451 \quad (4.19)$$

$$J_3 = 0.000214886331513(\text{Hartree}) \quad (4.20)$$

$$J_3 = 9.3683993949515 \times 10^{-22}(\text{Joule}) \quad (4.21)$$

3. $E_{FM} - E_{udud}$

$$0.005743078101659 = -18J_1 - 36J_2 - 36J_3 \quad (4.22)$$

$$-36J_2 = 0.005648963502608 \quad (4.23)$$

$$J_2 = -0.00015691565285(\text{Hartree}) \quad (4.24)$$

$$J_2 = -6.84105171731143 \times 10^{-22}(\text{Joule}) \quad (4.25)$$

Table 9: Calculated magnetic exchange coupling parameters (meV) for DPs $\text{Ca}_2\text{M}\text{IrO}_6$

interaction	description	nearest neighbour	M=Cr
J_1	M –Ir	6	–3.21
J_2	Ir–Ir	12	–4.25
J_3	M –M	12	5.85

The calculated J parameters, a characterization of each atom and its closest neighbors for double perovskite $\text{Ca}_2\text{CrIrO}_6$ are provided in the table. Our results are within the limitation regarding the DFT+ U approach that tries to localize orbitals, reducing magnetic orbital overlapping. Consequently, the spin exchange interactions will be reduced. This alter the magnetic transition temperature estimation in materials.

Magnetic ordering temperature T_C of the suggested materials has also been approximated under the mean field theory like,

$$T_C = S_i S_j \frac{2 \sum J_{ij}}{3 K_B} \quad (4.26)$$

where S_i and S_j are the corresponding spin quantum numbers at sublattices i and j . Our calculated T_C is 906 K for $\text{Ca}_2\text{CrIrO}_6$.

On comparing the measured and calculated Curie temperatures of different DPs as described by Mandal *et al.* (2008), we got a trend as in Fig. 25. We see that there is good agreement in its result although there is no experimental T_C reported on these materials.

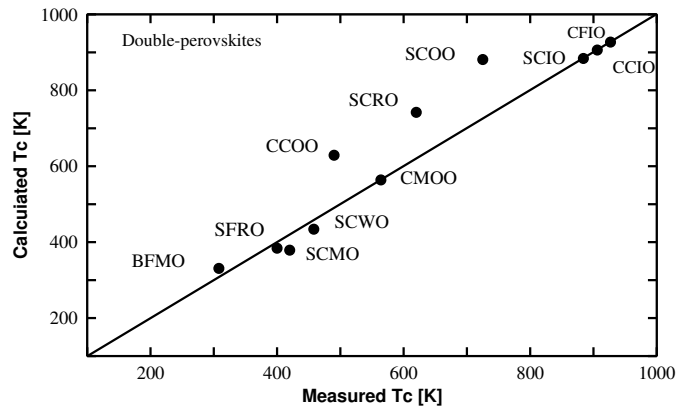


Figure 25: Calculated versus measured Curie temperatures for different double perovskites.

In graph different materials and their T_C have been taken as following references: $\text{Ba}_2\text{FeMoO}_6$

(BFMO), Sr₂FeReO₆ (SFRO), Sr₂CrMoO₆ (SCMO), Sr₂CrWO₆ (SCWO), Ca₂CrOsO₆ (CCOO), Ca₂MnOsO₆ (CMOO), Sr₂CrReO₆ (SCRO), Sr₂CrOsO₆ (SCOO), Sr₂CrIrO₆ (SCIO), Ca₂CrIrO₆, Ca₂FeIrO₆ (CFIO), respectively (Morrow *et al.*, 2016; Serrate *et al.*, 2007; Mandal *et al.*, 2008). Our theoretical value of T_C for all the compounds may be a little bit higher than their actual values in comparable materials. This is due to the fact that the mean-field theory frequently overestimates T_C and that T_C's absolute value relies on the chosen *U* values. However, our findings can support the T_C trend as in Fig. 25 for the proposed material.

4.5 Fe and Ir Doped at Cr and Os Site on Parent Material: Ca₂FeIrO₆

The material Ca₂FeIrO₆ is obtained in the same way like in Ca₂CrIrO₆, by doping Fe and Ir in place of Cr and Os with the same occupancy ratio of 76% and 24% in recently synthesized material Ca₂CrOsO₆ which possesses a large Curie temperature (T_C) of 490 K (Morrow *et al.*, 2016). The detail experimental or theoretical information regarding the properties of these materials are not available yet.

4.5.1 Stability of the Structure

For the substitution of different transition metals on parent materials, on the basis of tolerance factor,

$$t = \frac{r_A + r_O}{\sqrt{2}\left(\frac{r_B}{2} + \frac{r_{B'}}{2} + r_O\right)} \quad (4.27)$$

where *r_A*, *r_B*, *r_{B'}* and *r_O* are the ionic radii of the respective ions and oxygen (Correa *et al.*, 2006). We choose the components iron and iridium for doping to obtain Ca₂FeIrO₆ structure.

To evaluate the stability of proposed material, the cohesive and formation energy for Ca₂FeIrO₆ structure are determined as,

$$E_{for} = E_{Ca_2B_2IrO_6}^{tot} - [2E_{Ca}^{bulk} + E_B^{bulk} + E_{Ir}^{bulk} + 6E_O^{bulk}] \quad (4.28)$$

$$E_{coh} = E_{Ca_2B_2IrO_6}^{tot} - [2E_{Ca}^{iso} + E_B^{iso} + E_{Ir}^{iso} + 6E_O^{iso}] \quad (4.29)$$

Where, B= Fe, $E_{Ca_2B_2IrO_6}^{tot}$ is the total energy and E_{Ca}^{bulk} , E_B^{bulk} , E_{Ir}^{bulk} , E_O^{bulk} being energy of the bulk of calcium, iron, iridium and oxygen elements and E_{Ca}^{iso} , E_B^{iso} , E_{Ir}^{iso} , E_O^{iso} being the individual elemental energy of calcium, iron, iridium and oxygen. It is discovered that the

materials $\text{Ca}_2\text{FeIrO}_6$ have cohesive and formation energies of -4.54 and -4.25 eV/atom, respectively. The fact that the cohesive and formation energies are negative demonstrates that both materials are experimentally synthesizable and have thermodynamically stable structures.

4.5.2 Electronic and Magnetic Properties

First, we find the magnetic GS of the proposed material. Five different magnetic arrangements have been taken into consideration after optimizing the internal parameters: FM1- $\uparrow\uparrow\uparrow$, AFM1- $\uparrow\downarrow\uparrow\downarrow$, AFM2- $\uparrow\downarrow\downarrow\uparrow$, FiM1- $\uparrow\uparrow\downarrow\downarrow$ and FiM2- $\uparrow\uparrow\downarrow$, respectively. Here, we find that FiM1 has the least value of energy for predicting the magnetic GS. Magnetic easy axis is achieved in $[100]$ orientation and MAE is found to be 12 meV.

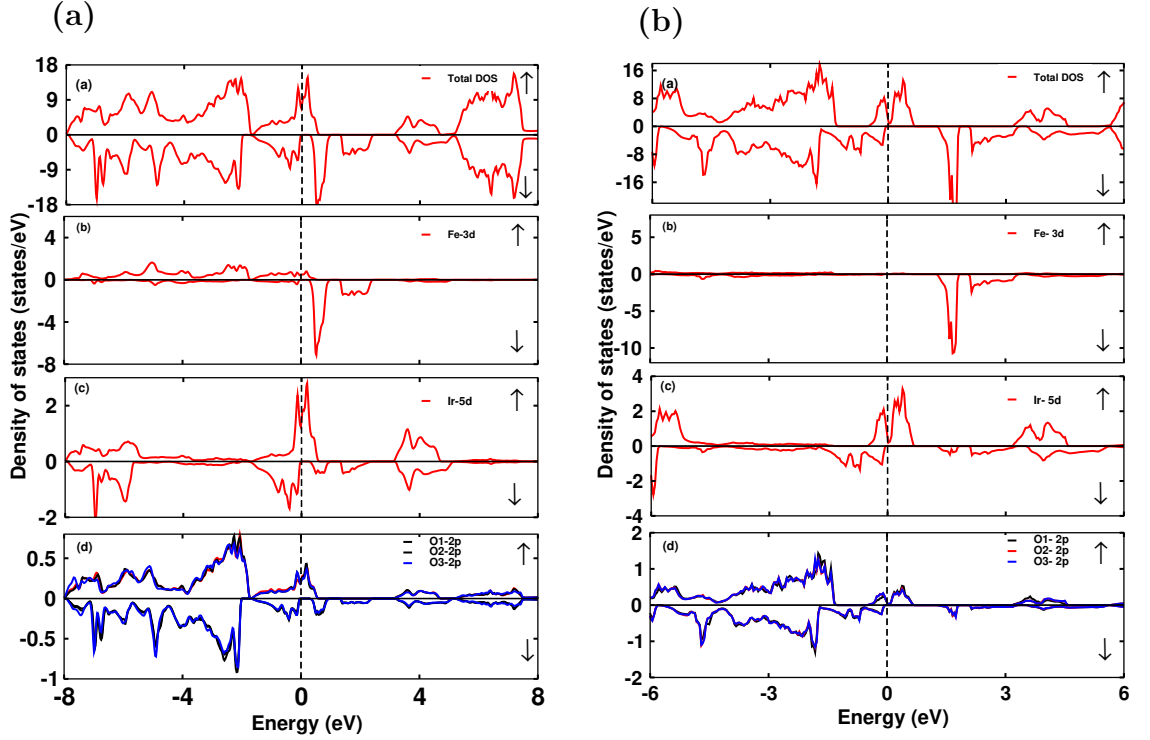


Figure 26: The total and partial DOS of $\text{Ca}_2\text{FeIrO}_6$ within (a) GGA and (b) GGA+ U functional, respectively.

In $\text{Ca}_2\text{FeIrO}_6$, five outer most electrons of Fe with $3d^5$ configuration has a charge state +3, are discovered to be filled in the up spin state and to be vacant in the down spin state. Regarding Ir, which has $5d^3$ configuration with charge state +5, the unoccupied t_{2g} states lie in the conduction region. As seen in Fig. 26, the three outer electrons shift to the spin-down

state and reside in the uppermost valence area beyond the E_F , creating a high spin state.

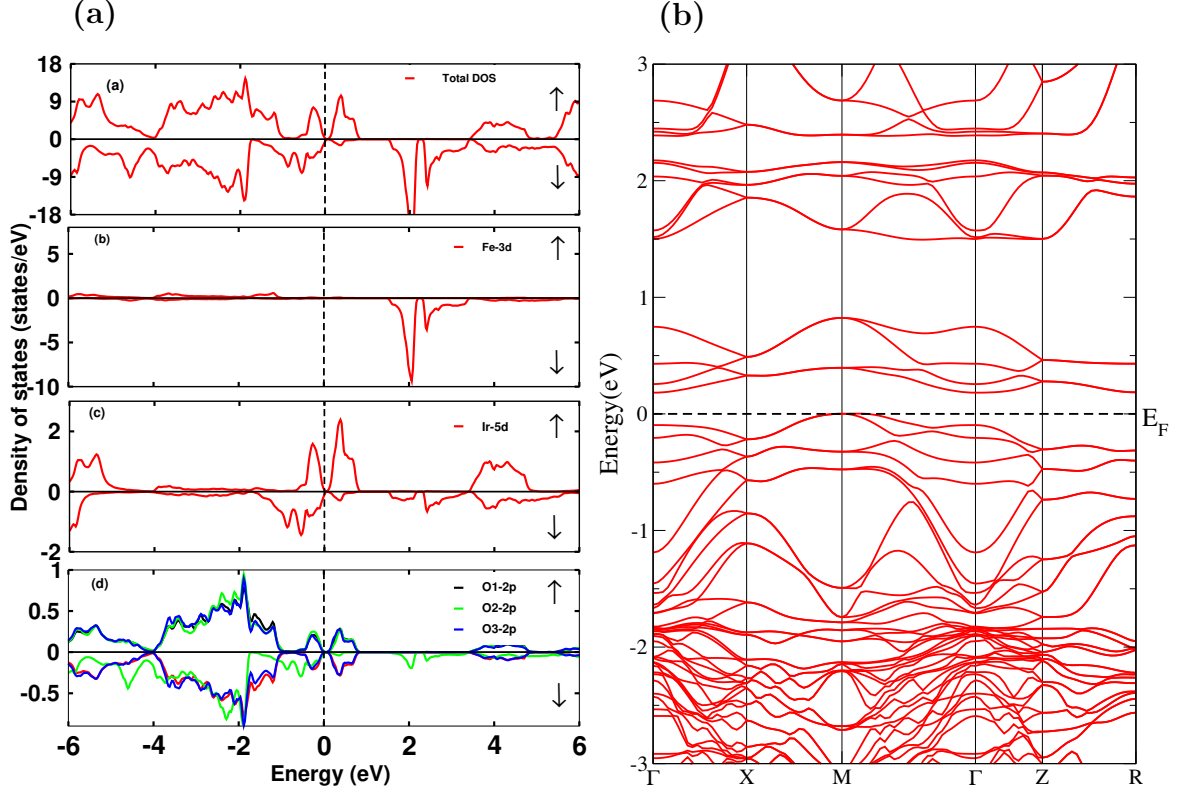


Figure 27: (a) The total and partial DOS and (b) band structures of $\text{Ca}_2\text{FeIrO}_6$ under GGA+ U +SOC.

The material should have a large correlation effect when 3d transition elements are present, however this impact is disregarded in GGA calculations. As a result, we extended our computation with DFT+ U approximation. As the material contains Ir-5d element, so we further extended our calculation to consider GGA+ U +SOC. SOC has been applied to investigate spin quantization's impact in five different direction [100], [010], [001], [110], [111] and investigated that SOC has a significant effect on the magnetic as well as electronic properties., specifically it opens the gap of 0.13 eV in $\text{Ca}_2\text{FeIrO}_6$ Hence, presence of gap on the material confirms that the material is semiconductor.

The DOS for $\text{Ca}_2\text{FeIrO}_6$ with different functional are presented in Fig. 29 and Fig. 30. The main role around E_F is contributed by d orbitals of transition metal and hybridized p orbitals of oxygen. It can be seen that Ir- t_{2g} states are completely filled in spin-down cases and reside in the filled region. In contrast, the states for the spin-up channel are vacant and are located in the conduction area together with empty Ir- e_g states. Strong hybridization results small moment in oxygen that are polarized in same direction with Ir atom which plays a role to increase the total magnetic moment.

Table 10: Calculated effective and individual moments (μ_B) and energy gap ‘ E_g ’ (eV) for $\text{Ca}_2\text{FeIrO}_6$ compound.

$\text{Ca}_2\text{FeIrO}_6$			
site	GGA	GGA+ U	GGA+ U +SOC
Fe	3.48	4.12	4.12/0.027
Ir	-0.55	-0.87	-0.73/-0.263
O ₁	0.01	-0.04	-0.01
O ₂	0.02	-0.02	0.03
O ₃	0.01	-0.03	-0.01
Net	6.0	5.99	6.66
E_g	Metallic	Metallic	0.13

The computed magnetic moments for the iron and iridium sites are $4.12 \mu_B$ and $-0.73 \mu_B$, correspondingly, as shown in table 10. At the Fe site, the computed orbital moment is found to be $0.027 \mu_B$. Computed orbital moment lie in the parallel direction with spin moment, indicating the half filled $5d^5$ configuration of Fe in $\text{Ca}_2\text{FeIrO}_6$ which resembles with Hund’s third rules (Kittel, 2006). At the Ir site, the estimated orbital moment is discovered to be $-0.26 \mu_B$. This orbital moment alligns in the same plane as spin magnetic moments, which add up to effective moment of $6.66 \mu_B$ per unit cell.

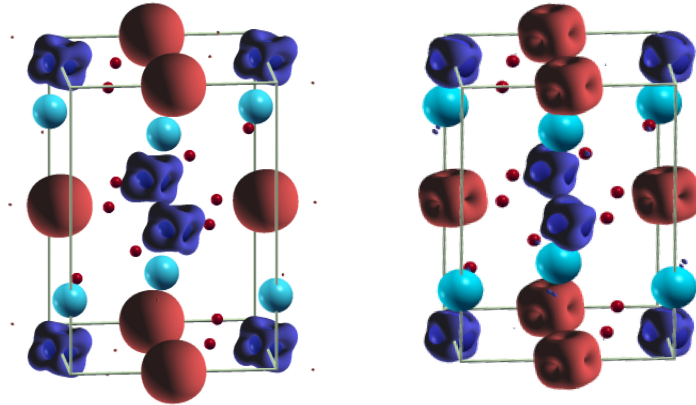


Figure 28: Spin magnetization density at $\pm 0.23 e/\text{\AA}^3$ for $\text{Ca}_2\text{FeIrO}_6$ (left) and $\text{Ca}_2\text{CrIrO}_6$ (right), respectively.

After replacing Cr atom with Fe atom, its t_{2g} state and e_g state are filled only the up channel and the down channel is unoccupied. Thus, charge distribution is contributed by both t_{2g} and e_g state and hence isosurface of iron is spherical and iridium contribution remains unchanged that can be seen in Fig. 28 (left).

4.5.3 Magnetic Ordering Temperature and Exchange Coupling Constant

Magnetic ordering temperature of the proposed material is also estimated by calculating the spin exchange parameters within DFT. We have used the exchange parameters for calculating the Curie temperature which is based upon Heisenberg model of the mean field approximation (MFA).

The Hamiltonian for spin interactions is expressed as:

$$\hat{H} = - \sum_{i < j} J_{ij} \hat{S}_i \hat{S}_j \quad (4.30)$$

(J_{ij}) is the spin coupling constant between spin at sites i and j , where i, j specify atomic sites in the crystal ($S_{Fe} = \frac{5}{2}$, $S_{Cr} = \frac{3}{2}$, $S_{Ir} = \frac{3}{2}$). As shown in the figure 6, J_1 is represented for J_{Cr-Cr} (on-plane), J_2 for J_{Fe-Fe} (on-plane), J_3 for J_{Cr-Fe} (out-of-plane), respectively.

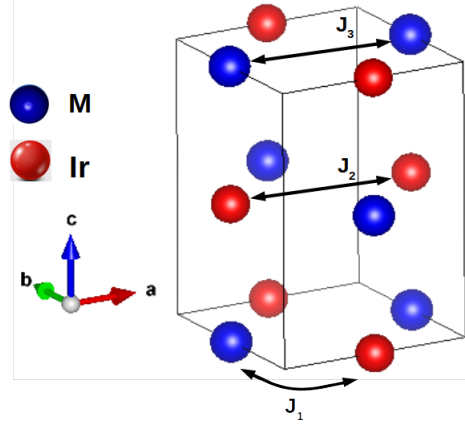


Figure 29: Calculated magnetic exchange interactons in the DPs configurtion $\text{Ca}_2\text{CrIrO}_6$ and $\text{Ca}_2\text{FeIrO}_6$.

we used the energies of four spin configurations converged using on-site potential $+U$ and drafted following equations on the basis of spin Heisenberg hamiltonian.

$$E_{FM} = E_o + \frac{15}{4}(-6J_1) + \frac{9}{4}(-12J_2) + \frac{25}{4}(-12J_3) \quad (4.31)$$

$$E_{FIM} = E_o + \frac{15}{4}(+6J_1) + \frac{9}{4}(-12J_2) + \frac{25}{4}(-12J_3) \quad (4.32)$$

$$E_{AF1} = E_o + \frac{15}{4}(+2J_1) + \frac{9}{4}(+4J_2) + \frac{25}{4}(+4J_3) \quad (4.33)$$

$$E_{AF2} = E_o + \frac{15}{4}(+2J_1) + \frac{9}{4}(-12J_2) + \frac{25}{4}(+4J_3) \quad (4.34)$$

The table provides the computed J parameters, atom descriptions, and nearest neighbors for the DPs $\text{Ca}_2\text{FeIrO}_6$. Our results are within the limitation regarding the DFT+ U approach.

Table 11: Computed spin exchange coupling parameters (in meV) for DPs $\text{Ca}_2\text{FeIrO}_6$

interaction	description	nearest neighbour	M=Fe
J_1	M –Ir	6	–3.55
J_2	Ir–Ir	12	–0.8
J_3	M –M	12	– 0.32

By localizing orbitals, this method reduces the overlap between magnetic orbitals. Consequently, this will lessen spin exchange interactions and influence how material’s magnetic transition temperatures are estimated.

We also calculated Curie temperature T_C of the $\text{Ca}_2\text{FeIrO}_6$ on the basis of the mean field theory and calculated T_C is found to be 827 K for $\text{Ca}_2\text{FeIrO}_6$ which is found to be in valid trend of other calculated as in Fig. 25.

4.6 Ni and Ir Doped at Cr and Os Site on Parent Material: $\text{Ca}_2\text{NiIrO}_6$

The material $\text{Ca}_2\text{NiIrO}_6$ (CNIO) is obtained by substituting Ni and Ir in place of Cr and Os with the same occupancy ratio of 76% and 24% in recently synthesized material $\text{Ca}_2\text{CrOsO}_6$ which possesses a large Curie temperature (T_C) of 490 K (Morrow *et al.*, 2016). The detail experimental or theoretical information regarding the properties of these materials are not available yet.

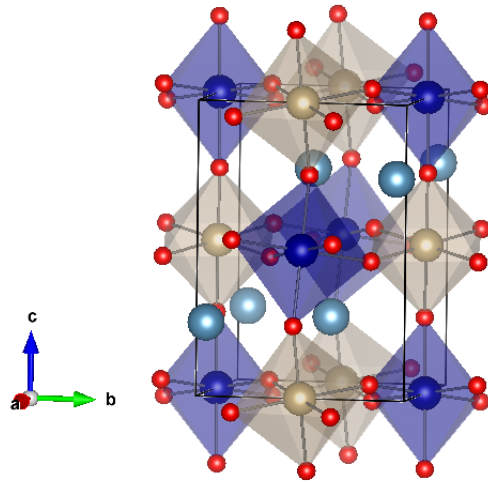


Figure 30: Crystal structure of $\text{Ca}_2\text{NiIrO}_6$ (colors in sky blue, blue, grey and red spheres corresponds to Ca, Ni, Ir and O atoms, respectively).

4.6.1 Electronic and Magnetic Properties

In $\text{Ca}_2\text{NiIrO}_6$, magnetic atoms Ni/Ir carry on opposite spin orientations. The electronic structure and magnetic properties of $\text{Ca}_2\text{NiIrO}_6$ are investigated through first principles approach. Figure 30 illustrates the crystal structure of double perovskites $\text{Ca}_2\text{NiIrO}_6$ and its primitive Brillouin zone. The ionic charge of each element can be assigned as Ca^{2+} , Ni^{3+} , Ir^{5+} , O^{2-} . Using the experimental parameters, we performed total energies of a supercell with different magnetic alignments. we calculate taking four possible magnetic configurations using up/dn spins of magnetic moments on Ni1/Ir1, Ni2/Ir2 atoms. These are one FM, two AFM and one FIM, i.e., FM1- $\uparrow\uparrow\uparrow\uparrow$, AF1- $\uparrow\downarrow\uparrow\downarrow$, AF2- $\uparrow\downarrow\downarrow\uparrow$ and FiM- FiM1- $\uparrow\uparrow\downarrow\downarrow$, FiM2- $\uparrow\uparrow\downarrow$, respectively and found that FiM configuration is stable with lowest energy indicating its ground states in $\text{Ca}_2\text{NiIrO}_6$.

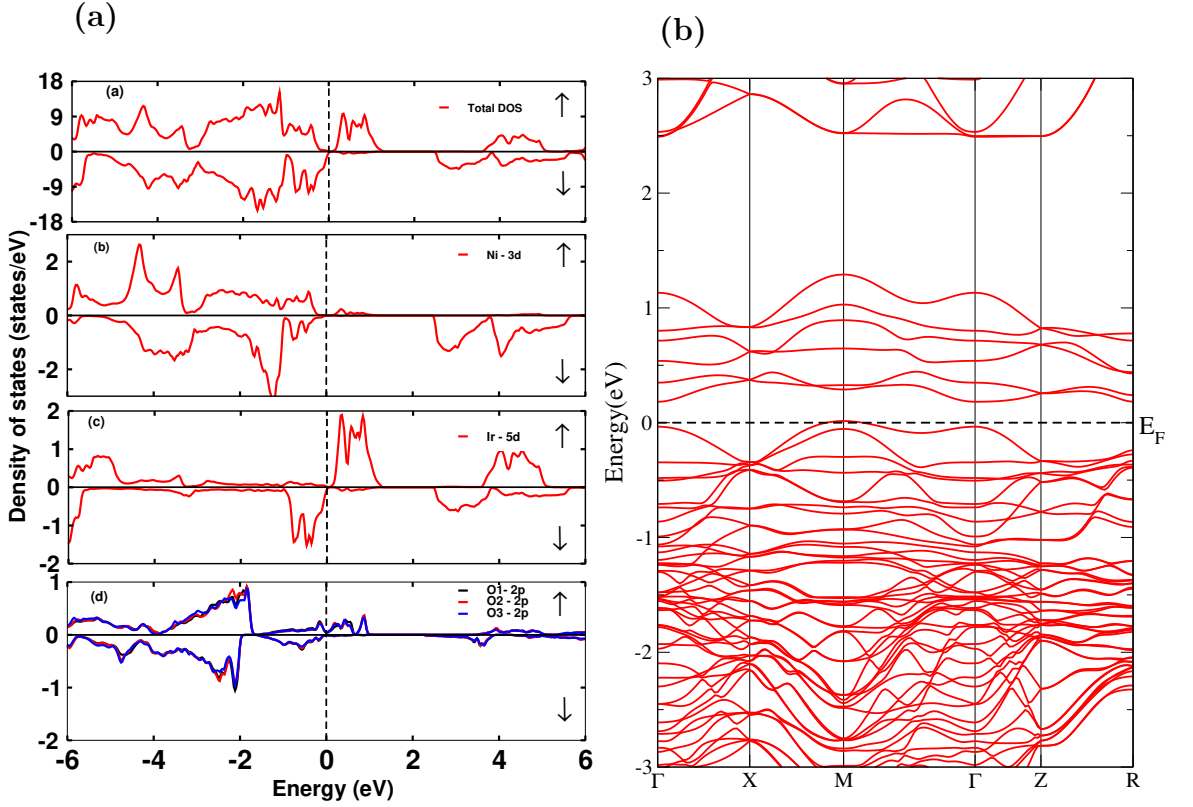


Figure 31: (a) The DOS and (b) band structures of $\text{Ca}_2\text{NiIrO}_6$ under GGA+ U +SOC.

Nickel has $3d^7$ configuration with a charge state +3. Seven outer most electrons of Ni moves to t_{2g} and e_g states in up channel while remaining 2 electron go to down channel in t_{2g} state. In case of Ir, which has $5d^3$ configuration with charge state +5. The three d electrons are found in the top most valence region a few levels down the Fermi level E_F offering high spin state as in Fig. 31.

Table 12: Calculated effective and individual moments (μ_B) and energy gap ‘ E_g ’ (eV) for $\text{Ca}_2\text{NiIrO}_6$ compound.

$\text{Ca}_2\text{NiIrO}_6$			
site	GGA	GGA+ U	GGA+ U +SOC
Ni	0.87	1.63	1.62/0.131
Ir	-0.98	-1.31	-1.19/ 0.067
O1	-0.10	-0.16	-0.14
O2	-0.10	-0.16	-0.16
O3	-0.10	-0.15	-0.14
Net	1.99	1.99	1.54
E_g	Metallic	2.43	0.08

Due to the presence of 3d and 5d transition elements in the proposed material, we applied DFT+ U approximation with U equals 5 eV for nickel and 1.5 eV for iridium and further extended our calculation to consider GGA+ U +SOC. SOC has been applied to investigate spin quantization’s impact in five different direction [100], [010], [001], [110], [111] and investigated that SOC has a significant effect on the magnetic as well as electronic properties., specially it opens the gap of 0.08 eV in $\text{Ca}_2\text{NiIrO}_6$. Hence, presence of small gap on the material confirms that the materials is semiconductor (Fig. 31).

On the other hand, it is discovered that the Ir-5d states are crucial in determining the electronic characteristics. In both spin channels, it is discovered that they substantially hybridize with O- 2p states. Their hybridization takes place mainly around E_F . We see that Ir- t_{2g} states are completely filled in spin-down channels. Hence, they are found in the valence area. While for spin-up case, the empty states are located in conduction area along vacant Ir- e_g states. Because of intense hybridization, oxygen atom experience significant moments.

The first principle result shows that the magnetic moment of Ni, Ir are $1.6 \mu_B$, $-1.19 \mu_B$ with effective moment to be 1.54 per unit cell. This difference in the magnetic moment is due to the partial charge transfer of moment to inequivalent oxygens from Ni and Ir. Due to hybridization with Ni and Ir, oxygen also gain small magnetic moment and polarization is mainly found on p-orbitals. Here, the orbital magnetic moment of Ir-5d atom is slightly greater than the Ni-3d atom. The orbital moment of Ni is in parallel direction with individual moment indicating 3d orbital is occupied by either half or greater than half. While incase of Ir-5d, the orientation of orbital magnetic moments are antiparallel is caused by less than half-

occupied inconsistency with Hund's rules (Jeng *et al.*, 2003). Hence, The orbital magnetic moment on Ir is anti parallel with spin magnetic moment as shown in table (12) which decreases the net magnetic moments.

4.6.2 Magnetic Ordering Temperature and Exchange Coupling Constant

Curie temperature (T_C) of the material is estimated using the Heisenberg model. The Hamiltonian for the spin-spin interactions is given by,

$$\hat{H} = -\sum_{i<j} J_{ij} \hat{S}_i \hat{S}_j \quad (4.35)$$

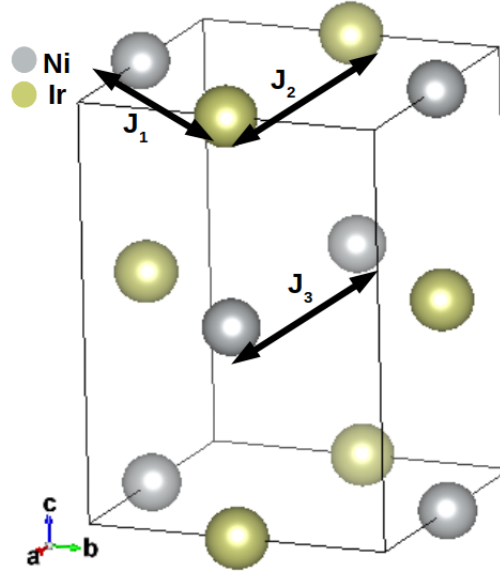


Figure 32: Spin exchange interactions paths in DPs configuration $\text{Ca}_2\text{NiIrO}_6$.

J_{ij} represents spin coupling constant between spin at sites i and j , where i, j specify atomic sites in the crystal ($S_{Ni} = \frac{3}{2}$, $S_{Ir} = \frac{3}{2}$). Our calculated T_C is found to be 272 K.

4.7 Mn and Ir Doped at Cr and Os Site on Parent Material: $\text{Ca}_2\text{MnIrO}_6$

The material $\text{Ca}_2\text{MnIrO}_6$ (CMIO) is prepared by replacing Cr and Os with Mn and Ir with the same occupancy ratio of 76 percent and 24 percent in the newly synthesized material $\text{Ca}_2\text{CrOsO}_6$ (Morrow *et al.*, 2016). There is no detail information available on the characteristics of these materials yet.

The total energies for four magnetic configurations (FM-uuuu, FiM-uudd, AFM1-udud, and

AFM2-uddu) are calculated first. It's worth noting that each Mn and Ir atom has two magnetic configurations: Mn1, Mn2, Ir1 and Ir2. The Mn1-up, Mn2-down, Ir1-up, and Ir2-down alignment of spins in magnetic configurations is implied by the AFM1-udud arrangement. FiM is the magnetic ground state, according to the calculations above. As a result, the following discussion is limited to the FiM configuration in $\text{Ca}_2\text{MnIrO}_6$.

4.7.1 Electronic and Magnetic Properties

The Mn atom in $\text{Ca}_2\text{MnIrO}_6$ carry a charge state of +3 with a $3d^3$ configuration. Three electrons are distributed in the t_{2g} orbitals in up channel and lie in valence region nearby to the E_F , while the e_g state is empty and lies in the conduction region in both spin channels. Ir with a charge state of +3 and a $5d^5$ structure, on the other hand, has five topmost electrons. The five electrons are found to fill only the t_{2g} state due to their low spin state, with e_g lying far in the conduction area for both spin channels. The spin-up channel is metallic, whereas spin down is insulating, as seen in the partial DOS of Ir in Fig. 34. Consequently, spin-down channel are filled, resulting in a band gap, while two out of three are partially occupied in the spin-up channel, dictating the metallic state.

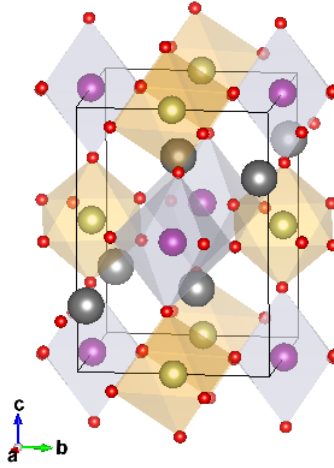


Figure 33: Crystal structure of $\text{Ca}_2\text{MnIrO}_6$ DPs.

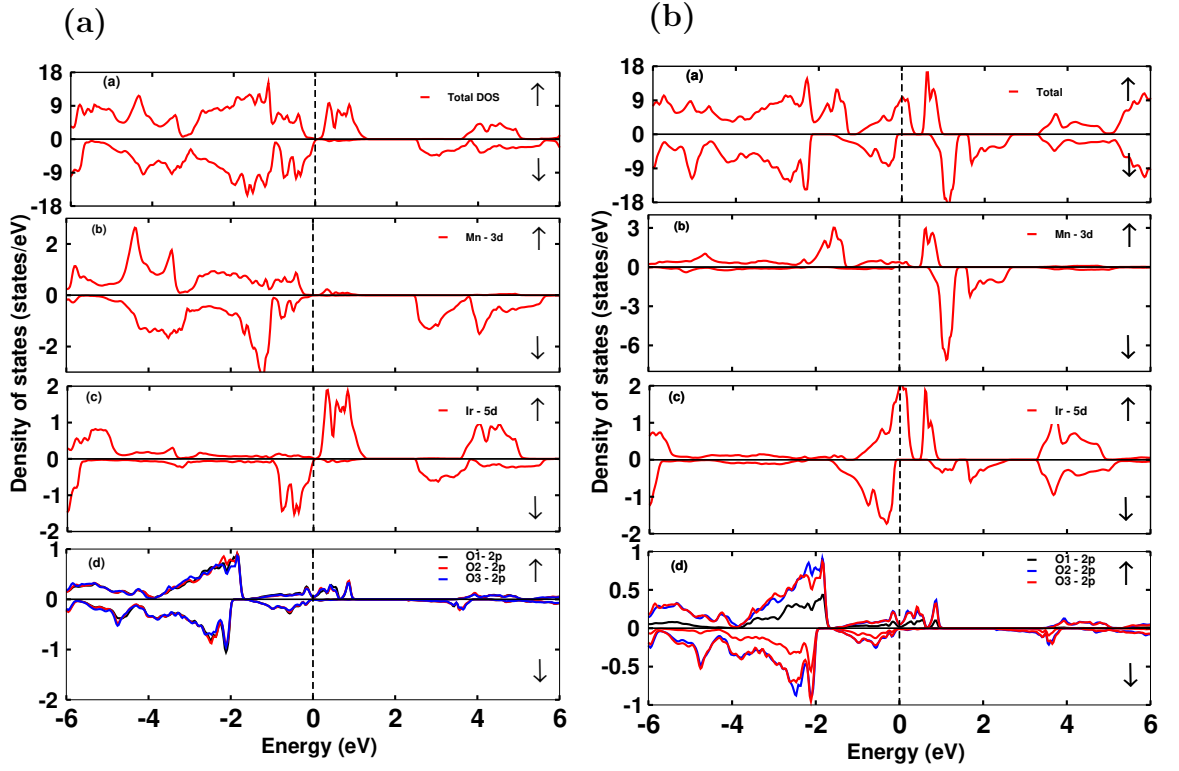


Figure 34: Total and partial DOS of $\text{Ca}_2\text{MnIrO}_6$ under (a) GGA and (b) GGA+ U functional.

Figures 34 and 35 show the spin resolved partial and total DOS of $\text{Ca}_2\text{MnIrO}_6$. Mn-3d, Ir-5d, and O-2p states all play a role in partial DOS near E_F (Fig. 35 (a) (left)). As seen in the spin down channel, Ir- t_{2g} states are in a high spin state, whereas spin up channels are around the conduction region. In the valence region, Ir-5d states are shown to be hybridized with O-2p levels. Charge transfer from Ir-5d to O-2p states was seen as a result of this hybridization.

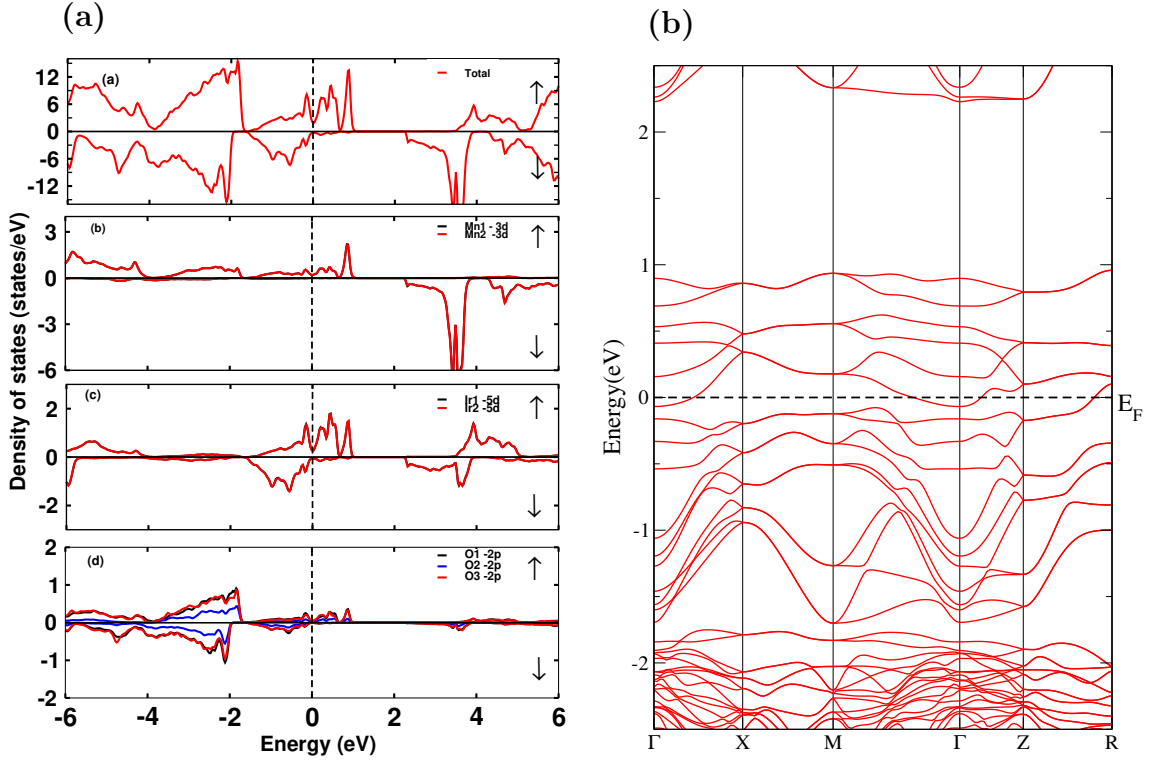


Figure 35: (a) Total and partial DOS and (b) band structures of $\text{Ca}_2\text{MnIrO}_6$ under GGA+ U +SOC.

As demonstrated in Fig. 35(b), the mixed effect of U and SOC results in a pseudo band gap (or semi-metallic state) in the band structure. Despite Ir's high SOC strength, crystal distortion appears to dominate during spin up, resulting in the metallic state. Its effect is most noticeable in Ir, where the Ir-5d bands split greatly, as shown in Fig. 35. This can be compared to Figure 37 (b). $\text{Ca}_2\text{MnIrO}_6$ displays HM-FiM state with up spin being metallic and down spin being insulating, which can be proven both by DOS and band structure.

Within the FiM ground state, the individual moments of Mn and Ir are determined to be $2.05 \mu_B$ and $-0.62 \mu_B$, respectively. The net moment of the material is $1.15 \mu_B$ per unit cell. The charge transfer effect causes a finite transfer of charges from Mn and Ir to oxygens, resulting in a difference in magnetic moment. As a result of their hybridization with Mn and Ir, oxygen gains a tiny moment ($0.06 \mu_B$) and becomes polarized. As shown in table 13, the orbital moment of Ir is larger than that of Mn. Because of the Ir-O hybridization, Ir's spin magnetic moment is reduced.

Table 13: Calculated effective and individual moments (μ_B) and energy gap ‘ E_g ’ (eV) for $\text{Ca}_2\text{MnIrO}_6$ compound.

$\text{Ca}_2\text{MnIrO}_6$			
site	GGA	GGA+ U	GGA+ U +SOC
Mn	2.84	2.84	3.06/−0.003
Ir	−0.574	−0.57	−0.62/ −0.238
O1	−0.05	−0.05	−0.06
O2	−0.05	−0.05	−0.06
O3	−0.05	−0.05	−0.06
Net	3.99	4	4.15
E_g	Metallic	Metallic	HM

4.7.2 Magnetic Ordering Temperature and Exchange Coupling Constant

The proposed material’s Curie temperature (T_C) is calculated using exchange parameters that depends upon the Heisenberg model. The interaction of spins Hamiltonian is given by,

$$\hat{H} = - \sum_{i < j} J_{ij} \hat{S}_i \hat{S}_j \quad (4.36)$$

J_{ij} represents the spin coupling constant between spin at sites i and j , where i, j specify atomic sites in the crystal ($S_{Mn} = \frac{5}{2}, S_{Ir} = \frac{3}{2}$).

we used the energies of four spin configurations converged using on-site potential $+U$ and drafted following equations on the basis of spin Heisenberg hamiltonian.

$$E_{FM} = E_o + \frac{15}{4}(-6J_1) + \frac{9}{4}(-12J_2) + \frac{25}{4}(-12J_3) \quad (4.37)$$

$$E_{FIM} = E_o + \frac{15}{4}(+6J_1) + \frac{9}{4}(-12J_2) + \frac{25}{4}(-12J_3) \quad (4.38)$$

$$E_{AF1} = E_o + \frac{15}{4}(+2J_1) + \frac{9}{4}(+4J_2) + \frac{25}{4}(+4J_3) \quad (4.39)$$

$$E_{AF2} = E_o + \frac{15}{4}(+2J_1) + \frac{9}{4}(-12J_2) + \frac{25}{4}(+4J_3) \quad (4.40)$$

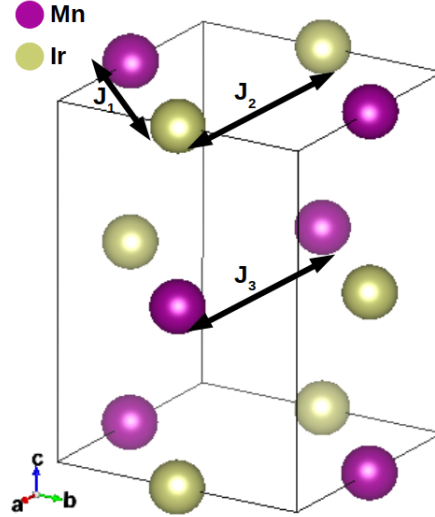


Figure 36: Computed magnetic exchange interactions in DPs configuration $\text{Ca}_2\text{MnIrO}_6$.

The magnetic ordering temperature T_C of $\text{Ca}_2\text{MnIrO}_6$ is then estimated using mean field theory and calculated T_C is found to be 280 K for $\text{Ca}_2\text{MnIrO}_6$.

4.8 Sr-Based Double Perovskites:

Parent Material: SrLaNiOsO_6

In this section, we discuss different properties of Sr-based double perovskites. The parent materials SrLaNiOsO_6 is taken from the recently synthesized groups of materials $\text{ALaBB}'\text{O}_6$ ($A = \text{Ca}, \text{Sr}$; $B = \text{Co}, \text{Ni}$; $B' = \text{Ru}, \text{Os}$)(Morrow *et al.*, 2018). The crystal structure of $\text{SrLaBB}'\text{O}_6$ as shown has a space group $\text{P}2_1/\text{n}$ (14) in which BO_6 and $\text{B}'\text{O}_6$ octahedra maintains the monoclinic structure. There are three sort of oxygen atoms in $\text{B}(\text{B}')\text{-O1}$, $\text{B}(\text{B}')\text{-O2}$ and $\text{B}(\text{B}')\text{-O3}$. For the calculation of Sr- based double perovskites, we used both GGA and LDA fuctional but the results obtained from LDA fuctional are more comparable with experimental results. So we reported the results of LDA fuctional here.

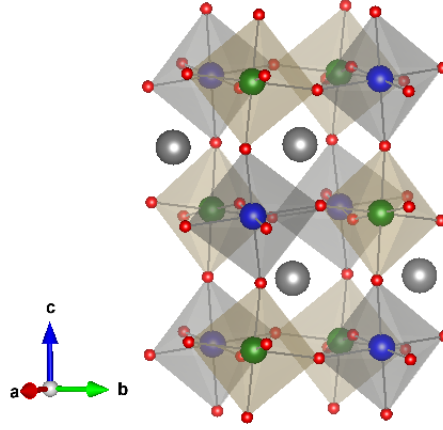


Figure 37: Crystal structure of double perovskites $\text{SrLaBB}'\text{O}_6$ (where grey, blue, green, and red spheres correspond to Sr(La), B, B' and O sites).

The material SrLaNiOsO_6 (SLNOO) contains four atoms of Sr/La at the same positions with equal occupancy and with on SrLaLaSr arrangement. By calculating the energy for the five possible magnetic configuration taking experimental lattice parameters, we found that compound SLNOO is stable with lowest energy on AF2($\uparrow\downarrow\uparrow$)-configuration which gives its ground state consistent with experimental result (Morrow *et al.*, 2018; Feng *et al.*, 2014). Thus, this system is antiferromagnetic in nature with total magnetic moment zero.

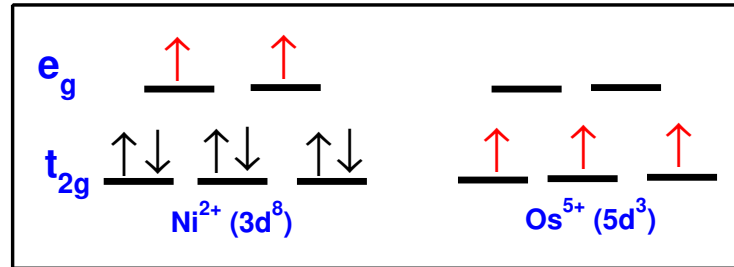


Figure 38: Schematic representation of the super-exchange interactions between Ni and Os with d^3 - d^5 electronic configurations.

4.8.1 Electronic and Magnetic Properties

The DOS of osmium containing compound SLNOO is calculated using experimental lattice parameters obtained at 10 K. From, Fig. 40, it is clear that the Ni-3d and Os-5d have greatest contribution near Fermi level than other atoms. So, we have not plotted PDOS of Sr, La-atoms. Oxygen atoms has small contribution near Fermi-level, because the p-orbitals of O-atom is half filled orbital. Up and down DOS are symmetric nature that means that there is no magnetic moment, which means antiferromagnetic in nature. Fermi level with the

presence of small DOS with very small gap 0.04 eV shows that the system is insulating in nature as shown in Fig. 42.

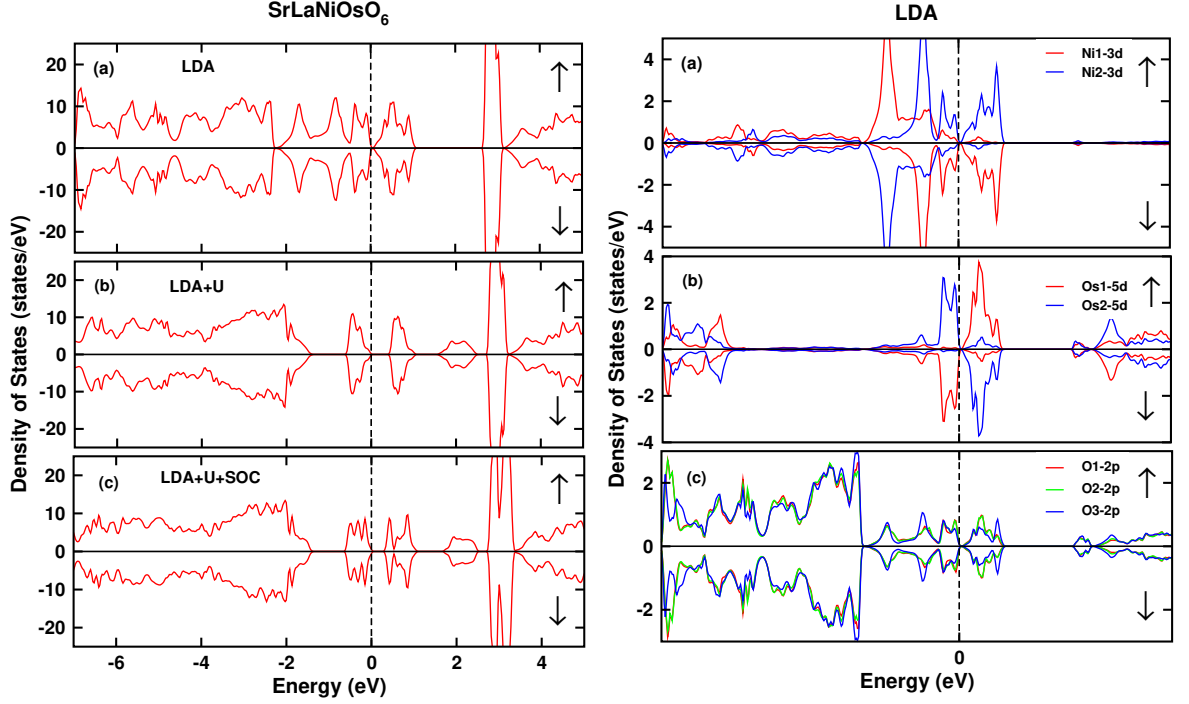


Figure 39: Total and partial DOS for SrLaNiOsO₆.

From figure, we examine the PDOS of the main DOS contributions at Fermi level by Ni-3d and Os-5d atoms. From the PDOS of LDA and LDA+ U , it's obvious that the main contribution near Fermi level is due to by Os after applying U -values. In these DOS plot, the contributions of Ni1 and Ni2 is very small near E_F around 0.5 eV energy and larger number of DOS are shifted from Fermi level. For Os atoms contribution of DOS is slightly shifted outward from E_F in valence and conduction region. The contributions of band for Ni is larger in valence band than conduction band but for Os both bands contribution is nearly equal. After applying Coulomb potential, the partially filled O-2p orbital has a tiny contribution at E_F with a bigger contribution in the valence area, as seen in Fig. 40. SOC also plays an important role in heavy elements like Os. 5d oxides have a larger spatial extension and hence SOC affect more in 5d as a comparison to 3d/4d atoms, which lead interesting and unexpected electronic and magnetic behavior. After applying SOC, band gap decreases by 0.11 eV and slightly affects the orientations of PDOS of Ni and Os as shown in figures.

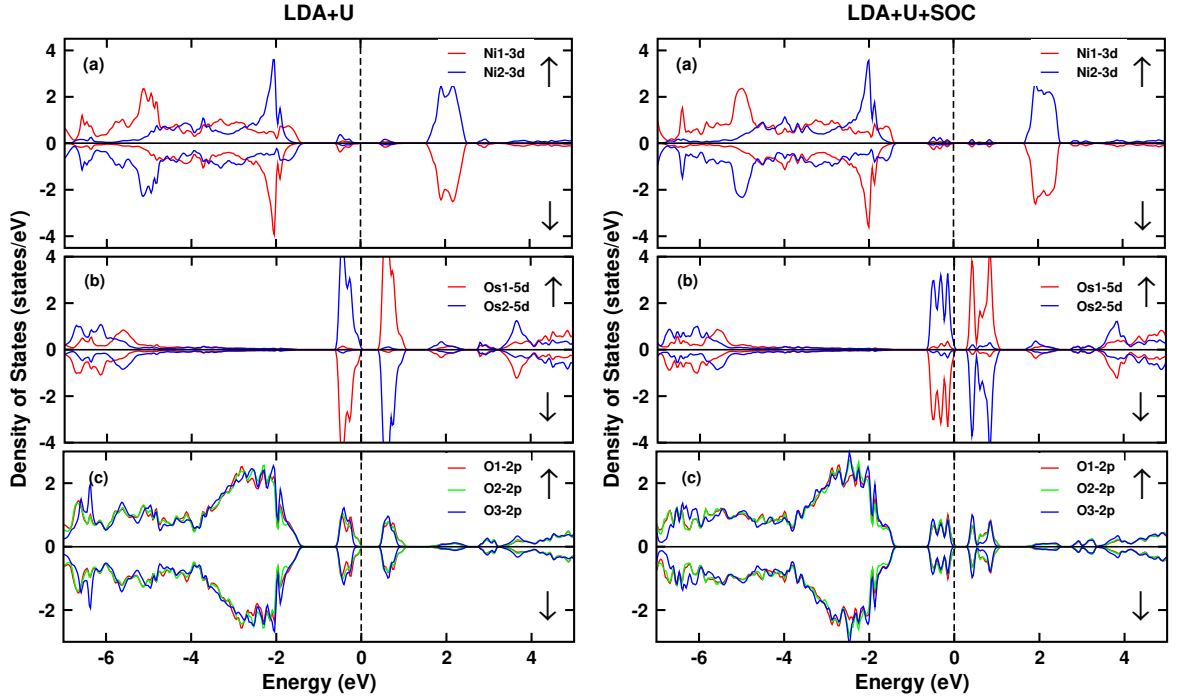


Figure 40: Partial DOS within LDA+ U and LDA+ U +SOC functional for SrLaNiOsO₆.

Due to the empty shell of La-atoms, the largest peak of total DOS is exhibited in the conduction band at roughly 3 eV. In the valence band, Ni-3d and O-2p atoms contribute the largest peak in the energy range 2-3 eV. When compared to Os-atoms, the DOS of Ni and O-atoms is near Fermi level. Because d-orbitals are half-filled, but s and p orbitals are totally filled, d-orbitals dominate in both valence and conduction band in Ni and Os-atoms. Because of the significant SOC, DOS peaks near the E_F divide. Oxygen bands below E_F are hybridized with the Ni-3d and Os-5d states, as shown in Fig. 40. This is due to octahedron distortions, which result in three different types of oxygen locations with varied Ni(Os)-O bond lengths. Both spin channels have oxygen 2p states that strongly hybridize with Os-5d states around E_F .

SLNOO has highly distorted structure due to which 3d/5d orbitals are split into five orbitals with different energy. The Ni and Os PDOS graphs for these five orbitals are presented in Fig. 40. It is obvious from these PDOS that both e_g and t_{2g} have contributions close to Fermi level. Because of the significant Os-O hybridization and the SOC there is slight decrease in magnetic moment in SLNOO.

With the AF2 magnetic configuration, effective moment in SLNOO is zero per unit cell. When U is applied, the spin magnetic moment of Ni and Os increases, but when SOC is applied, the Os magnetic moment falls while the Ni magnetic moment practically stays the same. The table (14) shows the orbital moments of Ni and Os. The orbital quenching of Ni

Table 14: Computed effective, individual and orbital magnetic moments (μ_B) and energy gap ‘ E_g ’ (eV) for SrLaNiOsO₆ compound.

SrLaNiOsO ₆			
site	GGA	GGA+ U	GGA+ U +SOC
Ni	1.38	1.68	1.68(0.22)
Os	1.36	1.52	1.36(0.15)
O1	0.06	0.09	0.08
O2	0.06	0.09	0.08
O3	0.16	0.14	0.13
Net	-		
E_g	0.04	0.44	0.33

results in a rather significant orbital moment. Oxygen gains a minor magnetic moment as a result of its hybridization with Ni and Os, and polarization is mostly seen on p-orbitals. Because 5d oxides have a longer spatial extension, the influence of Coulomb interaction is smaller than in 3d oxides. However, Ni-3d oxides have a bigger orbital magnetic moment i.e., $0.22 \mu_B$ than Os-5d oxide i.e., $0.15 \mu_B$. SOC plays a major function in this compound SLNOO due to the presence of heavy components Os. As a result of the combined influence of U and SOC, the gap approaches the experimental gap. As a result, for SLNOO, we use LDA+ U +SOC computations.

We studied band structure calculation, which requires integration over the Brillouin zone (BZ), to better understand the electrical structure. For the reciprocal space integrations to a monoclinic unit cell, we sampled the linear tetrahedron approach with 500 k-points across the full first BZ which gives $8 \times 8 \times 6$ k-mesh. For band structure calculations, we must choose a path in the Brillouin zone with the high symmetry points. The Y-axis depicts energy in eV, while the X-axis displays the wave vector of the first Brillouin zone with different symmetry points. We also analyzed fat band topologies to clearly distinguish contributions in the bands from distinct orbitals of the different elements in SLNOO. The transition elements Ni-3d and Os-5d make considerable contributions of orbitals through band structure at E_F , as seen in fat band plots. On the Fermi level, the d-orbitals of both atoms play a crucial role in band formation. Whereas, s and p-orbitals have a little role in band formation because s and p-orbitals are fulfilled (3p, 4s) at the atomic core, while d-orbitals (3d, 4d) are half-filled in the valence shell. However, because Sr and La have orbitals on the valence shell, their

contributions to band formation are minimal. d-orbitals are also empty, according on the electrical configuration. Conduction bands are located above the E_F , while valence bands are located below the E_F .

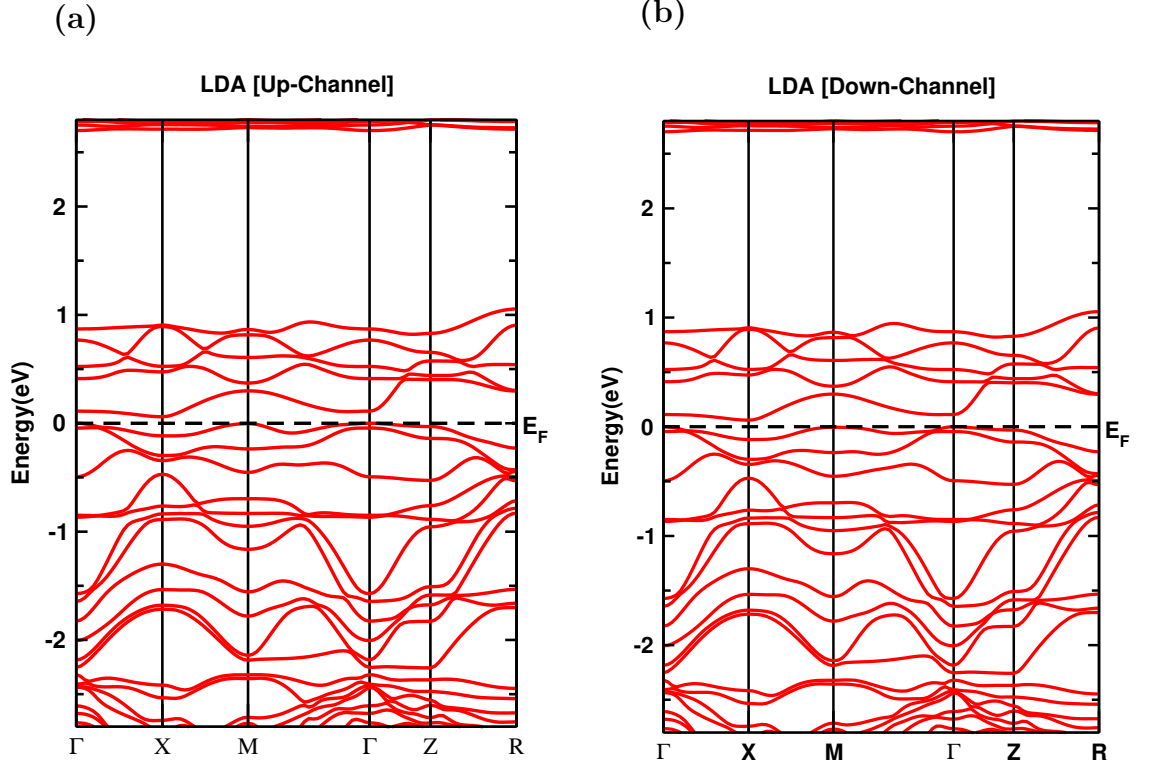


Figure 41: Band structures of SrLaNiOsO₆ within LDA functional.

Bands are symmetric in nature for both up and down spins, as can be seen in band plots. Near Fermi level, the contribution of t_{2g} and e_g -orbitals of Ni and Os containing system SLNNO is substantial enough. The presence of 3d and 5d-orbitals near Fermi region on both region is clearly visible in the fat band plots for Ni and Os of d-orbitals. The Fermi level is only touched by conduction bands with a energy gap of 0.04 eV, as seen in Fig. 41. Fat band analysis for Ni1-3d and Os1-5d is displayed in Figs. 44 and 45, respectively, to visualize the main contributions of individual atoms. We can observe from the d-orbital fat bands that the valence and conduction bands have approximately the same amount of electrons loaded in them. Analyzing these fat bands of Ni1 and Os1, we can say that 3d/5d-orbital electrons contributes in the major fundamental properties of this compound.

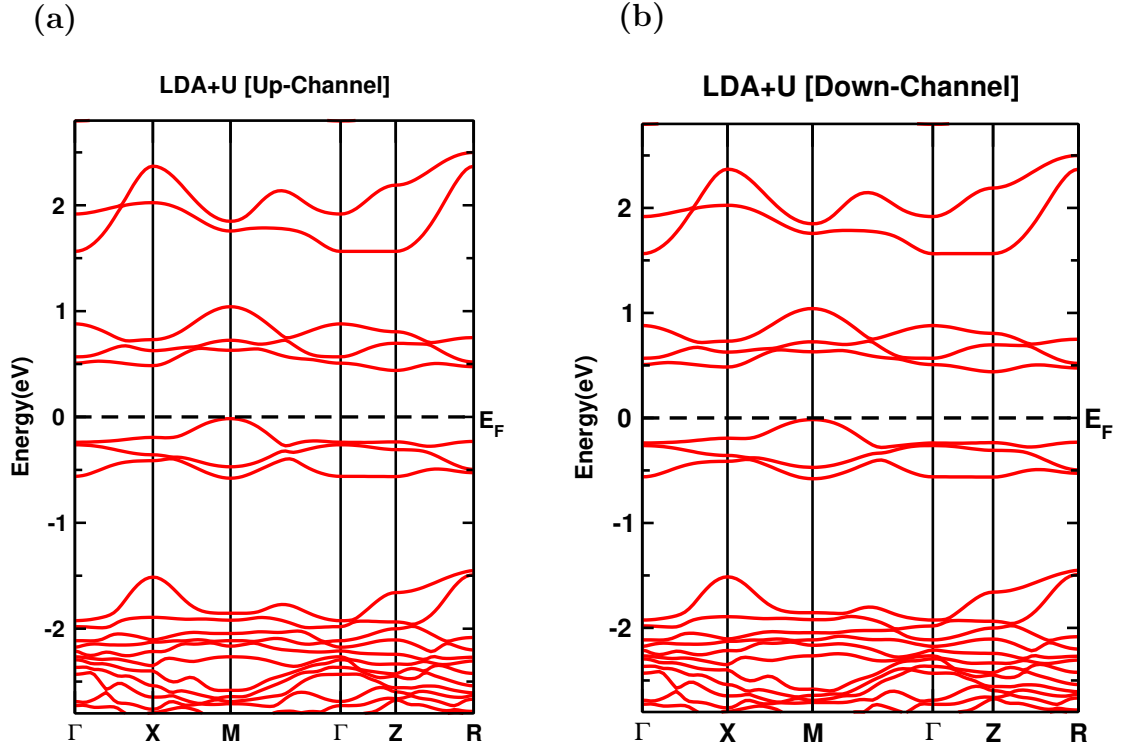


Figure 42: Band structures of SrLaNiOsO₆ within LDA+ U functional.

We discovered a 0.44 eV band gap after choosing the proper U -value of Ni and Os atoms, as illustrated in Fig. 42.

The highest energy on the valence band is at M-symmetry point, and the minimum energy on the conduction band is at Z-symmetry point, indicating that this system has an indirect band gap. The electrical properties are dominated by Os in this case.

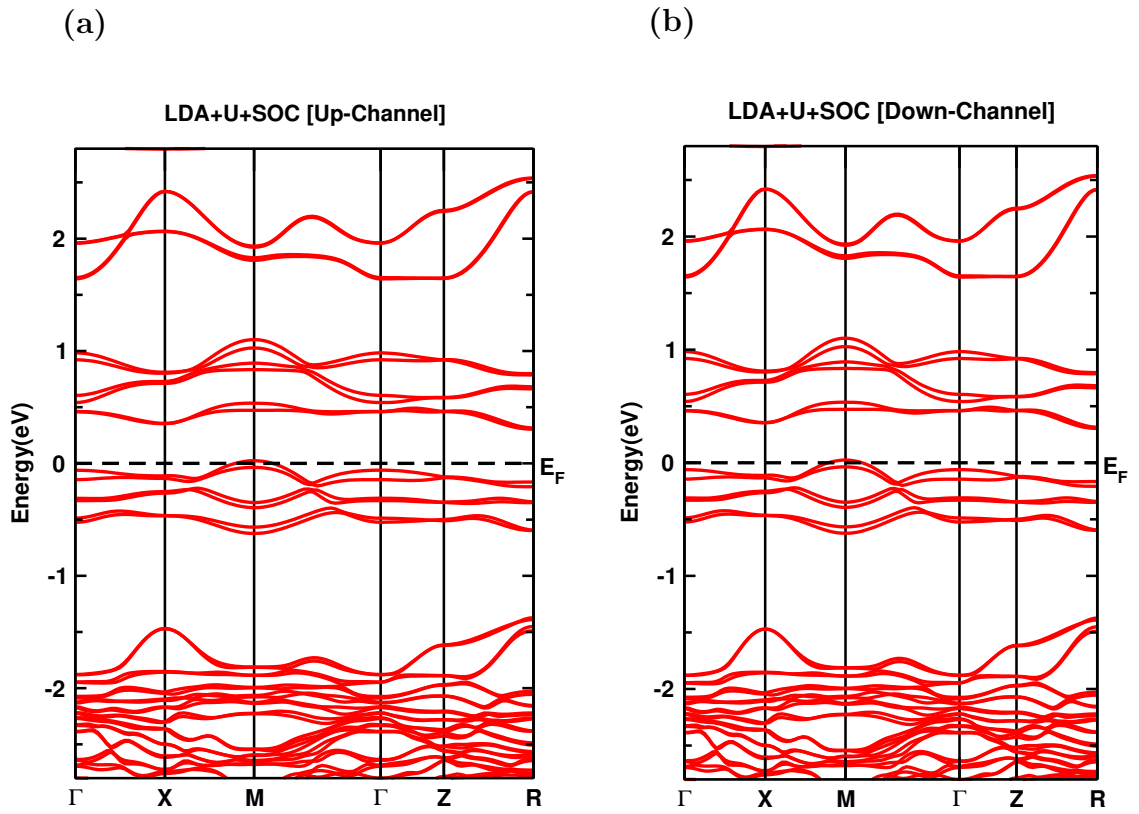


Figure 43: Band structures of SrLaNiOsO₆ within LDA+*U*+SOC functional.

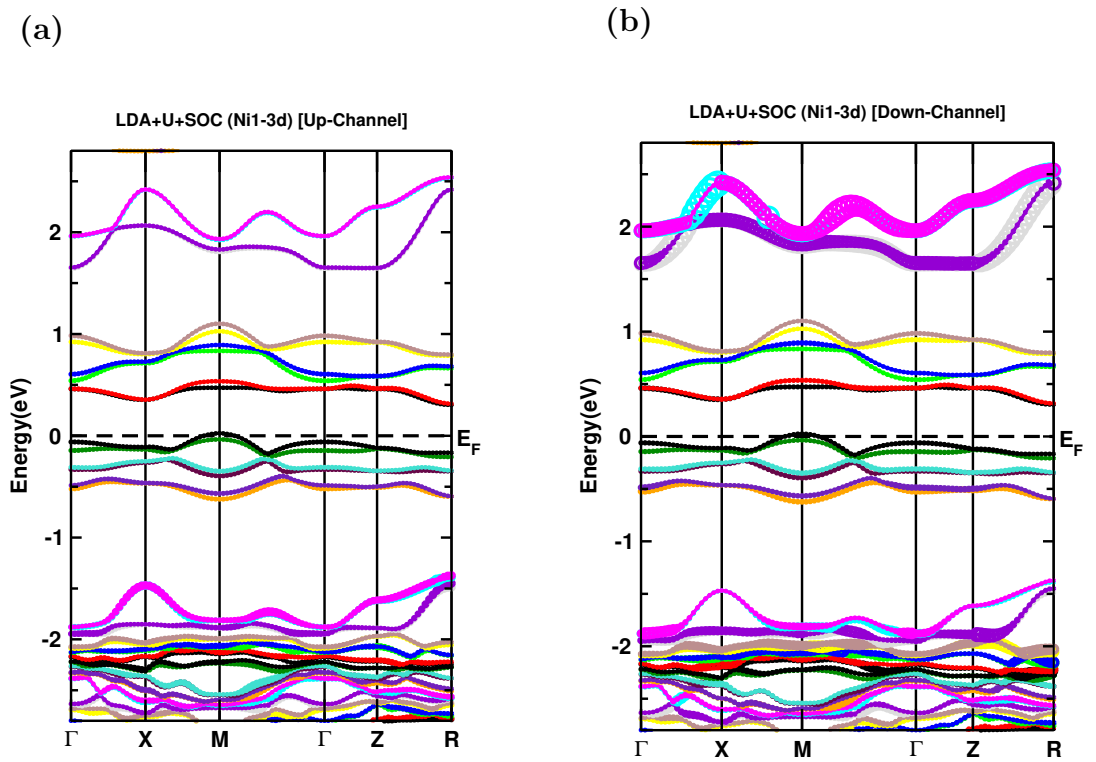


Figure 44: Fat band structures on Ni-3d of SrLaNiOsO₆ within LDA+*U*+SOC functional.

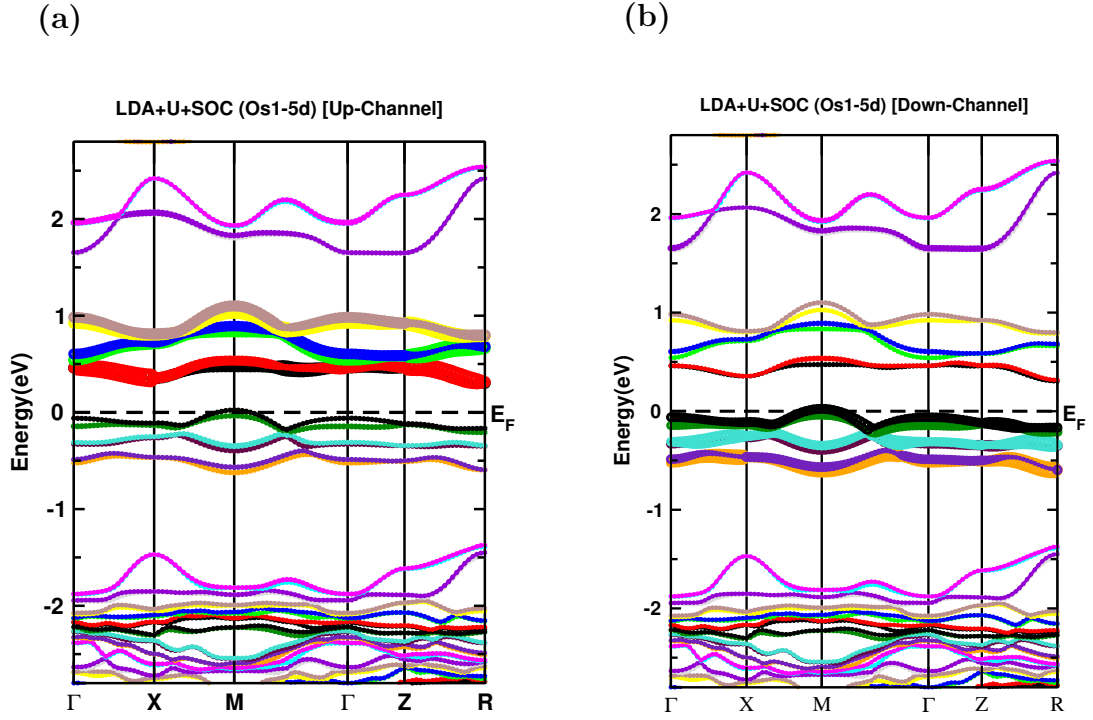


Figure 45: Fat band structures Os1-5d on SrLaNiOsO₆ within LDA+ U +SOC functional.

Figure 44 shows band plots for both spins after applying SOC, Having a energy gap of 0.33 eV in the 001-direction. SOC is crucial to the operation of this system to ensure that the experimental outcomes are consistent. Here, the band plots reveals an indirect band gap. This band gap plainly indicates that this system is semiconducting in nature, and it is also known as a Mott-insulator. Fat bands of Ni1-3d and Os-5d indicate that after applying U and SOC, Ni bands move further away from Fermi level, whilst Os bands stay close to Fermi level. As illustrated in fat band plots, Os plays a major impact in electrical characteristics. By examining DOS and band, it is evident that DOS peaks are higher when there are more bands and lower peaks where there are less bands. As a result, DOS and band structures are very similar.

4.9 Fe Doped at Ni Site on Parent Material: SrLaFeOsO₆

The material SrLaFeOsO₆ acquired by doping Fe at Ni site in SrLaNiOsO₆ with same occupancy ratio. For magnetic GS, we calculated the energy of SrLaFeOsO₆ (SLFOO) for the four possible magnetic configuration and found that AF2($\uparrow\downarrow\uparrow$)- magnetic configuration is stable with lowest energy indicating its ground state. Thus, this system is antiferromagnetic in nature with total magnetic moment zero.

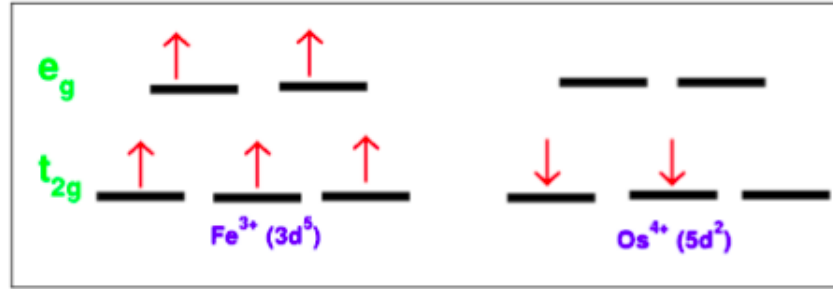


Figure 46: Schematic representation of the super-exchange interactions between Fe and Os with d^3 - d^5 electronic configurations.

4.9.1 Electronic and Magnetic Properties

Using experimental lattice parameters obtained at 10 K, the density of states of the osmium-containing compound SLFOO is computed. The density of states is depicted using Fermi energy as a reference. We investigated the nature of compounds using LDA, LDA+ U and LDA+ U +SOC and analyzed DOS plots. Fig. 47 shows that the Fe-3d and Os-5d atoms contribute more than the other atoms. Because the p-orbitals of the O-atom are half-filled orbitals, they have a minor contribution at Fermi-level. DOS are symmetric in nature, which indicates magnetic moment is zero, making them antiferromagnetic. In Fig. 50, Fermi level crossovers are visible, indicating that the system is metallic. Because 3d and 5d-electrons are substantially localized, SLFOO is actually a strongly correlated system. LDA+ U , as mentioned in the prior theory part, accounts for this. Using U -values for Fe= 5 eV and Os= 1.5 eV in the LDA+ U approximation, metallic nature was discovered once more. Near Fermi level, there is a minor amount of DOS. As a result, we applied the second variational approach of spin-orbit coupling in five different directions, and the ground state energy was discovered along the 001-direction with a narrow band gap of 0.03 eV. As a result, electron correlation and SOC both helped the Mott-insulator.

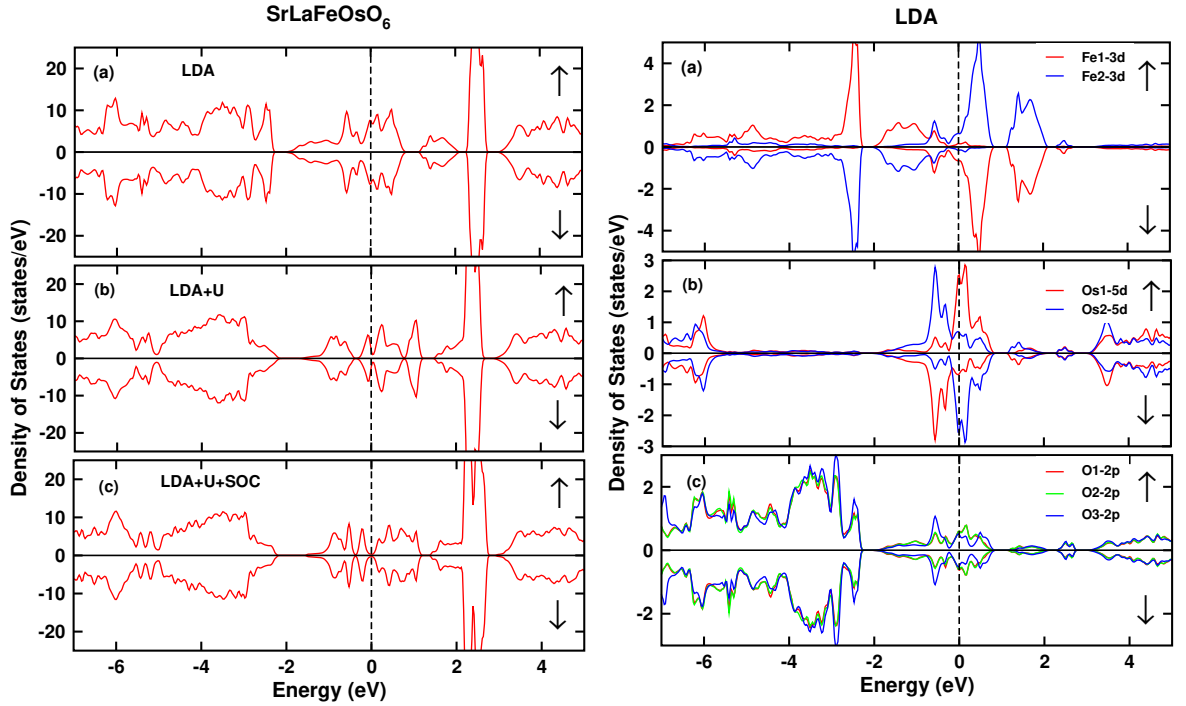


Figure 47: Total and partial DOS for SrLaFeOsO₆.

The PDOS of the substantial DOS contributions at Fermi level by Fe-3d and Os-5d atoms is examined in Figures 47 and 48. Fe and Os both cross heavily on the Fermi level in LDA plots, but LDA+ U has a smaller impact on the Fermi level than LDA. Both Fe and Os atom contributions are slightly out of phase with Fermi level in both region, but they cross Fermi level marginally. Band contributions for Fe are greater in the conduction band (CB) than in the valence band (VB), but band contributions for Os are approximately equal in both bands. For example, after applying Coulomb potential to a partially filled O-2p orbital, it has a minor contribution at E_F with a bigger contribution in the VB, as seen in Figure. SOC is also crucial in heavier materials such as Os. Because 5d oxides have a longer spatial extent than 3d atoms, SOC affects them more, resulting in fascinating and surprising electrical and magnetic behavior. As a result, SOC is critical in concluding experimental findings. After applying SOC, a small gap of 0.03 eV developed on the Fermi level, which has a small effect on the orientations of Fe and Os PDOS.

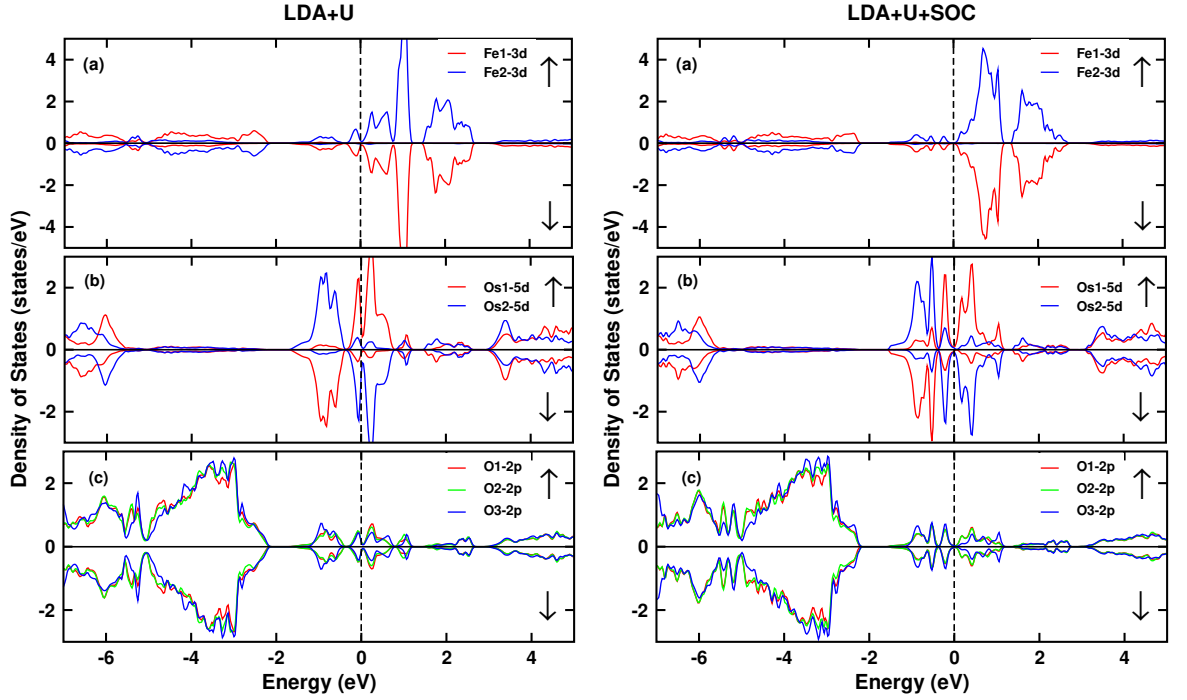


Figure 48: Partial DOS for SrLaFeOsO₆.

In comparison to Fe and Os-atoms, DOS contributions of Fe and O-atoms are very low near Fermi level. Because d-orbitals are half-filled whereas s, p orbitals are totally filled, d-orbitals dominate in valence and conduction bands in Fe and Os-atoms. Strong electron-correlations cause a DOS peak at the E_F split. Oxygen bands are hybridized with the Fe-3d and Os-5d states, as seen in Fig. 48. This is owing to octahedron distortions, which result in the appearance of three different types of oxygen locations with varied Fe(Os)-O bond lengths. In both spin channels, oxygen 2p states are hybridized with Os-5d states near Fermi level. In SLFOO the Fe and Os have electronic configuration Fe⁵⁺ ($3d^5:t_{2g}^3e_g^2$) and Os⁴⁺ ($5d^2:t_{2g}^2e_g^0$). It is obvious from these PDOS that both e_g and t_{2g} have contributions close to Fermi level. Significant Os-O hybridization and SOC causes the modest decrease in magnetic moment on SLFOO.

With the AF2-magnetic arrangement, the magnitude of the effective moment in SLFOO is zero per unit cell. When U is applied, the spin magnetic moment of Fe and Os increases, but when SOC is applied, the Os-moment falls while the Fe-moment practically stays the same. The table (15) shows the orbital moments of Fe and Os. The greater SOC of Os in contrast to Fe is responsible for its large orbital moment. Oxygen gains a minor magnetic moment as a result of hybridization with Fe and Os, and polarization is mostly seen on p-orbitals. Because 5d oxides have a longer spatial extension, the effect of Coulomb interaction is weaker than in 3d oxides, resulting in a smaller orbital magnetic moment in Fe-3d oxides. i.e., $0.097 \mu_B$ then

Table 15: Computed effective, individual and orbital moments (μ_B) and energy gap ‘ E_g ’ (eV) for SrLaFeOsO₆ compound.

SrLaFeOsO ₆			
site	GGA	GGA+ U	GGA+ U +SOC
Fe	3.54	4.02	4.04(0.09)
Os	0.77	1.09	0.88(0.23)
O1	0.02	0.02	0.01
O2	0.02	0.01	0.02
O3	0.14	0.14	0.12
Net	-		
E_g	Metallic	Metallic	0.03

Os-5d oxide i.e., $0.225 \mu_B$. Because of presence of heavy elements Os, SOC has a significant impact in SrLaFeOsO₆. Thus, the combined effect of U and SOC induced Mott-insulating nature.

Despite the fact that each Fe and Os atom has an independent spin magnetic moment of 5 and $2 \mu_B$, the first principle result reveals that the magnetic moments of iron and osmium are $4.04 \mu_B$ and $0.88 \mu_B$, respectively. The partial charge transfer between Fe-O and Os-O causes this discrepancy in magnetic moment. The orbital moments on iron and osmium are induced by SOC and parallel to spin moments. High Os-O hybridization reduces the spin moment on Os by $0.21 \mu_B$ moment, as seen in the table. Consequently, the tiny drop in effective moment is caused by the SOC and hybridization in SLFOO.

We studied band structure calculation, which requires integration over the Brillouin zone, to better understand the electrical structure. For the reciprocal space integrations in the case of monoclinic unit cell, we sampled the linear tetrahedron approach with 200 k-points across the full first BZ which gives $6 \times 6 \times 4$ k-mesh. We explored fat band structures, which help to observe the electrons occupancy orbitals of the atoms in the presented systems, to clearly identify contributions in the bands from various orbitals of the different elements in SLFOO. On the basis of fat band plots, we can clearly state that significant contributions of orbitals in band structure at Fermi level is due to the transition atoms Fe-3d and Os-5d. In which, d-orbitals of both atoms has very significant role in the band formation on Fermi level. Whereas, s, p-orbitals has insignificant role in the band formation because, at core of the atoms (1s, 2p) and p-orbitals are fulfilled (3p, 4s) while the d-orbitals (3d, 4d/5d) are at valence shell means half-filled.

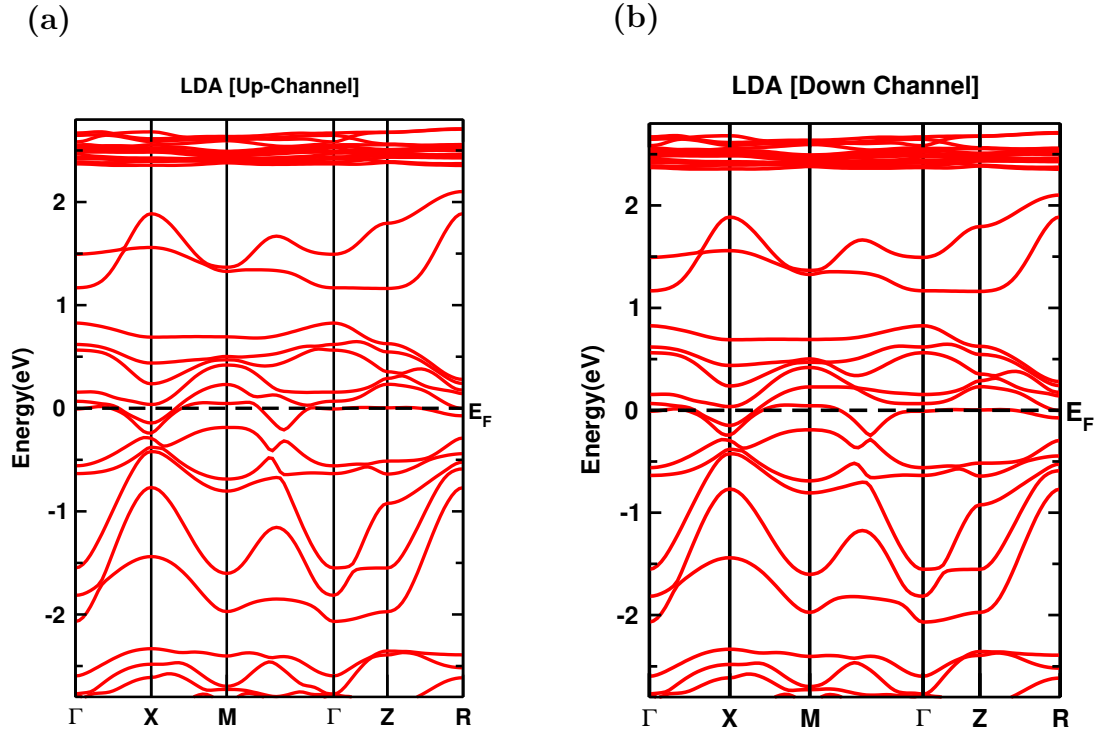


Figure 49: Band structures of SrLaFeOsO₆ within LDA functional.

We have calculated band structure of osmium containing double perovskite SLFOO by using LDA functional. From these calculations of band plots, we found that SLFOO shows metallic and symmetric in nature for both up and down spins. The contribution of t_{2g} and e_g -orbitals of Fe and Os are larger near Fermi level. From the above fat band plots for Fe and Os of d-orbital, It is obvious that the major contributions is of d orbitals near Fermi region on both valence and conduction band.

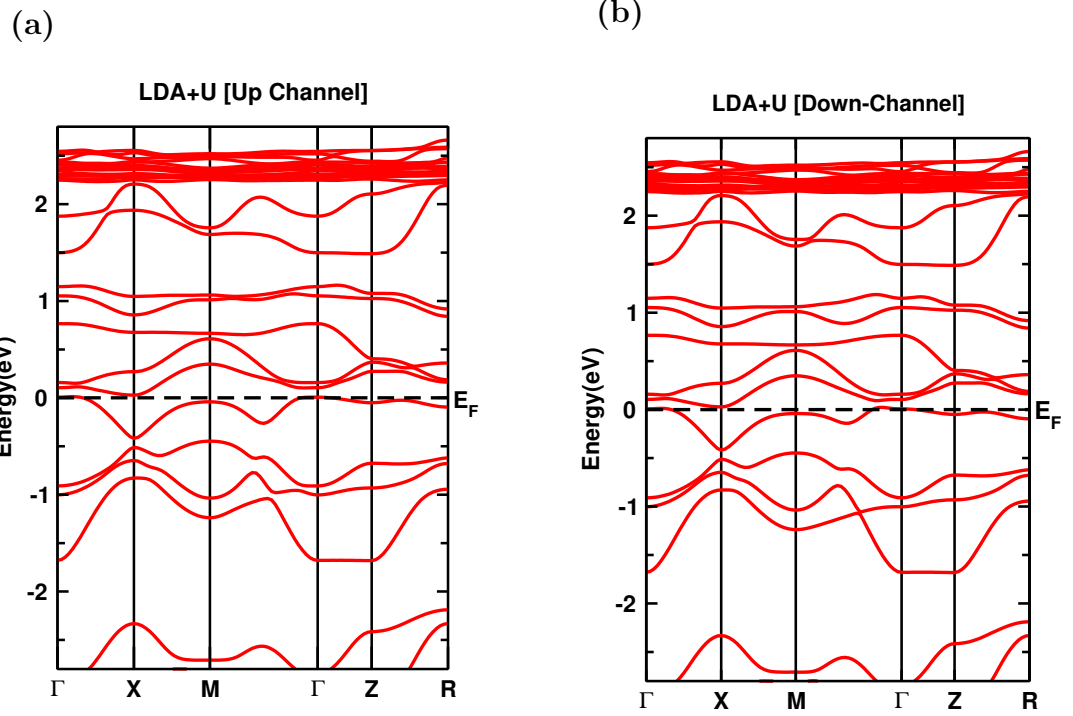


Figure 50: Band structures of SrLaFeOsO₆ within LDA+*U* functional.

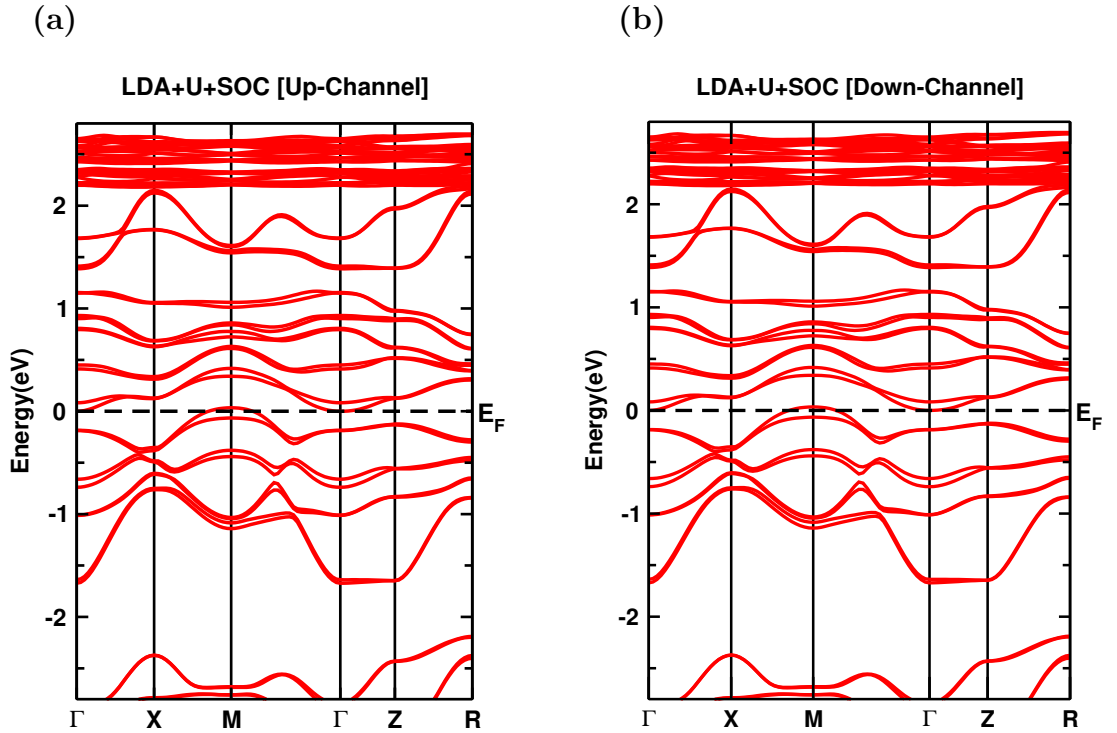


Figure 51: Band structures of SrLaFeOsO₆ within LDA+*U*+SOC functional.

Band plots for both spin after applying SOC as shown in Fig. 51 with band gap 0.03 eV called semi-conducting in nature along 001-direction. In this system SOC plays significant role to open gap at Fermi level. Fat bands of Fe1-3d and Os1-5d shows that, after applying *U*

and SOC, Fe and Os bands shift in small amount from the Fermi level. Thus, Fe and Os both plays main role for the electronic properties as shown in fat band plots. By analyzing DOS and band, it is seen that DOS peaks are high where more bands are located and peaks are low where less number of bands are located, thus we can says that DOS and band structures are in good agreement.

4.10 Ru doped at Os Site on parent material: SrLaNiRuO₆

The material SrLaNiRuO₆ is obtained by substituting Ru in place of Os in SrLaNiOsO₆ with same occupancy ratio. The magnetic GS is calculated by comparing the energy of SrLaNiRuO₆ (SLNRO) for the four possible magnetic configuration and found that AF1($\uparrow\downarrow\uparrow\downarrow$)-configuration is stable with lowest energy indicating its ground state. Thus, this system is antiferromagnetic in nature with total magnetic moment zero and metallic in nature. we have applied Coulomb potential (U) for Ni-3d and Ru-4d which are 5 and 0.5 eV, respectively.

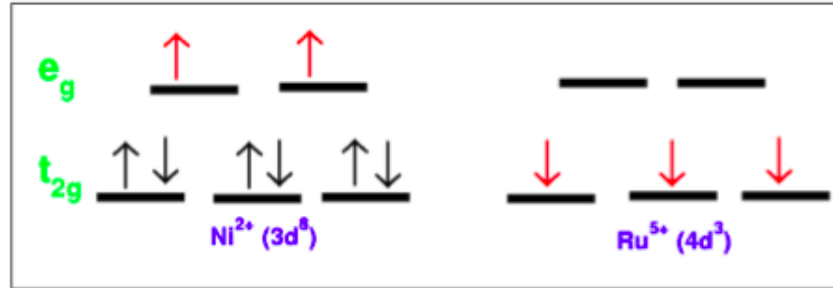


Figure 52: Schematic representation of the super-exchange interactions between Ni and Ru with d³-d⁴ electronic configurations.

4.10.1 Electronic and Magnetic Properties

Using experimental lattice parameters obtained at 10 K, the density of states of the ruthenium containing compound SLNRO is calculated. We investigated the nature of compounds using LDA, LDA+ U and LDA+ U +SOC by analyzing total and partial DOS plots. It is obvious from Fig. 56 that the Ni-3d and Ru-4d atoms contribute more than the other atoms. Because the p-orbitals of the O-atom are half-filled orbitals, they have a minor contribution at Fermi-level. DOS are symmetric in nature, implying that the magnetic moment is zero, confirming that they are antiferromagnetic. Fermi level crossovers by DOS in LDA indicate that the system is metallic. Table (16) can be used in conjunction with this figure to see the band gap, individual, and total magnetic moment. By treating d and f-electrons as delocalized, LDA underestimates the band gap. The system is metallic due to the delocalized electrons. Because 3d and 4d-electrons are substantially localized, SLNRO is actually a strongly correlated system. The band gap is opened by using $U= 5$ eV and $Ru = 0.5$ eV in the LDA+ U approximation. There is no DOS near Fermi level, resulting in a 0.58 eV band gap. The second variational method we employed was spin-orbit coupling in five distinct directions with ground energy in the 001-direction with a band gap of 0.58 eV. So, both electron correlation and SOC assisted Mott-insulator.

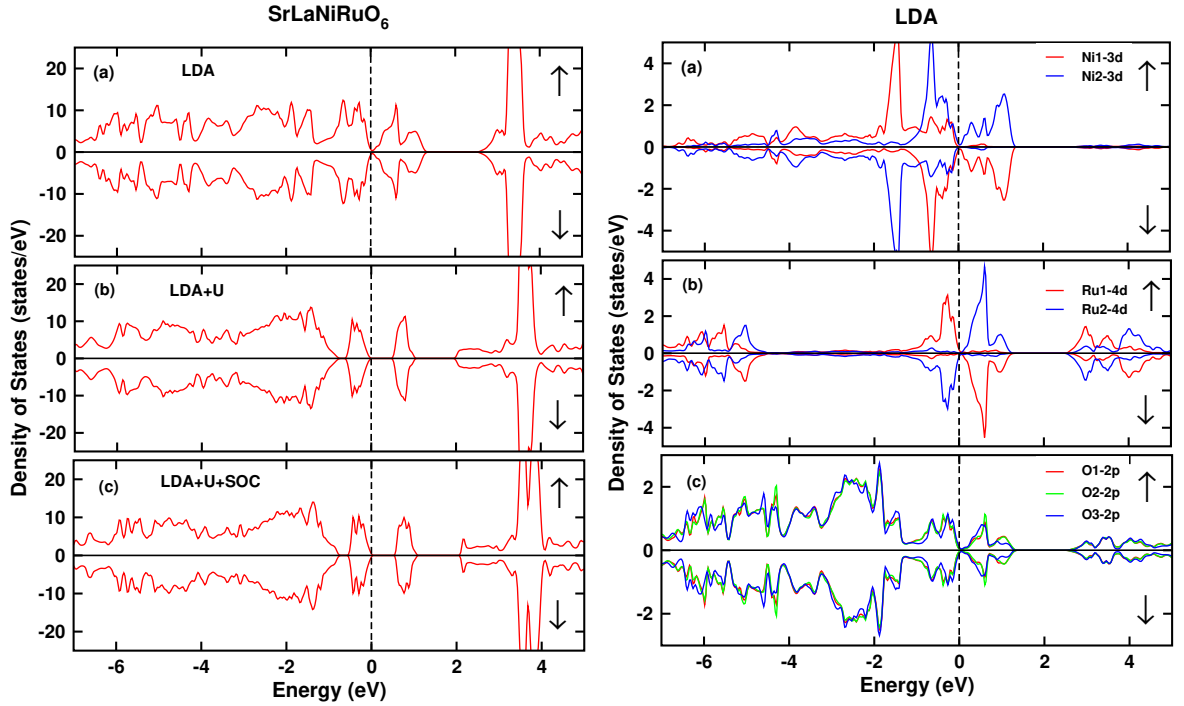


Figure 53: Total and partial density of states for SrLaNiRuO_6 .

We examine the PDOS of the substantial DOS contributions at Fermi level by Ni-3d and Ru-4d atoms in Figures 53 and 54. The significant contribution of Ru after applying U -values is obvious from the PDOS of LDA and LDA+ U . The contribution of Ni1 and Ni2 at Fermi level around 0.5 eV energy is quite minor in these DOS plots, with a larger number of DOS shifted from Fermi level. According to these plots, Ni is near Fermi level in the LDA case, but its contribution near Fermi level in the LDA+ U plots is small in compared to Ru. For Ru atoms, DOS causes a tiny movement out of E_F in the valence and conduction regions. Band contributions for Ni are larger in VB than CB, although contributions for Ru are roughly equal in both bands. As illustrated in the picture, the partially filled Os-2p orbital has a tiny contribution near Fermi level after applying Coulomb potential, but a higher contribution in the valence band. Because 4d oxides have a longer spatial extent than 3d atoms, SOC affects them more, resulting in fascinating and surprising electrical and magnetic behavior. The band gap rose by 0.07 eV after SOC, and the orientations of Ni and Ru PDOS were somewhat affected, as indicated in the figures.

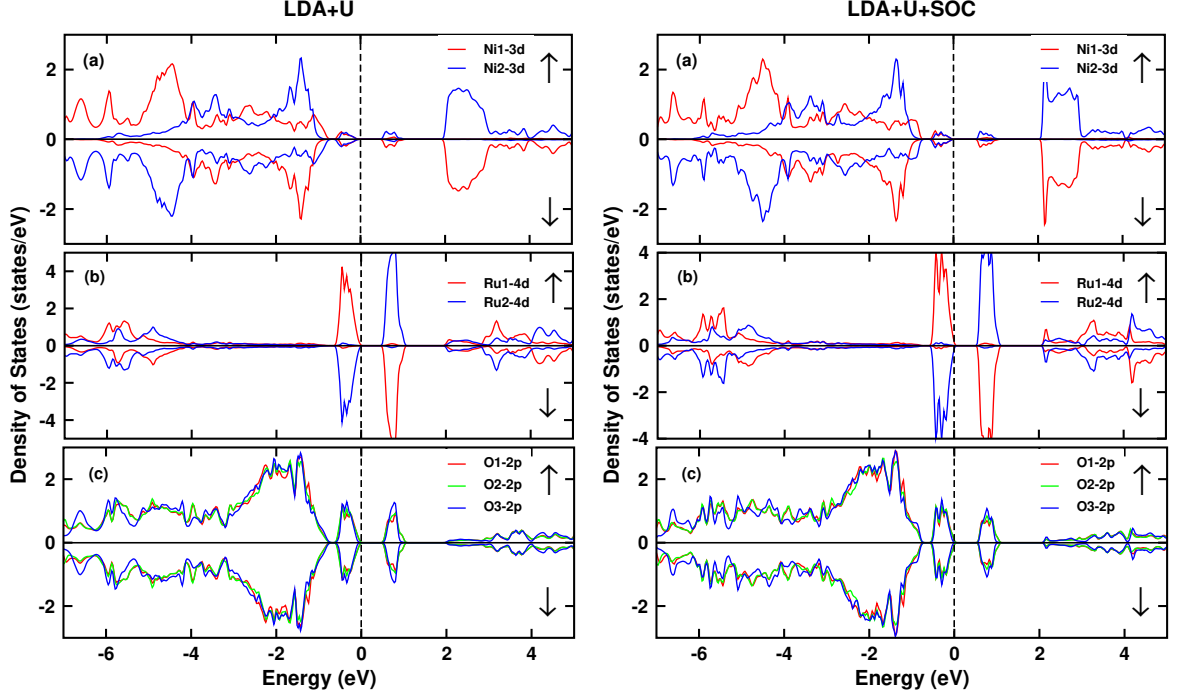


Figure 54: Partial density of states for SrLaNiRuO_6 .

The empty shell of La-atoms causes the largest peak of total DOS in the CB around 3.5 eV. In the valence band, Ni-3d and O-2p atoms contribute the largest peak in the energy range 1.5-2.0 eV. When compared to Ru-atoms, the DOS of Ni and O-atoms is near Fermi level. Because d-orbitals are half-filled whereas s, p orbitals are totally filled, d-orbitals dominate in both VB and CB in Ni and Ru-atoms. Strong electron-correlations cause a DOS peak at the E_F split. Oxygen bands are strongly hybridised with Ni-3d and Os-5d states below E_F in both channels. This is caused due to octahedron distortions, which result in the appearance of three different types of oxygen positions with various Ni(Ru)-O bond-lengths. In both spin channels, it is discovered that oxygen 2p states substantially hybridize with ruthenium 4d states around E_F .

With the AF1 magnetic configuration, the magnitude of effective moment in SLNRO is zero per unit cell. When U is applied, the spin magnetic moments of Ni and Ru rise, but when SOC is applied, the magnetic moments of both atoms remain the same. The table (16) shows the orbital moments of nickel and ruthenium. The greater SOC of Ni in comparison to Ru causes its unusually significant orbital moment. Oxygen gains a modest magnetic moment as a result of its hybridization with Ni and Ru, and polarization is mostly seen on p-orbitals. Because 4d oxides have a larger spatial extension, the influence of Coulomb interaction is weaker than in 3d oxides. However, Ni-3d oxides have a bigger orbital magnetic moment $0.24\mu_B$ than Ru-4d oxide $0.029\mu_B$. Because of octahedral distortion, oxygen bands distribu-

Table 16: Computed effective, individual and orbital moments (μ_B) and energy gap ‘ E_g ’ (eV) for SrLaNiRuO₆ compound.

SrLaNiRuO ₆			
site	GGA	GGA+ U	GGA+ U +SOC
Ni	1.49	1.70	1.70(0.24)
Ru	1.54	1.66	1.65(0.03)
O1	0.19	0.16	0.16
O2	0.19	0.16	0.16
O3	0.05	0.08	0.08
Net	-		
E_g	Metallic	0.51	0.58

tion above E_F is minimal, but below the E_F , both channels hybridize with Ni-3d and Ru-4d states.

Since, individual spin moments of nickel and ruthenium atoms are $2 \mu_B$ and $3 \mu_B$, respectively. The computed magnetic moments of Ni and Ru are $1.70 \mu_B$ and $1.65 \mu_B$, respectively, according to the first principle result. The partial charge transfer between Ni-O and Ru-O causes this minor variance in magnetic moment. The SOC causes antiparallel orbital magnetic moments on Ni and Ru, lowering the net magnetic moments. In SrLaNiRuO₆ the Ni and Os have electronic configuration Ni²⁺ (3d⁸: $t_{2g}^6 e_g^2$) and Ru⁵⁺ (5d³: $t_{2g}^3 e_g^0$).

We studied band structure calculation, which requires integration over the Brillouin zone, to better understand the electrical structure. For the reciprocal space integrations in the case of monoclinic unit cell, we sampled the linear tetrahedron approach with 200 k-points across the full first BZ giving $6 \times 6 \times 4$ k-mesh. We also looked into fat band topologies to see how they contributed to the bands from various orbitals of the different elements in SLNRO. On the basis of fat band plots, we can clearly conclude that the transition elements Ni-3d and Ru-4d contribute large orbital contributions to band structure at E_F . On the E_F , the d-orbitals of both atoms play a crucial role in band formation. Whereas, s and p-orbitals have a little role in band formation because s and p-orbitals are fulfilled (3p, 4s) at the atomic core, while d-orbitals (3d, 4d) are half-filled in the valence shell. However, because Sr and La have orbitals on the valence shell, their contributions to band formation are minimal. However, band formations on the Fermi level have a minor contribution for O-atoms. d-orbitals are also empty, according on the electrical configuration.

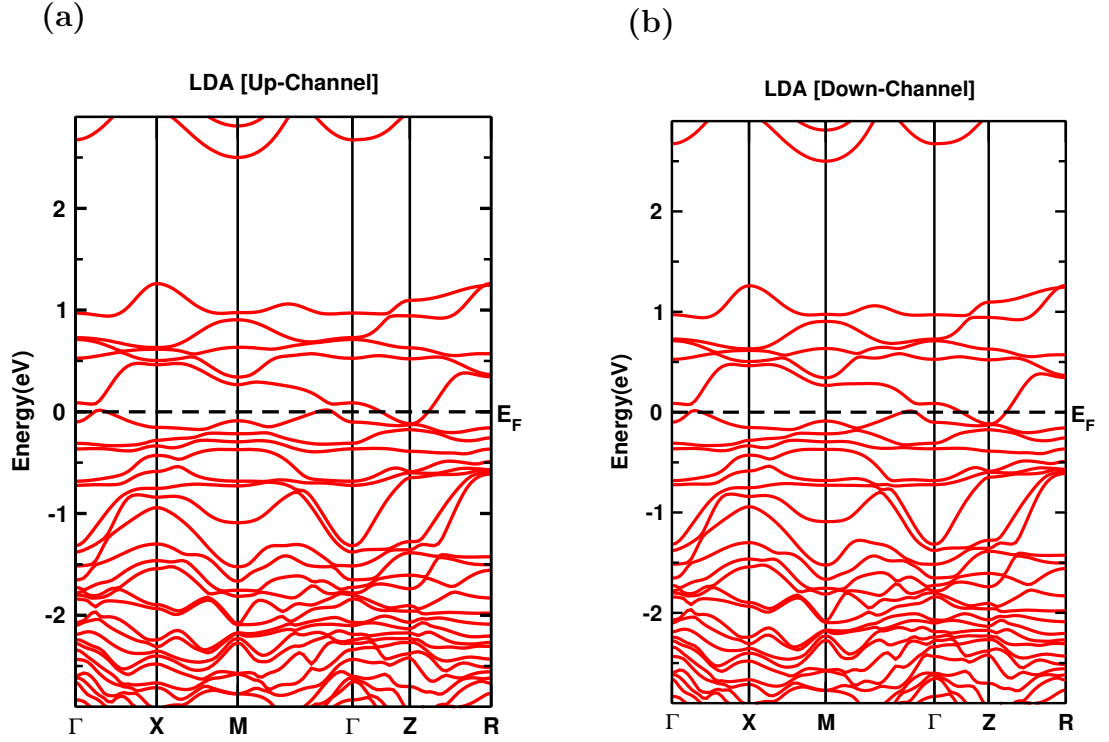


Figure 55: Band structures of SrLaNiRuO₆ within LDA functional.

We have calculated band structure of ruthenium containing double perovskite SLNRO. The band graphs shown above show that bands are symmetric in nature for both up and down spins. The contribution of t_{2g} and e_g -orbitals of Ni and Ru containing system SLNRO is larger enough near Fermi level. In this structure due to the highly distorted structure, d orbital splits into t_{2g} and e_g -orbitals. From the above fat band plots for Ni and Ru of d-orbital, main contributions near Fermi region is due to d orbitals on both valence and conduction band. In order to visualize the main contributions of individual atoms we perform fat band analysis for Ni1-3d and Ru1-4d as shown in Fig. 58 and Fig. 59, respectively. The fat bands of other orbitals s, p-orbital for these transition atoms does not contribute near Fermi level. Also, Sr, La atoms are not contribute near Fermi level so, we have not plotted here fat bands of these atoms. 2P-orbitals of oxygen has also a small contribution on the VB and CB. From the fat bands of d-orbital, we clearly see that nearly equal amount of electrons are filled in the d-orbitals on VB and CB. Analyzing these fat bands of Ni1 and Ru1, we can say that 3d/4d-orbital electrons contributes in the major fundamental properties of this compound.

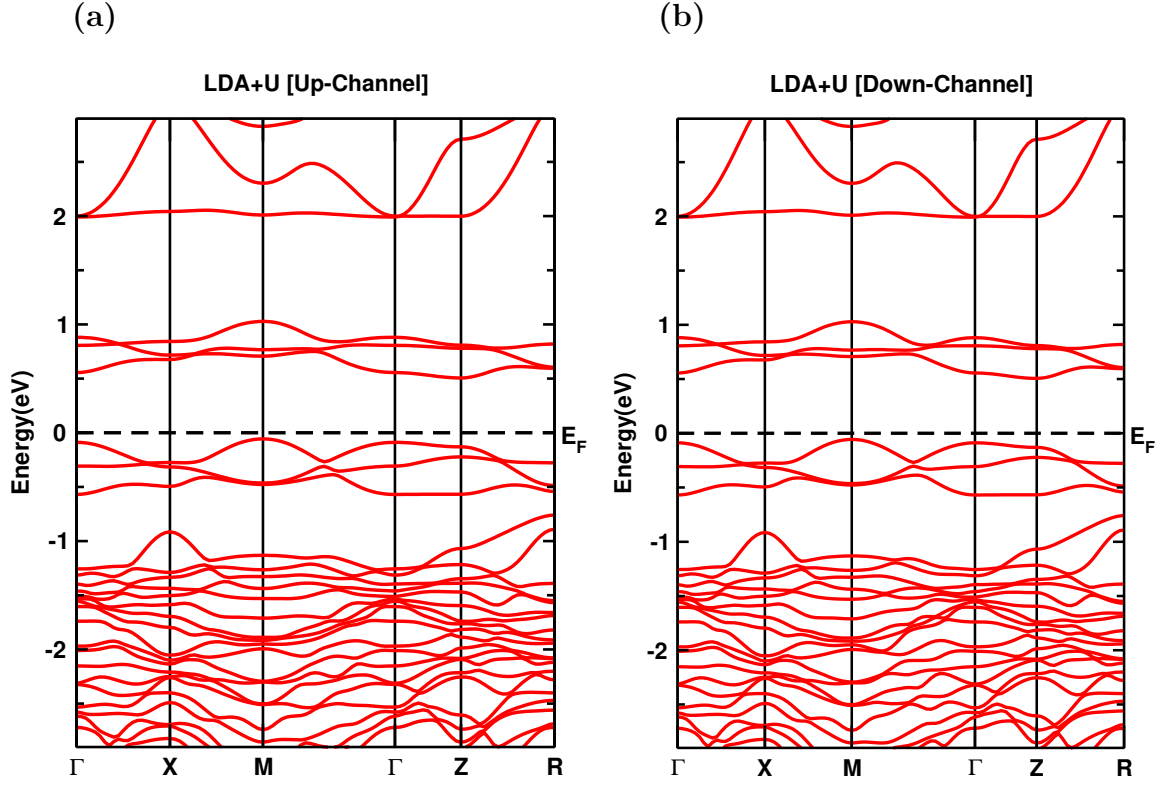
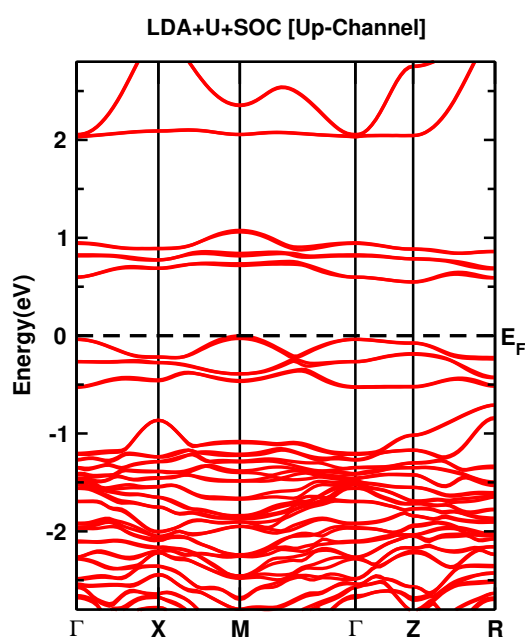


Figure 56: Band structures of SrLaNiRuO₆ within LDA+ U functional.

We discovered a 0.51 eV band gap after choosing the proper U -value of Ni and Ru atoms, as illustrated in Fig. 56. The highest energy on the VB is at M-symmetry point, and the minimum energy on the CB is at Z-symmetry point, indicating that this system has an indirect band gap. Ru is the most important element in terms of electrical characteristics. Because the atom Ru in our system SLNRO is larger, we must use a second variational approach called spin-orbit coupling.

(a)



(b)

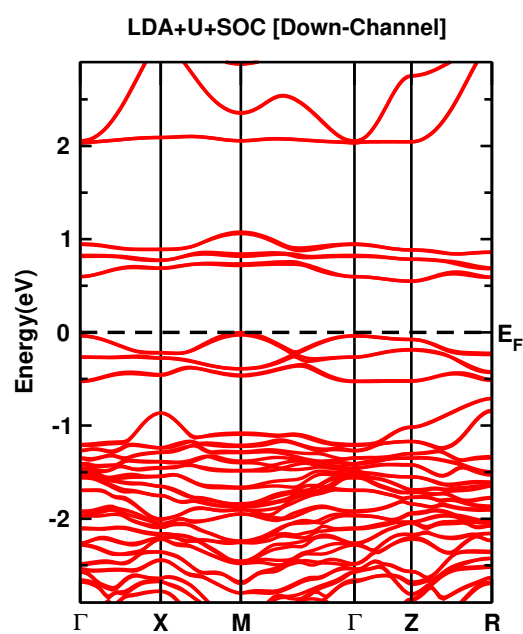
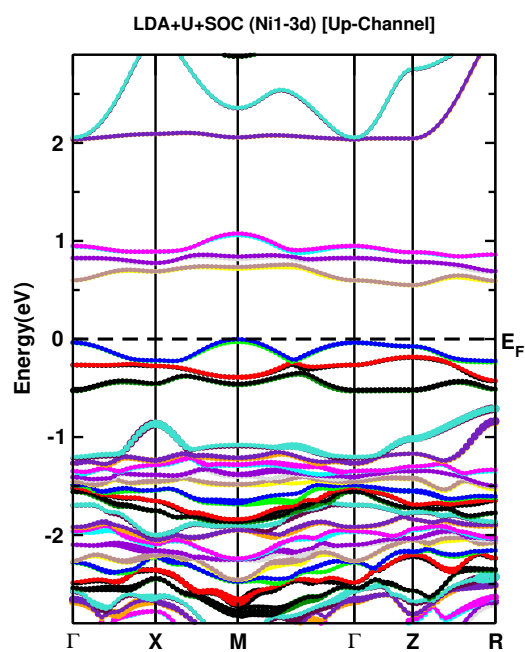


Figure 57: Band structures of SrLaNiRuO₆ within LDA+U+SOC functional.

(a)



(b)

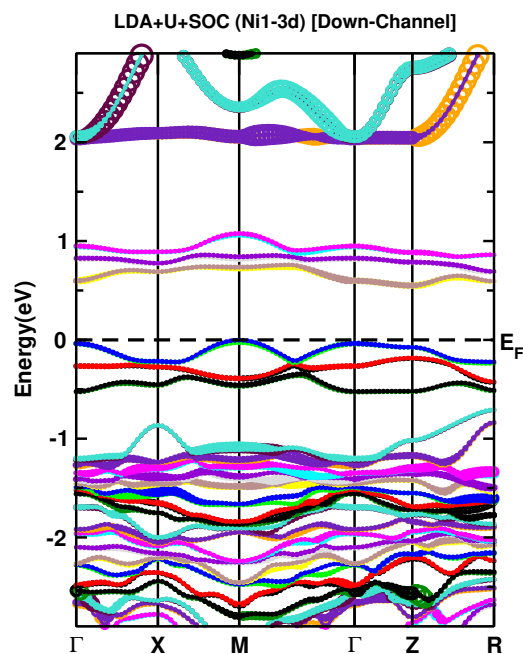


Figure 58: Fat band structures of SrLaNiRuO₆ within LDA+U+SOC functional.

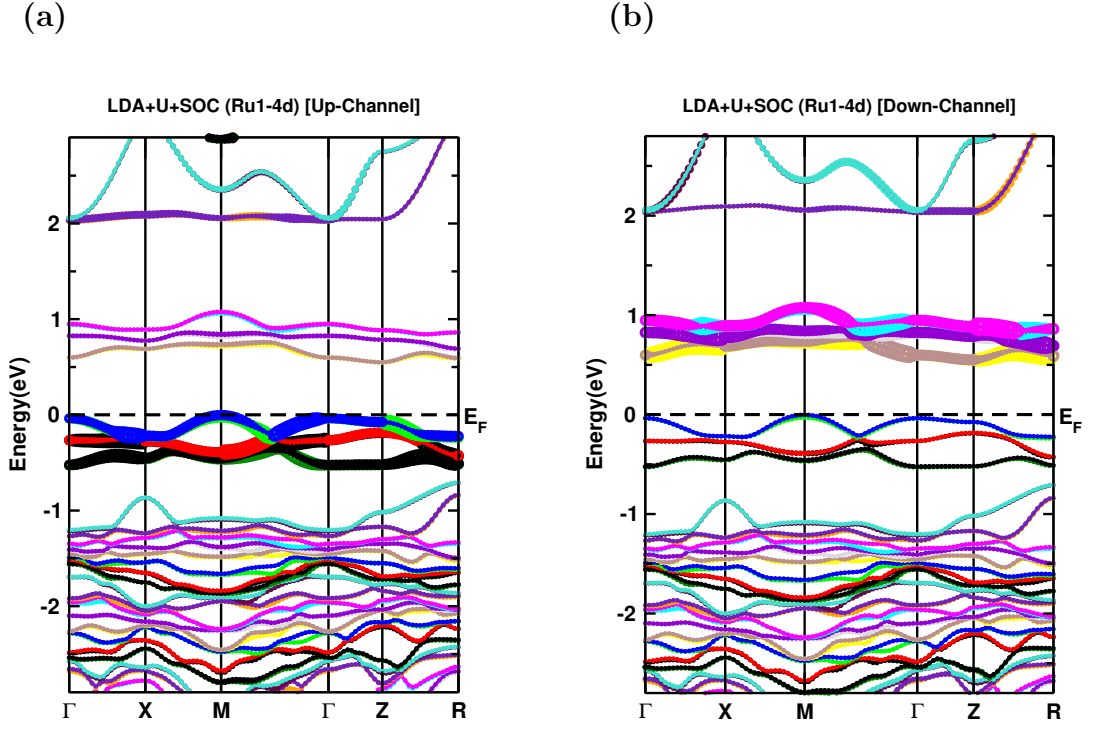


Figure 59: Fat band structures of SrLaNiRuO₆ within LDA+ U +SOC functional.

Figure 57 shows band plots for both spins following SOC, having a band gap of 0.58 eV in the 001-direction. SOC is crucial to the operation of this system to ensure that the experimental outcomes are consistent. The maximum energy of the VB plots at M-symmetry point in this scenario, but the minimum energy of the conduction band maps at Z-symmetry point due to coupling effects. As a result, the band plots revealed an indirect band gap. This band gap plainly indicates that this system is semiconducting in nature and is also known as a Mott-insulator. After applying U and SOC, fat bands of Ni1-3d and Ru-4d reveal that Ni bands travel further away from Fermi, whilst Ru bands stay close to Fermilevel. As illustrated in fat band plots, Ru has a major impact in electrical characteristics. By examining DOS and band structures, it is obvious that DOS peaks are higher where there are more bands and lower where there are less bands; DOS and band structures are in good agreement.

4.11 Tb-Based Double Perovskites: $\text{Tb}_2\text{FeCrO}_6$

This material $\text{Tb}_2\text{FeCrO}_6$ is first synthesized experimentally by our collaborator using neutron powder diffractometer. We have mainly contributed in its theoretical DFT part and results were analyzed. So we discuss here more about its DFT part which we did and a brief experimental details which was done by our collaborating group. We started our calculation by taking the experimental data structure with lattice constant $a=5.53913 \text{ \AA}$, $b=7.59173 \text{ \AA}$, $c=5.31242 \text{ \AA}$ and angles are $\alpha=90^\circ$, $\beta=90^\circ$, $\gamma=90^\circ$. The structure lies in $Pnma$ space group (62) which has orthorhombic crystal structure.

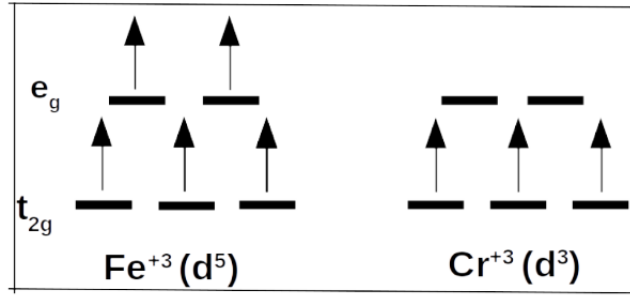


Figure 60: Schematic representation of the super-exchange interactions between Fe and Cr with d^5 - d^3 electronic configurations.

4.11.1 Electronic and Magnetic Properties

We started our calculation by calculating the total energy of different magnetic orientations. They represent FM, AFM1, AFM2, FiM1 and FiM2 configurations. In this case, two Fe and two Cr atoms are given different spin direction for different orientations.

By comparing the energies for different magnetic configurations, AFM1 ($\uparrow\downarrow\uparrow\downarrow$) is obtained with the lowest energy confirming its GS consistent with experiment. The different magnetic configuration are ordered by their relative stability as follows: AFM1 > AFM2 > FIM2 > FIM1 > FM. The MAE is found to be $\sim 4.7 \text{ meV}$ per formula unit of $\text{Tb}_2\text{FeCrO}_6$ along inplane easy axes. In $\text{Tb}_2\text{FeCrO}_6$, Terbium carry a charge state 3+ which has $4f^8$ electronic configuration. The transitional metal Fe also ostensibly adopts the charge state 3+ and has $3d^5$ ($d^5 - t^3_{2g}e^2_g$) structure. Similar to that, Cr must have charge state 3+ and electronic configuration of $3d^3$ ($d^3 - t^3_{2g}$) for charge neutrality. The computed spin moments for terbium, iron, and chromium in every site with in sustained AFM1 state found to be $\pm 5.9 \mu_B$, $\pm 3.7 \mu_B$, and $\pm 2.4 \mu_B$, respectively. The orbital moment are $\pm 1.03 \mu_B$, $\pm 0.05 \mu_B$, and $\pm 0.03 \mu_B$, respectively. The spin moments of terbium, iron, and chromium are $\pm 5.9 \mu_B$, $\pm 4.1 \mu_B$, and $\pm 2.6 \mu_B$, respectively, assuming GGA+ U functional. The antiferromagnetic coupling between terbium, iron, and chromium causes the total magnetic moment to adapt to zero, which can

Table 17: Calculated effective and individual moments (μ_B) and energy gap ‘ E_g ’ (eV) for $\text{Tb}_2\text{FeCrO}_6$ compound.

$\text{Tb}_2\text{FeCrO}_6$		
site	GGA	GGA+ U
Tb	± 1.03	± 5.97
Fe	± 0.05	± 4.14
Cr	∓ 0.034	± 2.57
O2	-0.102	-0.158
O3	-0.097	-0.149
Net	0	0
E_g	0.048	2.372

be seen in table 17. Figure 63 shows how five up spin electrons have singly occupied the d orbital in Fe and three up spin electrons singly occupied the t_{2g} with empty e_g . There exist the d^5 - d^3 superexchange interaction between Fe and Cr, that gives rise to exciting magnetic properties of the compound.

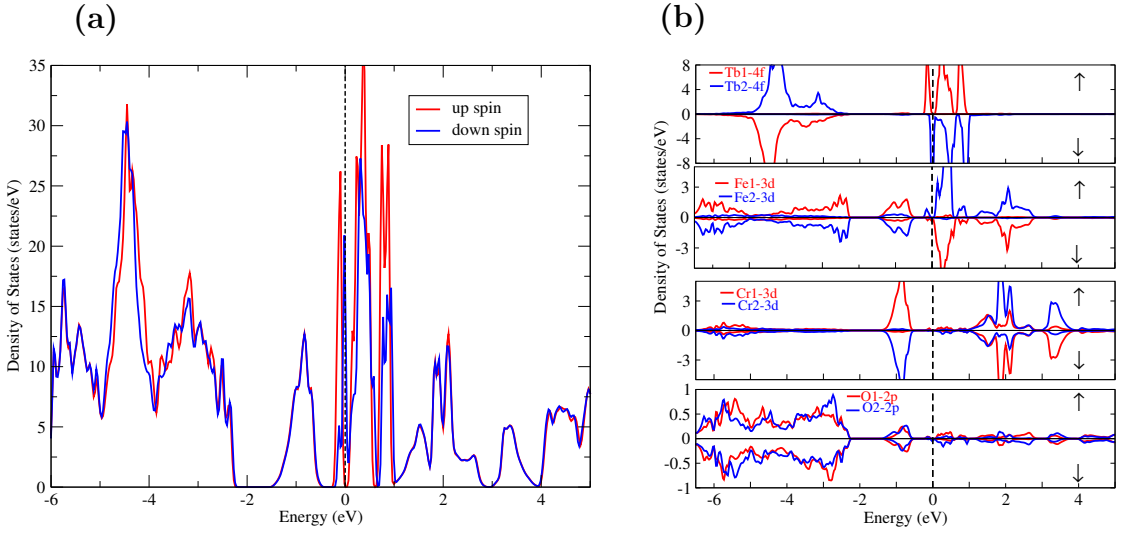


Figure 61: Total and partial DOS of $\text{Tb}_2\text{FeCrO}_6$ with GGA functional. The vertical dotted line indicates E_F .

(a) spin up

(b) spin down

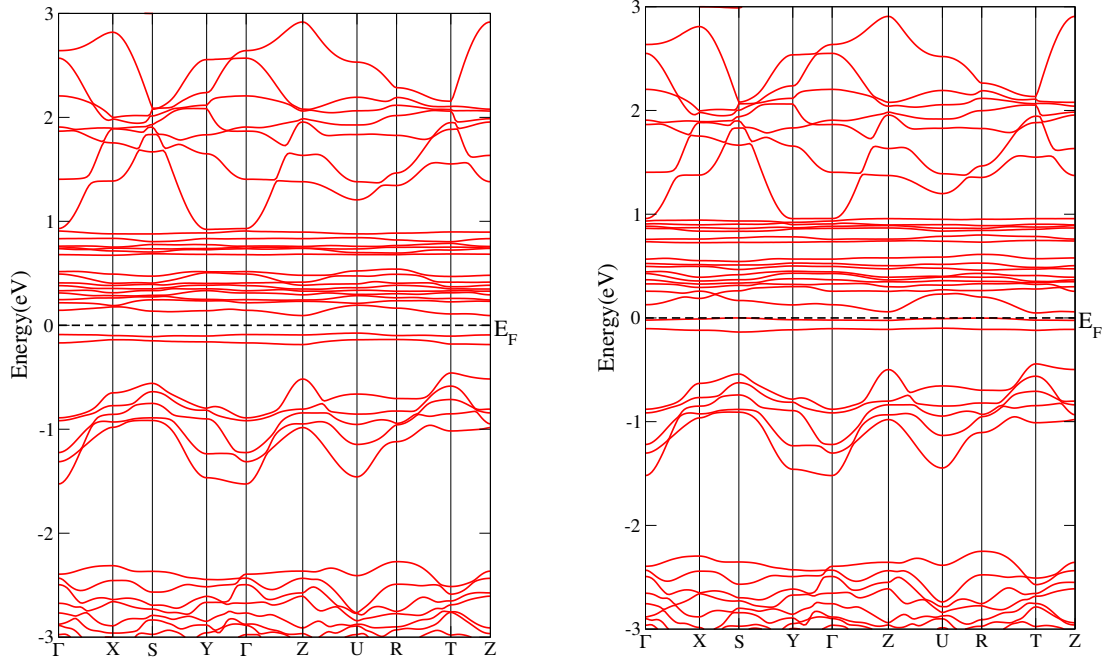


Figure 62: Bands of $\text{Tb}_2\text{FeCrO}_6$ within GGA. The horizontal dotted line indicates $E_F=0$.

We now discuss the electronic structure of $\text{Tb}_2\text{FeCrO}_6$. Figure 64 shows the spin resolved DOS. $\text{Tb}_2\text{FeCrO}_6$ is investigated to be insulator with energy gap of 0.12 and 2.4 eV under GGA and GGA+ U functional. Our system consists of localized electrons so we used on-site Coulomb potential (U) which is an orbital dependent potential. GGA only calculation fails to describe the localized system. The compound has the d-elements (Fe and Cr) and f-element (Tb) due to which $\text{Tb}_2\text{FeCrO}_6$ is a strongly correlated system. The additional potential + U pushes the local orbitals away which are present as localized states and hence increasing the band gap of the system. The values of U used are Tb–6 eV, Fe– 5 eV and Cr–3 eV. Inclusion of U countably changes the electronic properties. From the partial DOS, the significant contribution from Tb–4f states that can be seen near E_F are moving away from each other. Filled states travel downward in the valence area, while empty states go upward and distant in the conduction region. This type of characteristics can also be seen for Fe–3d states close to the E_F . Likewise, as seen in Fig. 64, the Cr–3d states that are vicinity of E_F highly hybridized with the O–2p orbitals. The 3d states of chromium and iron can hybridize with the oxygen–2p states to produce bands close to the Fermi level. As can be seen in the partial DOS Fe–3d, t_{2g} and e_g are completely filled by five electrons in up spin channel. While incase of Cr–3d, t_{2g} are completely filled up spin channel whereas e_g states remain unoccupied.

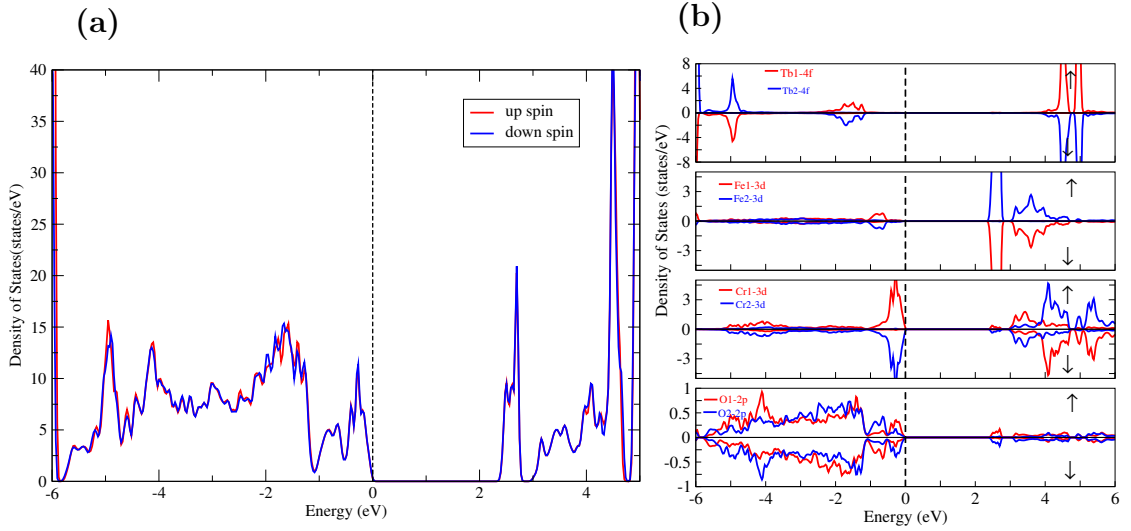


Figure 63: Total and partial DOS of DPs $\text{Tb}_2\text{FeCrO}_6$ under GGA+ U functional.

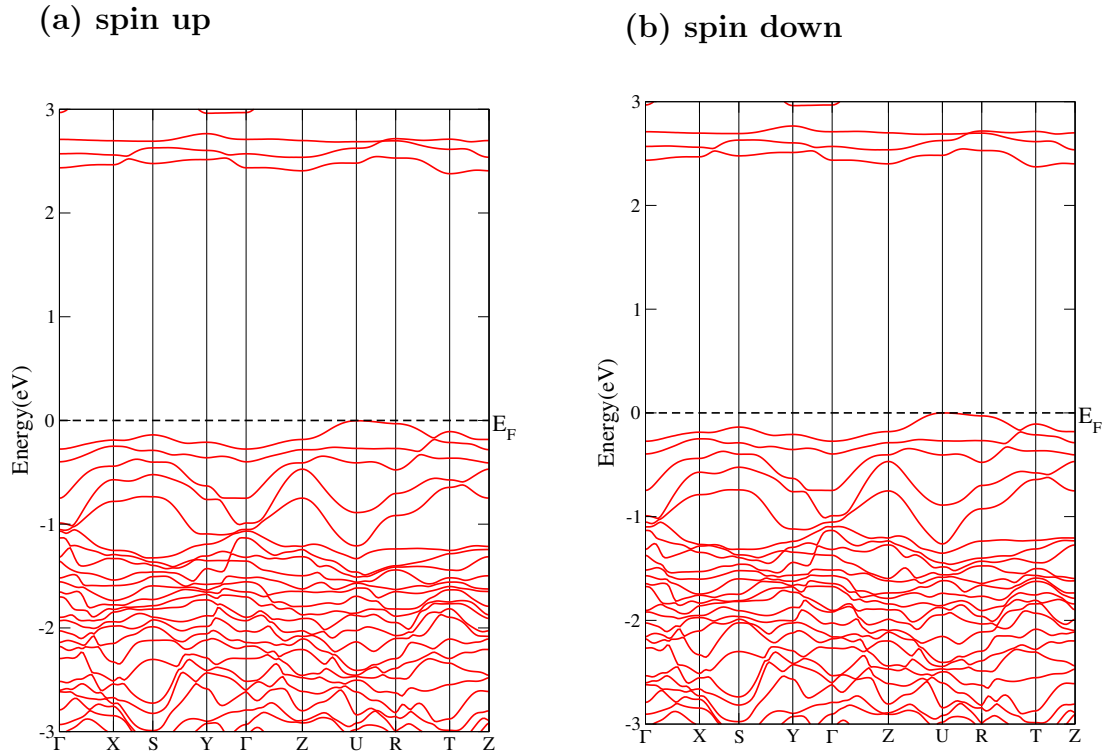


Figure 64: Band structure of $\text{Tb}_2\text{FeCrO}_6$ DP within GGA+ U functional.

4.11.2 Evaluation of Exchange Coupling Constant

We define spin exchange parameters using Heisenberg spin Hamiltonian. For simplicity, we planned to evaluate three nearest neighbour exchange interaction between 3d-transitional elements only. We have evaluated exchange coupling following certain steps (Xiang *et al.*, 2017).

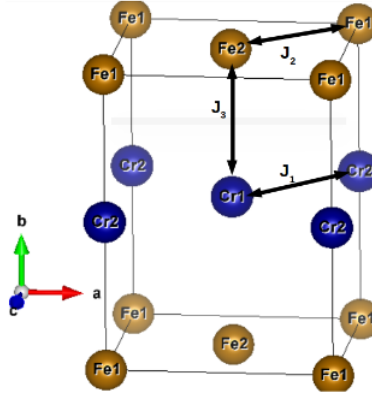


Figure 65: Exchange paths between transitional elements Cr–Cr, Fe–Fe and Cr–Fe. Spins are assigned in [010] direction.

Firstly, the set of three spin exchange paths J_{Cr-Cr} (J_1), J_{Fe-Fe} (J_2) and J_{Fe-Cr} (J_3), i.e., superexchange paths (M–O–M, M =Fe, Cr) were drawn. Figure shows the pathway we have selected. Then we used the energies of four spin configurations converged using on-site potential $+U$ and drafted following equations on the basis of spin Heisenberg hamiltonian.

$$E_{FM} = E_o + \frac{9}{4}(-4J_1) + \frac{25}{4}(-4J_2) + \frac{15}{4}(-2J_3) \quad (4.41)$$

$$E_{FIM} = E_o + \frac{9}{4}(-4J_1) + \frac{25}{4}(-4J_2) + \frac{15}{4}(+2J_3) \quad (4.42)$$

$$E_{AF1} = E_o + \frac{9}{4}(-4J_1) + \frac{25}{4}(+4J_2) + \frac{15}{4}(-2J_3) \quad (4.43)$$

$$E_{AF2} = E_o + \frac{9}{4}(+4J_1) + \frac{25}{4}(4J_2) + \frac{15}{4}(-2J_3) \quad (4.44)$$

The values of J_s are calculated, for example the value of superexchange interaction between Cr–Fe (J_3) is evaluated as:

$$J_{Cr-Fe} = \frac{E_{FM} - E_{FIM}}{-15} \quad (4.45)$$

The values of J_s are tabulated in a table.

The superexchange interaction Fe–O–Fe is found to be stronger than remaining two. All these values of J are negative, hence these interactions are antiferromagnetic in nature. According to Goodenough-Kanamori rule, the superexchange parameters J_1 and J_2 are antiferromagnetic which are found to be true in our case but the interaction between Fe–O–Cr

Table 18: Computed spin exchange coupling parameters (in meV) for DPs $\text{Tb}_2\text{FeCrO}_6$ (Pnma) with $U_{\text{Tb}} = 6$ eV, $U_{\text{Fe}} = 5$ eV and $U_{\text{Cr}} = 3$ eV, $M = \text{Cr}$ or Fe .

interaction	description	nearest neighbour	J value
J_1	Cr–O –Cr	6	–0.99
J_2	Fe–O –Fe	12	–5.68
J_3	Cr–Fe	12	–1.36

should be ferromagnetic (Kanamori, 1959) however we obtained different results from expected.

From mean field theory approximation, calculated theoretical transition temperature called Neel temperature T_N is 853.69 K. This high value of theoretical value may be because of

a) the effect of f– transitional element Tb on exchange parameters J 's, because the investigations about f– electrons is insufficient by our computational tools.

b) angle between the transitional elements Cr and Fe are not exactly 180° but around 145° .

CHAPTER 5

CONCLUSION AND RECOMMENDATIONS

5.1 Conclusion

From DFT calculations, we looked on electronic structure and related properties of double perovskites $A_2M_{1-x}M'_xTO_6$. We have divided our study mainly into three sections. In the first section, we studied Ca-based double perovskites in which we have taken Ca_2CrOsO_6 as a parent material and all other proposed transition metals are substituted in it. First, we revisit the parent material taking experimental lattice parameters and found that it is stable with a FiM ground state showing an insulating state with an energy gap of 0.6 eV and an effective moment of $0.23 \mu_B$ per unit cell which resembles with the experimental findings.

Doping with transition metals in parent material, started with Ni (50%) to the Cr-site in Ca_2CrOsO_6 to obtain $Ca_2Cr_{0.5}Ni_{0.5}OsO_6$. Doping with Ni at the Cr site adds additional five electrons to the system. Three Ni electrons in a spin down state provide a repelling effect on the Os- t_{2g} bands as they react ferrimagnetically on Os, causing the Os band to move from VB to CB by transversing the Fermi level in the spin down channels. This produces a metallic state on the spin down and the spin up channel continues to be insulating. Hence, the material $Ca_2Cr_{0.5}Ni_{0.5}OsO_6$ is found to be a half-metallic in nature.

Substituting Fe and Ir to the Cr and Os site on parent material results in Ca_2CrIrO_6 and Ca_2FeIrO_6 which are found to be thermodynamically stable with their negative values of adhesive and cohesive energies and are possible to synthesize experimentally. Both materials are investigated as semiconductors with energy gaps of 0.3 eV and 0.13 eV, respectively. Both materials were studied within the general gradient approximation (GGA) with inclusion of U and SOC. The Curie temperature T_C of the materials are found to be 906 K and 836 K for Ca_2CrIrO_6 and Ca_2FeIrO_6 , respectively, which are in valid T_C trends when compared with other double perovskites. Similarly, Ca_2MnIrO_6 which is obtained with doping of Mn and Ir to the Cr and Os site is found to be a half-metallic FiM with the spin up channel metallic and

spin down channel insulating and this half-metallic state persists even with SOC. The T_C calculated for $\text{Ca}_2\text{MnIrO}_6$ was found to be 280 K. On the other hand, $\text{Ca}_2\text{NiIrO}_6$ which is obtained by substituting Ni and Ir to the Cr and Os site and is discovered to be FiM ground state. This material also shows insulating state even with SOC. The T_C calculated for this material is 270 K.

In second part of the work, we discuss Sr-based double perovskites. Based on first-principle DFT approach, we found SrLaFeOsO_6 to be semiconductor with gap of 0.03 eV. Two other perovskites SrLaNiOsO_6 and SrLaNiRuO_6 also shows semiconducting nature with larger band gap of 0.33 eV and 0.57 eV respectively. The systems $\text{SrLaBB}'\text{O}_6$ (B=Ni, Fe; B'=Os, Ru) having monoclinic structure are found to be AFM in nature. This material showed Mott-insulating state under the co-operative effect of electron correlation, SOC and crystal field. For all these systems, the net magnetic moment are zero per unit cell. In SrLaNiOsO_6 the calculated orbital magnetic moment are $0.21 \mu_B$ on Ni and $0.15 \mu_B$ on Os with different directions but in SrLaFeOsO_6 the orbital magnetic moment are $0.09 \mu_B$ on Ni and $0.22 \mu_B$ on Os. Since, the Os-5d element is much more extended than Ni-3d, so U_{Os} is smaller for Os as compared to Ni. Ruthenium containing compound SrLaFeRuO_6 with orbital magnetic moments are found to be $0.24 \mu_B$ on Ni and $0.03 \mu_B$ on Ru. All compounds are structurally distorted and their distortion is found larger than other two compounds. Thus it has smaller value of U i.e. $U_{Os} = 0.5$ eV, 1.5 eV and $U_{Ru} = 0.5$ eV.

In third section of this work, we studied Lanthanide based double perovskite $\text{Tb}_2\text{FeCrO}_6$ which is recently synthesized by our collaborators using the neutron powder diffractometer. On our part, we performed DFT calculation on $\text{Tb}_2\text{FeCrO}_6$ which have been investigated to be a insulator with a energy gap of 0.12 (2.4) eV under GGA (GGA+ U) functional. Our result is found to agree well with the experiment. Magnetic transition temperature T_N on this material is estimated to be 853 K.

Our calculations revealed that doped system shows many new and novel properties which are not yet reported in parent materials that might demonstrate the potential for their likely and workable uses, like in hard magnetic memory applications. Investigations have revealed that the cooperative impact of Coulomb interaction, SOC, and the crystal field for atomic interaction take the main roles in atomic interactions. It can be concluded from our study that one can easily tune the band gap of the materials and change the state of magnetism to find various novel properties by substituting 3d, 4d and 5d transition metals at M, M' and T site which are essential in the investigation of modern technological devices. We hope that our investigations will start more experimental work to confirm the intriguing assumptions raised in this paper.

5.2 Recommendations for Future Work

Many DPs have been found with novel properties which are essential for future technological device fabrication. We have found half metallic and insulating properties in these materials. If we explore more materials with substitution, we can predict new materials with novel properties. Hence, we recommend for future extension of this work. We explored some DPs like $\text{Ca}_2\text{Cr}_{0.5}\text{Ni}_{0.5}\text{OsO}_6$, $\text{Ca}_2\text{CrIrO}_6$, $\text{Ca}_2\text{FeIrO}_6$ and $\text{Ca}_2\text{MnIrO}_6$ which are not yet experimentally synthesized. So we recommend to experiment group to synthesize these materials for its practical applications.

The proposed work has a large scope in terms of spintronics which is relevant and necessary to extend scientific research in Nepal. This study is expected to be a resource program of studies for those who are interested in the field. Since every research work has its own importance, the current work may play crucial role in the enhancement of osmium, iridium and ruthenium containing double perovskites. The following studies can be done as further enhancement in our present study:

- To study and find topological properties within double perovskites.
- To study optical & thermoelectric properties with substitution of other 3d, 4d and 5d transition metals.
- To study novel properties of osmium, iridium & ruthenium containing double perovskites.
- To study with changing MM' with platinum group oxides that may be useful in spintronics and quantum devices.
- More discussion can be made in materials containing f-electrons based on our Tb-based systems with strong computational tools.
- Surface state calculations for all the above materials to study their role as a quantum device.
- Experimental synthesis of explored DPs for its applications.

CHAPTER 6

SUMMARY

Electronic structure and associated properties of $A_2M_{1-x}M'_xTO_6$ DPs are studied using DFT calculations. We started our work by focusing on the newly synthesized DP material Ca_2CrOsO_6 that was claimed to be a FiM ground state with insulating character. By substitution of 3d, 4d and 5d transition metals, we investigated different properties for application in spintronic devices. The spin-exchange coupling parameters have been calculated in some of the doped materials such as in Ca-based double perovskites. We use these exchange parameters for predicting Curie temperature T_C on the basis of Heisenberg model. Our calculated value of T_C was found to be comparable with different literatures. Additionally, we looked into the thermoelectric properties and optical properties of the parent material. It turns out that the results does not show promising as a thermoelectric and optical device in Ca_2CrOsO_6 .

Upon substantial doping of Ni (50%) to the Cr-site on parent material Ca_2CrOsO_6 , this adds additional five electron on the system. From the five extra electrons, two are constrained to travel e_g states in up channel whereas other three are compelled to move in down channel and fill the t_{2g} states. A repelling action on the Os- t_{2g} bands is produced by such three Ni electrons in the spin-down channel. This action compell the Os band to move from valence region to the conducton region crossing Fermi level in spin down state. This produces a metallic state in spin down and spin up channel continues to be an insulator. Hence, the material $Ca_2Cr_{0.5}Ni_{0.5}OsO_6$ is found to be a half metallic nature. Likewise, we investigated two additional double perovskite Ca_2CrIrO_6 and Ca_2FeIrO_6 by substituting Fe and Ir at Cr and Os site. They are found to be thermodynamically stable on the basis of obtained cohesive and formation energy. Based on this, we predicted that these materials can be synthesized in laboratory. Both materials retain their semiconducting behaviour even with strong SOC. Curie temperature on both the materials are calculated based on MFA. The Curie temperature T_C of the materials are found to be 906 K and 827 K for Ca_2CrIrO_6 and Ca_2FeIrO_6 , respec-

tively, which are in valid T_C trends as in other double perovskites. Similarly, we also studied $\text{Ca}_2\text{MnIrO}_6$ and $\text{Ca}_2\text{NiIrO}_6$ by substituting transition metals in parent material. $\text{Ca}_2\text{MnIrO}_6$ which is obtained with doping of Mn and Ir at Cr and Os site is found to be half-metallic FiM with spin up being metallic and spin down as a insulator in nature and this half-metallic nature persists even with strong SOC effect. Estimation of T_C for $\text{Ca}_2\text{MnIrO}_6$ is found to be 280 K. On the other hand, $\text{Ca}_2\text{NiIrO}_6$ which is obtained by substituting Ni and Ir at Cr and Os site and is found to be FiM. This material also shows insulating nature even with strong SOC. T_C of this material is calculated to be 270 K.

On the basis of DFT, we begin our examination of Sr-based double perovskites by looking at the electronic and magnetic properties of recently synthesized $\text{SrLaBB}'\text{O}_6$ (B= Ni, Fe; B'= Os, Ru). With their magnetic easy axis along the [001]-direction, we discovered the anti-ferromagnetic (AFM) ground state for SrLaNiOsO_6 , SrLaFeOsO_6 and SrLaNiRuO_6 . These compounds' electronic behavior is shown to be insulating. When SOC is added to the Os-5d site, it causes a very modest band gap (0.03 eV) to open, indicating that SOC has a considerable influence in SrLaFeOsO_6 , with dominating contributions from the Os-5d and Ru-4d bands around E_F . For these systems, our results are fairly consistent with the experimental findings.

Similarly, for Tb-based double perovskites, we investigate $\text{Tb}_2\text{FeCrO}_6$ which has been synthesized by our collaborators. An investigation by DFT calculation on this material $\text{Tb}_2\text{FeCrO}_6$ shows an AFM insulator having a energy gap of 0.12 (2.4) eV with GGA (GGA+ U) functional this resembles with the outcomes of the experiment. Neel temperature T_N of the material estimated from our calculations is 853 K.

REFERENCES

- Alonso, J. A., Casais, M. T., Martinez, L. M. J., Martinez, J. L., Velasco, P., Munoz, A., & Fernandez D. M. T. (2000). Preparation, crystal structure, magnetic and magneto-transport properties of the double perovskite $\text{Ca}_2\text{FeMoO}_6$. *Chem. Mater.*, **12**(1), 161–168.
- Anderson, M. T., Greenwood, K. B., Taylor, G. A., & Poepelmeier, K. R. (1993). B-cation arrangements in double perovskites. *Prog. Solid. State Chem.*, **22**(3), 197–223.
- Anisimov, V. I., Aryasetiawan, F., & Lichtenstein, A. I. (1997). First-principles calculations of the electronic structure and spectra of strongly correlated systems: the LDA+ U method. *J Phys.:Condens. Matter*, **9**(4), 767–808.
- Aschroft, N. W., & Mermin, N. D. (1976). *Solid States Physics*, Saunders College, Philadelphia.
- Bhandari, S., Thapa, R., & Ghimire, M. (2016). First principles investigations on the electronic and magnetic properties of $\text{La}_4\text{Ba}_2\text{Cu}_2\text{O}_{10}$. *J. Nep. Phys. Soc.*, **3**(1), 89–96.
- Bidault, O., Maglione, M., Actis, M., Kchikech, M., & Salce, B. (1995). Polaronic relaxation in perovskites. *Phys. Rev. B*, **52**(6), 4191–4197.
- Blaha, P., Schwarz, K., Madsen, G. K. H., Kvasnicka, D., Luitz, J., & Schwarz, K. (2008). *An augmented plane wave plus local orbitals program for calculating crystal properties: Wien2K Users Guide*, Techn. Universitat Wien.
- Blaha, P., Schwarz, K., Madsen, G. K. H., Kvasnicka, D., & Luitz, J. (2001). *WIEN2k, An augmented plane wave+local orbitals program for calculating crystal properties*, Technische Universität Wien, Vienna, Austria.
- Boona, S. R. (2017). Nanomagnets boost thermoelectric output. *Nature*, **549**(5), 169–174.
- Bugaris, D. E., Hodges, J. P., Huq, A., & Loye, Z. H.-C. (2011). Crystal growth, structures, and optical properties of the cubic double perovskites Ba_6MgWO_6 and Ba_2ZnWO_6 . *J. Solid State Chem.*, **184**(8), 2293–2298.

- Calder, S., Garlea, V. O., McMorrow, D. F., Lumsden, M. D., Stone, M. B., Lang, J. C., Kim, J.-W., Schlueter, J. A., Shi, Y. G., Yamaura, K., Sun, Y. S., Tsujimoto, Y., & Christianson, A. D. (2012). Magnetically driven metal-insulator transition in NaOsO₃. *Phys. Rev. Lett.*, **108**(25), 257209–257214.
- Carvajal, J. R. (1993). Recent advances in magnetic structure determination by neutron powder diffraction. *Physica B: Condensed Matter*, **192**(1), 55–69.
- Ceperley, D. M. & Alder, B. J. (1984). Quantum Monte Carlo for molecules: Greens function and nodal release. *J. Chem. Phys.*, **81**(12), 5833–5841.
- Chattopadhyay, A., & Millis, A. J. (2001). Theory of transition temperature of magnetic double perovskites. *Phys. Rev. B*, **64**(2), 024424–024428.
- Correa, H. P. S., Cavalcante, I. P., Souza, D. O., Santos, E. Z., Orlando, M. T. D., Belich, H., Silva, F. J., Medeiro, E. F., Pires, J. M., Passamai, J. L., Martinez, L. G., & Rossi, J. L. (2010). Synthesis and structural characterization of the Ca₂MnReO₆ double perovskite. *Cermica*, **56**(338), 193–197.
- Erten, O., Meetei, O. N., Mukherjee, A., Randeria, M., Trivedi, N., & Woodward, P. (2013). Theory of half-metallic double perovskites. II. Effective spin Hamiltonian and disorder effects. *Phys. Rev. B*, **87**(16), 165105–165112.
- Eschrig, H., Koepf, K., & Chaplygin, I. (2003). Density functional application to strongly correlated electron systems. *J. Solid State Chem.*, **176**(2), 482–495.
- Fang, Z., Terakura, K., & Kanamori, L. (2001). Strong ferromagnetism and weak antiferromagnetism in double perovskites: Sr₂FeMO₆ ($M = \text{Mo, W, and Re}$). *Phys. Rev. B*, **63**(18), 180407–180411.
- Feng, H. L., Arai, M., Matsushita, Y., Tsujimoto, Y., Guo, Y., Sathish, C. I., Wang, X., Yuan, Y. H., Tanaka, M., & Yamaura, K. (2014). High-temperature ferrimagnetism driven by lattice distortion in double perovskite Ca₂FeOsO₆. *J. Am. Chem. Soc.*, **136**(9), 3326–3329.
- Fert, A. (2008). Nobel lecture: origin, development, and future of spintronics. *Rev. Mod. Phys.*, **80**(4), 1517–1530.
- Geprags, S., Majewski, P., & Gross, R. (2006). Electron doping in the double perovskite La_xA_{2-x}CrWO₆ with A= Sr and Ca. *J. Appl. Phys.*, **99**(8), 08102–08106.
- Ghimire, M. P., & Hu, X. (2016). Compensated half metallicity in osmium double perovskite driven by doping effects. *Mater. Res. Express*, **3**(10), 106107–106113.

- Ghimire, M. P., Thapa, R. K., Rai, D. P., Sandeep, Sinha, T. P., & Hu, X. (2015). Half metallic ferromagnetism in tri-layered perovskites $\text{Sr}_4\text{T}_3\text{O}_{10}$ ($\text{T} = \text{Co}, \text{Rh}$). *J. Appl. Phys.*, **117**(6), 063903–063908.
- Ghimire, M. P., Wu, L-H., & Hu, X. (2016). Possible half-metallic antiferromagnetism in an iridium double-perovskite material *Phys. Rev. B*, **93**(13), 134421–134425.
- Gopalakrishnan, J., Chattopadhyay, A., Ogale, S. B., Venkatesan, T., Greene, R. L., Millis, A. J., Ramesha, K., Hannoyer, B., & Marest, G. (2000). Metallic and nonmetallic double perovskites: A case study of $A_2\text{FeReO}_6$ ($A = \text{Ca}, \text{Sr}, \text{Ba}$). *Phys. Rev. B*, **62**(14), 9538–9542.
- Grosso, G., & Pastori, G. (2000). *Solid State Physics*, Academic Press, London.
- Groot, D. R. A., Mueller, F. M., Engen van, P. G., & Buschow, K. H. J. (1983). New class of materials: half-metallic ferromagnets. *Phys. Rev. Lett.*, **50**(25), 2024–2027.
- Hiroi, Z., Yamaura, J., & Hattori, K.(2012). Rattling good superconductor : β -pyrochlore oxides AOs_2O_6 (Recent Developments in Superconductivity). *J. Phys. Soc. Jpn*, **81**(1), 011012–0110124.
- Hohenberg, P., & Kohn, W. (1964). Inhomogeneous electron gas. *Phys. Rev. B*, **136**(3B), 864–871.
- Hu, X. (2012). Halfmetallic antiferromagnet as a prospective material for spintronics. *Adv. Mater.*, **24**(2), 294–298.
- Hua, W. (2001). Electronic structure study of double perovskites $A_2\text{FeReO}_6$ ($A = \text{Ba}, \text{Sr}, \text{Ca}$) and Sr_2MMoO_6 ($M = \text{Cr}, \text{Mn}, \text{Fe}, \text{Co}$) by LSDA and LSDA + U . *Phys. Rev. B*, **64**(12), 125–126.
- Ishida, S., Fujii, S., Kashiwagi, S., & Asano S.,(1995). Search for half-metallic compounds in Co_2MnZ ($Z=\text{IIIb}, \text{IVb}, \text{Vb}$ Element). *J. Phys. Soc. Jpn.*, **64**(7), 2152–2157.
- Iwakura, H., Einaga, H., & Teraoka, Y. (2011). Photocatalytic properties of ordered double perovskite oxides. *J. Novel Carbon Resour. Sci.*, **3**(1), 1–5.
- Jeng, H. T. & Guo, G. Y. (2003). First-principles investigations of orbital magnetic moments and electronic structures of the double perovskites $\text{Sr}_2\text{FeMoO}_6$, $\text{Sr}_2\text{FeReO}_6$, and Sr_2CrWO_6 . *Phys. Rev. B*, **67**(9), 094438–094445.
- Kanamori, J. (1959). Superexchange interaction and symmetry properties of electron orbitals. *J. Phys. Chem. Solids.*, **10**(2), 87–98.

- Kato, H., Okuda, T., Okimoto, Y., Tomioka, Y., Oikawa, K., Kamiyama, T., & Tokura, Y. (2002). Metal-insulator transition of ferromagnetic ordered double perovskites: $(\text{Sr}_{1-y}\text{Ca}_y)_2\text{FeReO}_6$. *Phys. Rev. B*, **65**(14), 144404–144409.
- Kittel, C. (1996). *Introduction to solid states Physics*, John Wiley & Sons, Inc., NewYork.
- Kobayashi, K. I., Kimura, T., Sawada, H., Terakura, K., & Tokura, Y. (1998). Room-temperature magnetoresistance in an oxide material with an ordered double-perovskite structure. *Nature (London)*, **395**(6703), 677–680.
- Koepernik, K., & Eschrig, H. (1999). Full-potential nonorthogonal local-orbital minimum-basis band-structure scheme. *Phys. Rev. B*, **59**(3), 1743–1757.; <https://www.fplo.de/>
- Koepernik, K., Velicky, B., Hayn, R., & Eschrig, H. (1997). Self-consistent LCAO-CPA method for disordered alloys. *Phys. Rev. B*, **55**(9), 5717–5729.
- Kohn, W., & Sham, L. J. (1965). Self-consistent equations including exchange and correlation effects. *Phys. Rev. A*, **140**(4A), A1133–A1138.
- Lee, K. W., & Pickett, W. E. (2008). Half semimetallic antiferromagnetism in the Sr_2CrTO_6 system ($T = \text{Os, Ru}$). *Phys. Rev. B*, **77**(11), 115101–115107.
- Lee, K. -W., & Pickett, W. E. (2007). Orbital-quenching induced magnetism in $\text{Ba}_2\text{NaOsO}_6$. *EPL*, **80**(3), 37008–37013.
- Lee, M.-S., Poudeu, F. P., & Mahanti, S. D. (2011). Electronic structure and thermoelectric properties of Sb-based semiconducting half-Heusler compounds. *Phys. Rev. B*, **83**(8), 085204–085215.
- Liechtenstein, A. I., Anisimov, V. I., & Zaanen, J. (1995). Density-functional theory and strong interactions: Orbital ordering in Mott-Hubbard insulators. *Phys. Rev. B*, **52**(8), R5467–R5470.
- Madsen, G. K. H.(2006). Automated search for new thermoelectric materials: the case of LiZnSb . *J. Am. Chem. Soc.*, **128**(37), 12140–12146.
- Mandal, T. K., Felser, C., Greenblatt, M., & Kubler, J. (2008). Magnetic and electronic properties of double perovskites and estimation of their Curie temperatures by ab initio calculations. *Phys. Rev. B*, **78**(13), 134431–134439.
- Marder, M. P. (2010). *Condensed Matter Physics*, John Wiley & Sons.
- Martin, R. M. (2004). *Electronic structure: basic Theory and Practicle Methds*, Cambridge University Press, United Kingdom.

- Meetei, O. N., Erten, O., Mukherjee, A., Randeria, M., Trivedi, N., & Woodward, P. (2013). Theory of half-metallic double perovskites. I. double exchange mechanism. *Phys. Rev. B*, **87**(16), 165104–165111.
- Miessler, G. L., & Tarr, D. A. (1996). *Inorganic Chemistry*, Prentice Hall, UK.
- Moreira, M. L., Paris, E. C., Nascimento, G. S., Longo, V. M., Sambrano, J. R., Mastelaro, V. R., Bernardi, M. I. B., Andrs, J., Varela, J. A., & Longo, E. (2009). Structural and optical properties of CaTiO₃ perovskite-based materials obtained by microwave-assisted hydrothermal synthesis: An experimental and theoretical insight. *Acta Materialia*, **57**(17), 5174–5185.
- Morrow, R., Soliz, J. R., Hauser, A. J., Gallagher, J. C., Susner, M. A., Sumption, M. D., Aczel, A. A., Yan, J., Yang, F., & Woodward, P. M. (2016). The effect of chemical pressure on the structure and properties of A₂CrOsO₆ (A= Sr, Ca) ferrimagnetic double perovskite. *J. Solid Stat. Chem.*, **238**(4), 46–52.
- Morrow, R., McGuire, M. A., Yan, J., & Woodward, P. M. (2018). The crystal structure and magnetic behavior of quinary osmate and ruthenate double perovskites LaABBO₆ (A = Ca, Sr; B = Co, Ni; B' = Ru, Os). *Inorg. Chem.*, **57**(6), 2989–2996.
- Morrow, R. C. (2015). *Competing superexchange interactions in double perovskite osmates*. The Ohio State University, USA.
- Pashov, D., Acharya, S., Lambrecht, W. R. L., Jackson, J., Belashchenko, K., Chantis, A., Jamet, F., & van, S. M., (2020). "Questaal: A package of electronic structure methods based on the linear muffin-tin orbital technique". *Computer Physics Communications* **249**(7), 107065–107115.
- Parrey, K. A., Khandy, S. A., Islam, I. Ishtihadah, L., Gupta, A., D. C., Niazi, A., Aziz, Ansari, S. G., Khenata, R., & Rubab, S. (2018). Electronic structure, optical and transport properties of double perovskite La₂NbMnO₆. *J. Elect. Mater.*, **47**(7), 3615–3621.
- Perdew, J. P., & Zunger, A. (1981). Self-interaction correction to density-functional approximations for many-electron systems. *Phy. Rev. B*, **23**(10), 5048–5079.
- Perdew, J. P., Burke, K., & Ernzerhof, M. (1996). Generalized gradient approximation made simple. *Phys. Rev. Lett.*, **77**(18), 3865–3868.
- Rafique, M., Young, S., & Tan, H. (2017). first-principles study on alkaline earth metal atom substituted monolayer boron nitride (BN). *J. Mat. Chem. C*, **88**(32), 115–121.

- Rai, D. P., Shankar, A., Ghimire, M. P., Sandeep, & Thapa, R. K. (2015). The electronic, magnetic and optical properties of double perovskite $A_2\text{FeReO}_6$ ($A = \text{Sr, Ba}$) from first principles approach. *Comp. Mater. Sci.*, **101**(6), 313–320.
- Ramesha, K., Thangadurai, V., Sutar, D., Subramanyam, S. V., Subbanna, G. N., & Gopalakrishnan, J. (2000). ALaMnBO_6 ($A = \text{Ca, Sr, Ba}$; $B = \text{Fe, Ru}$) double perovskites. *Materials Research Bulletin*, **35**(4), 559–565.
- Rietveld, H. M. (1969). A profile refinement method for nuclear and magnetic structures. *J. Appl. Cryst.*, **2**(2), 65–71.
- Ritter, C., Ibarra, M. R., Morellon, L., Blasco, J., Garca J., & De Teresa, J. M. (2000). Structural and magnetic properties of double perovskites $\text{AA}'\text{FeMoO}_6$ ($\text{AA}' = \text{Ba}_2, \text{Sr}_2$ and Ca_2), *Journal of Physics: Condensed Matter*. **12**(38), 8295–8308.
- Rogado, N. S., Li, J., Sleight, A. W., & Subramanian, M. A. (2005). Magneto-capacitance and magneto-resistance near room temperature in a ferromagnetic semiconductor: $\text{La}_2\text{NiMnO}_6$. *Adv. Mater.*, **17**(18), 2225–2227.
- Roy, P., Waghmare, V., & Maiti, T. (2016). Environmentally friendly $\text{Ba}_x\text{Sr}_{2-x}\text{TiFeO}_6$ double perovskite with enhanced thermopower for high temperature thermoelectric power generation. *RSC Adv.*, **6**(60), 54636–54643.
- Roy, P., Bose, I., & Maiti, T. (2016). Synthesis and characterization of Sr_2TiMO_6 ($M = \text{Fe, Co}$) double perovskites for high temperature thermoelectric applications. *Integr. Ferroelectr.*, **34**(1), 34–42.
- Sadoc, A., de Graaf, C., & Broer, R., (2007). Quantum chemical study of the nature of the ground state and the pressure-induced spin transition in CaFeO_3 . *Phys. Rev. B*, **75**(16), 165116–165123.
- Salce, S., Gravi, J. L., & Boatner, L. A. (1994). Disorder and thermal transport in undoped KTaO_3 . *J. Phys.: Condens. Matter*, **6**(22), 4077–4092.
- Sarma, D. D., Mahadevan, P., Saha-Dasgupta, T., Ray, S., & Kumar, A. (2000). Electronic structure of $\text{Sr}_2\text{FeMoO}_6$. *Phys. Rev. Lett.*, **85**(22), 2549–2552.
- Saxena, M., Tanwar, K., & Maiti, T. (2017). Environmental friendly $\text{Sr}_2\text{TiMoO}_6$ double perovskite for high temperature thermoelectric applications. *Scr. Mater.*, **130**(6), 205–209.

- Schwarz, K., Blaha, P., & Madsen, G. K. H. (2002). Electronic structure calculations of solids using the WIEN2k package for material sciences. *Comp. Phys. Commun.*, **147**(1), 71–76.
- Serrate, D., Teresa, J. M. D., & Ibarra, M. R. (2007). TOPICAL REVIEW: Double perovskites with ferromagnetism above room temperature. *J. Phys.: Condens. Matter*, **19**(2), 023201–023287.
- Shimakawa, Y., Azuma, M., & Ichikawa, N. (2011). Multiferroic compounds with double-perovskite structures. *Materials*, **4**(1), 153–168.
- Shi, Y. G., Guo, Y. F., Wang, X., Princep, A. J., Khalyavin D., Manuel, P., Michiue, Y., Sato, A., Tsuda, T., Yu, S., Arai, M., Shirako, Y., Akaogi, M., Wang, N. L., Yamaura, K., & Boothroyd, A. T. (2013). A ferroelectric-like structural transition in a metal. *Nat. Mater.*, **12**(11), 1023–1027.
- Singh, D., & Nordström, L. (2006). *Plane wave, pseudopotential and LAPW method*, 2nd edition, Springer, New York.
- Sleight, A. W., & Weiher, J. F. (1972). Magnetic and electrical properties of Ba₂MReO₆ ordered perovskites. *J. Phys. Chem. Solids*, **33**(13), 679–687.
- Sleight, A. W., Longo, J., & Ward, R. (1962). Compounds of osmium and rhenium with the ordered perovskite structure. *Inorg. Chem.*, **1**(2), 245–250.
- Solovyev, I. V., Dederichs, P. H., & Anisimov, V. I. (1994). Corrected atomic limit in the local-density approximation and the electronic structure of d impurities in Rb. *Phys. Rev. B*, **50**(23), 16861–16871.
- Song, W., Zhao, E., Meng, J., & Wu, Z. (2009). Near compensated half metal in Sr₂NiOsO₆. *J. Chem. Phys.*, **130**(11), 114707–114713.
- Sugahara, T., Ohtaki, M., & Souma, T. (2008). Thermoelectric properties of double-perovskite oxide Sr_{2-x}M_xFeMoO₆ (M = Ba, La). *J. Ceram. Soc. Jpn.*, **116**(1360), 1278–1282.
- Tan, G., Hao, S., Zhao, J., Wolverton, C., & Kanatzidis, M. G. (2017). High thermoelectric performance in electron-doped AgBi₃S₅ with ultralow thermal conductivity. *J. Am. Chem. Soc.*, **139**(18), 6467–6473.
- Teller, E. (1962). On the stability of molecules in the Thomas-Fermi theory, *Rev. Mod. Phys.*, **34**(4), 627–631.

- Telling, N. D., Keatley, P. S., vander Laan, G., Hicken, R. J., Arenholz, E., Sakuraba, Y., Oogane, M., Ando, Y., Takanashi, K., Sakuma, A., & Miyazaki, T. (2008). Evidence of local moment formation in Co-based Heusler alloys. *Phys. Rev. B*, **78**(18), 184438–184445.
- Tian, S. Z., Zhao, J. C., Qiao, C. D., Ji, X. L., & Jiang, B. Z. (2006). Structure and properties of the ordered double perovskites Sr_2MWO_6 (M= Co, Ni) by solgel route. *Materials Letters*, **60**(21), 2747–2750.
- Toll, J. S. (1956). Causality and the dispersion relation: logical foundations. *Physical review*, **104**(6), 1760–1770.
- Tokura, Y. (2006). Critical features of colossal magnetoresistive manganites. *Rep. Prog. Phys.*, **69**(3), 797–851.
- Tritt, T. M. (2011). Thermoelectric phenomena, materials, and applications. *Annu. Rev. Mater. Res.*, **41**(1), 433–448.
- Viana, R., Lunkenheimer, P., Hemberger, J., Bohmer, R., & Loidl, A. (1994). Dielectric spectroscopy in SrTiO_3 . *Phys. Rev. B*, **50**(1), 601–604.
- Wigner, E. P. (1934). On the Interaction of Electrons in Metals. *Phys. Rev*, **46**(11), 1002–1011.
- Wills, A. (2000). A new protocol for the determination of magnetic structures using simulated annealing and representational analysis (SARAh). *Physica B: Condensed Matter*, **276**(278), 680–681.
- Wolf, S. A., Awschalom, D. D., Buhrman, R. A., Daughton, J. M., von Molnar, S., Roukes, M. L., Chtchelkanova, A. Y., & Treger, D. M. (2001). Spintronics: a spin-based electronics vision for the future. *Science*, **294**(5546), 1488–1495.
- Xiang, H., Lee, C., Koo, H. J., Gong, X., & Whangbo, M. H., (2013). Magnetic properties and energy-mapping analysis. *Dalton Trans.*, **42**(4), 823–853.
- Yamaura, J., Ohgushi, K., Ohsumi, H., Hasegawa, T., Yamauchi, I., Sugimoto, K., Takeshita, S., Tokuda, A., Takata, M., Udagawa, M., Takigawa, M., Harima, H., Arima, T., & Hiroi, Z. (2012). Tetrahedral magnetic order and the metal-insulator transition in the pyrochlore lattice of $\text{Cd}_2\text{Os}_2\text{O}_7$. *Phys. Rev. Lett.*, **108**(24), 247205–247210.
- Ylvisaker, E. R., Pickett, W. E., & Koepf, K. (2009). Anisotropy and magnetism in the LSDA + U method. *Phys. Rev. B*, **79**(3), 035103–035115.

- Yuan, Y., Feng, H. L., Ghimire, M. P., Matsushita, Y., Tsujimoto, Y., He, J., Tanaka, M., Katsuya, Y., & Yamaura, K. (2015). High-pressure synthesis, crystal structures, and magnetic properties of 5d double-perovskite oxides $\text{Ca}_2\text{MgOsO}_6$ and $\text{Sr}_2\text{MgOsO}_6$. *Inorg. Chem.*, **54**(7), 3422–3431.
- Zeeshan, M., Singh, H. K., van den Brink, J., & Kandpal, H. C. (2017). Ab initio design of new cobalt-based half-Heusler materials for thermoelectric applications. *Phys. Rev. Mater.*, **1**(7), 075407–075411.
- Zeeshan, M., Brink, V. D. J., & Kandpal, H. C. (2018). Ab-initio design of new Heusler materials for thermoelectric applications. *Phys. Rev. Mater.*, **1**, 074401–074417.
- Zhao, F., Yue, Z., Gui, Z., & Li, L. (2005). Preparation, Characterization and microwave dielectric properties of A_2BWO_6 (A= Sr, Ba; B= Co, Ni, Zn) double perovskite. *J. Appl. Phys.*, **44**(11), 8066–8070.

APPENDIX:

PAPER PUBLICATIONS:

- 1) Bhandari, S. R., Yadav, D. K., Belbase, B. P., Zeeshan, M., Sadhukhan, B., Rai, D. P., Thapa, R. K., Kaphle, G. C. and Ghimire, M. P. (2020). Electronic, magnetic, optical and thermoelectric properties of $\text{Ca}_2\text{Cr}_{1-x}\text{Ni}_x\text{OsO}_6$ double perovskites. *RSC Adv.*, **10**, 16179-16186.
- 2) Bhandari, S. R., K. C., S., Lawaju, S., Thapa, R. K., Kaphle, G. C. and Ghimire, M. P. (2021). Electronic structure and estimation of Curie temperature in $\text{Ca}_2\text{B}\text{IrO}_6$ (B = Cr, Fe) double perovskites. *J. Appl. Phys.*, **130**(17), 173902-173907.
- 3) Yadav, D. K., Bhandari, S. R., Belbase, B. P., Kaphle, G. C., Rai, D. P., Ghimire, M. P. (2019). Effects of electron-correlation, spin-orbit coupling, and modified Becke-Johnson potential in double perovskites SrLaBBO_6 (B=Ni, Fe; B'=Os, Ru). *Comp. Mat. Sci.*, **170**, 109168-109174.
- 4) Mali, B., Nair, H. S., Heitmann, T. W., Nhalil, H., Antonio, D., Gofryk, K., Bhandari, S. R., Ghimire, M. P. and Elizabeth, S. (2020). Re-entrant spin reorientation transition and Griffiths-like phase in antiferromagnetic $\text{TbFe}_{0.5}\text{Cr}_{0.5}\text{O}_3$. *Phy. Rev. B*, **102**(1), 014418-014428.
- 5) Yadav, D. K., Bhandari, S. R., and Kaphle, G. C. (2020). Structural, elastic, electronic, and magnetic properties of MnNbZ (Z=As, Sb) and FeNbZ (Z=Sn, Pb) semi-Heusler alloys. *Mater. Res. Express*, **7**, 116527-116533.
- 6) Bhandari, S. R., K. C., S., Lawaju, S., Kaphle, G. C. and Ghimire, M. P. (2022). Electronic structure and magnetic properties on $\text{Ca}_2\text{MnIrO}_6$ double perovskites. *BIBECHANA*, **19**(1-2),127132.
- 7) Joshi, R. K., Bhandari, S. R. and Ghimire, M. P. (2022). Structural stability, electronic, optical, and thermoelectric properties of layered perovskite $\text{Bi}_2\text{LaO}_4\text{I}$. *RSC Adv.*, **12**, 24156-24162.

INTERNATIONAL VISIT AND SEMINAR:

1) Bhandari, S. R. (2022, Feb. 20th). *Electronic structure and Related Properties of $A_2M_{1-x}M'_xTO_6$ Double perovskites*. ANPA COLLOQUIUMS, ANPA, USA.

Oral Presentation (Online)

2) Bhandari, S. R. (2018, 10th July – 3rd September). *Leibniz Institute for Solid State and Materials Research, IFW- Dresden, Dresden, Germany*, under HUMBOLT fellowship.

Guest Scientist, Four Oral Presentation

3) Bhandari, S. R. (2018, 4th September – 3rd October). *Leibniz Institute for Solid State and Materials Research, IFW- Dresden, Dresden, Germany*, under IFW fellowship.

Research Scholar, Two Oral Presentation

4) Bhandari, S. R. (2018, August 29-31). *Electronic structure and Related Properties of Ca_2CrOsO_6 and $Ca_2Cr_{0.5}Ni_{0.5}OsO_6$ Double perovskites*. The 4th Condensed Matter Summer School on Interface From Spins to Nanomembranes, Wroclaw, Poland.

Oral and Poster Presentation

CONFERENCES:

1) Bhandari, S. R., K. C., Santosh, Lawaju, S., Kaphle, G. C., and Ghimire, M. P. (2022). *Electronic structure and estimation of Curie temperature in $Ca_2B\text{Ir}O_6$ ($B = \text{Cr}, \text{Fe}$) double perovskites*. APS March meeting (2022), Chicago, IL, USA

Poster Presentation

2) Bhandari, S. R. (2021, September 15-19). *Refresher Course on Material science*. Central Department of Physics, Tribhuvan University, Kirtipur, Kathmandu, Nepal.

Participation

3) Bhandari, S. R. (2021, October 4-6). *International workshop on computational material engineering (CME-2021)*. Central Department of Physics, Tribhuvan University, Kirtipur, Kathmandu, Nepal.

Participation

4) Bhandari, S. R. (2021, November 22-24). *First International Conference on Material Sciences and Applied Physics (ICMSAP2021)*. Department of Physics, Pachhunga University College, Mizoram University, Aizawl, India.

Participation

5) Lawaju, S., Bhandari, S. R., K. C., Santosh, Ghimire, M. P. (2020). *First-Principle Study of Electronic Structure and Magnetic Properties of Tb_2FeCrO_6* .

Presentation

<https://iocc2020.sciforum.net/event/IOCC2020/submissions>

6) Yadav, D., Lamichhane, S., Bhandari, S., Belbase, B., Kaphle, G. C., Ghimire, M. P. (2018). *A Possible Spin-Orbit Coupling Assisted Semiconductor in $ALaNiOsO_6$ ($A=Sr, Ba$)*.

Presentation

<https://meetings.aps.org/APS March Meeting Abstracts 2018, K23. 007>

7) Yadav, D., Belbase, B., Bhandari, S., Ghimire, M.P., Kaphle, G. C. (2019). *Electronic Structure and Magnetic Phase Transition in Double Perovskite $La_{2-x}Na_xMnMoO_6$ ($x=0, 0.5, 1.0, 1.5, 2.0$)*.

Presentation

<https://meetings.aps.org/APS March Meeting 2019, abstract id.B07.013>

8) Belbase, B., Bhandari, S., Yadav, D., Kaphle, G. C. Ghimire, M. P. (2018). *Investigations on the Electronic and Optical Properties of Double Perovskites Ba_2BiSbO_6* ,

Presentation

<http://meetings.aps.org/APS March Meeting-2018, Abstracts Volume 2019,P33. 014>

9) Bhandari, S. R. (2017, December 27-29). *Electronic and Related Properties of $PrVSb_3$ and $PrSrVSb_3$* . The 7th International Conference on Nano-Materials and Computational Physics, (ICNMCP-2017), Kirtipur, Nepal.

Oral Presentation

10) Bhandari, S. R. (2016, March 26-29). *Electronic and Magnetic Properties of $PrVSb_3$ and $PrSrVSb_3$* . The 7th national conference on science and technology. NAST, Nepal.

Oral Presentation

CERTIFICATES AND PUBLISHED PAPERS:



First International Conference on Material Sciences and Applied Physics (ICMSAP–2021), 22–24 November 2021

Organized by

**Department of Physics, Pachhunga University College
Mizoram University, Aizawl, India**



CERTIFICATE OF PARTICIPATION

We are pleased to award this certificate to **Mr. Shalika Ram Bhandari, PhD Scholar** from Central Department of Physics, Tribhuvan University Kathmandu, Nepal for participating in **ICMSAP-2021** held at Pachhunga University College, Mizoram University, Aizawl, India, during November 22–24, 2021.

Prof. H. Lalthanzara
(Patron/Principal)

Dr. Shivraj Gurung
(Chairman)

Dr. Lalhriatzuala
(Convener)

Dr. Dibya Prakash Rai
(Convener)



Province Government
Province No. 5
Ministry of Industry, Tourism, Forest and Environment (MoITFE)
Butwal, Nepal

Scientific Research & Publication Award

Is hereby awarded to

SHALIKA RAM BHANDARI

In recognition of awardee's contribution in Scientific Innovation in Province No. 5

Awarded in

**"A Felicitation Program to Individual/Organization for Research, Study & Innovation
in the field of Science & Techonology"**

15th June 2019


.....
Dhananjaya Paudyal
Secretary

Ministry of Industry, Tourism, Forest and Environment




.....
Honorable Lila Giri
Minister

Ministry of Industry, Tourism, Forest and Environment

IFW Dresden · Helmholtzstraße 20 · 01069 Dresden

Landeshauptstadt Dresden
Bürgeramt
Abt. Staatsangehörigkeits- und
Ausländerangelegenheiten

Institut für
Theoretische Festkörperphysik

Prof. Dr. Jeroen van den Brink
Direktor

Helmholtzstr. 20
D-01069 Dresden
Tel.: +49 / (0)351 4659-380
Fax: +49 / (0)351 4659-750
j.van.den.brink@ifw-dresden.de

1. August 2018

Verlängerung Aufenthaltstitel Shalika Ram Bhandari

Sehr geehrte Damen und Herren,

Herr Shalika Ram Bhandari arbeitet mit Mitarbeitern des Theorie-Institutes im IFW Dresden am Thema „Dichtefunktionalrechnungen an kristallinen Systemen, speziell an schwachen topologischen Isolatoren“. Die Zusammenarbeit hat sich in den letzten Wochen als nutzbringend erwiesen und wir möchten eine Verlängerung seines Aufenthaltes um 1 Monat, vom 04.09.-03.10.18 fördern, um Herrn Bhandari die Möglichkeit zu geben, noch tiefer in die Materie einzudringen und seinen Anteil an der Zusammenarbeit zu stärken.

Wir bitten Sie deshalb um einsprechende Verlängerung seines Aufenthaltstitels.

Mit freundlichen Grüßen



Jeroen van den Brink
Direktor des Institutes für Theoretische Festkörperphysik
im IFW Dresden

VERTRAG

für einen Gastaufenthalt mit einem ausländischen Wissenschaftler

Zwischen dem

Leibniz-Institut für Festkörper- und Werkstoffforschung Dresden e. V. (IFW Dresden e. V.)
vertreten durch den Vorstand des Leibniz-Institutes für Festkörper- und Werkstoffforschung Dresden e. V.
- nachfolgend IFW genannt -

und

Herrn: Shalika Ram Bhandari
geboren am: 25.11.1982
wohnhaft: Würzburger Straße 89, 01187 Dresden
- nachfolgend Vertragspartner genannt-

§ 1 Gastaufenthalt

(1) Das IFW nimmt Herrn *Bhandari* als Gast zu einem Arbeitsaufenthalt in der Zeit vom **10.07.2018** bis **03.09.2018** im Institut für Theoretische Festkörperphysik (ITF) zum Zwecke der wissenschaftlichen Zusammenarbeit am Thema „Dichtefunktionalrechnungen an kristallinen Systemen, speziell an schwachen topologischen Isolatoren“ auf. Ein abhängiges Arbeitsverhältnis wird durch den Vertrag nicht begründet.

Der Vertrag ist auflösend bedingt, sofern kein gültiger Aufenthaltstitel mit gültiger Nebenbestimmung für die Vertragsdauer nachgewiesen wird.

- (2) Als Betreuer für den Gastaufenthalt werden Herr Dr. Madhav Prasad Ghimire und Herr PD Dr. Manuel Richter benannt.
- (3) Der Vertragspartner wird eine etwaige vorzeitige Beendigung oder Unterbrechung seines Aufenthaltes rechtzeitig der Personalabteilung mitteilen.
- (4) Die Regeln guter wissenschaftlicher Praxis der Leibniz-Gemeinschaft werden respektiert und befolgt.

§ 2 Entgelt, Nebenkosten

- (1) Das IFW zahlt dem Vertragspartner eine Aufwandsentschädigung in Höhe von **1.344,00 €** für die o. g. Aufenthaltsdauer aus.
- (2) Der Vertragspartner erhält zuzüglich zur o. g. Aufwandsentschädigung die Reisekosten (An- und Abreise) in nachgewiesener Höhe bei Vorlage der Fahrkarten bzw. Flugtickets erstattet.
- (3) Für eine ggf. erforderliche Versteuerung hat der Vertragspartner selbst zu sorgen.
- (4) Sind Dienstreisen im Rahmen der satzungsgemäßen Aufgaben des IFW erforderlich, können Aufwendungen in Anlehnung an das Sächsische Reisekostenrecht erstattet werden.

§ 3 Arbeitsergebnisse

- (1) Im Rahmen der wissenschaftlichen Zusammenarbeit stellt der Vertragspartner dem IFW, zu Händen des Institutsdirektors des ITF, seine Arbeitsergebnisse, z.B. schriftliche und bildliche Unterlagen, Materialien etc., zur Verfügung, die er im Zusammenhang mit seinem Gastaufenthalt im IFW macht.
- (2) Die §§ 2 bis 26 des Arbeitnehmererfindergesetzes (ArbEG) gelten entsprechend.
- (3) Im Falle der Erarbeitung von Computerprogrammen gilt § 69 b des Urhebergesetzes.

§ 4 Veröffentlichungen

Veröffentlichungen (Aufsätze, Vorträge, Gutachten und ähnliche Publikationen), die die Interessen des IFW berühren, bedürfen der vorherigen schriftlichen Zustimmung des Institutsdirektors des ITF im IFW.

§ 5 Verschwiegenheit

- (1) Der Vertragspartner wird dienstliche Angelegenheiten und Arbeitsergebnisse vertraulich behandeln. Dies gilt auch für die Zeit nach Beendigung des Aufenthaltes im IFW.
- (2) Das IFW, hierbei vertreten durch den Institutsdirektor des ITF, und der Vertragspartner werden vor Beendigung des Aufenthaltes gemeinsam feststellen, welche schriftlichen und bildlichen Unterlagen und Materialien ihm überlassen werden. Diese Unterlagen usw. darf der Vertragspartner nur mit Zustimmung des IFW an Dritte weitergeben oder Dritten zugänglich machen.

§ 6 Gesundheit und Sicherheit

- (1) Der Vertragspartner wird alle durch Gesetz, Verordnungen, Unfallverhütungsvorschriften oder Regelung des IFW geforderten Sicherheitsmaßnahmen beachten.
- (2) Das Eigentum des IFW behandelt der Vertragspartner sorgsam. Er haftet für Schäden, die er dem Institut grob fahrlässig oder vorsätzlich oder Dritten, denen das IFW Ersatz zu leisten hat, zufügt. Für Schäden, die der Vertragspartner erleidet, haftet das IFW nicht.
- (3) Unfallversicherungsschutz über die zuständige Berufsgenossenschaft besteht nicht, dass gilt auch für Dienstreisen.
- (4) Für alle zusätzlich erforderlichen Sach- und Personenversicherungen ist der Vertragspartner persönlich verantwortlich. Im Krankheitsfall werden durch das IFW eventuell anfallende Arzt-, Zahnarzt- oder Krankenhauskosten nicht übernommen sowie keine Zuschüsse zu entstehenden Kosten gewährleistet. Das IFW weist darauf hin, dass sich der Vertragspartner in einer gesetzlichen bzw. privaten Krankenkasse versichern kann.

§ 7 Mitteilungen

Änderungen zu persönlichen Verhältnissen (Anschriften und dergleichen) wird der Vertragspartner dem Institut mitteilen.

§ 8 Änderungen und Ergänzungen


Änderungen und Ergänzungen des Vertrages bedürfen zu ihrer Gültigkeit der Schriftform.

§ 9 Gerichtsstand

- (1) Für alle Rechtsstreitigkeiten aus diesem Vertrag wird Dresden als Gerichtsstand vereinbart.
- (2) Der Vertrag kann mit einer Frist von 14 Tagen zum Ende eines Kalendermonats gekündigt werden.

Dresden, 14.06.2018

Leibniz-Institut für Festkörper- und Werkstoffforschung Dresden e. V.


.....
i.A. Giacomo Contassot
Abteilung Personal und Soziales





Nepal Academy of Science and Technology

CERTIFICATE

Awarded to

SHALIKA RAM BHANDARI.....

for active participation/paper presentation/poster presentation

in

THE 7th NATIONAL CONFERENCE ON SCIENCE AND TECHNOLOGY

SCIENCE, TECHNOLOGY AND INNOVATION FOR NEPAL'S GRADUATION TO DEVELOPING COUNTRY STATUS

March 29-31, 2016

Kathmandu, Nepal

Ramila Raut

Mrs. Ramila Shrestha Raut
Chief, Promotion Division

Buddhi

Dr. Buddhi Ratna Khadge

Secretary

Jiba Raj Pokharel

Prof. Dr. Jiba Raj Pokharel
Vice-Chancellor

INTERNATIONAL WORKSHOP ON COMPUTATIONAL MATERIALS ENGINEERING




Certificate of Participation

This certificate is awarded to Prof. Dr. / Dr. / Mr. / Ms. *Shalika Ram Bhandari* for participating in three days program from October 04th - 06th, 2021 on “**International Workshop on Computation Materials Engineering (CME-2021)**” organized by Central Department of Physics, Tribhuvan University. This program is supported by University Grants Commission, Nepal and Advanced Materials Research Laboratory of the Central Department of Physics.


Head Ghimire
Central Department of Physics
Tribhuvan University


Prof. Dr. Om Prakash Niraula
Head
Central Department of Physics
Tribhuvan University


Patron
Prof. Dr. Binil Aryal
Dean
Institute of Science & Technology
Tribhuvan University


Chief Guest
Prof. Dr. Shekhar Gurung
Central Department of Physics
Tribhuvan University

Electronic Structure and Related Properties of $\text{Ca}_2\text{CrOsO}_6$ and $\text{Ca}_2\text{Cr}_{0.5}\text{Ni}_{0.5}\text{OsO}_6$ Double Perovskites

Shalika Ram Bhandari^{1,2,3}, Dinesh Kumar Yadav^{2,3}, Gopi Chandra Kaphe^{2,3} and Madhav Prasad Ghimire^{1,2,3}

¹ IFW Dresden e. V., D-01069 Dresden, Germany.

² Central Department of Physics, Tribhuvan University, Kirtipur, Kathmandu, Nepal.

³ Condensed Matter Physics Research Center (CMPRC) Butwal, Rupandehi, Nepal.

Introduction

- Recent research is focused on metal oxides containing 3d, 4d and 5d transition metals including double perovskites $\text{Ca}_2\text{BB}'\text{O}_6$ (where B and B' are 3d, 4d, 5d transition elements)
- Such double perovskites are found to exhibit novel properties desirable in modern technological applications like spintronic, half-metallicity, Ferromagnetic Mott-insulator, thin-film magnetic heterostructures and high-temperature superconductivity.
- These and other ground state properties are of particular interest for spintronic device fabrication and their applications.

Crystal Structure

- $\text{Ca}_2\text{CrOsO}_6$ crystallizes in an ordered double perovskite structure with space group $\text{P2}_1/\text{n}$ (monoclinic)[1]
- Experimental lattice parameters are used; $a=5.3513 \text{ \AA}$, $b=5.4561 \text{ \AA}$, $c=7.6204 \text{ \AA}$ and $\beta=90.092^\circ$
- The inter-octahedral Cr-O-Os bond angles are 153.3° , 152.6° and 153.8°
- Average Cr-O and Os-O distances are 1.972 \AA and 1.954 \AA respectively
- Charge state: Ca^{2+} , Cr^{3+} , Os^{5+} , O^{2-} ($4s^2, 3d^3, 5d^3, 2p^6$)

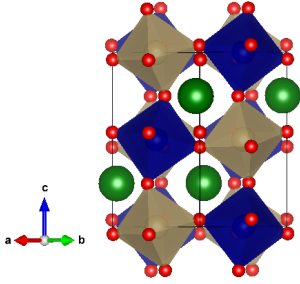


Figure 1: Crystal structure of double perovskite $\text{Ca}_2\text{BB}'\text{O}_6$. Where green, blue, brown, and red spheres correspond to Ca, B, B' and O sites.

Computational Details

- FP-LAPW+LO method implemented in the WIEN2k code [2]
- Supercell approach is considered to calculate the total energies and different magnetic configurations
- The symmetrized structure (space group 14) has been transformed to P1 symmetry consisting of four atoms of Ca and two atoms of each Cr, Os and the remaining twelve atoms are oxygens
- Four types of magnetic configurations have been studied which correspond to one FM, two AFM and one FIM orderings
- Up/Dn spins of magnetic atoms Cr1, Cr2, Os1 and Os2 ordering are FM1-uuuu, AF1-udud, AF2-uddu and FI1-uddd
- Standard GGA/LDA with electron correlation effects (+U) is considered [3]
- Spin-orbit coupling considered with magnetic moment orientation along 100, 010, 001, 110 and 111-directions
- Self consistency achieved with energy convergence 10^{-5} Ry and charge convergence $10^{-4}e$

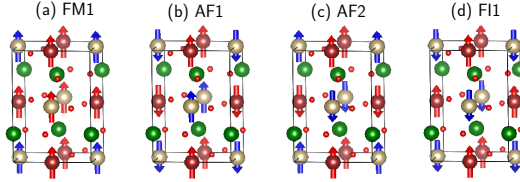


Figure 2: The red (blue) arrows indicate the direction of Cr/Ni(Os) spins along the direction of easy axis (100).

Results and Discussion

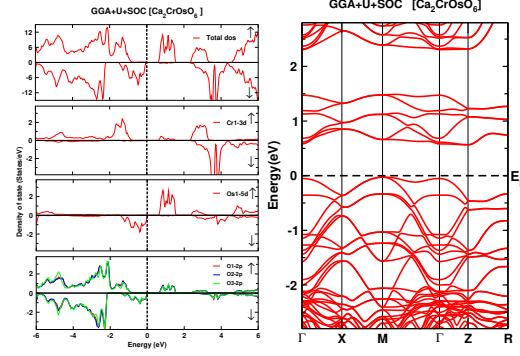


Figure 3: Total and PDOS for CCOO

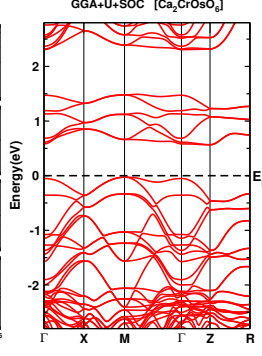


Figure 4: Band structure for CCOO

- Ferrimagnetic ground state is found consistent with experiment
- Total DOS plot and band structure shows insulating behavior assisted with SOC
- The values of U for Cr, Ni and Os are chosen 4 eV, 5 eV and 1.5 eV, respectively
- GGA, GGA+U and GGA+U+SOC shows 0.53 eV, 0.66 eV and 0.59 eV band gap and 0, 0 and $0.23 \mu_B$ total magnetic moment, respectively
- Spin and orbital magnetic moment for Cr and Os are $2.52 \mu_B$, $-1.59 \mu_B$, $-0.047 \mu_B$ and $0.136 \mu_B$, respectively.

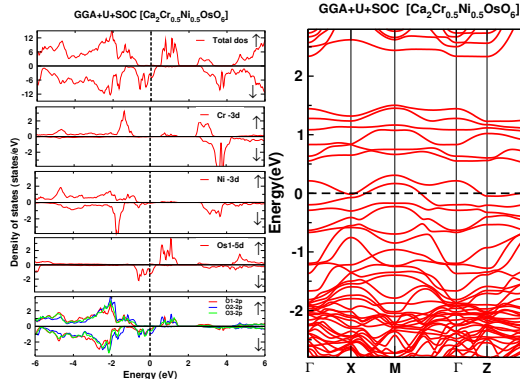


Figure 5: Total and PDOS for CCNOO

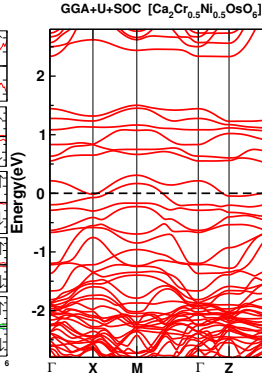


Figure 6: Band structure for CCNOO

- GGA, GGA+U and GGA+U+SOC shows 0.18 eV, 0.66 eV and 0.28 eV band gap for up spin and metallic for down spin with 0, 0 and $0.21 \mu_B$ total Magnetic moment, respectively, in $\text{Ca}_2\text{Cr}_{0.5}\text{Ni}_{0.5}\text{OsO}_6$
- Spin magnetic moments for Ni and Os are $1.71 \mu_B$ and $1.36 \mu_B$
- The orbital magnetic moment for Cr, Ni and Os are $-0.048 \mu_B$, $0.144 \mu_B$ and $0.156 \mu_B$, respectively
- The O-2p orbitals hybridize strongly with Cr and Ni-3d orbitals and Os-5d orbitals
- The most interesting band located at the Fermi level is composed of mainly Os-5d states

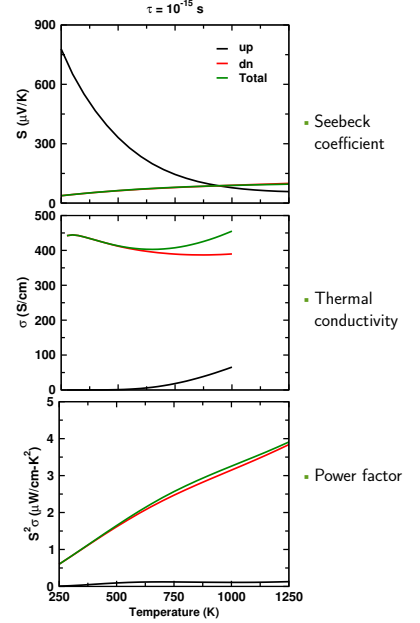


Figure 7: Transport properties of $\text{Ca}_2\text{CrOsO}_6$

Conclusion

- Magnetic ground state is found to be ferrimagnetic insulator for $\text{Ca}_2\text{CrOsO}_6$ and half metallic for $\text{Ca}_2\text{Cr}_{0.5}\text{Ni}_{0.5}\text{OsO}_6$ consistent with experiment.
- Replacing Cr by 3d elements with more than five valence electrons one can make a fine control on charge and spin
- Ni doping will influence the system by (i) shifting the Os bands towards the conduction region, and (ii) compensating magnetic moment by $2 \mu_B$ per each Cr replacement. In this way, one can modify the material to design the desired HMFim and HMAFM.
- Power factor on $\text{Ca}_2\text{CrOsO}_6$ is found to be 4 at 1250 kelvin.
- Combined effect of electron correlations and SOC opens band gap at E_F , making an SOC assisted Mott-Insulator
- Magnetic easy axis is found along the [100] direction with band gap of 0.594 eV and 0.282 eV for $\text{Ca}_2\text{CrOsO}_6$ and $\text{Ca}_2\text{Cr}_{0.5}\text{Ni}_{0.5}\text{OsO}_6$

Acknowledgements

We are thankful to NAST Nepal for its financial support for the research.

References

- R. Morrow, J. R. Soliz, A. J. Hauser, et al., The Effect of Chemical Pressure on the Structure and Properties of A_2CrOsO_6 (A=Sr, Ca) Ferrimagnetic Double Perovskite, *J. of Solid State Chem.* **243**, 49 (2016).
- P. Blaha, K. Schwarz, G. K. H. Madsen, D. Kvasnicka, and J. Luitz, *WIEN2k*, An Augmented Plane Wave+Local Orbitals Program for Calculating Crystal Properties (Technische Universität Wien, Vienna, Austria, 2001), ISBN 3-9501031-1-2.
- J. P. Perdew, K. Burke, and M. Ernzerhof, Generalized Gradient Approximation Made Simple, *Phys. Rev. Lett.* **77**, 3865 (1996).



International conference on
Nano-Materials and Computational Physics

27-28 December 2017
Central Department of Physics
Tribhuvan University, Kirtipur, Nepal



Participation Certificate

Shalika Ram Bhandari

Central Department of Physics, T.U., Kirtipur

participated the conference during 27-28 December 2017 and
contributed oral/poster presentation entitled

Electronic and Magnetic Properties of PrVsb_3 and PrSrVsb_3 .

[Signature]

Prof. Dr. Ram Pd Khatiwada
Dean
IoST, Tribhuvan University, Kirtipur

[Signature]

Dr. Gopi Chandra Kaphle
Secretary
Organizing Committee

[Signature]

Prof. Dr. Binil Aryal
Head
CDP, TU, Kirtipur

Antrag auf Gastaufenthalt/IT-Zugang im IFW ohne Entgelt
Application for guest residence/IT access at the IFW without charge

Angaben zur Person:

Titel: _____

Title: _____

Name: Bhandari

Name: _____

Vorname(n): Shalika

First name(s): _____

Geschlecht: männlich weiblich divers
Gender: male female non-binary

Geburtsdatum: 25.11.1982
Date of birth: _____

Staatsangehörigkeit: Nepal
Nationality (if more than one, please specify all)

Anschrift: Siddartha Highway, Tilottama 21, Rupandehi, Nepal
Address: _____

Arbeitgeber während der unten genannten Aufenthaltsdauer am Institut (nicht IFW)
Employer during the period of stay at the institute mentioned below (not IFW)

Central Dept. of Physics, Tribhuvan Univ., Nepal

mit Arbeitsvertrag gegen Entgelt bis:
with employment contract against remuneration until

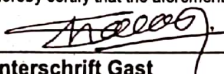
Stipendienggeber während der unten genannten Aufenthaltsdauer am Institut (nicht IFW)
Scholarship provider during the period of stay at the institute mentioned below (not IFW)

mit Stipendium für (Dauer):
with scholarship for (duration)

1 yrs

Projekt des Gasts (z.B. Durchführung von Messung oder Abschluss der Promotion):
Project of the guest (e.g. carrying out measurement or completing doctoral studies):

Ich versichere, dass die oben genannten Angaben richtig und vollständig sind. Sollten die Angaben falsch oder unrichtig sein, so kann das IFW den Gastvertrag auflösen.
I hereby certify that the aforementioned information is correct and complete. If the statements are false or incorrect, the IFW may dissolve the contract or terminate.



Unterschrift Gast
Signature of guest

Voraussichtliche Aufenthaltsdauer am Institut: vom 01.01.2023 bis 31.12.2023

Gast mit Zutrittsberechtigung - mit Gastvertrag

Stipendium (Stipendienzusage/Finanzierungsnachweis inkl. etwaiger Anlagen (z.B. AvH „Mitteilung Bankverbindung Gastinstitut“) sind beizufügen)
Hinweis: Stipendien externer Mittelgeber werden auch dann als Drittmittelprojekt in die IFW-Statistik aufgenommen, wenn keine Mittel für das IFW, sondern lediglich für den Stipendiaten vorgesehen sind.

Gast-Rechnerzugang (ohne Anwesenheit im IFW) - **ohne Gastvertrag** (nur für Angehörige von EU-Mitgliedsstaaten)

Betreuer*in (im IFW): PD Dr. Manuel Richter

IT-Ressourcen notwendig: ja nein

Hinweis: Gäste haben eingeschränkte IT-Rechte.
 erweiterte IT-Rechte sind erforderlich

Angaben zu dem/n Forschungsgebiet/en:

Forschungsgebiet 1 mit _____ % Forschungsgebiet 2 mit _____ % Forschungsgebiet 3 mit _____ % Forschungsgebiet 4 mit _____ %

Dresden, _____
Abteilungsleiter*in, Arbeitsgruppenleiter*in
Institutsdirektor*in
Bereichsleiter Forschungstechnik

Abteilung Personal und Soziales:

Aufenthaltstitel von _____ bis _____

Vorvertrag: _____

Aufenthaltstitel von _____ bis _____

Sachbearbeiter*in Personal und Soziales: _____

Drittmittelmanagement/
PROMAN-Erfassung: _____
sowie ggf. Beantragung Forschungskostenzuschuss

Abteilungsleiter*in Personal und Soziales: _____

INTERACTIVE WORKSHOP
ON
SCIENCE AND TECHNOLOGY: PRESENT SCENARIO,
FUTURE POSSIBILITIES AND CHALLENGES IN
PROVINCE-5



Shalika Ram Bhandari

Researcher

Bhairahawa Multiple Campus

Organized by
Ministry of Industry, Tourism, Forest and Environment
Province-5, Nepal

Co-convener

Electronic structure and estimation of Curie temperature in Ca_2BIrO_6 (B = Cr, Fe) double perovskites

Cite as: J. Appl. Phys. **130**, 173902 (2021); <https://doi.org/10.1063/5.0069884>

Submitted: 02 September 2021 • Accepted: 14 October 2021 • Published Online: 02 November 2021

 Shalika Ram Bhandari,  Santosh KC,  Sarita Lawaju, et al.



View Online



Export Citation



CrossMark

ARTICLES YOU MAY BE INTERESTED IN

[Living up to its potential—Direct-write nanofabrication with focused electron beams](#)

Journal of Applied Physics **130**, 170901 (2021); <https://doi.org/10.1063/5.0064764>

[Scalable memory elements based on rectangular SiSFS junctions](#)

Journal of Applied Physics **130**, 173901 (2021); <https://doi.org/10.1063/5.0063274>

[Realization of 366 nm GaN/AlGaN single quantum well ultraviolet laser diodes with a reduction of carrier loss in the waveguide layers](#)

Journal of Applied Physics **130**, 173105 (2021); <https://doi.org/10.1063/5.0069567>



Webinar
Quantum Material Characterization
for Streamlined Qubit Development



Register now

Electronic structure and estimation of Curie temperature in $\text{Ca}_2\text{B}(\text{IrO}_6)$ (B = Cr, Fe) double perovskites

Cite as: J. Appl. Phys. **130**, 173902 (2021); doi: 10.1063/5.0069884

Submitted: 2 September 2021 · Accepted: 14 October 2021 ·

Published Online: 2 November 2021



Shalika Ram Bhandari,^{1,2,3} Santosh KC,⁴ Sarita Lawaju,¹ Ram Kumar Thapa,⁵ Gopi Chandra Kaphle,¹ and Madhav Prasad Ghimire^{1,2,3,a)}

AFFILIATIONS

¹Central Department of Physics, Tribhuvan University, Kirtipur, Bagmati 44613, Nepal

²Leibniz Institute for Solid State and Materials Research Dresden (IFW-Dresden), Dresden 01609, Germany

³Condensed Matter Physics Research Center, Butwal-11, Lumbini 32907, Nepal

⁴Chemical and Materials Engineering, San José State University, San Jose, California 95192, USA

⁵Department of Physics, Mizoram University, Aizawl, Mizoram 796004, India

^{a)}Author to whom correspondence should be addressed: madhav.ghimire@cdp.tu.edu.np

ABSTRACT

We investigate the electronic and magnetic properties of $\text{Ca}_2\text{CrIrO}_6$ and $\text{Ca}_2\text{FeIrO}_6$ by means of density functional theory. These materials belong to a family of recently synthesized $\text{Ca}_2\text{CrOsO}_6$ whose properties show possible applications in a room temperature regime. Upon replacement of Os by Ir in $\text{Ca}_2\text{CrOsO}_6$, we found the system to exhibit a stable ferrimagnetic configuration with a bandgap of ~ 0.25 eV and an effective magnetic moment of $\sim 2.58\mu_B$ per unit cell. Furthermore, when chemical doping is considered by replacing Cr with Fe and Os with Ir, the material retains the insulating state but with a reduced bandgap of 0.13 eV and large increment in the effective magnetic moment of $\sim 6.68\mu_B$ per unit cell. These observed behaviors are noted to be the consequence of the cooperative effect of spin-orbit coupling; Coulomb correlations from Cr-3d, Fe-3d, and Ir-5d electrons; and the crystal field effect of the materials. These calculations suggest that by chemical tuning, one can manipulate the bandgap and their effective magnetic moment, which may help in material fabrication for device applications. To check further the suitability and applicability of $\text{Ca}_2\text{CrIrO}_6$ and $\text{Ca}_2\text{FeIrO}_6$ at higher temperatures, we estimate the Curie temperature (T_C) by calculating the spin-exchange coupling. We found that our findings are in a valid T_C trend similar to other perovskites. Our findings are expected to be useful in experimental synthesis and transport measurement for potential applications in modern technological devices.

Published under an exclusive license by AIP Publishing. <https://doi.org/10.1063/5.0069884>

I. INTRODUCTION

Double perovskites (DPs), derived from the general formula $\text{A}_2\text{BB}'\text{O}_6$ [where B and B' cations are transition metals (TMs) and A and A' sites are alkaline or rare earth metals], are found to have various properties with potential applications. Transition metal (TM)-based DPs are of interest due to their remarkable properties including structural stability, high charge mobility, finite bandgap, superconductivity, half-metallicity, piezo-electricity, thermo-electricity, topological properties, etc. These peculiar properties are important to integrate with modern technological devices.¹⁻⁹ Recently, various DP materials have been reported with different

novel properties, such as antiferromagnetism (AFM) in SrLaNiIrO_6 , weak paramagnetism (PM) in SrLaMgIrO_6 ,¹⁰ ferromagnetism in Ba_2NiUO_6 ,¹¹ magnetic insulating state in $\text{Sr}_2\text{CuOsO}_6$ and $\text{Sr}_2\text{NiOsO}_6$,¹² half-semi-metallic AFM in $\text{Sr}_2\text{CrOsO}_6$ (SCOO) and $\text{Sr}_2\text{CrRuO}_6$,¹³ ferrimagnetism with high Curie temperature in $\text{Sr}_2\text{CrIrO}_6$ (SCIO),¹⁴ Dirac insulating ferromagnetic (FM) state near 100 K,¹⁵ and quantum anomalous Hall (QAH) effect in $\text{Ba}_2\text{NiOsO}_6$.¹⁶ The A-site occupied with a transition metal in DP $\text{Mn}_2\text{FeReO}_6$ shows half-metallic ferrimagnetism with a transition temperature of 520 K above room temperature with a positive magnetoresistance behavior.¹⁷ In a few cases, Coulomb correlation is

sufficient to explore the Mott insulating state in AFM systems such as $\text{Ca}_2\text{MgOsO}_6$ and $\text{Sr}_2\text{MgOsO}_6$.¹⁸ Based on density functional theory (DFT) calculations, it was reported that the Mott insulating state of $\text{Sr}_2\text{NiOsO}_6$, $\text{Sr}_2\text{FeOsO}_6$, and $\text{Sr}_2\text{NiRuO}_6$ arises as a result of electron-correlation and spin-orbit coupling (SOC).¹⁹ A study by Monte Carlo simulations on Sr_2VMoO_6 shows the dependency of blocking temperature, magnetic properties on the crystal field, the system size, and the coupling constants, and on $\text{Lu}_2\text{MnCoO}_6$, phase transitions and the magnetic stability along with exchange coupling were calculated.^{20,21}

In addition, the correlated-metal oxides, in particular, iridates and rhodates, lead to unconventional phases.^{22,23} Among them, iridate-based materials that yield various unconventional phases in cooperation with strongly correlated effects due to the strong Coulomb interaction among electrons have shown interesting features. For example, Sr_2IrO_4 ^{24,25} is reported as a Mott insulator, $\text{Ln}_2\text{Ir}_2\text{O}_7$ ²² is a topological Mott insulator, $\text{Y}_2\text{Ir}_2\text{O}_7$ ²⁶ is a topological semimetal with a Fermi-arc on the surface, $\text{Pr}_2\text{MgIrO}_6$ ²⁷ is a ferrimagnetic (FIM) Mott-Hubbard insulator, $\text{Bi}_2\text{FeIrO}_6$ ²⁸ is an FM insulator, and PrSrMgIrO_6 shows half-metallic AFM (HMAFM) with zero effective moment per unit cell.²⁹ A second-order transition and ferrimagnetism have been reported on $\text{Sr}_2\text{RuHoO}_6$ ³⁰ with the mean-field approximation (MFA) and Monte Carlo calculations.

Here, we report $\text{Ca}_2\text{CrIrO}_6$ (CCIO) and $\text{Ca}_2\text{FeIrO}_6$ (CFIO), which have no experimental or theoretical information on the magnetic transition temperature yet. For investigating the electronic and magnetic transition temperatures, we take $\text{Ca}_2\text{CrOsO}_6$ (CCOO) as a reference material, which is found to be an FIM insulator with a large Curie temperature (T_C) of 490 K.³¹ The reference material $\text{Ca}_2\text{CrOsO}_6$ was reported by some of us as an FIM insulator with a total magnetic moment $\mu_{\text{tot}} = 0.21\mu_B$ per unit cell.³² In this work, we propose $\text{Ca}_2\text{CrIrO}_6$ and $\text{Ca}_2\text{FeIrO}_6$, obtained by substituting Fe in place of Cr and Ir in place of Os, as new FIM insulators in the family of $\text{Ca}_2\text{BB}'\text{O}_6$. The materials are expected to be

suitable for spintronic device applications. To our knowledge and survey, there is no report yet on these new materials. The main motivation to explore $\text{Ca}_2\text{CrIrO}_6$ and $\text{Ca}_2\text{FeIrO}_6$ was to obtain (i) high transition temperature (T_C) above room temperature, (ii) FIM insulating ground state, and (iii) small effective moment. With electron doping, the material is expected to show new properties with rise in T_C . The associated features are expected to be important in new DP-based spintronic devices that work at room temperature. With this report, we expect that new materials can be synthesized experimentally based on this result. Here, we report the structural, electronic, and magnetic properties on the basis of DFT calculations. Section II presents the computational methods, while results and discussion are presented in Sec. III. Finally, conclusions of the research are provided in Sec. IV.

II. COMPUTATIONAL METHOD

To investigate the electronic and magnetic properties^{38,39} of the proposed materials, DFT calculations were performed with the full-potential linearized augmented plane wave method as implemented in WIEN2k code³⁵ and the all-electron full-potential local-orbital (FPLO)^{36,37} code using the standard generalized gradient approximation (GGA) of Perdew-Burke-Ernzerhof (PBE).⁴⁰ To incorporate the correlation effects, Coulomb interaction U is 4 eV for Cr, 5 eV for Fe, and 1.5 eV for Ir.^{41,42} The magnetic anisotropy energy (MAE) was calculated by a self-consistent full-relativistic mode. A set of 500 k -points was used within the full Brillouin zone, which produces a set of $8 \times 8 \times 6$ k -mesh. To consider different magnetic configurations, the monoclinic structure (space group 14) was split to lower symmetry (space group $2:P\bar{1}$) that corresponds to 20 inequivalent atoms.

III. RESULTS AND DISCUSSION

The crystal structure of Ca_2BIRo_6 shown in Fig. 1 falls in the space group $P2_1/n$ with monoclinic structure maintained by BO_6 (where $B = \text{Cr, Fe}$) and IrO_6 octahedra. The experimental lattice

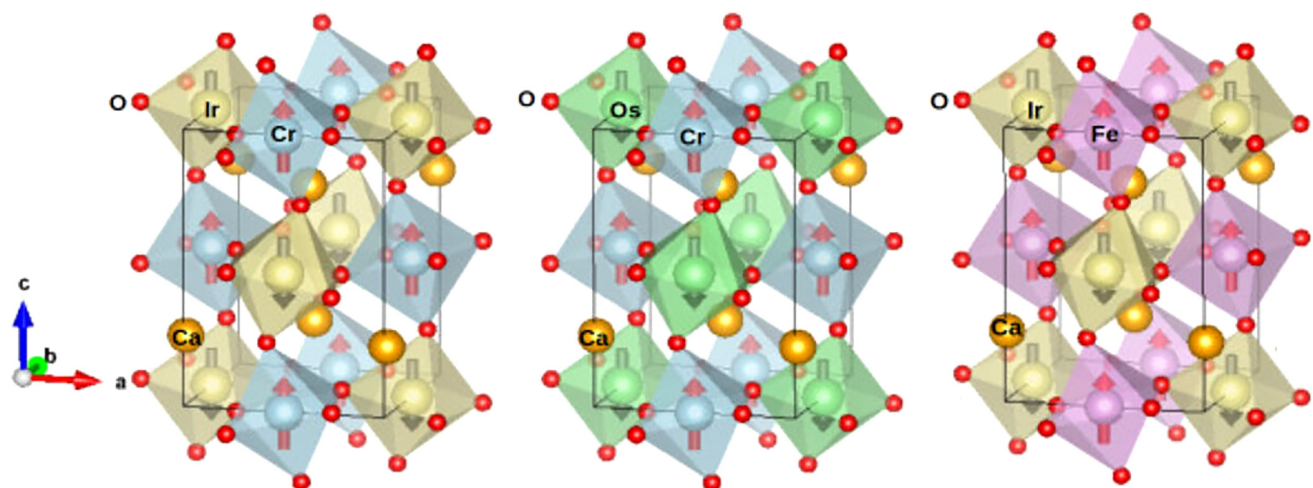


FIG. 1. Crystal structure of Ca_2BIRo_6 (gray, purple, sky blue, green, maroon, and red spheres correspond to Ca, Cr, Ir, Os, Fe, and O atoms, respectively).

parameters opted for the calculations are $a = 5.351 \text{ \AA}$, $b = 5.456 \text{ \AA}$, and $c = 7.620 \text{ \AA}$. On the basis of adaptation of the Goldschmidt tolerance factor $t = (r_A + r_O) / \sqrt{2}((r_B/2) + (r'_B/2) + r_O)$,³³ where r_A , r_B , and r'_B are the ionic radii of the respective ions and r_O is the ionic radius of oxygen, we select Fe and Ir elements for substitutions to obtain $\text{Ca}_2\text{CrIrO}_6$ and $\text{Ca}_2\text{FeIrO}_6$ structure, respectively. For the DP family, it is well known that if $t < 0.97$, the compound is either monoclinic or orthorhombic.³⁴

To check the stability of the substituted compounds, the cohesive and formation energies for both the compounds are calculated,

$$E_{For} = E_{\text{Ca}_2\text{BIR}_6}^{\text{Tot}} - [2E_{\text{Ca}}^{\text{bulk}} + E_{\text{B}}^{\text{bulk}} + E_{\text{Ir}}^{\text{bulk}} + 6E_{\text{O}}^{\text{bulk}}] \quad (1)$$

and

$$E_{\text{Coh}} = E_{\text{Ca}_2\text{BIR}_6}^{\text{Tot}} - [2E_{\text{Ca}}^{\text{iso}} + E_{\text{B}}^{\text{iso}} + E_{\text{Ir}}^{\text{iso}} + 6E_{\text{O}}^{\text{iso}}], \quad (2)$$

where B = Cr, Fe; $E_{\text{Ca}_2\text{BIR}_6}^{\text{Tot}}$ is the total energy obtained from DFT for Ca_2BIR_6 ; $E_{\text{Ca}}^{\text{bulk}}$, $E_{\text{B}}^{\text{bulk}}$, $E_{\text{Ir}}^{\text{bulk}}$, and $E_{\text{O}}^{\text{bulk}}$ are energies of the bulk of Ca, B, Ir, and O elements; and $E_{\text{Ca}}^{\text{iso}}$, $E_{\text{B}}^{\text{iso}}$, $E_{\text{Ir}}^{\text{iso}}$, and $E_{\text{O}}^{\text{iso}}$ are energies of isolated Ca, B, Ir, and O elements, respectively. The formation and cohesive energies per atom for the materials $\text{Ca}_2\text{CrIrO}_6$ and $\text{Ca}_2\text{FeIrO}_6$ are found to be -2.84 , -2.66 , -4.54 , and -4.25 eV, respectively. The negative values for both cohesive and formation energies confirm that both the materials have a thermodynamically stable structure and are possible to synthesize experimentally.

We then analyze the electronic and magnetic properties of DP. We begin our discussion starting from the magnetic ground state. For this, we first optimize the internal parameters and have

considered five types of magnetic configurations: one FM ($\text{FM1-}\uparrow\uparrow\uparrow\uparrow$), two AFM ($\text{AF1-}\uparrow\downarrow\downarrow\downarrow$, $\text{AF2-}\uparrow\downarrow\downarrow\downarrow$), and two FIM ($\text{FIM1-}\uparrow\uparrow\downarrow\downarrow$, $\text{FIM2-}\uparrow\uparrow\uparrow\downarrow$), respectively, for both the systems with an energy difference of 159 and 80 meV between FIM1 and first excited FM structure for $\text{Ca}_2\text{CrIrO}_6$ and $\text{Ca}_2\text{FeIrO}_6$, respectively. FIM1 is found to have the lowest energy for both the materials indicating the magnetic ground state with a magnetic easy axis along the [010] direction for $\text{Ca}_2\text{CrIrO}_6$ and along the [100] direction for $\text{Ca}_2\text{FeIrO}_6$, and MAE is found to be 8 and 12 meV, respectively.

In $\text{Ca}_2\text{CrIrO}_6$, within GGA, the TM Cr takes the charge state the +3 with $3d^3$ configuration and is coupled ferrimagnetically with Ir. The three d electrons of Cr go to t_{2g} states for the spin-up channel and hence remain in the valence region, while for the spin-down channel, they remain in the conduction region and the e_g state remains empty for both channels so it lies in the conduction region. For Ir, it takes charge state +5 with the d^4 configuration where three electrons go to the spin-down channel in the t_{2g} state and hence remain close to the Fermi level (E_F) in the valence region and one remaining electron goes to the t_{2g} state with spin-up forming a low spin state as seen in Fig. 2.

Likewise, in $\text{Ca}_2\text{FeIrO}_6$, Fe has five outer most electrons with a $3d^5$ configuration and has a charge state +3 and is found to be occupied in the spin-up channel and empty in the spin-down channel. Hence, the density of states (DOS) lies deep in the valence region while states in the spin-down channel lie far in the conduction region giving rise to the high spin state of Fe. In the case of Ir, it has a $5d^4$ configuration with the charge state +5. The three outermost electrons reside for the spin-down channel and hence they remain in the upper most valence region just below the Fermi level (E_F) and one remaining electron goes to the t_{2g} state giving a low

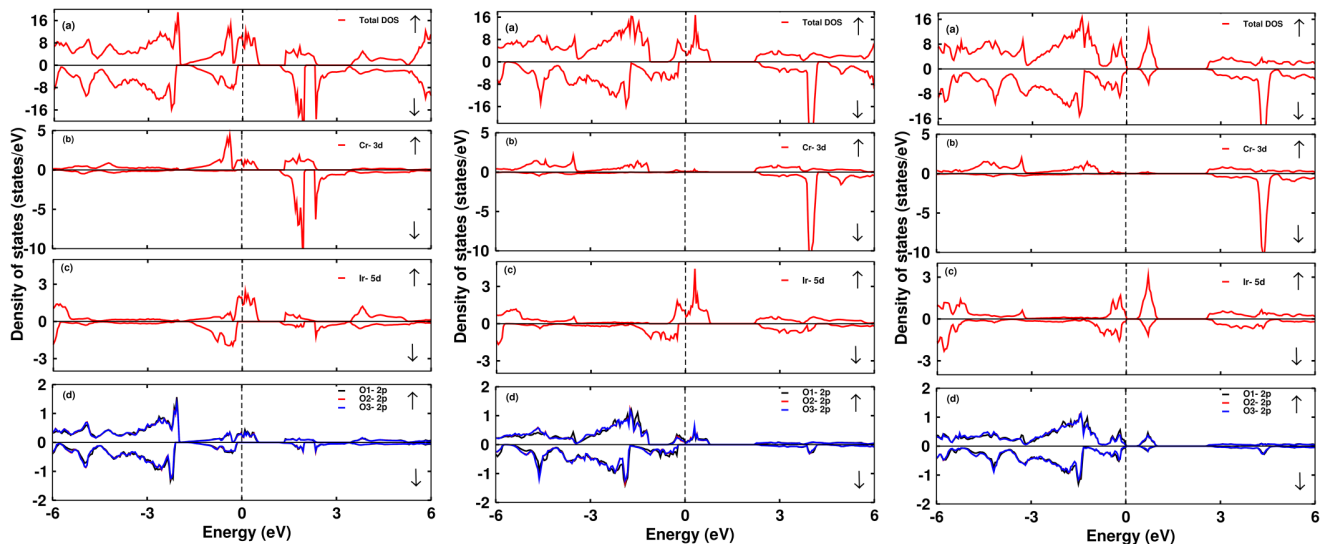


FIG. 2. The total and partial density of states (PDOS) of $\text{Ca}_2\text{CrIrO}_6$ within GGA (left), GGA + U (middle) and GGA + U + SOC functional (right), respectively. (a) Total density of states (DOS), (b) partial DOS of Cr-3d, (c) PDOS of Ir-5d, and (d) PDOS of O-2p atoms for spin-up (\uparrow) and spin-down (\downarrow) for $\text{Ca}_2\text{CrIrO}_6$. The vertical dotted line indicates $E_F = 0$.

spin state as in Fig. 3. Two unoccupied t_{2g} states are found in the conduction region represented by a peak for the spin-up channel.

The presence of $3d$ elements in the material is supposed to have a strong correlation effect, which was ignored in the calculations within GGA. Here, we extend our calculation with GGA + U taking $U = 4$ eV for Cr, 5 eV for Fe, and 1.5 eV for Ir. Since the strength of the SOC in Ir plays a significant role indicating the electronic properties, we further performed calculations with GGA + U + SOC. As expected, the metallic state transforms to the semiconducting state with bandgaps of 0.25 and 0.13 eV for Cr and Fe, respectively. After SOC, we observe a noticeable change in the Ir- $5d$ bands in which it splits near E_F as observed in DOS and band structures (see Figs. 2–4).

The spin resolved total and partial density of states (PDOS) for $\text{Ca}_2\text{CrIrO}_6$ within GGA, GGA + U , and GGA + U + SOC are shown in Figs. 2 and 3. The major contribution to the total DOS around E_F is mainly from Cr- $3d$, Ir- $5d$, and O- $2p$ states. The Ir- $5d$ states are found to play a key role indicating the electronic properties. They are found to hybridize strongly with the O- $2p$ states in both spin channels. Their hybridization occurs mostly in the valence region near E_F and in the conduction region. We observe that Ir- t_{2g} states are fully occupied in spin-down channels and thus lie in the valence region, whereas in the spin-up channel, the states being empty lie in the conduction region along with other unoccupied Ir- e_g states. This is found to be consistent with the ionic picture of Ir. The charge transfer effect is prominent between Ir- $5d$ and O- $2p$ states due to strong hybridization. This induces sizable moments in oxygen atoms, which get polarized in parallel with Ir atoms.

We further considered the magnetic behavior of $\text{Ca}_2\text{BiIrO}_6$. As tabulated in Table I, the calculated magnetic moments for Fe and Ir sites are found to be $4.12\mu_B$ and $-0.73\mu_B$, respectively. The

calculated orbital moment at the Fe site is small, that is, $0.027\mu_B$, and aligns in the same direction as the spin moment, confirming the half-filled $5d^5$ configuration of Fe in $\text{Ca}_2\text{FeIrO}_6$, which is in accordance with Hund's third rule.⁴³ The calculated orbital moment at the Ir site is found to be $-0.26\mu_B$ in a parallel direction with spin magnetic moments contributing to an effective magnetic moment of $6.66\mu_B$ per unit cell.

Moving on to $\text{Ca}_2\text{CrIrO}_6$, the spin and orbital moments for Cr are found to be $2.54\mu_B$ and $-0.1\mu_B$, respectively, and align in the antiparallel direction showing that the $3d$ orbital is either less or more than half filled. From Table I, the spin magnetic moment in Ir is slightly reduced due to the Ir-O hybridization and influence of SOC, whereas in Ir- $5d$, orbital magnetic moments are found to be $-0.28\mu_B$ in the same direction of the orbital magnetic moment of Cr, which increases the net magnetic moment to $2.59\mu_B$.

Due to the partial charge transfer from Cr, Fe, and Ir to oxygen, it also gains a sizeable moment of $0.08\mu_B$ in $\text{Ca}_2\text{CrIrO}_6$ and $0.01\mu_B$ in $\text{Ca}_2\text{FeIrO}_6$, and polarization is mainly on O- $2p$ orbitals consistent with the spin magnetization isosurface plot shown in Fig. 5. Here, the polarization is mainly found in $2p$ orbitals, and this hybridized moment in oxygen increases the resultant moment. Interestingly, the developed magnetic moments at the O site are aligned in the direction of the Ir moment, suggesting a stronger interaction among Ir-O than that of Cr-O in $\text{Ca}_2\text{CrIrO}_6$.

Further to note in Fig. 5 is that the isosurface of Cr- $3d$ states is in a dumb-bell-like shape, which is formed due to the t_{2g} orbitals. The contribution of charge distribution is due to the t_{2g} state, and to Ir, charge distribution is in the spin-down channel in t_{2g} states. Upon replacement of the Cr by Fe atom, both the t_{2g} state and the e_g state are fully occupied in the spin-up channel but remain empty in the spin-down channel. Hence, the contribution

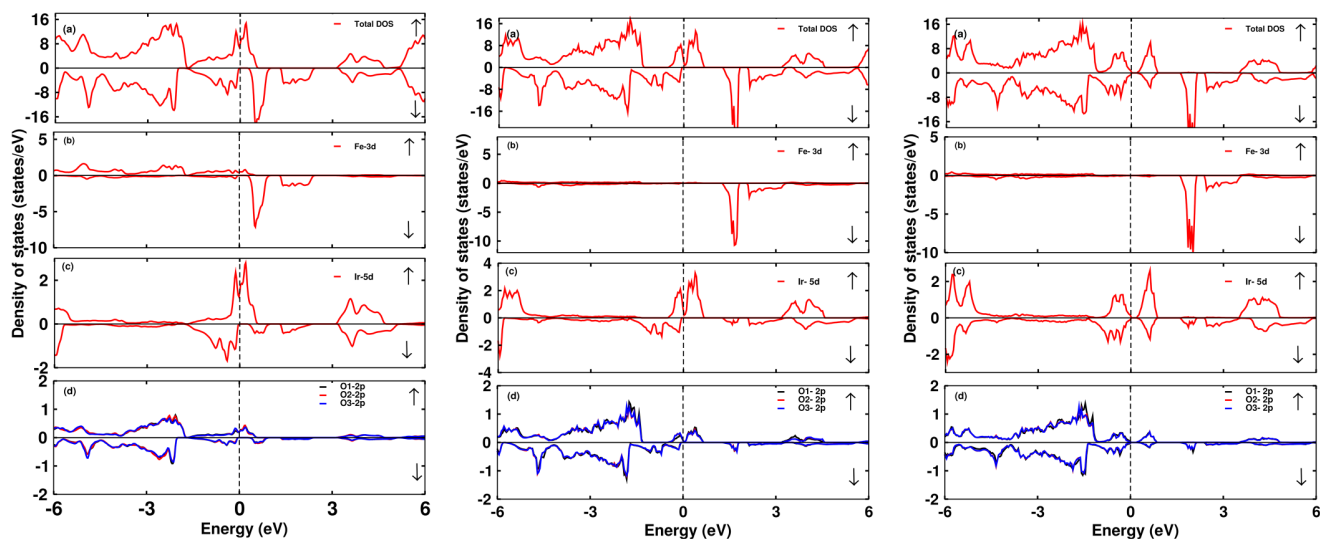


FIG. 3. The total and partial DOS of $\text{Ca}_2\text{FeIrO}_6$ within GGA (left), GGA + U (middle), and GGA + U + SOC functional (right), respectively. (a) Total density of states (DOS), (b) partial DOS of Fe- $3d$, (c) PDOS of Ir- $5d$, and (d) PDOS of O- $2p$ atoms for spin-up (\uparrow) and spin-down (\downarrow) for $\text{Ca}_2\text{FeIrO}_6$. The vertical dotted line indicates $E_F = 0$.

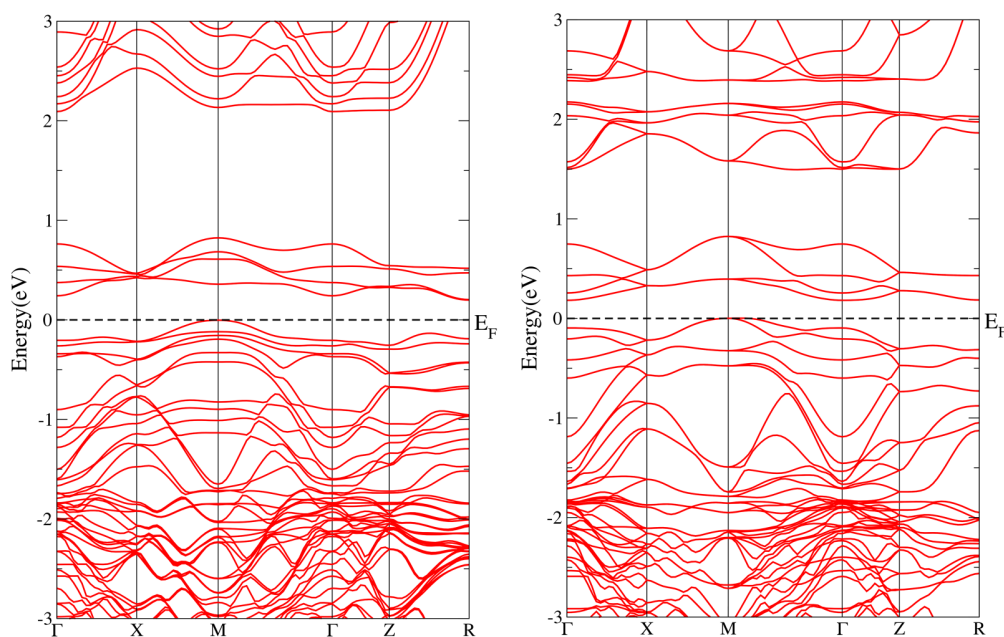


FIG. 4. The band structures of $\text{Ca}_2\text{CrIrO}_6$ (left) and $\text{Ca}_2\text{FeIrO}_6$ (right) within GGA + U + SOC. The horizontal dotted line indicates $E_F = 0$.

to the spin magnetization is by both t_{2g} and e_g states. As a result, the isosurface of Fe is spherical, and Ir contribution remains the same as in Fig. 5 (right).

In order to understand the suitability of the proposed materials, we have computed the spin-exchange coupling parameters by computing the total energy for several collinear spin configurations of Cr, Fe, and Ir and are mapped into the spin model. For the same, we utilize the exchange parameters for estimating the magnetic transition temperature based on the Heisenberg model of mean-field approximation (MFA).

The Hamiltonian for the interaction of spins can be written as

$$\hat{H} = - \sum_{i < j} J_{ij} \hat{S}_i \hat{S}_j, \quad (3)$$

where (J_{ij}) is the exchange coupling constant between spins at sites i and j , where i, j represent the atomic sites in the crystal ($S_{\text{Fe}} = 5/2$, $S_{\text{Cr}} = 3/2$, $S_{\text{Ir}} = 3/2$), as shown in Fig. 6; J_1 is for $J_{\text{Cr-Cr}}$ (in-plane); J_2 is for $J_{\text{Fe-Fe}}$ (in-plane); and J_3 is for $J_{\text{Cr-Fe}}$ (out-of-plane) with nearest neighbors of 6, 12, and 12, respectively, considered for calculations.

The estimated J parameters, description of the atoms, and respective nearest neighbors for DP $\text{Ca}_2\text{CrIrO}_6$ and $\text{Ca}_2\text{FeIrO}_6$ are shown in Table II. Our results are found to be within the limitation with GGA + U calculations, which tends to localize the orbitals decreasing the overlap between magnetic orbitals. As a result, this reduces the spin-exchange interactions and, hence, the estimation of magnetic transition temperature in the materials.

TABLE I. Calculated spin magnetic moments (in μ_B) of B (Cr/Fe), B' (Ir), three oxygen atoms, and bandgap " E_g " (eV). The calculated orbital moments at B and B' sites are shown within parentheses for $\text{Ca}_2\text{BiIrO}_6$ HM denotes the half-metallic state.

Site	$\text{Ca}_2\text{CrIrO}_6$			$\text{Ca}_2\text{FeIrO}_6$		
	GGA	GGA + U	GGA + U + SOC	GGA	GGA + U	GGA + U + SOC
B	2.12	2.55	2.54/−0.073	3.48	4.12	4.12/0.027
B'	−0.72	−0.96	−0.82/−0.284	−0.55	−0.87	−0.728/−0.263
O1	−0.08	−0.10	−0.078	0.0061	−0.038	−0.007
O2	−0.076	−0.11	−0.083	0.015	−0.023	0.003
O3	−0.072	−0.10	−0.085	0.012	−0.025	−0.009
Tot. mom.	2.0	2.0	2.59	6.0	5.99	6.66
E_g	HM	HM	0.25	HM	HM	0.13

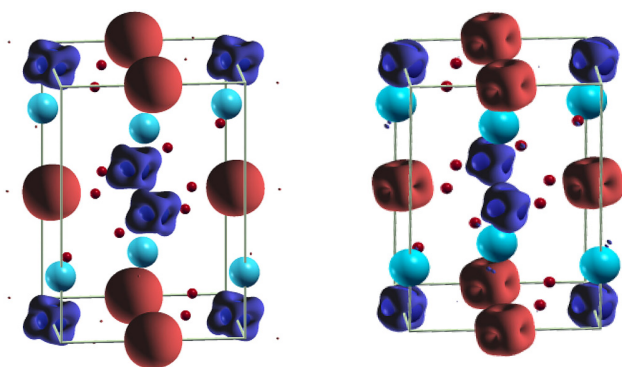


FIG. 5. Isosurface of spin magnetization density at $\pm 0.23e/\text{\AA}^3$ with red (blue) for spin-up (down): left, $\text{Ca}_2\text{FeIrO}_6$; right, material with Cr replacement $\text{Ca}_2\text{CrIrO}_6$ [royal blue, sky blue, maroon, and red colors represent Ir, Ca, Cr (Fe), and O, respectively].

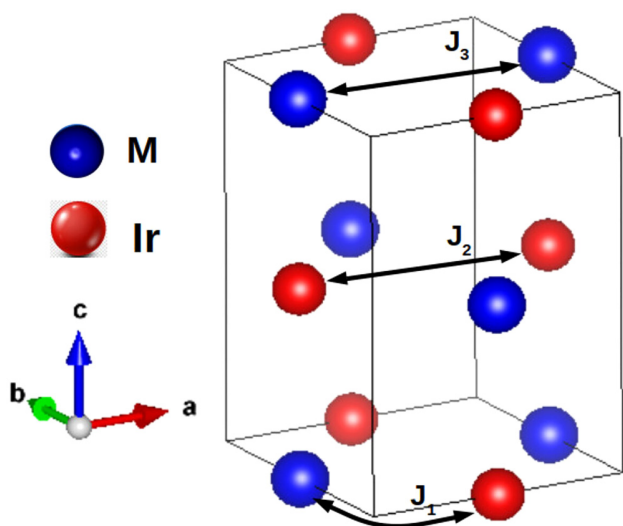


FIG. 6. Computed magnetic exchange interactions in the double perovskite configuration Ca_2MlrO_6 and $\text{Ca}_2\text{FeIrO}_6$. The atom label M in the figure refers to Cr or Fe.

TABLE II. Estimated magnetic exchange coupling parameters (in meV) for double perovskite Ca_2MlrO_6 , M = Cr/Fe.

Interaction	Description	Nearest neighbor	Distance	
			M = Cr	M = Fe
J_1	M–Ir	6	–3.21	–3.55
J_2	Ir–Ir	12	–4.25	–0.8
J_3	M–M	12	5.85	–0.32

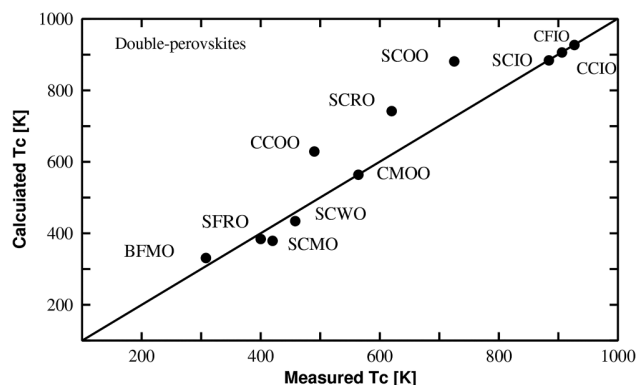


FIG. 7. Calculated vs measured Curie temperatures for different double perovskites.

We have also estimated the Curie temperature of the proposed materials using the mean-field theory as

$$T_C = S_i S_j \frac{2 \sum J_{ij}}{3 K_B}, \quad (4)$$

where S_i and S_j are the spin quantum numbers at i and j sublattices, respectively. Our calculated T_C are found to be 906 and 836 K for $\text{Ca}_2\text{CrIrO}_6$ and $\text{Ca}_2\text{FeIrO}_6$, respectively. As shown in Fig. 7, we have compared the measured and calculated Curie temperatures. Different DPs with their respective T_C presented in Fig. 7 are $\text{Ba}_2\text{FeMoO}_6$ (BFMO),⁴⁴ $\text{Sr}_2\text{FeReO}_6$ (SFRO),⁴⁴ $\text{Sr}_2\text{CrMoO}_6$ (SCMO),⁴⁵ Sr_2CrWO_6 (SCWO),⁴⁴ $\text{Ca}_2\text{CrOsO}_6$ (CCOO),^{31,46} $\text{Ca}_2\text{MnOsO}_6$ (CMOO),⁴⁶ $\text{Sr}_2\text{CrReO}_6$ (SCRO),⁴⁷ $\text{Sr}_2\text{CrOsO}_6$ (SSCO),⁴⁸ $\text{Sr}_2\text{CrIrO}_6$ (SCIO),⁴⁹ $\text{Ca}_2\text{CrIrO}_6$ (CCIO), and $\text{Ca}_2\text{FeIrO}_6$ (CFIO). By comparing the calculated T_C of the materials with a similar work as reported by Mandal *et al.*,⁴⁹ we found a decent agreement of our result though no experimental report of T_C has been studied on these materials. Our theoretical value of T_C for the studied compounds may be slightly larger than their true values in similar materials. This may happen since the mean-field theory often overestimates the T_C , and the absolute value of T_C depends on the selected U values. Nonetheless, our results are expected to give a valid T_C trend as observed in Fig. 7 for the considered compounds.⁶

IV. CONCLUSIONS

We performed density functional theory to identify the electronic, magnetic, and ordering temperatures of yet to be synthesized materials $\text{Ca}_2\text{CrIrO}_6$ and $\text{Ca}_2\text{FeIrO}_6$. We found that they are insulating in nature under the cooperative effect of Coulomb interactions and spin-orbit coupling. The effect is found to be significant in opening the bandgap. The bandgap was noted to be 0.25 eV for $\text{Ca}_2\text{CrIrO}_6$ and 0.13 eV for $\text{Ca}_2\text{FeIrO}_6$. Furthermore, we estimated the Curie temperature (T_C) that was found to be 906 and 836 K for $\text{Ca}_2\text{CrIrO}_6$ and $\text{Ca}_2\text{FeIrO}_6$, respectively, which are in a valid T_C range as in other similar compounds. Our predicted value is expected to initiate further experimental efforts to verify the interesting predictions made in this work.

ACKNOWLEDGMENTS

S.R.B. acknowledges the Nepal Academy of Science and Technology, Khumaltar, Nepal, for the Ph.D. fellowship. M.P.G. acknowledges the Alexander von Humboldt Foundation, Germany, for the equipment subsidy grants. S.K.C. acknowledges the faculty start-up grant provided by Davidson College of Engineering at San José State University. S.R.B. and M.P.G. are grateful for fruitful discussions with M. Richter and J. van den Brink of IFW Dresden. Computations were performed at IFW Dresden, Germany, and Advanced Materials Research Laboratory, Central Department of Physics, Tribhuvan University, Nepal. We are thankful to Ulrike Nitzsche for the technical assistance.

AUTHOR DECLARATIONS

Conflict of Interest

The authors have no conflicts to disclose.



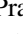

DATA AVAILABILITY

The data that support the findings of this study are available from the corresponding author upon reasonable request.

REFERENCES

- 1 K. Samanta and T. S. Dasgupta, *J. Phys. Soc. Jpn.* **87**, 041007 (2018).
- 2 R. A. de Groot, F. M. Mueller, P. G. Van Engen, and K. H. J. Buschow, *Phys. Rev. Lett.* **50**, 2024 (1983).
- 3 K. W. Lee and W. E. Pickett, *Phys. Rev. B* **77**, 115101 (2008).
- 4 M. P. Ghimire, L. H. Wu, and X. Hu, *Phys. Rev. B* **93**, 134421 (2016).
- 5 Y. P. Liu, H. R. Fuh, and Y. K. Wang, *Comput. Mater. Sci.* **92**, 63 (2014).
- 6 R. Morrow, K. Samanta, T. Saha-Dasgupta, J. Xiong, J. W. Freeland, D. Haskel, and P. M. Woodward, *Chem. Mater.* **28**, 3666 (2016).
- 7 M. T. Anderson, K. B. Greenwood, G. A. Taylor, and K. R. Poeppelmeier, *Prog. Solid State Chem.* **22**, 197 (1993).
- 8 S. Vasala and M. Karppinen, *Prog. Solid State Chem.* **43**, 1 (2015).
- 9 B. Mali, H. S. Nair, T. W. Heitmann, H. Nhalil, D. Antonio, K. Gofryk, S. R. Bhandari, M. P. Ghimire, and S. Elizabeth, *Phys. Rev. B* **102**, 014418 (2020).
- 10 K. K. Wolff, S. Agrestini, A. Tanaka, M. Jansen, and L. H. Tjeng, *Z. Anorg. Allg. Chem.* **643**, 2095 (2017).
- 11 M. Arejda, L. Bahmad, A. Abbassi, and A. Benyoussef, *Physica A* **437**, 375 (2015).
- 12 A. C. Tian, H. C. Wibowo, Z. Loye, and M. H. Whangbo, *Inorg. Chem.* **50**, 4142 (2011).
- 13 K. W. Lee and W. E. Pickett, *Phys. Rev. B* **77**, 115101 (2008).
- 14 S. Idrissi, R. Khalladi, S. Mtougui, S. Ziti, H. Labrim, I. El Housni, N. El Mekkaoui, and L. Bahmad, *Physica A* **523**, 714 (2019).
- 15 H. L. Feng, M. Arai, Y. Matsushita, Y. Tsujimoto, Y. Guo, C. I. Sathish, X. Wang, Y. H. Yuan, M. Tanaka, and K. Yamaura, *J. Am. Chem. Soc.* **136**, 3326 (2014).
- 16 H.-S. Lu and G.-Y. Guo, *Phys. Rev. B* **100**, 054443 (2019).
- 17 A. Hossain, P. Bandyopadhyay, and S. Roy, *J. Alloys Compd.* **740**, 414 (2018).
- 18 Y. Yuan, H. L. Feng, M. P. Ghimire, Y. Matsushita, Y. Tsujimoto, J. He, M. Tanaka, Y. Katsuya, and K. Yamaura, *Inorg. Chem.* **54**, 3422 (2015).
- 19 W. Song, E. Zhao, J. Meng, and Z. Wu, *J. Chem. Phys.* **130**, 114707 (2009).
- 20 M. El Yadari, L. Bahmad, A. El Kenz, and A. Benyoussef, *J. Alloys Compd.* **579**, 86 (2013).
- 21 S. Sidi Ahmed, M. Boujnah, L. Bahmad, A. Benyoussef, and A. El Kenz, *Chem. Phys. Lett.* **685**, 191 (2017).
- 22 D. Pesin and L. Balents, *Nat. Phys.* **6**, 376 (2010).
- 23 M. P. Ghimire, R. K. Thapa, D. P. Rai Sandeep, T. P. Sinha, and X. Hu, *J. Appl. Phys.* **117**, 063903 (2015).
- 24 B. J. Kim, H. Jin, S. J. Moon, J.-Y. Kim, B.-G. Park, C. S. Leem, J. Yu, T. W. Noh, C. Kim, S.-J. Oh, J.-H. Park, V. Durairaj, G. Cao, and E. Rotenberg, *Phys. Rev. Lett.* **101**, 076402 (2008).
- 25 Y. Okada, D. Walkup, H. Lin, C. Dhital, T.-R. Chang, S. Khadka, W. Zhou, H.-T. Jeng, M. Paranjape, A. Bansil, Z. Wang, S. D. Wilson, and V. Madhavan, *Nat. Mater.* **12**, 707 (2013).
- 26 X. Wan, A. M. Turner, A. Vishwanath, and S. Y. Savrasov, *Phys. Rev. B* **83**, 205101 (2011).
- 27 S. J. Mugavero III, A. H. Fox, M. D. Smith, and H.-C. zur Loye, *J. Solid State Chem.* **183**, 465 (2010).
- 28 P. C. Rout and V. Srinivasan, *Phys. Rev. B* **100**, 245136 (2019).
- 29 M. P. Ghimire and X. Hu, *Mater. Res. Express* **3**, 106107 (2016).
- 30 A. Nid-bahami, A. El Kenz, A. Benyoussef, L. Bahmad, M. Hamedoun, and H. El Moussaoui, *J. Magn. Magn. Mater.* **417**, 258 (2016).
- 31 R. Morrow, J. R. Soliz, A. J. Hauser, J. C. Gallagher, M. A. Susner, M. D. Sumption, A. A. Aczel, J. Yan, F. Yang, and P. M. Woodward, *J. Solid State Chem.* **238**, 46 (2016).
- 32 S. R. Bhandari, D. K. Yadav, B. P. Belbase, M. Zeeshan, B. Sadhukhan, D. P. Rai, R. K. Thapa, G. C. Kaphle, and M. P. Ghimire, *RSC Adv.* **10**, 16179 (2020).
- 33 H. P. S. Correa, I. P. Cavalcante, D. O. Souza, E. Z. Santos, M. T. D. Orlando, H. Belich, F. J. Silva, E. F. Medeiro, J. M. Pires, J. L. Passamai, L. G. Martinez, and L. Rossi, *Ceramica* **56**, 193 (2010).
- 34 D. Serrate, J. M. D. Teresa, and M. R. Ibarra, *J. Phys.: Condens. Matter* **19**, 023201 (2007).
- 35 P. Blaha, K. Schwarz, G. K. H. Madsen, D. Kvasnicka, and J. Luitz, *WIEN2k, An Augmented Plane Wave Plus Local Orbitals Program for Calculating Crystal Properties* (Technische Universität Wien, Vienna, 2001), ISBN: 3-9501031-1-2.
- 36 K. Koepf and H. Eschrig, *Phys. Rev. B* **59**, 1743 (1999).
- 37 See <https://www.FPLO.de> for detail information about the full-potential local-orbital minimum-basis code.
- 38 S. R. Bhandari, R. K. Thapa, and M. P. Ghimire, *J. Nepal Phys. Soc.* **3**, 89 (2015).
- 39 M. Rafique, S. Young, and H. Tan, *Physica E* **88**, 115 (2017).
- 40 J. P. Perdew, K. Burke, and M. Ernzerhof, *Phys. Rev. Lett.* **77**, 3865 (1996).
- 41 A. I. Liechtenstein, V. I. Anisimov, and J. Zaanen, *Phys. Rev. B* **52**, R5467 (1995).
- 42 V. I. Anisimov, F. Aryasetiawan, and A. I. Liechtenstein, *J. Phys.: Condens. Matter* **9**, 767 (1997).
- 43 C. Kittel, *Introduction to Solid State Physics*, 8th ed. (Wiley, Hoboken, NJ, 2005).
- 44 D. Serrate, J. M. De Teresa, and M. R. Ibarra, *J. Phys.: Condens. Matter* **19**, 023201 (2007).
- 45 A. Arulraj, K. Ramesha, J. Gopalkrishna, and C. N. N. Rao, *J. Solid State Chem.* **155**, 233 (2000).
- 46 N. Zu, R. Li, and R. Ai, *J. Magn. Magn. Mater.* **467**, 145 (2018).
- 47 H. Kato, T. Okuda, Y. Okimoto, Y. Oikawa, T. Kamiyama, and Y. Tokura, *Phys. Rev. B* **69**, 184412 (2004).
- 48 Y. Krockenberger, K. Mogare, M. Reehuis, M. Tovar, M. Jansen, G. Vaitheeswaran, V. Kanchana, F. Bultmark, A. Delin, F. Wilhelm, A. Rogalev, A. Winkler, and L. Alff, *Phys. Rev. B* **75**, 020404 (2007).
- 49 T. K. Mandal, C. Felser, M. Greenblatt, and J. Kubler, *Phys. Rev. B* **78**, 134431 (2008).

Re-entrant spin reorientation transition and Griffiths-like phase in antiferromagnetic $\text{TbFe}_{0.5}\text{Cr}_{0.5}\text{O}_3$

Bhawana Mali ^{1,*}, Hari Krishnan S. Nair,² T. W. Heitmann,³ Hariharan Nhalil,^{1,†} Daniel Antonio,⁴ Krzysztof Gofryk ⁴, Shalika Ram Bhandari ^{5,6}, Madhav Prasad Ghimire ^{5,6} and Suja Elizabeth¹

¹Department of Physics, Indian Institute of Science, Bangalore 560012, India

²Department of Physics, 500 W. University Ave., The University of Texas at El Paso, Texas 79968, USA

³The Missouri Research Reactor, University of Missouri, Columbia, Missouri 65211, USA

⁴Idaho National Laboratory, Idaho Falls, Idaho 83415, USA

⁵Central Department of Physics, Tribhuvan University, Kirtipur, 44613 Kathmandu, Nepal

⁶IFW Dresden, Helmholtzstr. 20, D-01069 Dresden, Germany



(Received 14 January 2020; revised 17 June 2020; accepted 24 June 2020; published 13 July 2020)

The perovskite $\text{TbFe}_{0.5}\text{Cr}_{0.5}\text{O}_3$ shows two anomalies in its magnetic susceptibility at $T_N = 257$ K and $T_{\text{SR}} = 190$ K which are, respectively, the antiferromagnetic and spin-reorientation transition that occur in the Fe/Cr sublattice. Magnetic susceptibility of this compound reveals canonical signatures of a Griffiths-like phase: a negative deviation from the ideal Curie-Weiss law and in less-than-unity power-law susceptibility exponents. Neutron-diffraction data analysis confirms two spin-reorientation transitions in this compound. The first one from Γ_2 (C_x, G_y, F_z) to Γ_4 (A_x, F_y, G_z) occurs at $T_N = 257$ K and a second one from Γ_4 (A_x, F_y, G_z) to Γ_2 (C_x, G_y, F_z) at $T_{\text{SR}} = 190$ K in the $Pnma$ space-group setting. The Γ_2 (C_x, G_y, F_z) structure is stable down to 7.7 K, leading to an ordered moment of $3.34(1) \mu_B/\text{Fe}^{3+}(\text{Cr}^{3+})$. In addition to the long-range magnetic order, experimental indication of diffuse magnetism is observed in neutron-diffraction data at 7.7 K. Tb develops a ferromagnetic component along the z axis at 20 K. Thermal conductivity and spin-phonon coupling of $\text{TbFe}_{0.5}\text{Cr}_{0.5}\text{O}_3$ studied through Raman spectroscopy are also presented in the paper. The magnetic anomalies at T_N and T_{SR} do not appear in the thermal conductivity of $\text{TbFe}_{0.5}\text{Cr}_{0.5}\text{O}_3$, which appears to be robust up to 9 T. On the other hand, they are revealed in the temperature dependence of full-width-at-half-maximum curves derived from Raman intensities. An antiferromagnetic structure with $\uparrow\downarrow\uparrow\downarrow$ arrangement of Fe/Cr spins is found as the ground state through first-principles energy calculations, supporting the experimentally determined magnetic structure at 7.7 K. The spin-resolved total and partial density of states show that $\text{TbFe}_{0.5}\text{Cr}_{0.5}\text{O}_3$ is insulating with a band gap of ~ 0.12 (2.4) eV within GGA (GGA+ U) functionals.

DOI: [10.1103/PhysRevB.102.014418](https://doi.org/10.1103/PhysRevB.102.014418)

I. INTRODUCTION

Rare-earth orthoferrites and orthochromites with the general formula RMO_3 , where R = rare earth or yttrium and M = Fe or Cr, crystallize in the perovskite structure (usually $Pnma$ space group) with orthorhombic distortion and an antiferromagnetic ground state [1]. Rare-earth orthoferrites possess a complex spin structure and have drawn considerable attention due to their unique physical properties [1] and potential applications such as ultrafast magneto-optical recording [2], laser-induced thermal spin reorientation (SR) [3], precision excitation induced by terahertz pulses [4], inertia-driven spin switching [5], and magnetism-induced multiferroicity [6]. Most orthoferrites are G-type canted antiferromagnets with a weak ferromagnetic (FM) component due to Dzyaloshinskii-Moriya interaction and show temperature-induced SR from one magnetic symmetry to another. In $R\text{FeO}_3$, exchange interactions between $\text{Fe}^{3+}-\text{Fe}^{3+}$, $R^{3+}-\text{Fe}^{3+}$, and $R^{3+}-R^{3+}$ play

an important role in determining complex magnetic structures. Isotropic $\text{Fe}^{3+}-\text{Fe}^{3+}$ exchange interaction determines the magnetic structure of Fe^{3+} spins below the antiferromagnetic ordering temperature. An exchange field due to the Fe^{3+} moment polarizes the R^{3+} spins of the R sublattice and the $\text{Fe}^{3+}-R^{3+}$ interaction, in turn, generating effective fields on Fe^{3+} spins which undergo SR transition and align perpendicular to the R^{3+} spins. The SR transition might be continuous or abrupt depending on the R element [7].

In TbFeO_3 , an unusual incommensurate magnetic phase was discovered [8] and it was shown that the exchange of spin waves between extended topological defects could result in novel magnetic phases which draws parallels with the Yukawa forces that mediate between protons and neutrons in a nucleus. The Fe^{3+} moments in TbFeO_3 exhibit $A_xF_yG_z$ ($Pn'ma'$) spin configuration at room temperature [9–11] which is accompanied by a SR to $C_xG_yF_z$ ($Pn'm'a$). At 3 K, another SR occurs to revert to the $A_xF_yG_z$ ($Pn'ma'$) structure. In recent years, a variety of interesting properties were achieved by substituting an Fe ion by different transition metal ions [12,13]. According to Goodenough-Kanamori rules [14], Cr^{3+} is a good choice to pair with Fe^{3+} to tune superior magnetic properties due to

*Corresponding author: bhawana@iisc.ac.in

†Present address: Department of Physics, Bar-Ilan University, Ramat-Gan 5290002, Israel.

superexchange interaction between empty e_g orbitals of Cr^{3+} and half-filled e_g orbitals of Fe^{3+} ions.

In TbCrO_3 , the exchange coupling between the nearest-neighbor Cr^{3+} is predominantly antiferromagnetic and the Cr^{3+} spins order spontaneously at $T_N = 167$ K [15]. Below this temperature, it exhibits weak ferromagnetism resulting from the canting of Cr^{3+} magnetic moments. In TbCrO_3 , the Cr^{3+} spin structure is G_yF_z below T_N and belongs to the Γ_2 configuration, which implies that a weak FM component of the Cr^{3+} moments orient along the z axis [16,17]. Tb^{3+} spins order antiferromagnetically at 3.05 K into a G_xA_z structure [16]. The Tb^{3+} spin system adopts a C_xF_z structure, which belongs to Γ_4 representation, in the temperature range 3.05 K $< T < T_N$ and is coupled to the ordered Cr^{3+} spins [16]. Spin reorientation, magnetization reversal, and weak ferromagnetism are often seen in similar compounds, for example, $\text{TbFe}_{0.5}\text{Mn}_{0.5}\text{O}_3$ [18], while a reentrant SR transition is reported in $\text{TbFe}_{0.75}\text{Mn}_{0.25}\text{O}_3$ [19] which transforms from Γ_4 to Γ_1 and subsequently to Γ_4 . The magnetic structures and SR transitions of the mixed orthochromite–orthoferrite perovskites $R\text{Fe}_{0.5}\text{Cr}_{0.5}\text{O}_3$, where $R = \text{Tb}, \text{Dy}, \text{Ho}, \text{Er}$ have recently been reported [20].

In this paper, we present a comprehensive understanding of the magnetism of $\text{TbFe}_{0.5}\text{Cr}_{0.5}\text{O}_3$ through magnetic susceptibility, neutron powder diffraction, Raman scattering, and thermal conductivity experiments in conjunction with density-functional-theory calculations. Our results support a reentrant SR transition, Griffiths-like phase features, and a coexisting diffuse magnetic component below the T_N .

II. METHODS

A. Experimental

Polycrystalline $\text{TbFe}_{0.5}\text{Cr}_{0.5}\text{O}_3$ was prepared by a standard solid-state reaction using high purity ($\geq 3N$) Tb_4O_7 , Fe_2O_3 , and Cr_2O_3 in stoichiometric amounts. The starting materials were thoroughly mixed and sintered at 1200 °C for 48 h with two stages of intermediate grinding. Phase purity of the sintered sample was verified by taking powder x-ray diffractograms using a Rigaku Smartlab x-ray diffractometer with $\text{Cu K}\alpha$ radiation ($\lambda = 1.548$ Å). Oxidation states of Fe and Cr ions were determined using x-ray photoelectron spectroscopy (XPS) in an AXIS Ultra spectrometer, and the data were analyzed using CASA XPS spectroscopy software [21]. Chemical composition analysis of the samples were performed using a JEOL–JXA–8530F electron probe micro analyzer, which yielded the Fe:Cr atomic ratio as 0.48:0.50 (Fe/Cr = 0.96). Temperature-dependent DC magnetization measurements were performed on sintered pellets using a commercial magnetic property measurement system (Quantum Design) in the temperature range of 5 K $\leq T \leq 400$ K at 100 Oe and 500 Oe in both zero-field-cooled (ZFC) and field-cooled (FC) protocols. Additionally, high-temperature magnetic susceptibility was recorded up to 800 K in the high-temperature vibrating sample magnetometer (VSM) oven option of a physical property measurement system (PPMS). The thermal conductivity of a parallelepiped sample of $\text{TbFe}_{0.5}\text{Cr}_{0.5}\text{O}_3$ was measured in the temperature range 2 K–300 K in 0 T and 9 T magnetic field using a commercial PPMS.

To investigate the nuclear and magnetic structure of $\text{TbFe}_{0.5}\text{Cr}_{0.5}\text{O}_3$, neutron powder diffraction experiments were performed at University of Missouri Research Reactor using the diffractometer, PSD. Patterns were collected at 350 K, 300 K, 215 K, 100 K, 20 K and 7.7 K on a 2 g powder sample using neutrons of wavelength 1.485 Å. The neutron-diffraction data were analyzed using the Rietveld method [22] coded in the FullProf suite of programs [23]. Magnetic representations belonging to the $Pnma$ symmetry were determined using the software *SARAh* [24] and the corresponding magnetic structure was refined using FullProf. Raman spectra was recorded from 110 K to 300 K temperature range in the backscattering geometry by using a HORIBA JOBIN–YVON spectrometer with a 633-nm laser as an excitation source. Low temperature was maintained by a closed cycle He–cryostat attached to spectrometer.

B. Computational details

The electronic and magnetic structure calculations were performed by means of density-functional-theory (DFT) approach using the full-potential linearized augmented plane wave plus local orbital method as implemented in the WIEN2k code [25]. The nonoverlapping muffin–tin sphere radii (R_{MT}) of 2.35, 2.0, 1.96, and 1.72 Bohr were used for Tb, Fe, Cr, and O, respectively. The linear tetrahedron method with 500 k points was employed for the reciprocal-space integrations in the whole Brillouin zone (BZ) that corresponds to 216 k points within the irreducible BZ. For the calculations, the standard generalized gradient approximation (GGA) in the parametrization of Perdew *et al.* was used [26]. To consider the strong correlation effects, GGA+ U functional with double-counting corrections according to Anisimov *et al.* [27] was used. The chosen values of U were 6 eV for Tb–4*f*, 5 eV for Fe–3*d*, and 3 eV for Cr–3*d* states, which are comparable to the values found in literature [28–33]. Calculations were performed using the lattice parameters obtained from neutron-diffraction data at 7.7 K (see Table I). The energy and charge convergence was set to 10^{-6} Ry and 10^{-4} of an electron, respectively, for self-consistent calculations. To obtain the magnetic ground states, we have considered five magnetic configurations by computing their total energies: They are ferromagnetic (FM– $\uparrow\uparrow\uparrow\uparrow$), two antiferromagnetic (AFM1– $\uparrow\downarrow\uparrow\downarrow$ and AFM2– $\uparrow\downarrow\downarrow\uparrow$), and two ferrimagnetic (FIM1– $\uparrow\downarrow\downarrow\downarrow$ and FIM2– $\uparrow\uparrow\uparrow\downarrow$). Here, the spin arrangements for two inequivalent atoms each of Fe and Cr atoms are arranged as Fe1, Fe2, Cr1, and Cr2, respectively.

III. RESULTS AND DISCUSSION

A. X-ray photoelectron spectroscopy

Core-level XPS measurements at room temperature using an Al $K\alpha$ x-ray source was performed to determine the valence states of cations in $\text{TbFe}_{0.5}\text{Cr}_{0.5}\text{O}_3$. Since the valence state of elements plays a crucial role in determining the magnetic ground states of a compound, it is important to identify the same. Figure 1 shows the experimental intensities along with the peak fits. The core-level binding energy was calibrated with carbon (B.E = 284.8 eV). The Cr 2*p*_{3/2} peak at 576.5 eV is close to the binding energy of Cr_2O_3 (576 eV)

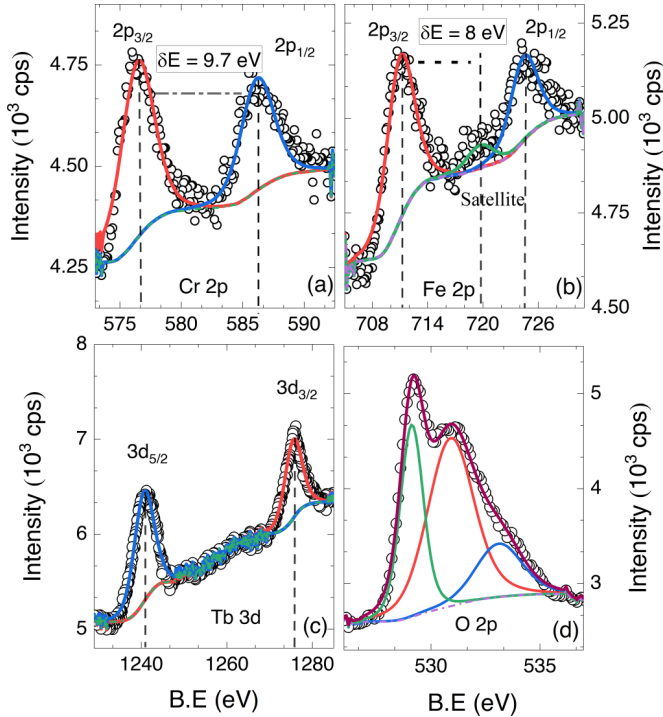


FIG. 1. X-ray photoelectron spectra of (a) Cr 2*p*, (b) Fe 2*p*, (c) Tb 3*d*, and (d) O 2*p* are shown in open circles. Solid lines are fitted peaks, deconvoluted components and background, respectively, in each graph. Oxidation state of 3+ is inferred for Fe, Cr, and Tb from this data.

[34]. However, the $2p_{3/2}$ peaks of Fe^{2+} and Fe^{3+} in oxides appear around 710.3 eV and 711.4 eV, respectively [35]. In $\text{TbFe}_{0.5}\text{Cr}_{0.5}\text{O}_3$, the peak at 711 eV is close to the binding energy value of Fe^{3+} . Additionally, a satellite peak at 8 eV above the Fe $2p_{3/2}$ confirms the Fe^{3+} state (Fe^{2+} gives a

satellite peak at 6 eV above the main peak). The XPS spectra of Tb $3d_{5/2}$ yields a peak at 1240.8 eV which is very close to that of Tb_2O_3 (1241.2 eV) [36]. Our XPS results thus indicate 3+ oxidation states in Tb, Fe, and Cr.

B. Magnetic properties: Spin reorientation and Griffiths-like phase

Figure 2(a) shows the temperature-dependent magnetization, $M(T)$, of $\text{TbFe}_{0.5}\text{Cr}_{0.5}\text{O}_3$ under ZFC and FC protocols at 100 Oe and 500 Oe (inset). Two anomalies occur in the $M(T)$ curve at ≈ 257 K and at 190 K. A bifurcation of the ZFC and FC curves is seen below ≈ 15 K. With the application of 500 Oe, the bifurcation vanishes [inset of Fig. 2(a)]. The magnetic phase transition temperatures of $\text{TbFe}_{0.5}\text{Cr}_{0.5}\text{O}_3$ are determined as $T_{\text{SR}} = 190$ K and $T_N = 257$ K by plotting dM/dT vs T as shown in the top inset of Fig. 2(b). The temperature-dependent inverse magnetic susceptibility, $\chi^{-1}(T)$, of $\text{TbFe}_{0.5}\text{Cr}_{0.5}\text{O}_3$ up to 800 K under 500 Oe is plotted in the main panel of Fig. 2(b) along with a curve fit using the Curie-Weiss (CW) law, shown by a red solid line. The equation $\chi^{-1} = (T - \theta)/C$, where, $C = N_A \mu_{\text{eff}}^2 / 3k_B$ is the Curie constant, N_A is the Avogadro's number, μ_{eff} is the effective magnetic moment, k_B is the Boltzmann constant, and θ is the CW temperature used for the fit [37]. The CW analysis yields an effective magnetic moment of $\mu_{\text{eff}} = 10.3(2) \mu_B$ and CW constant, $\theta = -40.4(2)$ K. By taking 3+ oxidation states for Tb, Fe, and Cr determined from the XPS analysis, the theoretical magnetic moment μ_{th} in the paramagnetic region was calculated using $\mu_{\text{th}} = \sqrt{\mu_{\text{Tb}}^2 + 0.5\mu_{\text{Cr}}^2 + 0.5\mu_{\text{Fe}}^2} = 10.9 \mu_B$ by considering the high-spin state of Tb^{3+} ($\mu_{\text{Tb}} = 9.7 \mu_B$), Fe^{3+} ($\mu_{\text{Fe}} = 5.9 \mu_B$), and Cr^{3+} ($\mu_{\text{Cr}} = 3.9 \mu_B$).

A downward deviation of inverse magnetic susceptibility from the ideal CW law description is a signature of Griffith's phase (GP) [38–40]. The characteristic temperature at which the inverse susceptibility deviates from the CW behavior is

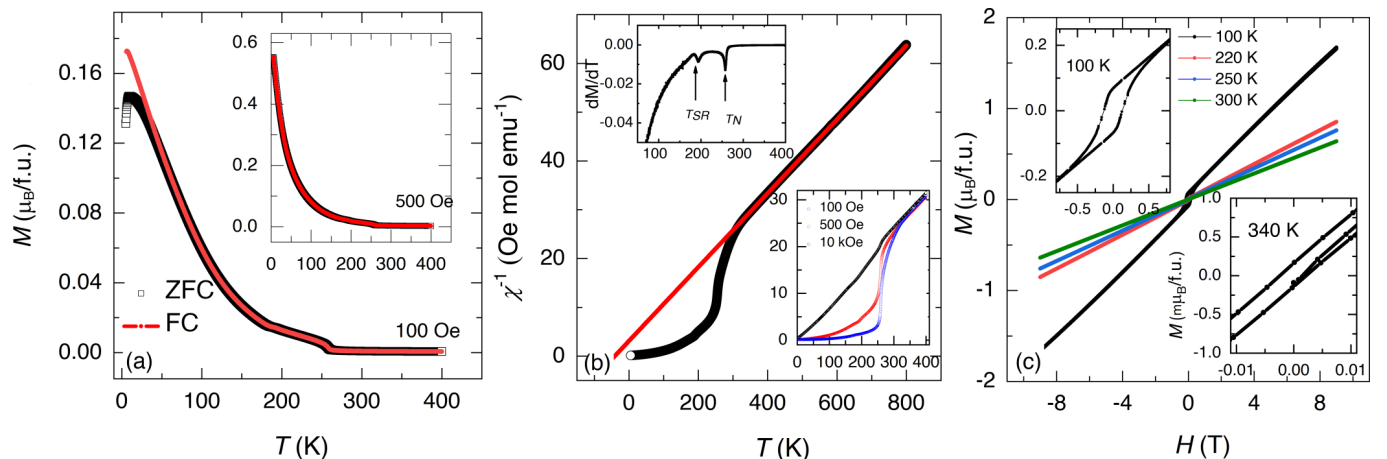


FIG. 2. (a) Magnetization $M(T)$ at 100 Oe shows a bifurcation of ZFC and FC curves and anomalies at $T_N \approx 257$ K and $T_{\text{SR}} \approx 190$ K. The inset shows the magnetization at 500 Oe. (b) Inverse susceptibility, $\chi^{-1}(T)$, at 500 Oe along with Curie-Weiss fit (red solid line). The upper inset shows the derivative dM/dT to identify the anomalies at T_N and T_{SR} . The lower inset shows the inverse magnetic susceptibility at 100 Oe, 500 Oe, and 10 kOe, which shows that the negative curvature vanishes at higher fields. (c) The magnetization isotherms, $M(H)$, at 100 K, 220 K, 250 K, and 300 K. A weak hysteresis that develops below the T_{SR} is shown in the upper inset for $T = 100$ K and the lower inset shows a magnified view of an isotherm above the T_N , at $T = 340$ K.

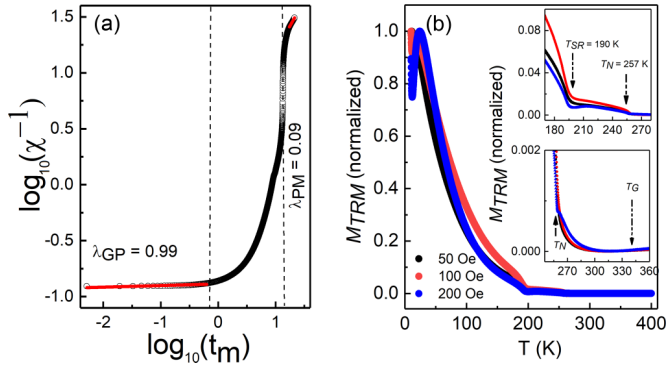


FIG. 3. (a) Power-law fit (red solid lines) to $\chi^{-1}(T)$ at 100 Oe is plotted in a log-log scale. $t_m = (T/T_c^R - 1)$ is the reduced-temperature. (b) Thermoremanent magnetization, M_{TRM} , measured at 50 Oe, 100 Oe, and 200 Oe cooling fields, shows the onset of spin reorientation transition T_{SR} and the antiferromagnetic T_N . The lower and upper insets show magnified regions near the T_N and T_{SR} , respectively.

known as the Griffiths temperature, T_G . Such a deviation of the inverse susceptibility from CW law above T_N at $T_G \approx 340$ K can be seen in Fig. 2(b). The downturn softens with increase in applied magnetic field as can be seen in the lower inset of Fig. 2(b), and supports the presence of Griffiths-like phase.

Figure 2(c) shows the magnetization isotherms of $\text{TbFe}_{0.5}\text{Cr}_{0.5}\text{O}_3$ at 100 K, 220 K, 250 K, 300 K, and 340 K measured up to ± 9 T, which do not reveal strong FM features. However, at 100 K, an opening of the magnetic hysteresis loop is observed at low applied field values [upper left inset of Fig. 2(c)]. A magnified view of the isotherm at 340 K ($>T_N$) shown in the lower inset of Fig. 2(c) reveals weak hysteresis that might be suggestive of the presence of short-range magnetism above T_N .

We noted earlier that the softening of the downturn in $\chi^{-1}(T)$ with increasing applied field supported a GP-like scenario [41–43]. At high magnetic fields, the sample gets strongly polarized and hence softens the downturn in $\chi^{-1}(T)$ seen at lower fields. GP consists of finite-size FM clusters in a paramagnetic matrix well above the transition temperature in which the spins are ferromagnetically correlated within those clusters. However, the magnetic system as a whole does not have long-range order in GP, thus, no spontaneous magnetization will appear. In GP, the FM clusters will appear with variable sizes, having local FM ordering due to which magnetization becomes nonanalytic; magnetic susceptibility will follow a power-law behavior in the low-field region [38,41,42] given by $\chi^{-1} \propto (T - T_c^R)^{1-\lambda}$, where T_c^R is the critical temperature of the FM clusters. Here susceptibility tends to deviate from CW law and λ ($0 \leq \lambda \leq 1$) is the exponent which signifies the deviation from CW behavior due to the formation of magnetic clusters in the paramagnetic (PM) state above the transition temperature. A power-law fit using the above-mentioned equation was administered on the magnetic susceptibility of $\text{TbFe}_{0.5}\text{Cr}_{0.5}\text{O}_3$ plotted as $\log_{10}(\chi^{-1})$ versus $\log_{10}(T/T_c^R - 1)$ in both PM and GP regions as shown in Fig. 3(a). Since the value of λ is highly sensitive to T_c^R , we have proceeded to estimate the value of T_c^R accurately [42,44]. Since the critical temperature of FM clusters, T_c^R , is always

greater than the transition temperature, we first estimated the value of T_c^R in the purely PM region. This yields a value of 18 K which was later used in the curve fitting for the GP regime to obtain $\lambda = 0.99(6)$. In the high-temperature region, we obtained λ as 0.09(4) which signifies that the system is in PM phase, following the CW behavior. The values for λ are consistent with the GP model, signifying a Griffiths singularity in $\text{TbFe}_{0.5}\text{Cr}_{0.5}\text{O}_3$.

Since the total magnetic susceptibility in the GP region contains contributions from both PM as well as short-range correlated regions, the downturn observed in the inverse magnetic susceptibility from ideal CW law is not expected to be sharp in the case of antiferromagnetically correlated regions. In RFeO_3 , five outer shell electrons of Fe^{3+} are in half-filled e_g (σ -bond component) and t_{2g} (π -bond component) orbitals, resulting in superexchange interactions that are antiferromagnetic. In the case of Cr^{3+} , superexchange interactions in the half-filled $t^3\text{-O-t}^3$ induce antiferromagnetism. Since Fe^{3+} and Cr^{3+} are randomly distributed in the lattice of $\text{TbFe}_{0.5}\text{Cr}_{0.5}\text{O}_3$, it results in the stabilization of both FM and antiferromagnetic couplings.

To confirm the GP-like scenario in antiferromagnetic $\text{TbFe}_{0.5}\text{Cr}_{0.5}\text{O}_3$, we employed thermoremanent magnetization, M_{TRM} , protocol to measure magnetization. Such a protocol has been used widely to study spin glass [45]. The protocol involves cooling a sample from well above the magnetic transition temperature in the presence of a magnetic field. The field is then switched off below T_c , and the magnetization measured upon warming in zero-field conditions. The thermoremanent magnetization M_{TRM} will exhibit a sharp upturn at the transition temperature. In the present case of $\text{TbFe}_{0.5}\text{Cr}_{0.5}\text{O}_3$, this protocol was repeated for three different cooling fields, 50 Oe, 100 Oe, and 200 Oe. The zero-field measurements performed here have the advantage that the contributions from the PM susceptibility are suppressed compared to an in-field measurement. Figure 3(b) shows $M_{TRM}(T)$ measured as per the above descriptions. A clear signature of the GP-like phase is seen in the form of an upturn in magnetization at a temperature well above T_N . The T_G obtained from thermoremanent measurement is 342 K, which is close to the value of 340 K, estimated from magnetic susceptibility earlier.

C. Thermal conductivity and Raman spectroscopy

Figure 4(a) shows the thermal conductivity, $\kappa_l(T)$, of $\text{TbFe}_{0.5}\text{Cr}_{0.5}\text{O}_3$ measured in zero and in an applied magnetic field of 9 T. The overall magnitude and temperature dependence of the thermal conductivity suggest that the lattice thermal transport is dominant in this material. As can be seen from the figure, there is no appreciable change in $\kappa_l(T)$ with the application of 9 T. The relatively low value of $\kappa_l(T)$ supports the presence of disorder giving rise to the observed Griffiths-like phase. In the context of the atomic disorder in UZr^2 and its impact on heat transport behavior, it is helpful to compare the measured thermal conductivity to the theoretically achievable minimum of the lattice contribution (fully disordered structure). In this model, the $\kappa_{l(\min)}(T)$ dependence can be calculated under Debye approximation by assuming that the transverse and longitudinal acoustic

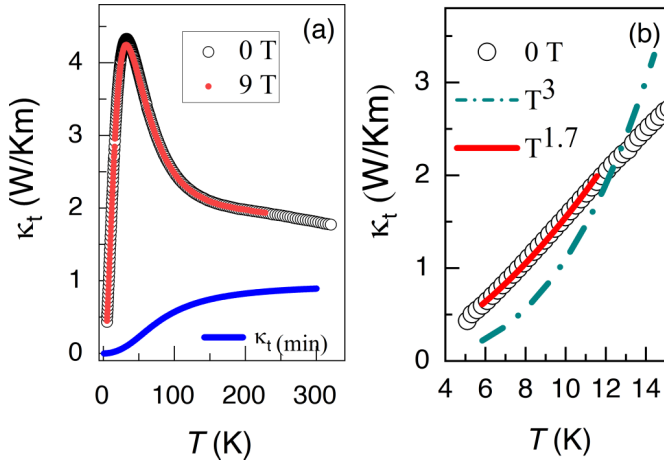


FIG. 4. (a) The variation of thermal conductivity, $\kappa_t(T)$ of $\text{TbFe}_{0.5}\text{Cr}_{0.5}\text{O}_3$ as a function of temperature. As seen, there is no appreciable change in $\kappa_t(T)$ with the application of 9 T. The magnetic anomalies at T_N and T_{SR} seen in the derivative of magnetization are not observed in $\kappa_t(T)$ or in the derivative (not shown). The blue solid line represents the minimum thermal conductivity (see text). (b) Solid and dashed lines represent $T^{1.7}$ and T^3 dependencies of $\kappa_t(T)$, respectively.

phonon modes are indistinguishable [46]. The results obtained for $\text{TbFe}_{0.5}\text{Cr}_{0.5}\text{O}_3$ using the Debye temperature, $\theta_D = 380$ K [47], and the number of atoms per unit volume, $n = 4.7528 \text{ m}^{-3}$, are shown in Fig. 4(a) by a blue solid line. The magnetic anomalies that occur at T_N and T_{SR} (seen in the derivative of magnetization) are absent in the derivative of $\kappa_t(T)$ (not shown here). In general, the behavior of $\kappa_t(T)$ of $\text{TbFe}_{0.5}\text{Cr}_{0.5}\text{O}_3$ is similar to the thermal conductivity in other $R\text{FeO}_3$ compounds like YFeO_3 , GdFeO_3 and DyFeO_3 [48]. However, in the work by Zhao *et al.* [48], single-crystal samples of orthoferrites were studied in the milli-Kelvin temperature range and in external magnetic fields up to 14 T. In earlier studies on GdFeO_3 and DyFeO_3 , magnetic anomalies were also reflected in the thermal conductivity [49,50]. Significantly low c -axis thermal conductivity was observed in YFeO_3 , GdFeO_3 , and DyFeO_3 . Considering that the present sample is polycrystalline, we observe higher values of thermal conductivity in $\text{TbFe}_{0.5}\text{Cr}_{0.5}\text{O}_3$. The total thermal conductivity could be compared to the T^3 boundary scattering limit of phonons [51]. In Fig. 4(b), the temperature dependence of the T^3 form of $\kappa_t(T)$ is shown as a dashed line. The solid line is a fit to $\kappa_t(T) \propto T^n$, where n is varied as a free parameter. A value of 1.7(3) was obtained for n . The $\kappa_t(T)$ of DyFeO_3 showed a weak curvature at low temperature (below 3 K) which is attributed to a magnonic contribution of Dy spin system [50]. Such a concave structure is not readily observed in the present case, however, there seems to be an indication near 2 K.

Raman spectroscopy was carried out at different temperatures to understand the phonon behavior across the magnetic anomalies seen in the susceptibility of $\text{TbFe}_{0.5}\text{Cr}_{0.5}\text{O}_3$. Raman spectra was recorded from 110 K to 300 K as shown in Fig. 5 (top panel) with the most intense mode assignment matching with $R\text{FeO}_3$ [52] and $R\text{CrO}_3$ [53]. $\text{TbFe}_{0.5}\text{Cr}_{0.5}\text{O}_3$ is an orthorhombically distorted perovskite with $Pnma$ space-

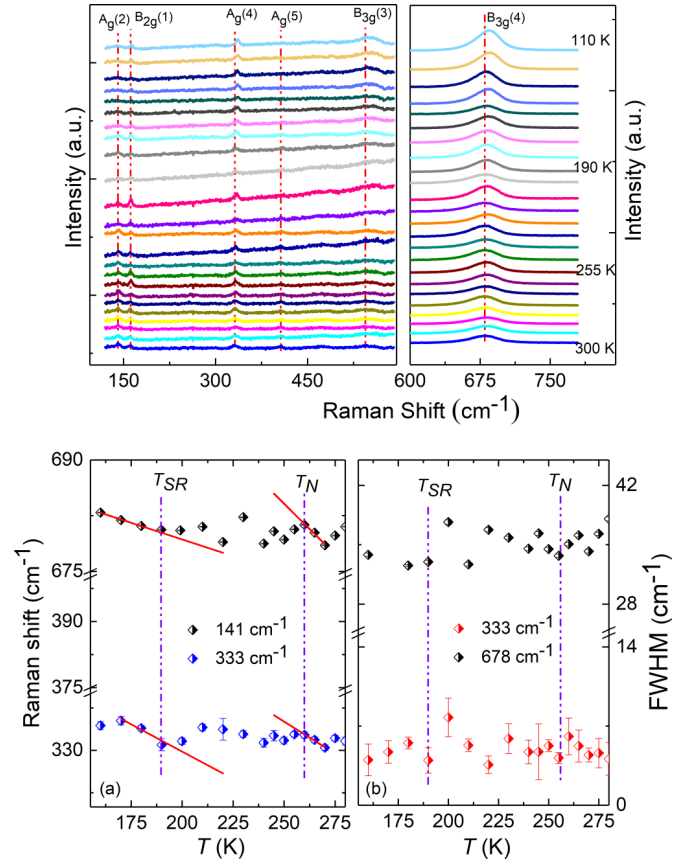


FIG. 5. Top panel: Raman spectrum of $\text{TbFe}_{0.5}\text{Cr}_{0.5}\text{O}_3$ as a function of temperature. The most intense phonon modes are assigned. Lower panel: (a) Temperature dependence of phonon frequency obtained from the fit of the spectral profile with Lorentzian function is shown. Red solid line is a fit using the anharmonic function, Eq. (1). (b) Temperature dependence of phonon linewidth. Vertical violet dashed lines in (a) and (b) mark the positions of T_N and T_{SR} .

group symmetry. The irreducible representations corresponding to the phonon modes at the BZ center [54] can be defined as $\Gamma = 7A_g + 5B_{1g} + 7B_{2g} + 5B_{3g} + 8A_u + 10B_{1u} + 8B_{2u} + 10B_{3u}$. Here, 24 ($7A_g + 5B_{1g} + 7B_{2g} + 5B_{3g}$) are the Raman active modes, 25 ($9B_{1u} + 7B_{2u} + 9B_{3u}$) are the infrared modes, A_u is an inactive mode, and three ($B_{1u} + B_{2u} + B_{3u}$) are acoustic modes. Among them, the modes which are above 300 cm^{-1} are related to the vibrations of oxygen, the modes below 200 cm^{-1} are associated with the rare-earth ions, and in the intermediate frequency range vibration patterns involve both ions [55]. However, the Raman vibrational modes corresponding to an orthorhombic structure are $A_g + B_{2g}$ and $2B_{1g} + 2B_{3g}$, which are symmetric and antisymmetric modes, respectively. In contrast, $A_g + 2B_{2g} + B_{3g}$, $2A_g + 2B_{1g} + B_{2g} + B_{3g}$, and $3A_g + B_{1g} + 3B_{2g} + B_{1g}$ are associated with the bending modes, rotation and tilt modes of the octahedra, and for the-rare earth vibrations, respectively [56]. Raman modes generally shift to low frequency as the temperature increases, accompanied by a monotonic increase in FWHM [57]. This is mainly due to the expansion of the lattice as thermal energy increases. Absence of any extra peak indicates that the spectral symmetry remains the same at all measured

temperatures, confirming that the magnetic anomalies are not associated with any structural phase transition. We analyzed the well-resolved Raman modes in detail, using a Lorentzian function. The temperature dependence of the phonon frequencies of modes $A_g(2)$ (141 cm^{-1}), $A_g(4)$ (333 cm^{-1}), and $B_{3g}(4)$ (678 cm^{-1}) along with the fit assuming a standard anharmonic dependence [58] of phonon modes are shown in Fig. 5(a).

The anharmonic dependence of the modes is given by

$$\omega_{\text{anh}}(T) = \omega_0 - C \left(1 + \frac{2}{(e^{\hbar\omega/k_B T} - 1)} \right). \quad (1)$$

Here ω_0 is temperature-independent part of linewidth, C is a constant determined from the fitting, $\hbar\omega$ is the phonon energy, and k_B is the Boltzmann constant. The deviation in the phonon frequency from anharmonic dependence near T_N and T_{SR} can be clearly seen in Fig. 5(a). Magnetostriction can also give rise to similar anomalous behavior in phonon frequency by modifying the unit cell volume [57]. But in that case, FWHM remains unchanged as it corresponds to phonon lifetime, which is not affected by subtle change in lattice volume caused by magnetostriction. But, from Fig. 5(b), it can be seen that FWHM abruptly drops near the magnetic-transition temperatures. The anomalous change in the mode frequencies and linewidths near the magnetic transition establishes the spin-phonon coupling in $\text{TbFe}_{0.5}\text{Cr}_{0.5}\text{O}_3$. Similar signatures of spin-phonon coupling were reported in RCrO_3 [53] and $\text{DyFe}_{0.5}\text{Cr}_{0.5}\text{O}_3$ [59]. The possible coupling mechanism involved is the phonon modulation of superexchange integral below the magnetic ordering temperature [60].

D. Neutron diffraction: Reentrant spin reorientation and short-range spin correlations

The macroscopic magnetic measurements (Sec. III B) on $\text{TbFe}_{0.5}\text{Cr}_{0.5}\text{O}_3$ explicitly suggest the antiferromagnetic ordering at T_N , the possibility of a SR transition at T_{SR} , and the presence of Griffiths-like phase. We now proceed to investigate $\text{TbFe}_{0.5}\text{Cr}_{0.5}\text{O}_3$ in detail using neutron scattering to understand the SR process and to ascertain the magnetic structures above and below the T_{SR} . For this purpose, neutron-diffraction experiments were carried out on powder samples of $\text{TbFe}_{0.5}\text{Cr}_{0.5}\text{O}_3$ at various temperatures in the range, 7.7 K to 350 K. The experimental neutron diffraction patterns at 300 K, 215 K, 100 K, 20 K, and 7.7 K are shown in Figs. 6(a)–6(e) (red circles). Orthoferrites adopt an orthorhombic structure as observed in a variety of $\text{RFe}_{0.5}\text{Cr}_{0.5}\text{O}_3$ [20]. For $R = \text{Tb}, \text{Dy}, \text{Ho}, \text{and Er}$, $\text{RFe}_{0.5}\text{Cr}_{0.5}\text{O}_3$ adopts a distorted orthorhombic structure and order antiferromagnetically below about 270 K in $F_y G_z$ configuration compatible with the Γ_4 representation.

They also exhibit a SR transition from $F_y G_z$ (Γ_4) to $G_y F_z$ (Γ_2). If the cations order crystallographically, the perovskite may adopt a doubled unit cell with monoclinic $P2_1/n$ space group [61]. In $\text{TbFe}_{0.5}\text{Cr}_{0.5}\text{O}_3$, Rietveld analysis of the diffraction data at 350 K with $P2_1/n$ space group resulted in

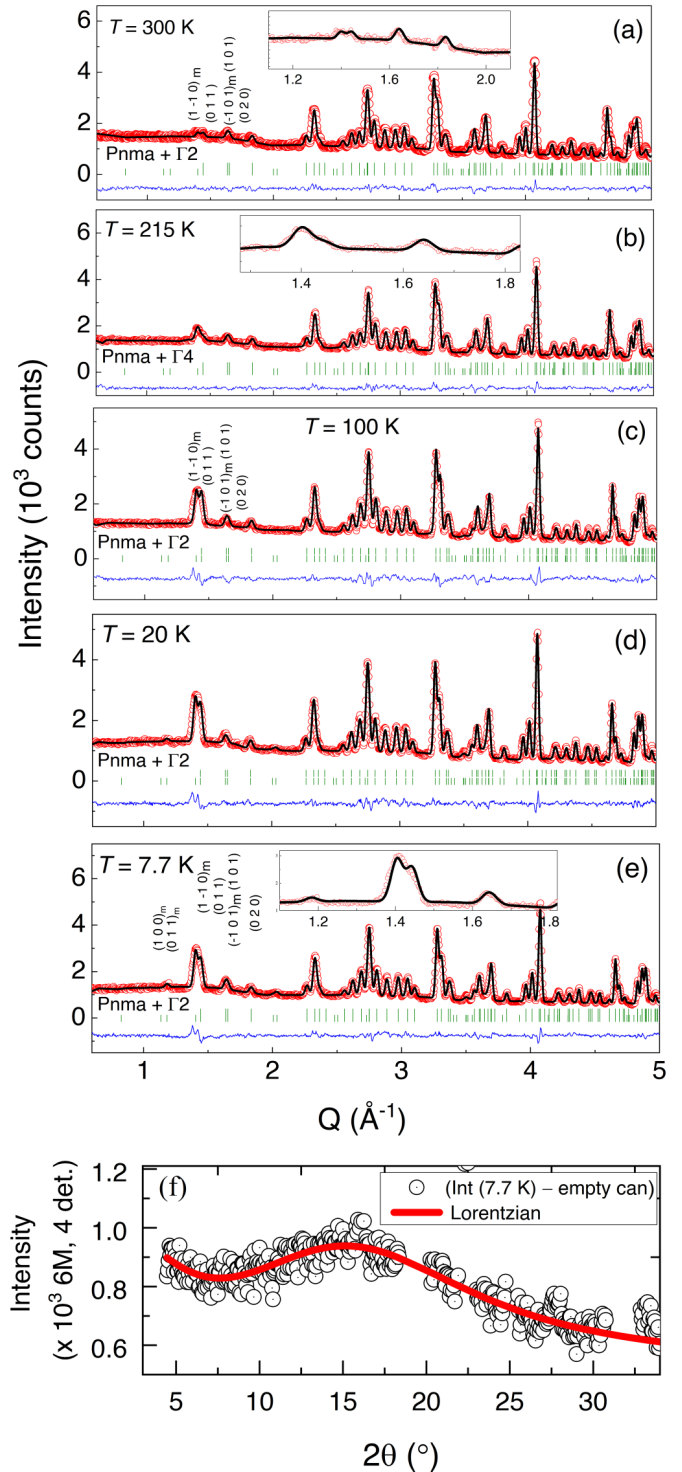


FIG. 6. (a)–(e) Rietveld refinement of the neutron powder diffraction patterns of $\text{TbFe}_{0.5}\text{Cr}_{0.5}\text{O}_3$ at 300 K, 215 K, 100 K, 20 K, and 7.7 K. There is a weak magnetic contribution even at 300 K which is above the T_N , observed in magnetometry. A magnified view of the low- Q region is provided in the inset of (a), (b), and (e). (f) Diffuse scattering intensity at 7.7 K, after subtracting the contribution from the empty can, along with a curve fit (solid line) using a Lorentzian function.

TABLE I. Structural parameters and selected bond distances and bond angles of $\text{TbFe}_{0.5}\text{Cr}_{0.5}\text{O}_3$ at different temperatures obtained from neutron diffraction. The nuclear space group is $Pnma$ where the atomic positions are Tb $4c$ (x, y, z), Cr/Fe $4b$ ($0.5, 0, 0.5$), and O $4c$ and $8d$ (x, y, z). Long (l) and short (s) bond lengths correspond to M -O(2) bonds in the ac plane. Medium (m) bond length corresponds to the out-of-plane M -O(1) apical bond.

	350 K	300 K	215 K	100 K	20 K	7.7 K
a (Å)	5.5532(4)	5.5554(6)	5.5511(6)	5.5449(1)	5.5404(1)	5.5392(1)
b (Å)	7.6097(6)	7.6108(6)	7.6035(5)	7.5977(6)	7.5936(3)	7.5919(3)
c (Å)	5.3104(8)	5.3125(0)	5.3097(3)	5.3128(4)	5.3139(2)	5.3127(3)
Fe(Cr)-O1 (m) (Å)	1.9875(6)	1.9879(1)	1.9860(4)	1.9847(3)	1.9834(3)	1.9830(1)
Fe(Cr)-O2 (l) (Å)	2.0114(2)	2.0122(1)	2.0107(5)	2.0094(2)	2.0079(2)	2.0075(1)
Fe(Cr)-O2 (s) (Å)	1.9923(1)	1.9931(6)	1.9918(4)	1.9918(0)	2.0005(2)	2.0001(5)
Fe(Cr)-O1-Fe(Cr)(°)	146.3(4)	146.3(3)	146.3(2)	146.2(5)	146.3(2)	146.3(2)
Fe(Cr)-O2-Fe(Cr)(°)	147.3(1)	147.3(1)	147.3(1)	147.3(1)	146.5(1)	146.5(1)

$R_p = 3.52$, $R_{wp} = 4.61$, $R_{exp} = 2.82$, $\chi^2 = 2.67$; whereas $R_p = 2.99$, $R_{wp} = 3.89$, $R_{exp} = 2.82$, $\chi^2 = 1.9$ were obtained for $Pnma$. The R factor indicates a reasonably good fit with $Pnma$. However, the intensity of the nuclear Bragg peak position (101) was not fully accounted for. Even at 350 K, an appreciable contribution from magnetic scattering toward the total scattered intensity was observed as shown in the Supplemental Material, Fig. S1 [62].

To determine the magnetic structure, we scrutinized the symmetry-allowed magnetic structures for $R\text{FeO}_3$ compounds in $Pnma$ space group. There exists eight irreducible representations, Γ_1 through Γ_8 , listed in Kovalev tables coded in the software *SARAh* are given in Table II. For the $4b$ Wyckoff position, the configurations Γ_5 to Γ_8 are incompatible with a net magnetic moment on the Fe [1]. The k -search utility in FullProf was used to obtain the propagation vector of the magnetic structure. Irreducible representation analysis using $k = (0,0,0)$ leads to four possibilities, $\Gamma_1(Pnma)$, $\Gamma_2(Pn'm'a)$, $\Gamma_3(Pnm'a')$, and $\Gamma_4(Pn'ma')$. Using Bertaut's notation, these four magnetic space groups can be written as $G_x C_y A_z$, $C_x G_y F_z$, $F_x A_y C_z$, $A_x F_y G_z$, respectively, corresponding to magnetic ordering of the Cartesian components of M^{3+} spins in unit cell. But Γ_3 is not consistent with the observed strong antiferromagnetic coupling between nearest Fe neighbours.

Subsequently, *SARAh* was used to obtain the magnetic representations of the allowed magnetic structures. After test-

TABLE II. The possible magnetic structures of $R\text{FeO}_3$ allowed for $Pnma$ and $Pbnm$ symmetry, where G denotes (+ - +), F (+ + +), A (+ - -), C (+ + -), O (0000). x, y , and z denote orientations parallel to the crystallographic directions a, b , and c .

Irreps	$Pnma$		$Pbnm$			
	Space group	$4b$	$4c$	space group	$4b$	$4c$
Γ_1	$Pnma$	$G_x C_y A_z$	C_y	$Pbnm$	$A_x G_y C_z$	C_z
Γ_2	$Pn'm'a$	$C_x G_y F_z$	$C_x F_z$	$Pbn'm'$	$F_x C_y G_z$	$F_x C_y$
Γ_3	$Pnm'a'$	$F_x A_y C_z$	$F_x C_z$	$Pb'nm'$	$C_x F_y A_z$	$C_x F_y$
Γ_4	$Pn'ma'$	$A_x F_y G_z$	F_y	$Pb'n'm$	$G_x A_y F_z$	F_z
Γ_5	$Pn'm'a'$	$O_x O_y O_z$	$A_x G_z$	$Pb'n'm'$	$O_x O_y O_z$	$G_x A_y$
Γ_6	$Pnma'$	$O_x O_y O_z$	A_y	$Pb'nm$	$O_x O_y O_z$	A_z
Γ_7	$Pn'ma$	$O_x O_y O_z$	G_y	$Pbn'm$	$O_x O_y O_z$	G_z
Γ_8	$Pnm'a$	$O_x O_y O_z$	$G_x A_z$	$Pbnm'$	$O_x O_y O_z$	$A_x G_y$

ing the different possible magnetic representations along with the nuclear phase in $Pnma$, a better visual fit to the experimental data with reasonable agreement factors were obtained for Γ_2 , and was accepted as the solution of the magnetic structure at 350 K (not shown here). The goodness-of-fit for the magnetic refinement, R_{mag} , for the three representations are as follows: $\Gamma_1 = 25.4$, $\Gamma_4 = 95.2$, $\Gamma_2 = 17.4$. A comparison of the refinement results for all the allowed representations are given in the Supplemental Material, Fig. S2 [63]. Figure 6(a) shows the neutron diffraction patterns at 300 K along with the refinement patterns using $Pnma$ nuclear space group and the magnetic structure according to Γ_2 representation. The nuclear space group of $\text{TbFe}_{0.5}\text{Cr}_{0.5}\text{O}_3$ at all temperatures down to 7.7 K was found to be $Pnma$. The refined values of the lattice and bond parameters at different temperatures are given in Table I. Here, three different M -O bond lengths are listed. Long (l) and short (s) bond lengths correspond to M -O(2) bonds in the ac plane while the medium (m) bond length corresponds to the out-of-plane M -O(1) apical bond length which is almost parallel to the b axis.

As understood from the $M(T)$ data presented in Fig. 2(a), an anomaly occurs in $\text{TbFe}_{0.5}\text{Cr}_{0.5}\text{O}_3$ at $T_N = 257$ K. Refinement of the diffraction pattern suggests that the magnetic structure is Γ_4 ($Pn'ma'$) at 215 K, implying that the magnetic structure changes from $\Gamma_2 \rightarrow \Gamma_4$ at T_N . The refined neutron-diffraction pattern at 215 K is shown in Fig. 6(b). A second SR transition back to Γ_2 ($Pn'm'a$) is observed at 100 K. This temperature is below T_{SR} (190 K), which is identified through the derivative of magnetization curve. Further, the Γ_2 magnetic structure remains stable down to 7.7 K. The refined magnetic moment values obtained at 7.7 K are $\text{Fe}^{3+}/\text{Cr}^{3+}$: $0.13(1) \mu_B$ (m_x), $3.19(4) \mu_B$ (m_y), and $1.27(1) \mu_B$ (m_z); and $\text{Tb}^{3+} = 1.14(2) (m_x)$. A detailed table of magnetic moments at different temperatures is provided in the Supplemental Material, Table S1 [64]. In Fig. 6(f), the neutron-diffraction pattern of $\text{TbFe}_{0.5}\text{Cr}_{0.5}\text{O}_3$ at 7.7 K is presented after subtracting the contribution from the empty vanadium can sample holder. The broad feature at low scattering angles lends support to the presence of short-range magnetic order in $\text{TbFe}_{0.5}\text{Cr}_{0.5}\text{O}_3$. Our attempt to analyze the diffuse intensity by fitting it to a Lorentzian curve is shown as a red solid line in Fig. 6(f). A spin-spin correlation length of approximately 9 Å is estimated.

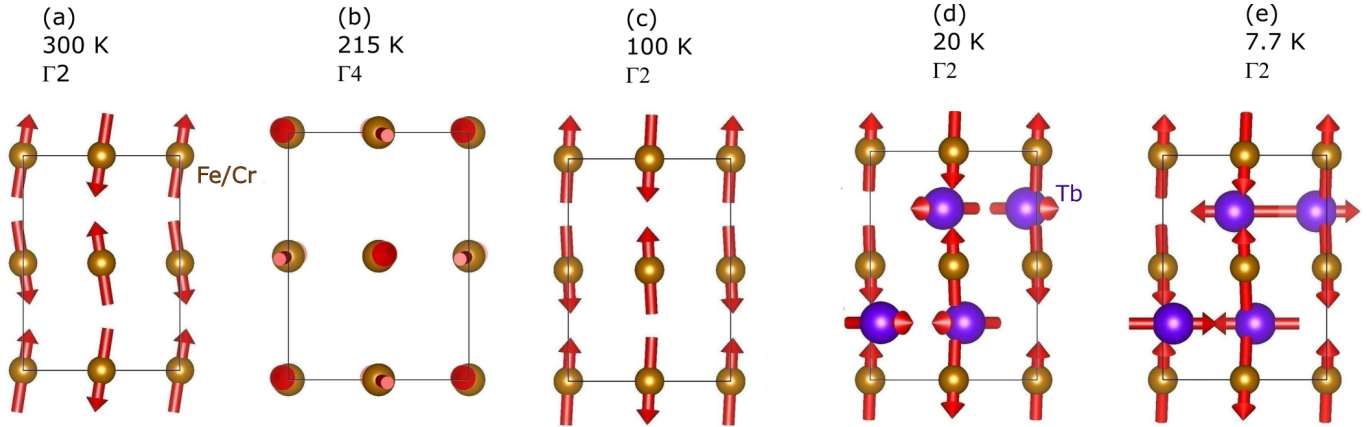


FIG. 7. The magnetic structure of $\text{TbFe}_{0.5}\text{Cr}_{0.5}\text{O}_3$ at (a) 300 K (Γ_2), (b) 215 K (Γ_4), and (c) 100 K (Γ_2). The Γ_2 structure remains stable down to 7.7 K, which was the lowest probed temperature by neutrons in this study. (d), (e) The magnetic structure at 20 K and 7.7 K, respectively (magnetic moment of Tb^{3+} is multiplied by three to make it visible).

Further, the magnetic rare earth in $R\text{Fe}_{0.5}\text{Cr}_{0.5}\text{O}_3$ is reported to develop magnetic ordering at low temperatures below 15 K [20]. Our refinement of diffraction data at 20 K is consistent with the picture that Tb^{3+} moments are magnetically ordered in C_xF_z structure with a FM component along the z axis and only C_x part remains till 7.7 K. It is reported in a recent work [20] on $\text{TbFe}_{0.5}\text{Cr}_{0.5}\text{O}_3$ that only the C_y (for $Pbnm$ space group) part remains whereas the FM interactions disappear with the SR at 1.9 K. As a result, diffuse magnetic scattering features emerge; this is well captured in our work as can be seen in Fig. 6(f). Direct observation of diffuse scattering in the neutron-diffraction signal suggests the presence of short-range ordering of the Tb^{3+} moments. The magnetic structures of the transition-metal and rare-earth moments as a function of temperature are shown in Fig. 7.

E. Density-functional-theory calculations

From the total energy calculations for five different collinear magnetic configurations, AFM1 ($\uparrow\downarrow\uparrow\downarrow$) is found to be the most stable with the lowest energy. The AFM1 spin structure is found to be consistent with our experimental observation for the Γ_2 state at 7.7 K. Similarly, the first excited AFM2 configuration is consistent with the spin structure for the Γ_4 state at 300 K whose total energy is ~ 36 meV per formula unit higher compared to the AFM1 state of $\text{TbFe}_{0.5}\text{Cr}_{0.5}\text{O}_3$. The order of relative stability of the magnetic states are AFM1 > AFM2 > FIM2 > FIM1 > FM. This may be an indication of the competing ground state between AFM1 and AFM2 observed as a GP transition from Γ_2 to Γ_4 and, subsequently, the reentrant to Γ_2 phase as seen in Fig. 7. The magnetic anisotropy energy calculated is ~ 4.68 meV per formula unit of $\text{TbFe}_{0.5}\text{Cr}_{0.5}\text{O}_3$ with in-plane easy axes. In $\text{TbFe}_{0.5}\text{Cr}_{0.5}\text{O}_3$, the lanthanide Tb takes the charge state

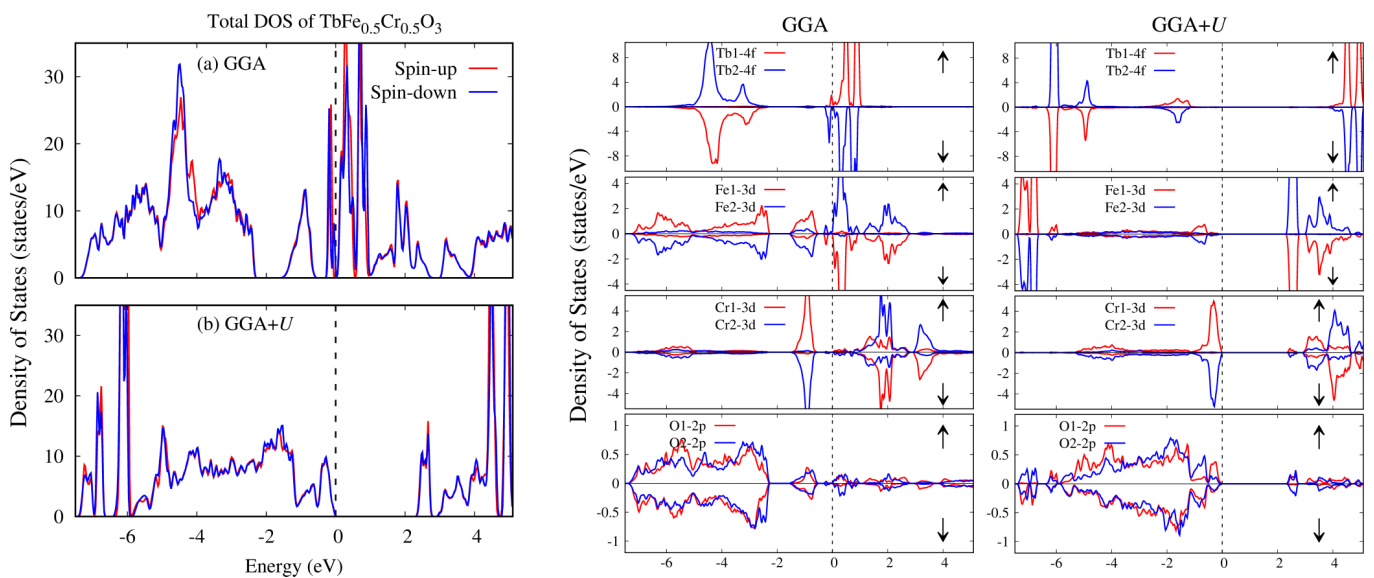


FIG. 8. Total and partial DOS of $\text{TbFe}_{0.5}\text{Cr}_{0.5}\text{O}_3$ in AFM1 configuration: Total DOS within GGA (top) and GGA+ U (bottom) (left) functionals; partial DOS contributions from Tb-4 f , Fe-3 d , Cr-3 d , and O-2 p states, respectively, within GGA (middle) and GGA+ U (right) functionals for the spin-up and spin-down channels.

3+ with $4f^8$ configuration. Likewise, the transition-element Fe nominally takes the charge state 3+ with $3d^5$ and Cr with charge state 3+ should take the $3d^3$ configurations, respectively. In the stable AFM1 state, the calculated spin moment at each site of Tb, Fe, and Cr are $\pm 5.9 \mu_B$, $\pm 3.65 \mu_B$, and $\pm 2.36 \mu_B$, respectively. Their respective orbital moments are $\pm 1.03 \mu_B$, $\pm 0.05 \mu_B$, and $\mp 0.034 \mu_B$, respectively. With GGA+ U effects, the spin moment of Tb, Fe, and Cr turns out to be $\pm 5.97 \mu_B$, $\pm 4.14 \mu_B$, and $\pm 2.57 \mu_B$, respectively. The total magnetic moment compensates to zero as Tb, Fe, and Cr couples antiferromagnetically among each other as observed in Fig. 7.

We now proceed to the electronic structure of $\text{TbFe}_{0.5}\text{Cr}_{0.5}\text{O}_3$ in AFM1 state within GGA and GGA+ U , respectively. The spin-resolved total and partial density of states (DOS) are shown in Fig. 8. $\text{TbFe}_{0.5}\text{Cr}_{0.5}\text{O}_3$ is found to be insulating with a band gap of ~ 0.12 (2.4) eV within GGA (GGA + U). The correlation effects U significantly change the electronic behavior. As seen in the partial DOS, the main contributions from Tb- $4f$ states that were observed around E_F are shifting away from each other.

Those states that are fully occupied shift deep in the valence region while the unoccupied state moves far away in the conduction region. Similar features were also observed for Fe- $3d$ states around E_F . On the other hand, Cr- $3d$ states are contributing at and around E_F , hybridizing strongly with the O- $2p$ orbitals (see partial DOS in Fig. 8). This is mainly due to the hybridization between the $3d$ states of Cr and Fe with the O- $2p$ states. From the partial DOS contributions of Fe- $3d$, three t_{2g} and two e_g are fully occupied by five electrons in spin up, but in Cr- $3d$, three t_{2g} are fully occupied in the spin-up channel while e_g bands are empty.

IV. CONCLUSIONS

We observe an antiferromagnetic transition T_N at 257 K and a SR transition T_{SR} at 190 K in the orthoferrite

$\text{TbFe}_{0.5}\text{Cr}_{0.5}\text{O}_3$. Interestingly, a reentrant SR is seen in this compound, where the spins reorient again at 100 K. Through detailed neutron-diffraction experiments and analysis, we find that the spin structure changes from the Γ_2 representation at 350 K to Γ_4 at 215 K and then reverts to Γ_2 at 100 K. This structure remains stable until 7.7 K. A clear signature of GP is observed in the magnetization response of $\text{TbFe}_{0.5}\text{Cr}_{0.5}\text{O}_3$ and also short-range spin fluctuations that extend up to high temperature. $\text{TbFe}_{0.5}\text{Cr}_{0.5}\text{O}_3$ exhibits low thermal-conductivity values, suggesting disordered cation arrangement which supports the Griffiths-like phase; and is not perturbed by the application of external magnetic field up to 9 T. The magnetic anomalies at T_N and T_{SR} are not directly seen in the thermal conductivity data, but the latter is dominated by the phonon contributions. Raman spectroscopic investigation reveals clear evidence of spin-phonon coupling in this compound.

ACKNOWLEDGMENTS

The authors acknowledge the Center for Nano Science and Engineering (CeNSE), Indian Institute of Science, Bengaluru. B.M. acknowledges financial support from University Grants commission (UGC-531996), India for Senior Research fellowship (SRF). H.S.N. acknowledges a faculty start-up grant from UTEP and a Rising Stars award. Work at INL was supported by DOE's Early Career Research Program. M.P.G. acknowledges the Higher Education Reform Project (HERP DLI-7B) of Tribhuvan University, Kirtipur, Nepal for the start-up grant, and Alexander von Humboldt Foundation, Germany for the partial support as a return fellowship. S.R.B. thanks NAST, Nepal for the Ph.D. fellowship and IFW-Dresden for funding during a research stay in Germany. M.P.G. and S.R.B. thank Manuel Richter for the fruitful discussion and Ulrike Nitzsche for technical assistance.

-
- [1] R. L. White, *J. Appl. Phys.* **40**, 1061 (1969).
 - [2] A. V. Kimel, C. D. Stanciu, P. A. Usachev, R. V. Pisarev, V. N. Gridnev, A. Kirilyuk, and T. Rasing, *Phys. Rev. B* **74**, 060403(R) (2006).
 - [3] A. V. Kimel, A. Kirilyuk, A. Tsvetkov, R. V. Pisarev, and T. Rasing, *Nature* **429**, 850 (2004).
 - [4] J. Jiang, Z. Jin, G. Song, X. Lin, G. Ma, and S. Cao, *Appl. Phys. Lett.* **103**, 062403 (2013).
 - [5] A. V. Kimel, B. A. Ivanov, R. V. Pisarev, P. A. Usachev, A. Kirilyuk, and T. Rasing, *Nat. Phys.* **5**, 727 (2009).
 - [6] Y. Tokunaga, N. Furukawa, H. Sakai, Y. Taguchi, T.-H. Arima, and Y. Tokura, *Nat. Mater.* **8**, 558 (2009).
 - [7] T. Yamaguchi, *J. Phys. Chem. Solids* **35**, 479 (1974).
 - [8] S. Artyukhin, M. Mostovoy, N. P. Jensen, D. Le, K. Prokes, V. G. de Paula, H. N. Bordallo, A. Maljuk, S. Landsgesell, H. Ryll *et al.*, *Nat. Mater.* **11**, 694 (2012).
 - [9] J. E. Bourée and J. Hammann, *J. Phys. France* **36**, 391 (1975).
 - [10] E. Bertaut, J. Chappert, J. Mareschal, J. Rebouillat, and J. Sivardière, *Solid State Commun.* **5**, 293 (1967).
 - [11] J. Tejada, X. X. Zhang, A. Roig, O. Nikolov, and E. Molins, *Europhys. Lett.* **30**, 227 (1995).
 - [12] H. Taguchi, *J. Solid State Chem.* **131**, 108 (1997).
 - [13] A. Dahmani, M. Taibi, M. Nogues, J. Aride, E. Loudghiri, and A. Belayachi, *Mater. Chem. Phys.* **77**, 912 (2003).
 - [14] J. B. Goodenough, *Phys. Rev.* **100**, 564 (1955).
 - [15] J. D. Gordon, R. M. Hornreich, S. Shtrikman, and B. M. Wanklyn, *Phys. Rev. B* **13**, 3012 (1976).
 - [16] E. Bertaut, J. Mareschal, and G. D. Vries, *J. Phys. Chem. Solids* **28**, 2143 (1967).
 - [17] E. Bertaut, J. Mareschal, G. De Vries, R. Aleonard, R. Pauthenet, J. Rebouillat, and V. Zarubicka, *IEEE Trans. Magn.* **2**, 453 (1966).
 - [18] H. Nhalil, H. S. Nair, S. R., A. M. Strydom, and S. Elizabeth, *J. Appl. Phys.* **117**, 173904 (2015).

- [19] Y. Fang, Y. Yang, X. Liu, J. Kang, L. Hao, X. Chen, L. Xie, G. Sun, V. Chandragiri, C.-W. Wang *et al.*, *Sci. Rep.* **6**, 33448 (2016).
- [20] J. P. Bolletta, F. Pomiro, R. D. Sánchez, V. Pomjakushin, G. Aurelio, A. Maignan, C. Martin, and R. E. Carbonio, *Phys. Rev. B* **98**, 134417 (2018).
- [21] N. Fairley and C. S. Ltd., CasaXPS 2.3.15: CasaXPS processing software for XPS spectra (2009), <http://www.casaxps.com>.
- [22] H. M. Rietveld, *J. Appl. Crystallogr.* **2**, 65 (1969).
- [23] J. Rodríguez-Carvajal, *Physica B: Condensed Matter* **192**, 55 (1993).
- [24] A. Wills, *Physica B: Condensed Matter* **276-278**, 680 (2000).
- [25] P. Blaha, K. Schwarz, G. K. Madsen, D. Kvasnicka, and J. Luitz, *An Augmented Plane Wave+ Local Orbitals Program for Calculating Crystal Properties* (Vienna University of Technology, Austria, 2001).
- [26] J. P. Perdew, K. Burke, and M. Ernzerhof, *Phys. Rev. Lett.* **77**, 3865 (1996).
- [27] V. I. Anisimov, F. Aryasetiawan, and A. I. Lichtenstein, *J. Phys.: Condens. Matter* **9**, 767 (1997).
- [28] M. P. Ghimire, L.-H. Wu, and X. Hu, *Phys. Rev. B* **93**, 134421 (2016).
- [29] M. P. Ghimire and X. Hu, *Mater. Res. Express* **3**, 106107 (2016).
- [30] M. P. Ghimire, Sandeep, and R. K. Thapa, *Mod. Phys. Lett. B* **24**, 2187 (2010).
- [31] Y. Yuan, H. L. Feng, M. P. Ghimire, Y. Matsushita, Y. Tsujimoto, J. He, M. Tanaka, Y. Katsuya, and K. Yamaura, *Inorg. Chem.* **54**, 3422 (2015).
- [32] H. L. Feng, S. Calder, M. P. Ghimire, Y.-H. Yuan, Y. Shirako, Y. Tsujimoto, Y. Matsushita, Z. Hu, C.-Y. Kuo, L. H. Tjeng *et al.*, *Phys. Rev. B* **94**, 235158 (2016).
- [33] H. L. Feng, M. P. Ghimire, Z. Hu, S.-C. Liao, S. Agrestini, J. Chen, Y. Yuan, Y. Matsushita, Y. Tsujimoto, Y. Katsuya *et al.*, *Phys. Rev. Mater.* **3**, 124404 (2019).
- [34] G. C. Allen, M. T. Curtis, A. J. Hooper, and P. M. Tucker, *J. Chem. Soc., Dalton Trans.* **16**, 1675 (1973).
- [35] G. C. Allen, M. T. Curtis, A. J. Hooper, and P. M. Tucker, *J. Chem. Soc., Dalton Trans.* **14**, 1525 (1974).
- [36] B. D. Padalia, W. C. Lang, P. R. Norris, L. M. Watson, and D. J. Fabian, *Proc. R. Soc. London. Series A: Math. Phys. Sci.* **354**, 269 (1977).
- [37] C. Kittel, *Introduction to Solid State Physics* (Wiley, New York, 2004).
- [38] R. B. Griffiths, *Phys. Rev. Lett.* **23**, 17 (1969).
- [39] H. S. Nair, D. Swain, H. N., S. Adiga, C. Narayana, and S. Elizabeth, *J. Appl. Phys.* **110**, 123919 (2011).
- [40] T. Chakraborty, H. S. Nair, H. Nhalil, K. R. Kumar, A. M. Strydom, and S. Elizabeth, *J. Phys.: Condensed Matter* **29**, 025804 (2016).
- [41] A. K. Pramanik and A. Banerjee, *Phys. Rev. B* **81**, 024431 (2010).
- [42] A. K. Pramanik and A. Banerjee, *J. Phys.: Condens. Matter* **28**, 35LT02 (2016).
- [43] C. Magen, P. A. Algarabel, L. Morellon, J. P. Araújo, C. Ritter, M. R. Ibarra, A. M. Pereira, and J. B. Sousa, *Phys. Rev. Lett.* **96**, 167201 (2006).
- [44] W. Jiang, X. Zhou, G. Williams, Y. Mukovskii, and R. Privezentsev, *J. Appl. Phys.* **107**, 09D701 (2010).
- [45] R. Mathieu, P. Jönsson, D. N. H. Nam, and P. Nordblad, *Phys. Rev. B* **63**, 092401 (2001).
- [46] D. G. Cahill and R. Pohl, *Solid State Commun.* **70**, 927 (1989).
- [47] M. Vagadia, S. Rayaprol, and A. Nigam, *J. Alloys Compd.* **735**, 1031 (2018).
- [48] J. Y. Zhao, Z. Y. Zhao, J. C. Wu, H. S. Xu, X. G. Liu, X. Zhao, and X. F. Sun, *AIP Adv.* **7**, 055806 (2017).
- [49] Z. Y. Zhao, X. M. Wang, C. Fan, W. Tao, X. G. Liu, W. P. Ke, F. B. Zhang, X. Zhao, and X. F. Sun, *Phys. Rev. B* **83**, 014414 (2011).
- [50] Z. Y. Zhao, X. Zhao, H. D. Zhou, F. B. Zhang, Q. J. Li, C. Fan, X. F. Sun, and X. G. Li, *Phys. Rev. B* **89**, 224405 (2014).
- [51] R. Berman and P. G. Klemens, *Phys. Today* **31**(4), 56 (1978).
- [52] M. C. Weber, M. Guennou, H. J. Zhao, J. Íñiguez, R. Vilarinho, A. Almeida, J. A. Moreira, and J. Kreisel, *Phys. Rev. B* **94**, 214103 (2016).
- [53] V. S. Bhadram, B. Rajeswaran, A. Sundaresan, and C. Narayana, *Europhys. Lett.* **101**, 17008 (2013).
- [54] S. Venugopalan, M. Dutta, A. K. Ramdas, and J. P. Remeika, *Phys. Rev. B* **31**, 1490 (1985).
- [55] M. K. Singh, H. M. Jang, H. C. Gupta, and R. S. Katiyar, *J. Raman Spectrosc.* **39**, 842 (2008).
- [56] M. N. Iliev, M. V. Abrashev, H.-G. Lee, V. N. Popov, Y. Y. Sun, C. Thomsen, R. L. Meng, and C. W. Chu, *Phys. Rev. B* **57**, 2872 (1998).
- [57] A. Nonato, B. S. Araujo, A. P. Ayala, A. P. Maciel, S. Yanez-Vilar, M. Sanchez-Andujar, M. A. Senaris-Rodriguez, and C. W. A. Paschoal, *Appl. Phys. Lett.* **105**, 222902 (2014).
- [58] M. Balkanski, R. F. Wallis, and E. Haro, *Phys. Rev. B* **28**, 1928 (1983).
- [59] L. H. Yin, J. Yang, R. R. Zhang, J. M. Dai, W. H. Song, and Y. P. Sun, *Appl. Phys. Lett.* **104**, 032904 (2014).
- [60] E. Granado, A. García, J. A. Sanjurjo, C. Rettori, I. Torriani, F. Prado, R. D. Sánchez, A. Caneiro, and S. B. Oseroff, *Phys. Rev. B* **60**, 11879 (1999).
- [61] M. T. Anderson, K. B. Greenwood, G. A. Taylor, and K. R. Poeppelmeier, *Prog. Solid State Chem.* **22**, 197 (1993).
- [62] See Supplemental Material at <http://link.aps.org/supplemental/10.1103/PhysRevB.102.014418> for neutron diffraction data at 350 K with a Rietveld refinement using purely nuclear model.
- [63] See Supplemental Material at <http://link.aps.org/supplemental/10.1103/PhysRevB.102.014418> for Rietveld refinement at 300 K, 215 K, 100 K, 20 K, and 7.7 K for all possible irreducible representations.
- [64] See Supplemental Material at <http://link.aps.org/supplemental/10.1103/PhysRevB.102.014418> for the values of refined magnetic moments at different temperatures obtained from the analysis of neutron diffraction data.


 Cite this: *RSC Adv.*, 2020, **10**, 16179

Electronic, magnetic, optical and thermoelectric properties of $\text{Ca}_2\text{Cr}_{1-x}\text{Ni}_x\text{OsO}_6$ double perovskites†

 Shalika R. Bhandari,^{abc} D. K. Yadav,^c B. P. Belbase,^{ac} M. Zeeshan,^d B. Sadhukhan,^b D. P. Rai,^{ib} R. K. Thapa,^c G. C. Kaphle^{ac} and Madhav Prasad Ghimire^{ib*abc}

With the help of density functional theory calculations, we explored the recently synthesized double perovskite material $\text{Ca}_2\text{CrOsO}_6$ and found it to be a ferrimagnetic insulator with a band gap of ~ 0.6 eV. Its effective magnetic moment is found to be $\sim 0.23 \mu_B$ per unit cell. The proposed behavior arises from the cooperative effect of spin-orbit coupling and Coulomb correlation of Cr-3d and Os-5d electrons along with the crystal field. Within the ferrimagnetic configuration, doping with 50% Ni in the Cr-sites resulted in a half-metallic state with a total moment of nearly zero, a characteristic of spintronic materials. Meanwhile, the optical study reveals that both ϵ_1^{xx} and ϵ_1^{zz} decrease first and then increase rapidly with increasing photon energy up to 1.055 eV. We also found optical anisotropy up to ~ 14 eV, where the material becomes almost optically isotropic. This material has a plateau like region in the σ_{xx} and σ_{zz} parts of the optical conductivity due to a strong 3d–5d interband transition between Cr and Os. In addition, we performed thermoelectric calculations whose results predict that the material might not be good as a thermoelectric device due to its small power factor.

Received 21st December 2019

Accepted 7th April 2020

DOI: 10.1039/c9ra10775d

rsc.li/rsc-advances

Introduction

In recent years, research on double perovskites (DPs) with chemical formula $\text{A}_2\text{BB}'\text{O}_6$ (where the B and B' cations are transition metals and A is an alkaline or rare earth metal) has gained significant interest due to their novel properties arising from the combination of crystal field, spin orbit coupling (SOC) and Coulomb correlation (U). Transition metal (TM) DPs are found to show remarkable properties such as structural stability, high charge mobility, finite band gap, superconductivity, half-metallicity (HM), piezoelectricity, thermoelectricity, *etc.*, which can be exploited in modern technological devices.^{1–5} Reports on the realization of room-temperature colossal magnetoresistance and a HM state in $\text{Sr}_2\text{FeMoO}_6$ and $\text{Sr}_2\text{-FeReO}_6$,^{6,7} multiferroicity in $\text{Bi}_2\text{NiMnO}_6$,⁸ and magnetodielectricity in $\text{La}_2\text{NiMnO}_6$ (ref. 9) have motivated researchers to rigorously study these types of materials. In this regard, DPs may help in overcoming today's major challenges through the

development of efficient energy converters and storage devices. TM doped DPs exhibit HM behaviour,^{10–13} in which the material exhibits a conducting state in one of the spin channels while the other spin channel is insulating or semiconducting. HM behaviour has been exhibited by diverse groups of materials such as Heusler alloys, shandites, the Ruddlesden–Popper series, *etc.*,^{14–21} and is a key property for potential applications in spintronics.^{22,23} The majority of experimentally determined HMs are ferromagnets (FMs) such as $\text{La}_{1-x}\text{Sr}_x\text{MnO}_3$, and some are ferrimagnets (FiMs) with finite values of magnetic moments.^{6,7,17,18}

Recently, osmium perovskites have been observed to show novel properties. For instance, NaOsO_3 was found to be magnetically driven by a metal–insulator (MI) transition,²⁴ while a ferroelectric type structural transition was observed in LiOsO_3 .²⁵ The CsOs_2O_7 , RbOs_2O_7 and KOs_2O_7 pyrochlores exhibit unusual superconductivity.²⁶ In DPs such as $\text{Sr}_2\text{CuOsO}_6$ and $\text{Sr}_2\text{NiOsO}_6$, a MI state was identified,²⁷ while HM antiferromagnetism (HMAFM) was predicted in $\text{Sr}_2\text{CrOsO}_6$ and $\text{Sr}_2\text{-CrRuO}_6$,¹ and for $\text{Ba}_2\text{NiOsO}_6$, FM with a Dirac–Mott insulating state was observed near 100 K for the bulk material and anomalous quantum Hall behavior was observed on the surface.^{28,29} In $\text{Sr}_2\text{ScOsO}_6$, a transition to AFM was observed at 92 K (ref. 30) and a transition to FiM was observed at 725 K.³¹ Similarly, Ca_2MOsO_6 (where M = Mn, Fe, Co, and Ni) displays a FiM state with Curie temperature (T_C) of 305, 320, 145, and 175 K, respectively.^{32–35} From density functional theory (DFT) calculations, PrSrMgIrO_6 was predicted to be an HMAFM with nearly zero effective magnetic moment per unit cell due to the

^aCentral Department of Physics, Tribhuvan University, Kathmandu, Nepal. E-mail: mpghimire@tucdp.edu.np; ghimire.mpg@gmail.com

^bInstitute for Theoretical Solid State Physics, IFW Dresden e. V., Dresden-01069, Germany

^cCondensed Matter Physics Research Center (CMPRC), Butwal, Rupandehi, Nepal

^dDepartment of Chemistry, Indian Institute of Technology Roorkee, Roorkee 247667, Uttarakhand, India

^ePhysical Sciences Research Center (PSRC), Department of Physics, Pachhunga University College, Aizawl, Mizoram, India

† Electronic supplementary information (ESI) available. See DOI: 10.1039/c9ra10775d

combined effect of Coulomb correlation, U , and SOC.¹¹ A few DPs such as $\text{Ca}_2\text{MgOsO}_6$, and $\text{Sr}_2\text{MgOsO}_6$ have finite gaps at the Fermi level (E_F) due to the correlation effect and are reported to be AFM Mott insulators,³⁶ while $\text{Sr}_2\text{NiOsO}_6$, $\text{Sr}_2\text{FeOsO}_6$, $\text{Sr}_2\text{NiRuO}_6$, and $\text{SrLaBB}'\text{O}_6$ ($B = \text{Ni, Fe; B}' = \text{Os, Ru}$)^{37,38} show Mott insulating states under the combined effect of U and SOC.

Electron doping has also been considered in FiM DPs such as $\text{La}_x\text{Ca}_{2-x}\text{CrWO}_6$, which demonstrates that doping generally increases the T_C .³⁹ DPs are known also as potential candidates for optoelectronic and photovoltaic device applications. The optically active region for these perovskites lies within 3 to 15 eV which is in the range of UV and IR spectra.^{40–42} Frequencies suitable for optoelectronics can be absorbed in this region. $\text{Bi}_2\text{FeMnO}_6$ is one such example with a band gap of ~ 0.8 eV that has been predicted as a suitable material for optical devices.⁴³

Recently, Morrow *et al.*⁴⁴ synthesized a new DP material $\text{Ca}_2\text{CrOsO}_6$ whose T_C was measured to be much higher than room temperature, *i.e.*, 490 K. This study further reports that the atomic sites occupied by the two transition metals, *i.e.*, Cr and Os cations, are in the ratios of 76% and 24%, respectively, which is a signature of antisite disorder in the system. Here, we are particularly motivated to explore the electronic and related properties of $\text{Ca}_2\text{CrOsO}_6$ due to (i) its high T_C above room temperature, (ii) the FiM insulating state, and (iii) the small effective magnetic moment. Upon electron doping, the material is expected to close the band gap in one spin-channel, giving rise to HM state; compensate the total moments nearly to zero; and the increase in T_C .³⁹ These features are expected to be important in new DP spintronic devices that work at room temperature.

In this work, we have carried out DFT calculations and found that $\text{Ca}_2\text{CrOsO}_6$ is a FiM insulator with a total magnetic moment, $\mu_{\text{tot}} = 0.23 \mu_B$ per unit cell. When Ni is partially substituted in the Cr-sites, it contributes an additional five electrons to the system. This significantly changes the electronic as well as magnetic behaviour, giving rise to a nearly compensated HMAFM state. The optical study on $\text{Ca}_2\text{CrOsO}_6$ shows a strong optical interband transition between the Cr-3d and Os-5d bands in a plateau like region. We further consider the transport properties and calculate the Seebeck coefficient, thermal conductivity and power factor of the parent material $\text{Ca}_2\text{CrOsO}_6$.

Crystal structures and computational details

$\text{Ca}_2\text{CrOsO}_6$ crystallizes in the monoclinic structure with space group $P2_1/n$ (14), and contains CrO_6 and OsO_6 octahedra [see Fig. 1]. The experimental lattice parameters chosen for the calculations are $a = 5.3513 \text{ \AA}$, $b = 5.4561 \text{ \AA}$, and $c = 7.6204 \text{ \AA}$, with $\beta = 90.092^\circ$. The inter-octahedral Cr–O–Os bond angles are 153.3° , 152.6° and 153.8° , with average Cr–O and Os–O bond lengths of 1.972 \AA and 1.954 \AA respectively.

We performed DFT calculations to explore the electronic, magnetic and related properties of 3D and 2D materials as reported recently.^{45–48} The electronic and magnetic properties

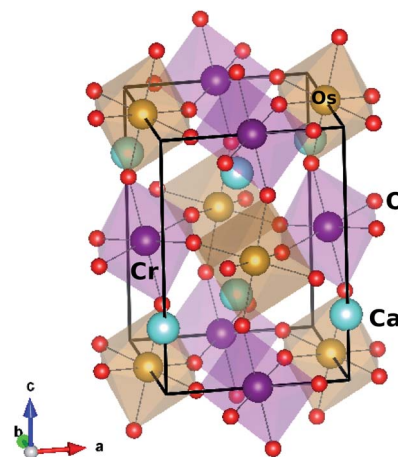


Fig. 1 Crystal structure of double perovskite $\text{Ca}_2\text{CrOsO}_6$.

were calculated using the full-potential linearized augmented plane wave (FP-LAPW) method as implemented in the WIEN2k code.⁴⁹ The standard generalized gradient approximation (PBE-GGA)⁵⁰ was used, incorporating U of 4 eV for Cr (Ni) and 1.5 eV for Os.^{35–37} The SOC was included *via* the second variational step.⁵¹ The magnetic anisotropy energy (MAE) was calculated by self consistent calculations in full relativistic mode considering five different orientations of the magnetization. The atomic sphere radii R_{MT} were 2.14, 1.94, 1.99, 2.01 and 1.64 Bohr for Ca, Cr, Ni, Os and O respectively, and a set of 500 k -points within the full Brillouin zone was used which corresponds to an $8 \times 8 \times 6$ k -mesh. The convergence was set to 1 mRy per a.u. which gives reliable results for materials that contain transition metals.⁵²

In order to consider different magnetic configurations, the symmetry of the crystal has been lowered to $P1$ which corresponds to a total of 20 inequivalent atoms in which three types of oxygen atoms are present and form octahedra with Cr and Os. The tilt and rotation of the CrO_6 and OsO_6 octahedra result in Cr–O–Os bond angles within 152.6° to 153.8° . This variation plays a significant role in the magnetic properties.⁴⁴

For the optical property calculations, the full potential local orbital (FPLO) code⁵³ (version 18.00) has been used, from which the velocity matrix elements for the optical parameters were extracted. In order to minimize the major fluctuations in the lower energy range, a $16 \times 16 \times 16$ k -mesh was used. The electrical transport properties have been calculated using the Boltzmann theory⁵⁴ and the relaxation time approximation as implemented in the Boltztrap code,⁵⁵ interfaced with WIEN2k.⁴⁹ The electrical conductivity and power factor are calculated with respect to time relaxation, τ ; the Seebeck coefficient is independent of τ .

Results and discussion

Electronic and magnetic properties

We begin our discussion with the magnetic ground state. For this, we have considered four types of magnetic configurations, one FM state (FM1- $\uparrow\uparrow\uparrow\uparrow$), two AFM states (AF1- $\uparrow\downarrow\uparrow\downarrow$, AF2- $\uparrow\downarrow\downarrow\uparrow$), and one FiM state (FiM- $\uparrow\uparrow\downarrow\downarrow$). This was done after

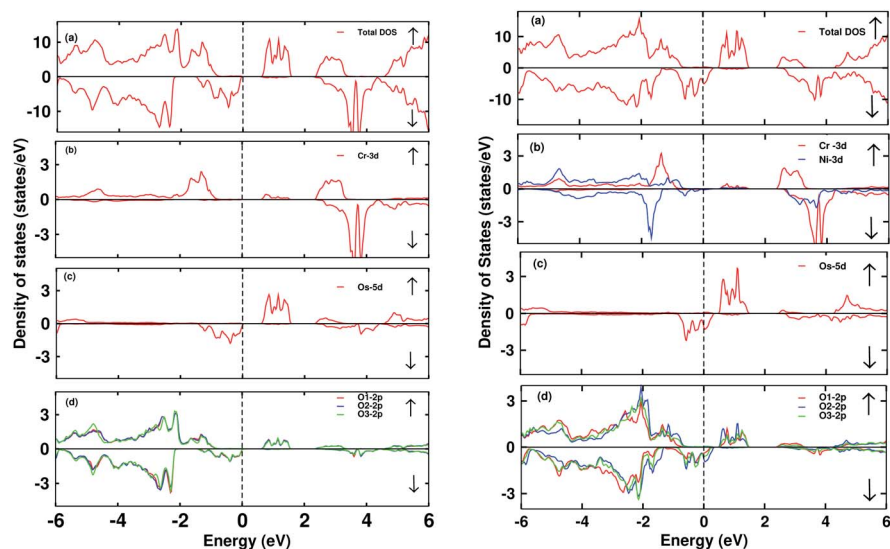


Fig. 2 The total and partial density of states (DOS) of $\text{Ca}_2\text{CrOsO}_6$ (left) and $\text{Ca}_2\text{Cr}_{0.5}\text{Ni}_{0.5}\text{OsO}_6$ (right). (a) Total DOS, (b) partial DOS of Cr-3d and Ni-3d, (c) PDOS of Os-5d, (d) PDOS of O-2p states for spin up (\uparrow) and spin down (\downarrow) channels within the GGA+U+SOC functional. The vertical dotted line indicates $E_F = 0$.

noting that the nonmagnetic (NM) state of the crystal was found to be the most unstable state, with the highest energy. The FiM configuration is found to be the magnetic ground state with the lowest energy among the other magnetic configurations. The relativistic calculations considered for spin quantisation align along the [100], [010], [001], [110] and [111] directions. For the easy axis along [001], the calculated MAE is 12.75 meV per unit cell.

In the parent material $\text{Ca}_2\text{CrOsO}_6$, Cr has a charge of +3 with a $3d^3$ configuration, involving the occupancy of the three t_{2g} states in the spin up channel and leaving the e_g states empty. As a result, in the density of states (DOS), the three occupied t_{2g} states lie in the valence region while the two empty e_g states move to the conduction region. In the spin down channel, all

the Cr-d bands are unoccupied and thus lie far into the conduction region. In the case of Os, its charge is +5 with a $5d^3$ configuration. Therefore, only three electrons from Os will occupy the t_{2g} states in the spin down channel, leaving all the other states to shift to the conduction region.

The electronic DOS and band structures of $\text{Ca}_2\text{CrOsO}_6$ and $\text{Ca}_2\text{Cr}_{0.5}\text{Ni}_{0.5}\text{OsO}_6$ within GGA+U+SOC are shown in Fig. 2 and 3, respectively. Starting with the parent material $\text{Ca}_2\text{CrOsO}_6$, a band gap of ~ 0.59 eV has been calculated (Fig. 2 and 3 (left)), signifying that $\text{Ca}_2\text{CrOsO}_6$ is an insulator. The results thus obtained are in good agreement with experimental and theoretical reports.^{44,56} The major contribution to the total DOS around E_F (Fig. 2(a) (left)) is mainly from the Cr-3d and Os-5d orbitals hybridizing strongly with the O-2p orbitals (Fig. 2(d) (left)).

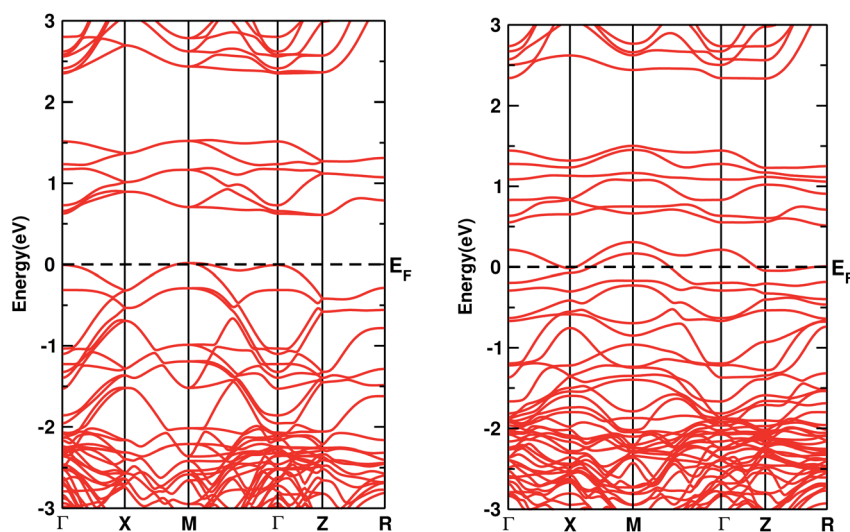


Fig. 3 The band structures of $\text{Ca}_2\text{CrOsO}_6$ (left) and $\text{Ca}_2\text{Cr}_{0.5}\text{Ni}_{0.5}\text{OsO}_6$ (right) within GGA+U+SOC. The horizontal dotted line indicates $E_F = 0$.

On the other hand, for the doped material $\text{Ca}_2\text{Cr}_{0.5}\text{Ni}_{0.5}\text{OsO}_6$, one Ni atom is substituted in a Cr-site in $\text{Ca}_2\text{CrOsO}_6$. This will add five extra electrons to the system as Ni with a charge of +2 has a $3d^8$ configuration. Out of five additional electrons, two occupy the e_g states of the spin up channel, while the remaining three are bound to go to the spin down channel to occupy the t_{2g} states. These three electrons of Ni in the spin down channel generate a repulsive effect in the Os- t_{2g} band, which causes the Os band to shift from the valence region towards the conduction region by crossing E_F in the spin down channel (see Fig. 2(c) (right)). This gives rise to a metallic state in the spin down channel, while the material remains insulating in the spin up channel. Thus, with an insulating state in the spin up channel and a metallic state in the spin down channel, the $\text{Ca}_2\text{Cr}_{0.5}\text{Ni}_{0.5}\text{OsO}_6$ material is predicted to be a HM. It is interesting to note that the HM state remains robust for U_{Os} as large as 4 eV. The DOS and band structures for the parent and the doped material within GGA and GGA+U are available in the ESI section for comparison (see Fig. S1–S4†).

We also considered the magnetic behaviour of $\text{Ca}_2\text{Cr}_{1-x}\text{Ni}_x\text{OsO}_6$. As tabulated in Table 1, for $x = 0$, the individual magnetic moments of the Cr and Os atoms are $2.52 \mu_B$ and $-1.59 \mu_B$ respectively, with an effective magnetic moment of $0.23 \mu_B$ per unit cell (2 f.u.). Similarly, for $x = 0.5$, the individual magnetic moments of the Cr, Ni and Os atoms are $2.52 \mu_B$, $1.64 \mu_B$ and $-1.42 \mu_B$ respectively, with an effective magnetic moment of $0.21 \mu_B$ per unit cell. Due to the partial charge transfer from Cr and Os to oxygen, the oxygen atoms are spin polarized in parallel with the Os ions and gain a sizable magnetic moment of $-0.07 \mu_B$, consistent with the isosurface plot shown in Fig. 4 (left). Here, the polarisation is mainly found in the 2p orbitals and this hybridized moment in oxygen increases the resultant magnetic moment.

To understand the charge transfer effects among Cr, Ni, Os and O atoms, spin density isosurfaces are drawn as shown in Fig. 4 (right). As observed for the parent compound $\text{Ca}_2\text{CrOsO}_6$ (see Fig. 4 (left)), the spin density contributions for Cr and Os are due to 3d and 5d states. The observed characteristics are due to the combination of d_{xy} , d_{xz} and d_{yz} (*i.e.*, t_{2g}) states that are indicative of d^3 configurations. In addition, the oxygen-2p states become spin-polarized due to the Cr-3d and Os-5d states. When one of the Cr atoms is replaced by Ni, the nature of the spin density changes significantly (see Fig. 4 (right)). Actually, Ni

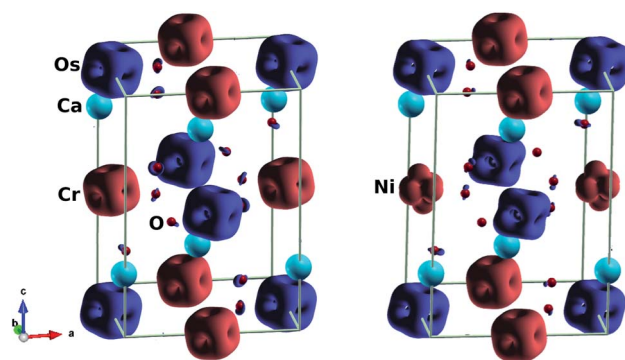


Fig. 4 Isosurfaces of spin magnetization density at $\pm 0.21 \text{ e \AA}^{-3}$ with red (blue) for spin up (down): (left) parent material $\text{Ca}_2\text{CrOsO}_6$, (right) material with 50% Cr replacement $\text{Ca}_2\text{Cr}_{0.5}\text{Ni}_{0.5}\text{OsO}_6$.

with a charge of +2 has a d^8 configuration. Thus, with five electrons fully occupying one spin channel, the remaining three electrons move to another spin channel to fill the t_{2g} states. As a result, the remaining visible states are the e_g states which are clearly seen in the isosurfaces of the Ni (see Fig. 4 (right)) atoms.

From Table 1, the spin magnetic moment in Os is reduced due to the strong Os–O hybridization, and SOC induces an orbital moment. Thus, the SOC is found to be responsible for the small reduction in spin magnetic moment. The alignment of the orbital magnetic moment of Cr is the same as that of the total spin magnetic moment, showing that the 3d orbital is either semi occupied or more than half filled. Whereas, in the Os-5d state, the spin orientations are antiparallel as compared to the orbital magnetic moments due to the less than half filled states, which is in accordance with Hund's third rule.⁵⁷ Hence, the orbital magnetic moments on Cr and Os are parallel which increases the net magnetic moment in $\text{Ca}_2\text{CrOsO}_6$.

Optical properties

In this work, we have investigated the optical properties of the double perovskite $\text{Ca}_2\text{CrOsO}_6$, considering the polarization directions E_{xx} and E_{zz} , as $E_{xx} = E_{yy}$ due to the tetragonal symmetry. The optical current j_a generated by an electric field E_b is given by: $j_a = \sigma_{ab}E_b$. For $\text{Ca}_2\text{CrOsO}_6$, we consider only E_x and E_z polarization as $E_x = E_y$ due to the tetragonal symmetry, leaving only two independent x and z components of the optical

Table 1 Calculated spin magnetic moments (in μ_B) of B (Cr/Ni), B' (Os) and the 3 types of oxygen atoms, net moments (per unit cell) and band gaps, E_g , (in eV). The calculated orbital moments at the B and B' sites are shown within parentheses for $\text{Ca}_2\text{CrOsO}_6$ and $\text{Ca}_2\text{Cr}_{1-x}\text{Ni}_x\text{OsO}_6$

Site	$\text{Ca}_2\text{CrOsO}_6$				$\text{Ca}_2\text{Cr}_{0.5}\text{Ni}_{0.5}\text{OsO}_6$		
	GGA	GGA+U	GGA+U+SOC	Expt.	GGA	GGA+U	GGA+U+SOC
B	2.20	2.52	2.52(0.05)	2.5	2.19/1.32	2.52/1.65	2.52(0.05)/1.64(0.14)
B'	-1.45	-1.66	-1.59(0.14)	1.26	-1.28	-1.48	-1.42(0.16)
O1	-0.10	-0.11	-0.10		-0.08	-0.09	-0.08
O2	-0.09	-0.10	-0.10		-0.03	-0.05	-0.05
O3	-0.09	-0.10	-0.10		-0.05	-0.07	-0.07
Net	0	0	0.23	0.2	0	0	0.21
E_g	0.53	0.65	0.59		Metallic	Metallic	Metallic

element. The complex dielectric function $\varepsilon(\omega) = \varepsilon_1(\omega) + i\varepsilon_2(\omega)$ describes the behavior of materials under incident light, where $\varepsilon_1(\omega)$ and $\varepsilon_2(\omega)$ are the real and imaginary parts of the dielectric function, respectively. The imaginary part $\varepsilon_2(\omega)$ is obtained from the electronic structure through the joint density of states and the momentum matrix elements between the occupied and unoccupied states:

$$\varepsilon_2(\omega) = \frac{Ve^2}{2\pi\hbar m^2 \omega^2} \int d^3k \sum |kn|p|kn'|^2 f(kn) [1 - f(kn')] \delta(E_{kn} - E_{kn'} - \hbar\omega) \quad (1)$$

where p is the momentum operator, kn is the eigenfunction with eigenvalue E_{kn} and $f(kn)$ is the Fermi distribution function. The real part of the dielectric function ε_1 is given by the Kramers-Kronig dispersion relations.⁵⁸

$$\varepsilon_1(\omega) = 1 + \frac{2}{\pi} \int \frac{\varepsilon_2(\omega')\omega'}{\omega'^2 - \omega^2} d\omega' \quad (2)$$

The other optical parameters like optical conductivity $\sigma(\omega)$ and electron loss function $L(\omega)$ are directly related to the dielectric function as follows.⁵⁹

$$\sigma(\omega) = \frac{-i\omega(\varepsilon_2(\omega) - 1)}{4\pi} \quad (3)$$

$$L(\omega) = \frac{\varepsilon_2}{\varepsilon_1^2(\omega) + \varepsilon_2^2(\omega)} \quad (4)$$

The real part of the complex dielectric function $\varepsilon_1(\omega)$ expresses the electronic polarizability of materials due to incident photons. Fig. 5 (left) shows the variation of the dielectric function (real and imaginary) as a function of photon energy. The calculated static dielectric constants for x and z polarization ($\varepsilon_1^{xx}(0)$ and $\varepsilon_1^{zz}(0)$) are 15.94 eV and 12.43 eV, respectively (Table 2). Both ε_1^{xx} and ε_1^{zz} decrease first and then increase rapidly with increasing photon energy up to 1.055 eV. With a small increase in photon energy above 0.0 eV, ε_1^{zz} decreases more as compared to ε_1^{xx} and then increases again. At a certain energy, both ε_1^{xx} and ε_1^{zz} show a maximum peak where ε_1^{xx} surpasses ε_1^{zz} in magnitude. The plot also indicates the presence of optical

Table 2 Calculated optical parameters at the main peak value for the $\text{Ca}_2\text{CrOsO}_6$ compound

Optical parameters	$\varepsilon_1^{xx}(0)$	$\varepsilon_1^{zz}(0)$	$L(\omega)$	$\sigma_1^{xx}(\omega)$	$\sigma_1^{zz}(\omega)$
eV	15.94	12.43	14.11	7.79	7.32

anisotropy up to ~ 14 eV, and after that the material becomes almost optically isotropic. Both ε_1^{xx} and ε_1^{zz} become zero at ~ 7.6 eV which may be due to the occurrence of plasmonic type oscillations. We know that the imaginary part $\varepsilon_2(\omega)$ of the complex dielectric function is related to optical absorption. The dependence of $\varepsilon_2(\omega)$ on photon energy is presented in Fig. 5 (left).

From the figure, we notice a rapid increase in $\varepsilon_2(\omega)$ beyond the threshold energy which corresponds to the calculated energy band gap and observed a maximum peak at 1.0–1.5 eV. After that, the value of $\varepsilon_2(\omega)$ decreases with severe fluctuations. A significant plateau like region is obtained in the energy range from 3.0 eV up to 10.0 eV. This can also be verified by the optical conduction plot which shows active absorption of photon energy due to direct electron transitions. The variation of the electron energy loss function $L(\omega)$ versus photon energy is also plotted in Fig. 5 (middle). $L(\omega)$ gives a description of the energy loss due to the scattering of a fast electron travelling in the material. The electron energy loss is very high in the low energy region in the case of intraband transitions. However, for interband transitions, $L(\omega)$ slowly increases up to 12.0 eV and then abruptly increases beyond 13.0 to 14.0 eV. The low value of electron energy loss is due to the fact that $L(\omega)$ is inversely related to $\varepsilon_2(\omega)$. The large peak in the energy loss spectra at around 13.0 eV to 14.0 eV corresponds to a plasmon frequency ω_p at 13.0–14.0 eV. We also calculated the optical conductivity $\sigma(\omega)$ as shown in Fig. 5 (right). The only independent components of $\sigma(\omega)$ in this material are $\sigma_{xx}(\omega)$, $\sigma_{zz}(\omega)$, $\sigma_{yx}(\omega)$ and $\sigma_{zx}(\omega)$. $\sigma_{yx}(\omega)$ and $\sigma_{zx}(\omega)$ are zero, and only the $\sigma_{xx}(\omega)$ and $\sigma_{zz}(\omega)$ components contribute. The optical conductivity of $\text{Ca}_2\text{CrOsO}_6$ has a plateau like region at 3–12 eV rather than a sharp peak like feature. This indicates a strong optical interband transition between the Cr-3d and Os-5d bands in this region.

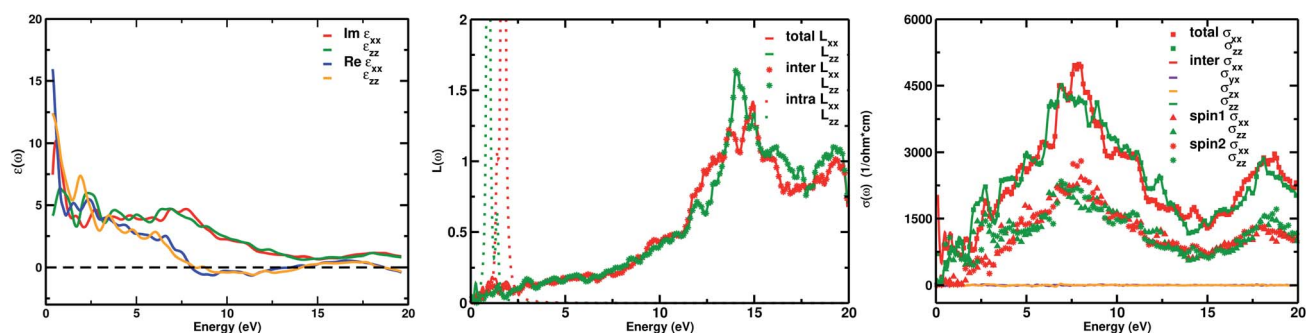


Fig. 5 (Left) The real and imaginary parts of the dielectric function $\varepsilon(\omega)$ for the interband part. The intraband part of $\varepsilon(\omega)$ diverges at $\omega = 0$; (middle) total, intraband and interband loss function $L(\omega)$; (right) total, interband and individual spin contributions to optical conductivity $\sigma(\omega)$. Here, for $\text{Ca}_2\text{CrOsO}_6$, $\sigma_{xx}(\omega)$ and $\sigma_{zz}(\omega)$ contribute.

Thermoelectric properties

The insulating behavior of $\text{Ca}_2\text{CrOsO}_6$ prompted us to investigate the thermoelectric properties. The performance of thermoelectric materials is given by a dimensionless parameter called the figure of merit, *i.e.*, $ZT = S^2\sigma T/\kappa$, where S , σ and κ represent the Seebeck coefficient, electrical conductivity, and thermal conductivity, respectively.^{60–62} Conventional materials such as Bi_2Te_3 and PbTe have shown a promising figure of merit, however, these alloys suffer from toxic compositions, low thermal stability, and expensive constituents. In this regard, oxide materials could be a promising alternative owing to their environmental friendliness, non-toxicity, good thermal stability, and low-cost compositions.^{63,64} Recently, good thermoelectric performances have been reported for double perovskite oxides.^{65,66} Motivated by these findings, we investigated the thermoelectric properties of $\text{Ca}_2\text{CrOsO}_6$ utilizing the Boltztrap code which is used for computing the electrical transport coefficients S and σ , and thereby $S^2\sigma$, within the rigid band approximation (RBA) and constant relaxation time approach (CRTA). The CRTA assumes the Seebeck coefficient to be independent of relaxation time, τ , and the electrical conductivity and power factor (PF) are expressed with respect to τ . These two approaches have been successful in the theoretical investigation of new thermoelectric materials by many groups.^{67–70}

Fig. 6 shows the Seebeck coefficient, electrical conductivity and power factor with respect to relaxation time, as a function of temperature for $\text{Ca}_2\text{CrOsO}_6$ for the spin up and spin down

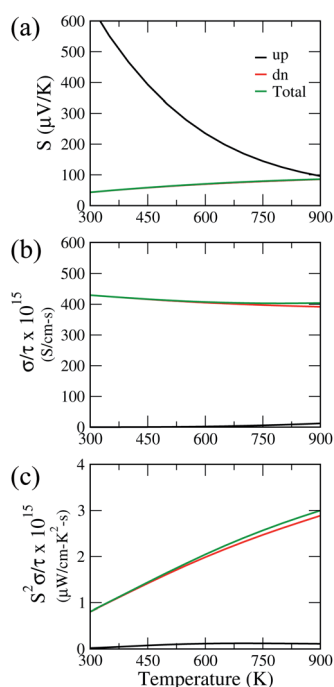


Fig. 6 (a) Seebeck coefficient, (b) electrical conductivity, and (c) power factor of $\text{Ca}_2\text{CrOsO}_6$ as a function of temperature for spin up (black), spin down (red) and total contribution (green). The electrical conductivity and power factor are plotted with respect to the relaxation time.

channels, and the total contribution. The parameters are calculated for both the spin channels according to the two current model.⁷¹ Within this model, the total electrical conductivity and Seebeck coefficients are given by $\sigma = \sigma(\uparrow) + \sigma(\downarrow)$ and $S = [S(\uparrow)\sigma(\uparrow) + S(\downarrow)\sigma(\downarrow)]/[\sigma(\uparrow) + \sigma(\downarrow)]$ where (\uparrow) and (\downarrow) represent the coefficients for spin up and spin down respectively. Utilizing this model, the total Seebeck coefficient obtained shows an increasing trend in the temperature range 300–900 K. The positive values are in the range 43–83 $\mu\text{V K}^{-1}$ and are indicative of p-type charge carriers. However, the Seebeck coefficient values are not significant as compared to benchmark values (150 $\mu\text{V K}^{-1}$).⁷² For evaluating the electrical conductivity and power factor, one needs to incorporate the relaxation time which is not trivial to calculate. The relaxation time is very sensitive as it may vary for different systems at different doping levels and temperatures.⁷³ Thus, the actual value of the relaxation time is quite essential for determining the transport properties. However, in previous theoretical studies, a relaxation time of 5×10^{-15} s has been used for evaluating the transport properties.⁷⁴ Utilizing the same value, we obtained good values of total electrical conductivity in the range 429–404 S cm^{-1} in the temperature range 300–900 K. These values can be attributed to the greater density of states at the VBM owing to the degenerate bands. The degenerate bands increase the density of states which results in a larger number of charge carriers. The greater density of states at the VBM close to the Fermi level as compared to the conduction band minimum suggests that hole doping would be beneficial for improving the transport properties.⁷⁵

The calculated total power factor with respect to the relaxation time is not significant, owing to the low Seebeck coefficient. The values range from 0.08 $\mu\text{W cm}^{-1} \text{K}^{-2} \text{s}^{-1}$ at room temperature to 3 $\mu\text{W cm}^{-1} \text{K}^{-2} \text{s}^{-1}$. Utilizing the relaxation time as before, *i.e.*, $\tau = 5 \times 10^{-15}$ s, the maximum obtained power factor is 15 $\mu\text{W cm}^{-1} \text{K}^{-2}$ at 900 K. The proposed value, though not significant, can be further improved by utilizing suitable dopants and synthesis approaches, meriting further experimental investigations.

Conclusions

By means of density functional calculations, we found that the double perovskite material $\text{Ca}_2\text{CrOsO}_6$ is a ferrimagnetic insulator. Upon substantial doping with Ni (50%) in the Cr-sites, the composition $\text{Ca}_2\text{Cr}_{0.5}\text{Ni}_{0.5}\text{OsO}_6$ shows nearly compensated half-metal behaviour which is desirable for spintronic device applications. The optical study of the parent material $\text{Ca}_2\text{CrOsO}_6$ reveals that both ϵ_1^{xx} and ϵ_1^{zz} decrease first and then increase rapidly with increasing photon energy up to 1.055 eV. At a certain energy, both ϵ_1^{xx} and ϵ_1^{zz} show a maximum peak where ϵ_1^{xx} surpasses ϵ_1^{zz} in magnitude. We also found that optical anisotropy is present up to ~ 14 eV. The promising optical response of $\text{Ca}_2\text{CrOsO}_6$ due to Cr-3d and Os-5d inter-band transitions makes it an important material for photovoltaic and optoelectronic applications. In addition, we investigated the thermoelectric properties, however, the material does not show promise as a thermoelectric device.

Conflicts of interest

There are no conflicts to declare.

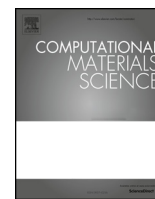
Acknowledgements

SRB thanks the Nepal Academy of Science and Technology, Kathmandu for the PhD fellowship. Computations were performed at IFW Dresden, Germany and CDP, Nepal. We thank Ulrike Nitzsche for technical assistance. SRB and MPG thank Manuel Richter and Jeroen van den Brink for fruitful discussions and suggestions to complete this work. MPG acknowledges the Higher Education Reform Project of Tribhuvan University for the start-up grant, and the Alexander von Humboldt Foundation, Germany for the equipment grants.

Notes and references

- 1 K. W. Lee and W. E. Pickett, *Phys. Rev. B: Condens. Matter Mater. Phys.*, 2008, **77**, 115101.
- 2 Y. P. Liu, H. R. Fuh and Y. K. Wang, *Comput. Mater. Sci.*, 2014, **92**, 63.
- 3 A. H. Reshak, *Phys. Chem. Chem. Phys.*, 2016, **6**, 92887.
- 4 D. P. Rai, A. Shankar, M. P. Ghimire and R. K. Thapa, *Comput. Mater. Sci.*, 2015, **101**, 313.
- 5 M. T. Anderson, K. B. Greenwood, G. A. Taylor and K. R. Poeppelmeier, *Prog. Solid State Chem.*, 1993, **22**, 197.
- 6 Y. Tokura, *Rep. Prog. Phys.*, 2006, **69**, 797.
- 7 K.-I. Kobayashi, T. Kimura, H. Sawada, K. Terakura and Y. Tokura, *Nature*, 1998, **395**, 677.
- 8 Y. Shimakawa, M. Azuma and N. Ichikawa, *Materials*, 2011, **4**, 153.
- 9 N. S. Rogado, J. Li, A. W. Sleight and M. A. Subramanian, *Adv. Mater.*, 2005, **17**, 2225.
- 10 W. E. Pickett, *Phys. Rev. B: Condens. Matter Mater. Phys.*, 1998, **57**, 10613.
- 11 M. P. Ghimire, L. H. Wu and X. Hu, *Phys. Rev. B*, 2016, **93**, 134421.
- 12 X. Hu, *Adv. Mater.*, 2012, **24**, 294.
- 13 Y.-M. Nie and X. Hu, *Phys. Rev. Lett.*, 2008, **100**, 117203.
- 14 M. Sargolzaei, M. Richter, K. Koepf, I. Opahle and H. Eschrig, *Phys. Rev. B: Condens. Matter Mater. Phys.*, 2006, **74**, 224410.
- 15 M. P. Ghimire, J. I. Facio, J.-S. You, L. Ye, J. G. Checkelsky, S. Fang, E. Kaxiras, M. Richter and J. van den Brink, *Phys. Rev. Res.*, 2019, **1**, 032044.
- 16 W. E. Pickett and J. S. Moodera, *Phys. Today*, 2001, **54**, 39.
- 17 G. M. Muller, J. Walowski, M. Djordjevic, G.-X. Miao, A. Gupta, A. V. Ramos, K. Gehrke, V. Moshnyaga, K. Samwer, J. Schmalhorst, A. Thomas, A. Hütten, G. Reiss, J. S. Moodera and M. Münzenberg, *Nat. Mater.*, 2009, **8**, 56.
- 18 G. Shibata, M. Kitamura, M. Minohara, *et al.*, *npj Quantum Mater.*, 2018, **3**, 3.
- 19 S. N. Ruddlesden and P. Popper, *Acta Crystallogr.*, 1957, **10**, 538.
- 20 M. P. Ghimire, R. K. Thapa, D. P. Rai, Sandeep, T. P. Sinha and X. Hu, *J. Appl. Phys.*, 2015, **117**, 063903.
- 21 H. van Leuken and R. A. de Groot, *Phys. Rev. Lett.*, 1995, **74**, 1171.
- 22 C. Felser, G. H. Fecher and B. Balke, *Angew. Chem., Int. Ed.*, 2007, **46**, 668.
- 23 M. I. Katsnelson, Y. Yu. Irkhin, L. Chioncel, A. I. Lichtenstein and R. A. de Groot, *Rev. Mod. Phys.*, 2008, **80**, 315.
- 24 S. Calder, V. O. Garlea, D. F. McMorrow, M. D. Lumsden, M. B. Stone, J. C. Lang, J. W. Kim, J. A. Schlueter, Y. G. Shi, K. Yamaura, Y. S. Sun, Y. Tsujimoto and A. D. Christianson, *Phys. Rev. Lett.*, 2012, **108**, 257209.
- 25 Y. G. Shi, Y. F. Guo, X. Wang, A. J. Princep, D. Khalyavin, P. Manuel, Y. Michiue, A. Sato, T. Tsuda, S. Yu, M. Arai, Y. Shirako, M. Akaogi, N. L. Wang, K. Yamaura and A. T. Boothroyd, *Nat. Mater.*, 2013, **12**, 1023.
- 26 Z. Hiroi, J. Yamaura and K. Hattori, *J. Phys. Soc. Jpn.*, 2012, **81**, 011012.
- 27 A. C. Tian, H. C. Wibowo, Z. Loye and M. H. Whangbo, *Inorg. Chem.*, 2011, **50**, 4142.
- 28 H. L. Feng, S. Calder, M. P. Ghimire, Y. Yehua, Y. Shirako, Y. Tsujimoto, Y. Matsushita, Z. Hu, C.-Y. Kuo, L. H. Tjeng, T.-W. Pi, Y.-L. Soo, J. He, M. Tanaka, Y. Katsuya, M. Richter and K. Yamaura, *Phys. Rev. B*, 2016, **94**, 235158.
- 29 H.-S. Lu and G.-Y. Guo, *Phys. Rev. B*, 2019, **100**, 054443.
- 30 A. E. Taylor, R. Morrow, D. J. Singh, S. Calder, M. D. Lumsden, P. M. Woodward and A. D. Christianson, *Phys. Rev. B: Condens. Matter Mater. Phys.*, 2015, **91**, 100406.
- 31 Y. Krockenberger, K. Mogare, M. Reehuis, M. Tovar, M. Jansen, G. Vaitheeswaran, V. Kanchana, F. Bultmark, A. Delin, F. Wilhelm, A. Rogalev, A. Winkler and L. Alff, *Phys. Rev. B: Condens. Matter Mater. Phys.*, 2007, **75**, 020404.
- 32 H. L. Feng, M. Arai, Y. Matsushita, Y. Tsujimoto, Y. Guo, C. I. Sathish, X. Wang, Y. H. Yuan, M. Tanaka and K. Yamaura, *J. Am. Chem. Soc.*, 2014, **136**, 3326.
- 33 M. P. Ghimire and X. Hu, *Mater. Res. Express*, 2016, **3**, 106107.
- 34 R. Morrow, K. Samanta, T. Saha-Dasgupta, J. Xiong, J. W. Freeland, D. Haskel and P. M. Woodward, *Chem. Mater.*, 2016, **28**, 3666.
- 35 H. L. Feng, M. P. Ghimire, Z. Hu, S.-C. Liao, S. Agrestini, J. Chen, Y. Yuan, Y. Matsushita, Y. Tsujimoto, Y. Katsuya, M. Tanaka, H.-J. Lin, C.-T. Chen, S.-C. Weng, M. Valvidares, K. Chen, F. Baudalet, A. Tanaka, M. Greenblatt, L. H. Tjeng and K. Yamaura, *Phys. Rev. Mater.*, 2019, **3**, 124404.
- 36 Y. Yuan, H. L. Feng, M. P. Ghimire, Y. Matsushita, Y. Tsujimoto, J. He, M. Tanaka, Y. Katsuya and K. Yamaura, *Inorg. Chem.*, 2015, **54**, 3422.
- 37 D. K. Yadav, S. R. Bhandari, B. P. Belbase, G. C. Kaple, D. P. Rai and M. P. Ghimire, *Comput. Mater. Sci.*, 2019, **170**, 109168.
- 38 W. Song, E. Zhao, J. Meng and Z. Wu, *J. Chem. Phys.*, 2009, **130**, 114707.
- 39 S. Geprags, P. Majewski and R. Gross, *J. Appl. Phys.*, 2006, **99**, 08J102.
- 40 M. Nabi and D. C. Gupta, *RSC Adv.*, 2019, **9**, 15852.
- 41 K. A. Parrey, S. A. Khandy, I. Islam, A. Laref, D. C. Gupta, A. Niazi, A. Aziz, S. G. Ansari, R. Khenata and S. Rubab, *J. Electron. Mater.*, 2018, **47**, 7.

- 42 M. Roknuzzaman, C. Zhang, K. Ostrikov, A. Du, H. Wang, L. Wang and T. Tesfamichael, *Sci. Rep.*, 2019, **9**, 718.
- 43 T. Ahmed, A. Chen, D. A. Yarotski, S. A. Trugman, Q. Jia and J.-X. Zhu, *APL Mater.*, 2017, **5**, 035601.
- 44 R. Morrow, J. R. Soliz, A. J. Hauser, J. C. Gallagher, M. A. Susner, M. D. Sumption, A. A. Aczel, J. Yan, F. Yang and P. M. Woodward, *J. Solid State Chem.*, 2016, **238**, 46.
- 45 S. R. Bhandari, R. K. Thapa and M. P. Ghimire, *J. Nep. Phys. Soc.*, 2015, **3**, 89.
- 46 M. Rafique, S. Yong and H. Tan, *Phys. E.*, 2017, **88**, 115.
- 47 M. Rafique, M. A. Unar, I. Ahmed, A. R. Chachar and Y. Shuai, *J. Phys. Chem. Solids*, 2018, **118**, 114.
- 48 M. Rafique, S. Yong and H. Tan, *J. Mater. Chem. C*, 2017, **5**, 8112.
- 49 P. Blaha, K. Schwarz, G. K. H. Madsen, D. Kvasnicka and J. Luitz, *An Augmented Plane Wave Plus Local Orbitals Program for Calculating Crystal Properties*, Technische Universität Wien, Vienna, Austria, 2001, ISBN 3-9501031-1-2.
- 50 J. P. Perdew, K. Burke and M. Ernzerhof, *Phys. Rev. Lett.*, 1996, **77**, 3865.
- 51 J. Kunes, P. Novak, M. Divis and P. M. Oppeneer, *Phys. Rev. B: Condens. Matter Mater. Phys.*, 2001, **63**, 205111.
- 52 R. Muhammad, M. A. Uqaili, Y. Shuai, M. A. Mahar and I. Ahmed, *Appl. Surf. Sci.*, 2018, **458**, 145.
- 53 K. Koepf and H. Eschrig, *Phys. Rev. B: Condens. Matter Mater. Phys.*, 1999, **59**, 1743, <https://www.fplo.de/>.
- 54 P. B. Allen, *Boltzmann theory and resistivity of metals in Quantum Theory of Real Materials*, ed. J. R. Chelikowsky and S. G. Louie, Kluwer, Boston, 1996.
- 55 G. K. H. Madsen and D. J. Singh, *Comput. Phys. Commun.*, 2006, **67**, 175.
- 56 N. Zu, R. Li and R. Ai, *J. Magn. Magn. Mater.*, 2018, **467**, 145–149.
- 57 H. T. Jeng and G. Y. Guo, *Phys. Rev. B: Condens. Matter Mater. Phys.*, 2003, **67**, 094438.
- 58 J. S. Toll, *Phys. Rev.*, 1956, **104**, 1760.
- 59 D. Hoat, J. R. Silva and A. M. Blas, *J. Solid State Chem.*, 2019, **85**, 270.
- 60 H. Sevincli, C. Sevik, T. Cagin and G. Cuniberti, *Sci. Rep.*, 2013, **3**, 1228.
- 61 S. R. Boona, *Nature*, 2017, **549**, 169.
- 62 G. Tan, S. Hao, J. Zhao, C. Wolverton and M. G. Kanatzidis, *J. Am. Chem. Soc.*, 2017, **139**, 6467.
- 63 P. Roy, V. Waghmare and T. Maiti, *RSC Adv.*, 2016, **6**, 54636.
- 64 M. Saxena, K. Tanwar and T. Maiti, *Scr. Mater.*, 2017, **130**, 205.
- 65 P. Roy, I. Bose and T. Maiti, *Integr. Ferroelectr.*, 2016, **34**, 174.
- 66 T. Sugahara, M. Ohtaki and T. Souma, *J. Ceram. Soc. Jpn.*, 2008, **116**, 1278.
- 67 G. K. H. Madsen, *J. Am. Chem. Soc.*, 2006, **128**, 12140.
- 68 J. Yang, H. Li, T. Wu, W. Zhang, L. Chen and J. Yang, *Adv. Funct. Mater.*, 2008, **18**, 2880.
- 69 M.-S. Lee, F. P. Poudeu and S. D. Mahanti, *Phys. Rev. B: Condens. Matter Mater. Phys.*, 2011, **83**, 085204.
- 70 M. Zeeshan, H. K. Singh, J. van den Brink and H. C. Kandpal, *Phys. Rev. Mater.*, 2017, **1**, 075407.
- 71 S. Sharma and S. K. Panday, *Phys. Lett. A*, 2015, **379**, 2357.
- 72 T. M. Tritt, *Annu. Rev. Mater. Res.*, 2011, **41**, 433.
- 73 M. Zeeshan, J. van den Brink and H. C. Kandpal, *Phys. Rev. Mater.*, 2017, **1**, 074401.
- 74 K. A. Parrey, S. A. Khandy, I. Islam, A. Laref, D. C. Gupta, A. Niazi, A. Aziz, S. G. Ansari, R. Khenata and S. Rubab, *J. Electron. Mater.*, 2018, **47**, 3615.
- 75 M. Zeeshan, T. Nautiyal, J. van den Brink and H. C. Kandpal, *Phys. Rev. Mater.*, 2018, **2**, 065407.



Effects of electron-correlation, spin-orbit coupling, and modified Becke-Johnson potential in double perovskites SrLaBB'O₆ (B = Ni, Fe; B' = Os, Ru)

Dinesh Kumar Yadav^a, Shalika Ram Bhandari^{a,b}, Bishnu Prasad Belbase^a, Gopi Chandra Kaphle^{a,b}, Dibya Prakash Rai^c, Madhav Prasad Ghimire^{a,b,*}

^a Central Department of Physics, Tribhuvan University, Kirtipur-44613, Kathmandu, Nepal

^b Condensed Matter Physics Research Center, Butwal-11, Rupandehi, Nepal

^c Physical Sciences Research Center (PSRC), Pachhunga University College, Mizoram University, Aizawl 796001, India

ARTICLE INFO

Keywords:

Double perovskites
Spintronics
Density functional theory
Coulomb-interaction
Spin orbit coupling
Modified Becke-Johnson potential
Mott-insulators

ABSTRACT

We investigate the electronic and magnetic properties of the newly synthesized SrLaBB'O₆ (B = Ni, Fe; B' = Os, Ru) materials on the basis of density functional theory. Within local-density approximation (LDA), except for SrLaNiOsO₆, the studied materials are found to be metallic. Inclusion of electron-correlation effects (*U*) and spin-orbit coupling (SOC) leads to the opening of the band gap at the Fermi level (*E_F*) for all the selected materials. Additionally modified Becke-Johnson (TB-mBJ) potential has been used which is found to enhance the band gap of 0.62 eV and 0.59 eV in SrLaNiOsO₆ and SrLaNiRuO₆, respectively while remains metallic for the SrLaFeOsO₆. The magnetic ground state is found to be antiferromagnetic (AFM) for SrLaNiOsO₆ and SrLaNiRuO₆ consistent with the experimental observations. Replacing Ni by Fe in SrLaNiOsO₆ resulted in SrLaFeOsO₆. The ground state was found to be AFM. The co-operative effects of *U* and SOC opens a band gap (~0.03 eV) dictating the significant influence on SrLaFeOsO₆. On the other hand, the Mott-insulating state is observed with a band gap opening of 0.33 eV and 0.58 eV for SrLaNiOsO₆ and SrLaNiRuO₆, respectively with the dominant contributions from the Os-5*d* and Ru-4*d* bands at and around the Fermi level. The magnetic anisotropy suggests an easy axis along the [001]-direction. Charge ordering is found to be prominent in these compounds. Our result agrees well with the experimental findings.

1. Introduction

The transition metal based double perovskites (DPs) are promising candidates due to the presence of *d*-orbitals which derives the fascinating chemical and physical properties. DPs exhibit diverse properties that includes metallicity, half-metallicity (HM), insulator, ferromagnetism (FM), ferrimagnetism (FIM) and antiferromagnetism (AFM) [1,2], etc. As such, DPs are potential candidates for spintronics application that resulted in faster data transfer and huge memory storage devices. The other reason being their structural stability and variation in the crystal structures from simple cubic to highly distorted monoclinic. The current research is mainly devoted to understand the structural, electronic and magnetic properties of such systems. There are two types of DP with chemical formula A₂BB'O₆ and AA'BB'O₆ respectively, where A, A' are alkaline earth or rare earth elements and B, B' are the transition elements. Among the family of DPs, the compound with Osmium-oxides are found to be rarely investigated due to the safety measures and difficulties in laboratory fabrication, as osmium

and oxygen are highly volatile, as reported in OsO₄[3]. However, the successful synthesis of osmium-oxide based DPs such as SrLaNiOsO₆ and SrLaNiRuO₆ from solid state reactions technique [4] motivates us to carry out thorough investigation and analyse their novel physical properties by means of first principles density functional theory (DFT) approach. It is interesting to note that the novel properties can be achieved by structural modification of A, A' and B, B' sites. For example, observation of a magnetic insulating state in Sr₂MOsO₆ (where M = Cu, Ni) [5], half semi-metallic AFM in Sr₂CrTO₆ (T = Os, Ru) [6], etc. AFM Mott-insulating state with an indirect band gap of 0.25 eV and 0.15 eV in Ca₂MgOsO₆ and Sr₂MgOsO₆, respectively under the effect of electron-correlations [7], and opening of the charge gap of ~0.17 eV in FM-Ba₂NiOsO₆ was found under the co-operative effect of electron-correlation and spin-orbit coupling (SOC) plays significant role. Furthermore, Ba₂NiOsO₆ shows metamagnetic transition and Dirac-Mott insulating FM state near 100 K [8]. An unusual superconducting behaviour has been observed in AOs₂O₇ (A = Cs, Rb and K) [9], magnetically driven metal-insulator transition (MIT) in NaOsO₃ at Neel

* Corresponding author at: Central Department of Physics, Tribhuvan University, Kirtipur-44613, Kathmandu, Nepal.

E-mail address: mpghimire@tucdp.edu.np (M.P. Ghimire).

<https://doi.org/10.1016/j.commsatsci.2019.109168>

Received 14 April 2019; Received in revised form 25 July 2019; Accepted 26 July 2019

0927-0256/ © 2019 Elsevier B.V. All rights reserved.

temperature (T_N) of 411 K [10]. The metallic LiOsO_3 shows ferroelectric type structural transition [11]. Moreover, DPs like $\text{Sr}_2\text{FeMoO}_6$ and $\text{Sr}_2\text{FeReO}_6$ are found to be HM-FIM which displays a giant tunneling magnetoresistance above room temperature [12–14]. $\text{Sr}_2\text{CrOsO}_6$ shows FIM order below Curie temperature ($T_C = \sim 725$ K), which seems to be the highest T_C known so far in DP oxides [15,16]. In addition, $\text{Sr}_2\text{ScOsO}_6$ shows AFM transition at 92 K [17] while $\text{Ca}_2\text{FeOsO}_6$ displays FIM transition at 320 K [18].

Recently, SrLaNiIrO_6 and SrLaMgIrO_6 have been studied and found to be AFM and weakly paramagnetic, respectively [19]. A first principles study reported the compensated HM, AFM semiconductor and HMF properties in $\text{Sr}_2\text{NiOsO}_6$, $\text{Sr}_2\text{FeOsO}_6$ and $\text{Sr}_2\text{NiRuO}_6$ respectively originated from the combine effect of electron correlation and SOC [3,20,21]. Likewise, a HM-FIM to HM-AFM transition is reported in Mott-Hubbard insulator type $\text{Pr}_2\text{MgIrO}_6$ when Sr is doped partially to the Pr sites. The materials are expected to be a novel candidate for spintronic applications [22].

Usually in DPs, LDA and or GGA is found to underestimate the band gap and magnetic moments. These can be corrected either by using LDA + U , GGA + U , or TB-mBJ potential [24,23,25]. Recently using TB-mBJ, electronic and magnetic properties are studied in DPs such as in A_2FeReO_6 ($A = \text{Sr}, \text{Ba}$), Sr_2XReO_6 ($X = \text{Cr}, \text{Mn}, \text{Fe}, \text{Ni}$) and $\text{Sr}_2\text{CrOsO}_6$, respectively [1,26,27]. The insulating state observed in experiment is confirmed for Sr_2XReO_6 ($X = \text{Mn}, \text{Ni}$) [26] and $\text{Sr}_2\text{CrOsO}_6$ [27], respectively, while HM state was observed for A_2FeReO_6 ($A = \text{Sr}, \text{Ba}$) and Sr_2XReO_6 ($X = \text{Cr}, \text{Fe}$) materials [1,26]. The accuracy of the band gap was found better as compared to LDA or GGA.

We recently noticed a newly synthesized $\text{SrLaBB}'\text{O}_6$ materials in which the magnetic atoms Ni (Fe) at B-site and Os (Ru) at B'-sites forms BO_6 and $\text{B}'\text{O}_6$ octahedra [4]. The octahedra in the structures exhibit a strong crystal distortion, which may provide a strong crystal field in addition to sizable strength of SOC. Due to the presence of heavy elements such as Os in DPs it induces larger SOC due to a large spatial extension of orbitals. This can lead to many desirable electronic and magnetic behaviors for technological applications. These intriguing combination are found in $\text{SrLaBB}'\text{O}_6$. This motivate us to explore the novel properties of this material, which are theoretically less studied due to their complex distribution of charges. The main goal here is to study the electronic and magnetic properties of these materials.

2. Crystal structures and computational details

The crystal structure of $\text{SrLaBB}'\text{O}_6$ as shown in Fig. 1 has a space group $P2_1/n$ in which BO_6 and $\text{B}'\text{O}_6$ octahedra maintains the monoclinic structure [4,28]. There are three sort of oxygen atoms in B (B')-O1, B (B')-O2 and B (B')-O3 (see in Fig. 1).

Here, we perform the DFT calculations to investigate the electronic and magnetic properties of $\text{SrLaBB}'\text{O}_6$. It is based on the full potential-linearized augmented plane wave plus local orbital (FP-LAPW + lo) method as implemented in the WIEN2k code [29]. The expansion in spherical harmonics was taken up to $l = 10$ for the radial wave function and charge densities and potentials were represented up to $l = 6$. The commonly used convergence criterion was chosen to be 7.0 of basis set $R_{MT} \times K_{max}$, where R_{MT} and K_{max} are smallest atomic sphere radius and plane wave cutoff respectively. The non-overlapping muffin-tin sphere radii (R_{MT}) of 2.34, 2.50, 2.06, 2.02, 2.02 and 1.65 Bohr radius are used for Sr, La, Ni, Fe, Ru, Os and O respectively. The full Brillouin zone was sampled with 500 k -points ($8 \times 8 \times 6$ -mesh). For the exchange-correlation potential local density approximation (LDA) [30] was chosen for the self-consistent calculations as this functional is sufficient to address the results similar to GGA [31] functional. In addition, we use mBJ-potential proposed by Tran and Blaha [24,25] to resolve the band gap and related properties. The calculations are considered to be converged when the energy and charge convergence are less than 10^{-5} Ry and $10^{-4}e$, respectively. The Coulomb interactions (U) for the

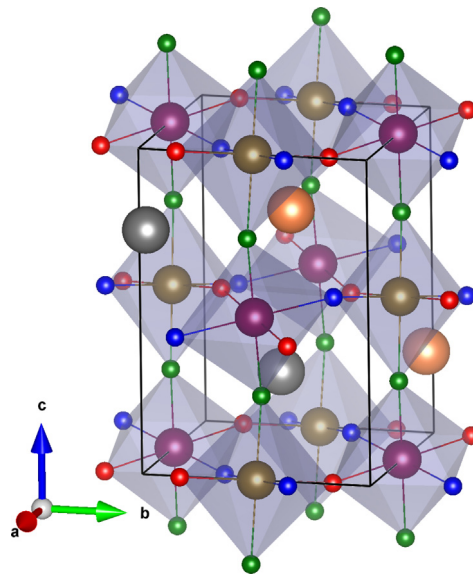


Fig. 1. Crystal structure of SrLaNiOsO_6 (colors in orange, grey, purple, gold, red, blue and green spheres corresponds to Sr, La, Ni, Os, O1, O2 and O3 atoms, respectively). (For interpretation of the references to colour in this figure legend, the reader is referred to the web version of this article.)

magnetic atoms Ni (Fe) and Os (Ru) are the system dependent quantity. The value of U generally separates the occupied and unoccupied states of the atoms. The values of U chosen in our calculations are based on the general values mostly used in literatures for Ni (Fe) and Os (Ru) atoms respectively. For SrLaNiOsO_6 and SrLaFeOsO_6 , U_{Os} used are 0.5 eV and 1.5 eV, respectively. U_{Ni} is fixed to 5.0 eV for all the systems, similar to the previous reported values such as in $\text{Sr}_2\text{NiOsO}_6$ [3], $\text{Ca}_2\text{FeOsO}_6$ [32] and $\text{Sr}_2\text{FeOsO}_6$ [33], respectively. For SrLaNiRuO_6 we use $U_{Ru} = 0.5$ eV comparable to the values used in $\text{Sr}_2\text{NiRuO}_6$ [21]. Since Ru-4d and Os-5d orbitals are delocalized compared to Ni-3d orbitals, the chosen values of Os (Ru) are small. In the present calculations, $U_{eff} = U - J$ with J fixed to zero in LDA + U . The SOC was included as the second variational step using the scalar-relativistic eigenfunctions as a basis [34]. Note that the experimental parameters with $P2_1/n$ consists only of 6 equivalent atoms with one magnetic atoms at the B and B' sites. In order to obtain the four different magnetic configurations, a $1 \times 1 \times 1$ supercell was generated which corresponds to a total of 20 atoms with two each of in-equivalent magnetic atoms at the B and B' sites.

3. Results and discussion

The experimental lattice parameters measured from neutron powder diffraction at 10 K [4] has been optimized. The obtained values are used for electronic and magnetic state calculations. We calculate the total energies for four possible magnetic configurations with alignments of inequivalent atoms Ni1, Ni2, Os1 and Os2 in SrLaNiOsO_6 as follows: one FM ($\uparrow\uparrow\uparrow$), two AFM (AF1- $\uparrow\downarrow\uparrow\downarrow$, AF2- $\uparrow\downarrow\downarrow\uparrow$) and one FIM ($\uparrow\downarrow\downarrow$) as shown in Fig. 2. The AF2 ($\uparrow\downarrow\downarrow$) magnetic configuration is found to be the ground states consistent with the experimental observation [4] indicating the AFM configuration at ground state. The energy difference to the next lowest order (FIM) is ~ 8 meV within LDA calculations. This shows the competing ground state among the AF states with a possibility of canting AFM state. Similarly, the ground state is AF2 for SrLaFeOsO_6 with energy difference of ~ 21 meV with respect to the next lowest order (AF1). In contrary, SrLaNiRuO_6 is found to have the AF1 ground state which competes with the AF2-state with an energy difference ~ 31 meV. SrLaNiRuO_6 undergo long range magnetic interaction by considering (Ni^{2+} - Ni^{2+} and Ru^{5+} - Ru^{5+}) AF coupling [35] consistent with our findings.

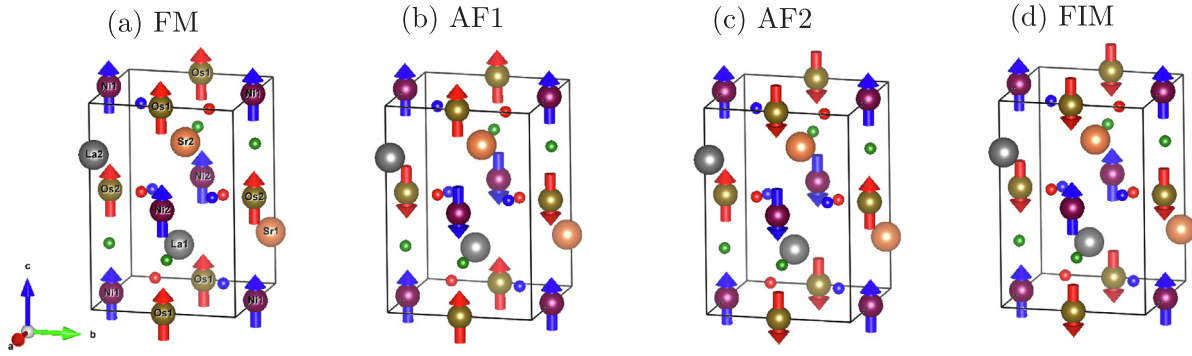


Fig. 2. Magnetic configuration of SrLaNiOsO₆: (a) FM, (b) AF1, (c) AF2, and (d) FIM. The blue and red arrows within the crystal structure indicates the direction of Ni and Os spins along the direction of easy axis [001].

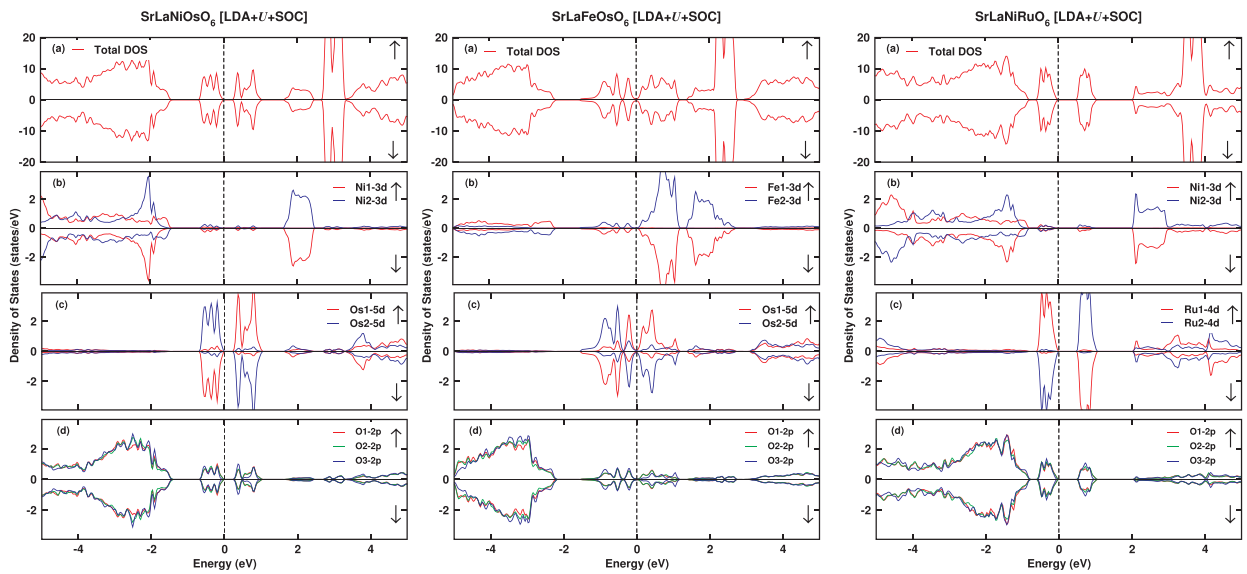


Fig. 3. (a) Total and partial DOS of (b) B (Ni, Fe), (c) B' (Os, Ru), and (d) O-atoms in spin up (\uparrow) and spin down (\downarrow) channel for SrLaBB'O₆ within LDA + U + SOC functional. The vertical dotted line indicates the $E_F = 0$.

Fig. 3 shows the density of state (DOS) within LDA + U + SOC functional for SrLaNiOsO₆, SrLaFeOsO₆ and SrLaNiRuO₆ with (a) the total DOS and partial DOS of (b) Ni (Fe)-3d states, (c) Ru-4d (Os-5d) states and (d) O-2p states, respectively. SrLaNiOsO₆ within LDA calculations shows a band gap of 0.04 eV with symmetric DOS in both spin up and spin down channels. The presence of transition elements Ni and Os derive strong correlation effect which is ignored in LDA or GGA functionals. The implementation of DFT + U approximation includes the electron-correlation (U) to get more accurate results close to experimental finding and the band gap is opened to 0.44 eV. As heavy atoms are strongly influenced by SOC, it has been applied to examine the effect of spin quantization along [100], [010], [001], [111]-directions. We found the easy axis along [001]-direction. Considering SOC in SrLaNiOsO₆ the band gap has been reduced to 0.33 eV, which is close agreement with the recent experimentally obtained activation energy of 0.35 eV at 300 K [36]. Thus, the combined effect of U and SOC in SrLaNiOsO₆ enhanced the result significantly.

We further consider the mBJ effects in SrLaBB'O₆ (B = Ni, Fe; B' = Os, Ru). A significant increase in the exchange splitting of Ni (Fe)-3d, Ru-4d and Os-5d states has been noted around (E_F). As a result large value of exchange splitting is seen in Ni-3d state as compared to Fe-3d states. Figs. 5 and 6 shows the DOS and band structure using mBJ potential for the selected system. It is interesting to note that the band gap which remains 0.04 eV in LDA rises to 0.62 eV when mBJ is applied in SrLaNiOsO₆, hence over-estimating the experimental band gap (0.35 eV).

The splitting of the *d*-state electrons from different transition metals due to mBJ are found around the Fermi level (E_F) (see Fig. 5 (b), (c)).

Similarly, SrLaNiRuO₆ which shows metallic state in LDA, is found to have a band gap of 0.51 eV and 0.58 eV when U and U + SOC is applied. Interestingly the band gap increases for this particular system within SOC, while another group in their calculation within LSDA + U + SOC reported insignificant effect of SOC in SrLaNiRuO₆ [35]. Further we observe a noticeable changes on the Ru-4d bands, in which it splits near E_F as can be seen in the DOS and band structure plots (see Fig. 3 and Fig. 4). With mBJ, the band gap is found to be 0.59 eV as can be seen in Figs. 5 and 6 with the detail informations on magnetic moments in Table 1. and 2, respectively.

Likewise, SrLaFeOsO₆ is found to be metallic for U_{Os} as large as 2 eV. With SOC, a tiny band gap of 0.03 eV is induced resulting in the semiconducting state. Unfortunately, the system remains metallic even when the mBJ potential is used. The related band structures for all the compounds shows an indirect band gap as shown in Fig. 4 and Fig. 6. The calculated band gaps suggest that SrLaNiOsO₆, SrLaFeOsO₆ and SrLaNiRuO₆ are Mott-insulators. The major contributions to the DOS around E_F are from the Os-5d and Ru-4d orbitals.

From the DOS plots shown in Fig. 3 for all the three compounds, we observe that the main contribution near E_F are from the *d* states of Ni, Fe, Os and Ru respectively hybridizing strongly with the oxygen 2p states. The spin polarized DOS shows symmetric behavior in spin up and spin down channel resulting in zero effective magnetic moment.

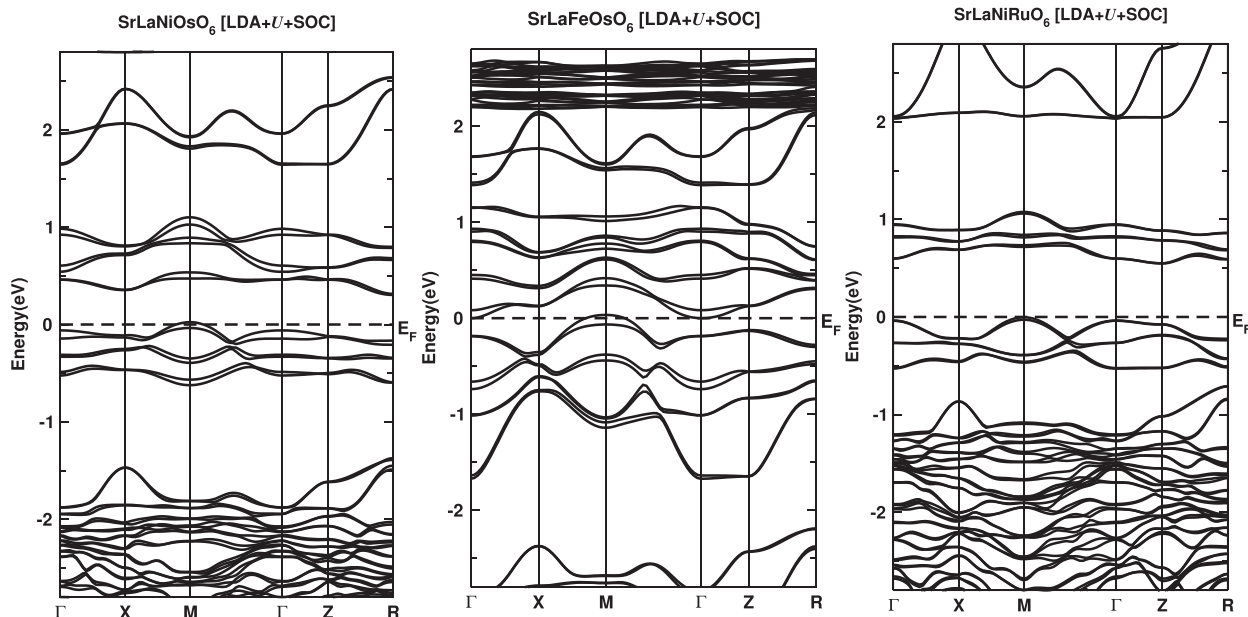


Fig. 4. Band structures of the SrLaBB'O₆ (B = Ni, Fe; B' = Os, Ru) within LDA + *U* + SOC functional. Dashed horizontal lines at zero energy corresponds to E_F .

The strong hybridization observed between oxygen 2*p* bands and *d* states of Ni (Fe)-3*d* and Ru-4*d* (Os-5*d*) around E_F are caused by octahedral distortion.

The band structure for the studied compounds are shown in Fig. 4 and Fig. 6 where Ru-4*d* (Os-5*d*) bands that are dominant near E_F splits due to finite strength of SOC. This resulted in the insulating behaviour with an indirect band gap for these systems.

In SrLaNiOsO₆ charge state of Ni is 2+ with $3d - t_{2g}^6 e_g^2$ configuration and that of Os is 5+ with $5d - t_{2g}^3 e_g^0$ respectively, as shown in Fig. 7. When comparing the partial DOS features around E_F (see Figs. 3 and 5) the major contributions are from Ni-3*d* and Os-5*d* characters with some mixing from the O-2*p* states. As can be seen, the Ni-3*d* states are fully occupied (d^5) in the spin up channel while only the t_{2g} occupied in spin down channel, whereas for Os only t_{2g} states are occupied in spin one of the spin channel with the remaining *d*-states empty in both spin channels. This lead to charge state of Ni²⁺ with d^8 occupancy and Os⁵⁺ with d^3 occupancy.

Moving onto SrLaFeOsO₆, the charge state of Fe becomes 3+ with $3d - t_{2g}^3 e_g^2$ and of Os is 4+ with $5d - t_{2g}^2 e_g^0$ configuration as shown in Fig. 7. From the partial DOS calculations we found that Fe-3*d* states are fully occupied in the spin up channel and empty in spin down channel,

while only t_{2g} is occupied in spin down channel leaving all the remaining bands empty in both spin channels. Likewise, the charge state of Ni is 2+ with d^8 and that of Ru is 5+ with d^3 configurations in SrLaNiRuO₆. This shows the similar features as discussed above for SrLaNiOsO₆. From the above discussion it clearly indicates a change in the charge transfer from B to B' when an atom are interchanged.

We further investigate the magnetic behavior in selected systems as tabulated in Table 1 and Table 2. As from the ionic picture for SrLaNiOsO₆, Ni and Os atoms carry spin magnetic moments of $2 \mu_B$ and $3 \mu_B$ each, while from DFT resulted Ni = $1.74 \mu_B$ and Os = $1.36 \mu_B$ respectively. The moment are found to increase when applying *U* while due to SOC, Os-moment decreases. Inclusion of mBJ is found to increase the spin magnetic moment of Ni and Os contradicting with the LDA but are closer to LDA + *U* and LDA + *U* + SOC results. Similar trends are noticed, for other materials as well which indicates the better agreement of the magnetic moments. When Fe is doped to Ni-site, the ionic magnetic moments rises to $5 \mu_B$ and $2 \mu_B$ each for Fe and Os respectively. The calculated moments are $4.04 \mu_B$ and $0.88 \mu_B$ for Fe and Os atoms with SOC included.

In SrLaNiRuO₆ although the ionic magnetic moments are same as of the SrLaNiOsO₆, the calculated magnetic moment of Ni and Ru are 1.70

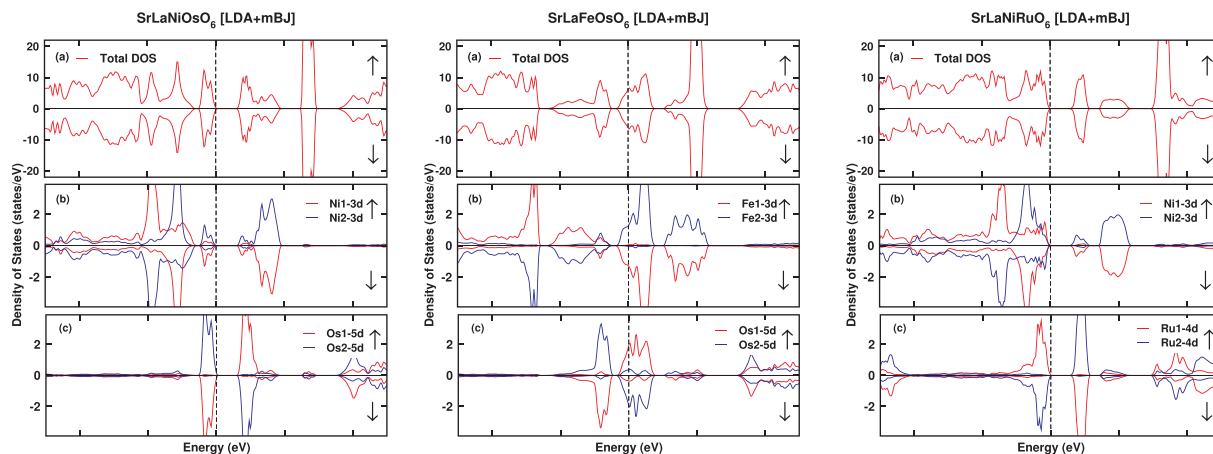


Fig. 5. (a) Total and partial DOS of (b) B (Ni, Fe), and (c) B' (Os, Ru) in spin up (↑) and spin down (↓) channel for SrLaBB'O₆ within LDA + mBJ functional. The vertical dotted line indicates $E_F = 0$.

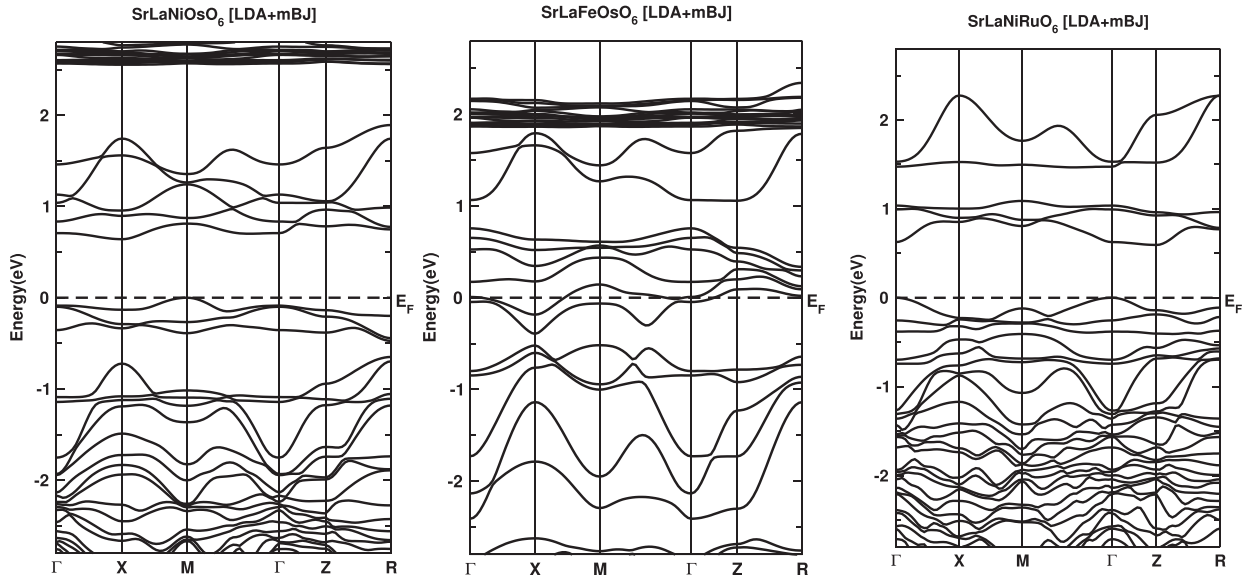


Fig. 6. Band structures of the SrLaBB'O₆ (B = Ni, Fe; B' = Os, Ru) within LDA + mBJ functional. Dashed horizontal lines at zero energy corresponds to the Fermi level.

Table 1

Calculated spin magnetic moments (in μ_B) of B (Ni, Fe), B' (Os, Ru), 3 inequivalent oxygens and the gap 'E_g' (eV) for SrLaBB'O₆.

Site	SrLaNiOsO ₆		SrLaFeOsO ₆		SrLaNiRuO ₆	
	LDA	LDA + mBJ	LDA	LDA + mBJ	LDA	LDA + mBJ
B	1.38	1.57	3.54	3.64	1.49	1.60
B'	1.36	1.58	0.77	1.17	1.54	1.70
O1	0.06	0.09	0.02	0.02	0.19	0.19
O2	0.06	0.08	0.02	0.01	0.19	0.20
O3	0.16	0.17	0.14	0.18	0.05	0.08
E _g	0.04	0.62	Metallic	Metallic	Metallic	0.59

μ_B and $1.65 \mu_B$ respectively. This difference in the magnetic moment is due to the partial charge transfer to inequivalent oxygens via charge transfer between B-O and B'-O site atoms in addition to octahedral distortions.

With consideration of SOC in SrLaNiOsO₆, orbital moment is induced on Ni and Os are antiparallel to that of the spin magnetic moment as tabulated in Table 2. This results in the reduction of the net magnetic moment. Additionally, orbital moment of Ni is relatively large (i.e., $0.22 \mu_B$) as compared to the Os atoms with $0.15 \mu_B$. The reason for large orbital moment is caused by the larger orbital coupling of Ni with the oxygen atoms in comparison to Os with the oxygen atoms. Similar features had been reported in Ca₂CoOsO₆ [37]. Due to hybridization with Ni and Os, oxygen also gain small magnetic moment and polarization is mainly found on 2p-orbitals. For the case of SrLaFeOsO₆ the

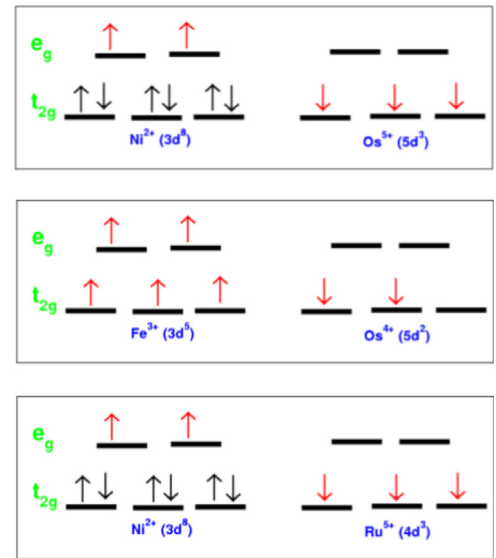


Fig. 7. Schematic picture of the occupancies of Ni, Fe, Os, and Ru d states in SrLaNiOsO₆ (top), SrLaFeOsO₆ (middle) and SrLaNiRuO₆ (bottom) as obtained from the DFT calculations.

orbital moment are $0.09 \mu_B$ and $0.22 \mu_B$ respectively similar to Sr₂FeOsO₆ [20]. In SrLaNiRuO₆, the orbital magnetic moment of Ni and Ru are $0.24 \mu_B$ and $0.03 \mu_B$, analogous to Sr₂NiRuO₆ [21] and

Table 2

Calculated spin magnetic moments (in μ_B) of B (Ni, Fe), B' (Os, Ru), 3 oxygens and band gap 'E_g' (eV). The calculated orbital moments at B and B' sites are shown within parentheses for SrLaBB'O₆.

Site	SrLaNiOsO ₆		SrLaFeOsO ₆		SrLaNiRuO ₆	
	LDA + U	LDA + U + SOC	LDA + U	LDA + U + SOC	LDA + U	LDA + U + SOC
B	1.68	1.68(0.22)	4.02	4.04(0.09)	1.70	1.70(0.24)
B'	1.52	1.36(0.15)	1.09	0.88(0.23)	1.66	1.65(0.03)
O1	0.09	0.08	0.02	0.01	0.16	0.16
O2	0.09	0.08	0.01	0.02	0.16	0.16
O3	0.14	0.13	0.14	0.12	0.08	0.08
E _g	0.44	0.33	Metallic	0.03	0.51	0.58

$\text{Sr}_2\text{CrRuO}_6$ [6].

4. Conclusions

On the basis of DFT calculations, we found the semiconducting behavior in SrLaBB'O_6 ($B = \text{Ni, Fe; B}' = \text{Os, Ru}$) materials. All the studied materials having monoclinic structure are found to have the antiferromagnetic ground state with their easy axis oriented along the [001]-direction. SrLaNiOsO_6 and SrLaNiRuO_6 shows Mott-like insulating state under the co-operative effect of Coulomb interaction, SOC in addition to the crystal field with a band gap of 0.33 eV and 0.58 eV, respectively. When Ni is replaced with Fe in SrLaNiOsO_6 , the electronic behavior shows metallic state within LDA + U . Upon inclusion of SOC, a tiny band gap of 0.03 eV has been obtained in SrLaFeOsO_6 . Similar to the effects of correlation, the band gap are found to be 0.62 eV in SrLaNiOsO_6 and 0.59 eV in SrLaNiRuO_6 , while remains metallic in SrLaFeOsO_6 . For all the systems, the net calculated magnetic moment is zero per unit cell with sizable spin and orbital magnetic moments. Our results are found consistent with the available experimental finding of Morrow et. al. [4]. Charge ordering is found to be prominent in these compounds. From this study SrLaFeOsO_6 and SrLaNiRuO_6 are predicted to be a semiconductor similar to the parent material SrLaNiOsO_6 . Further study on these type of materials are strongly suggested by varying the BB' sites, to tune the novel properties useful for spintronics and quantum magnetic devices fabrication.

CRediT authorship contribution statement

Dinesh Kumar Yadav: Conceptualization, Investigation, Methodology, Visualization, Writing - original draft, Writing - review & editing. **Shalika Ram Bhandari:** Investigation, Methodology, Visualization, Writing - original draft. **Bishnu Prasad Belbase:** Investigation, Writing - original draft. **Gopi Chandra Kaphle:** Resources, Writing - original draft, Project administration, Supervision. **Dibya Prakash Rai:** Resources, Formal Analysis. **Madhav Prasad Ghimire:** Conceptualization, Investigation, Methodology, Software, Validation, Visualization, Project administration, Resources, Supervision, Writing - original draft, Writing - review & editing.

Conflict of interest

There is no conflict of interest.

Acknowledgments

This work is a part of the Higher Education Reform Project (HERP DLI-7B) of Tribhuvan University, Kirtipur, Nepal. DKY and BPB acknowledges CMPRC-Butwal, Nepal for the computational facilities.

References

- [1] D.P. Rai, A. Shankar, M.P. Ghimire, R.K.Thapa Sandeep, *Comp. Mat. Sc.* 101 (2015) 313.
- [2] M.T. Anderson, K.B. Greenwood, G.A. Taylor, K.R. Poeppelmeier, *Prog. Solid State Ch.* 22 (1993) 197.
- [3] W. Song, E. Zhao, J. Meng, Z. Wu, *J. Chem. Phys.* 130 (2009) 114707.
- [4] R. Morrow, M.A. McGuire, Jiaqiang, P.M. Woodward, *Inorg. Chem.* 57 (2018) 2989.
- [5] C. Tian, A.C. Wibowo, H.C. zur Loye, M.H. Whangbo, *Inorg. Chem.* 50 (2011) 4142.
- [6] K.W. Lee, W.E. Pickett, *Phys. Rev. B* 77 (2008) 115101.
- [7] Y. Yahua, H.L. Feng, M.P. Ghimire, Y. Matsushita, Y. Tsujimoto, J. He, M. Tanaka, Y. Katsuya, K. Yamaura, *Inorg. Chem.* 54 (2015) 3422.
- [8] H.L. Feng, S. Calder, M.P. Ghimire, Y. Yuan, Y. Shirako, Y. Tsujimoto, Y. Matsushita, Z. Hu, C.Y. Kuo, L.H. Tjeng, T.W. Pi, Y.L. Soo, J. He, M. Tanaka, Y. Katsuya, M. Richter, K. Yamaura, *Phys. Rev. B* 94 (2016) 235158.
- [9] Z. Hiroi, J. Yamaura, K. Hattori, *J. Phys. Soc. Jpn.* 81 (2012) 011012.
- [10] S. Calder, V.O. Garlea, D.F. McMorrow, M.D. Lumsden, M.B. Stone, J.C. Lang, J.W. Kim, J.A. Schlueter, Y.G. Shi, K. Yamaura, Y.S. Sun, Y. Tsujimoto, A.D. Christianson, *Phys. Rev. Lett.* 108 (2012) 257209.
- [11] Y.G. Shi, Y.F. Guo, X. Wang, A.J. Princep, D. Khalyavin, P. Manuel, Y. Michiue, A. Sato, T. Tsuda, S. Yu, M. Arai, Y. Shirako, M. Akaogi, N.L. Wang, K. Yamaura, A.T. Boothroyd, *Nat. Mater.* 12 (2013) 1023.
- [12] K.I. Kobayashi, T. Kimura, H. Sawada, K. Terakura, Y. Tokura, *Nature (London)* 395 (1998) 677.
- [13] K.I. Kobayashi, T. Kimura, Y. Tomioka, H. Sawada, K. Terakura, Y. Tokura, *Phys. Rev. B* 59 (1999) 11159.
- [14] M. Sakai, A. Massuno, D. Kan, M. Hashisaka, K. Takata, A. Azuma, M. Takano, Y. Shimakawa, *Appl. Phys. Lett.* 90 (2007) 072903.
- [15] Y. Krockenberger, K. Mogare, M. Reehuis, M. Tovar, M. Jansen, G. Vaitheeswaran, V. Kanchana, F. Bultmark, A. Delin, F. Wilhelm, A. Rogalev, A. Winkler, L. Alff, *Phys. Rev. B* 75 (2007) 020404.
- [16] O.N. Meetei, O. Erten, M. Randeria, N. Trevedi, P. Woodward, *Phys. Rev. Lett.* 110 (2013) 087203.
- [17] A.E. Taylor, R. Morrow, D.J. Singh, S. Calder, M.D. Lumsden, P.M. Woodward, A.D. Christianson, *Phys. Rev. B* 91 (2015) 100406.
- [18] H.L. Feng, M. Arai, Y. Matsushita, Y. Tsujimoto, Y. Guo, C.I. Sathish, X. Wang, Y.H. Yuan, M. Tanaka, K. Yamaura, *J. Am. Chem. Soc.* 136 (2014) 3326.
- [19] K.K. Wolff, S. Agrestini, A. Tanaka, M. Jansen, L.H. Tjeng, *Z. anorg. allg. Chem.* 643 (2017) 2095.
- [20] J. Wang, N. Zu, X. Hao, Y. Xu, Z. Li, Z. Wu, F. Gao, *Physica Status Solidi-R* 8 (2014) 776.
- [21] S.E.A. Yousif, O.A. Yassin, *J. Alloy. Compd.* 506 (2010) 456.
- [22] M.P. Ghimire, L.H. Wu, X. Hu, *Phys. Rev. B* 93 (2016) 134421.
- [23] A.D. Becke, M.R. Roussel, *Phys. Rev. A* 39 (1989) 3761.
- [24] F. Tran, P. Blaha, *Phys. Rev. Lett.* 102 (2009) 226401.
- [25] A.D. Becke, E.R. Johnson, *J. Chem. Phys.* 124 (2006) 221101.
- [26] G. San-Dong, *Eur. Phys. J. B* 88 (2015) 82.
- [27] G. San-Dong, *Chin. Phys. Lett.* 31 (2014) 017101.
- [28] K. Momma, F. Izumi, *J. Appl. Crystallogr.* 44 (2011) 1272.
- [29] P. Blaha, K. Schwarz, G.K.H. Madsen, D. Kvasnicka, J. Luitz, WIEN2k (version 14.2), An Augmented Plane Wave + Local Orbitals Program for Calculating Crystal Properties, Technische Universität Wien, Vienna, Austria, 2001.
- [30] V.I. Anisimov, I.V. Solovyev, M.A. Korotin, M.T. Czyzyk, G.A. Sawatzky, *Phys. Rev. B* 48 (1993) 16929.
- [31] J.P. Perdew, K. Burke, M. Ernzerhof, *Phys. Rev. Lett.* 77 (1996) 3865.
- [32] M.P. Ghimire, X. Hu, *Mater. Res. Express* 3 (2016) 106107.
- [33] S. Kanungo, B. Yan, M. Jansen, C. Felser, *Phys. Rev. B* 89 (2014) 214414.
- [34] J. Kuneš, P. Novák, M. Diviš, P.M. Oppeneer, *Phys. Rev. B* 63 (2001) 205111.
- [35] X. Ou, F. Fan, X. Chen, T. Li, L. Jiang, A. Stroppa, X. Ouyang, H. Wu, *Europhys. Lett.* 123 (2018) 57003.
- [36] H.L. Feng, W. Schnelle, L.H. Tjeng, M. Jansen, *Solid State Commun.* 243 (2016) 49.
- [37] R. Morrow, K. Samanta, T.S. Dasgupta, J. Xiong, J.W. Freeland, D. Haskel, P.M. Woodward, *Chem. Mater.* 28 (2016) 3666.

PAPER • OPEN ACCESS

Structural, elastic, electronic, and magnetic properties of MnNbZ (Z = As, Sb) and FeNbZ (Z = Sn, Pb) semi-Heusler alloys

To cite this article: Dinesh Kumar Yadav *et al* 2020 *Mater. Res. Express* 7 116527

View the [article online](#) for updates and enhancements.

Recent citations

- [Strain induced electronic structure, and magnetic and structural properties in quaternary Heusler alloys ZrRhTiZ \(Z=Al, In\)](#)
Ram Babu Ray *et al*



240th ECS Meeting ORLANDO, FL
Orange County Convention Center Oct 10-14, 2021



Abstract submission due: April 9

SUBMIT NOW



PAPER

Structural, elastic, electronic, and magnetic properties of MnNbZ (Z = As, Sb) and FeNbZ (Z = Sn, Pb) semi-Heusler alloys

OPEN ACCESS

RECEIVED

28 August 2020

REVISED

3 November 2020

ACCEPTED FOR PUBLICATION

20 November 2020

PUBLISHED

2 December 2020

Dinesh Kumar Yadav^{1,*}, Shalika Ram Bhandari^{1,2} and Gopi Chandra Kaphle^{1,2}¹ Central Department of Physics, Tribhuvan University, Kirtipur-44613, Kathmandu, Nepal² Condensed Matter Physics Research Center, Butwal-11, Rupandehi, Nepal

* Author to whom any correspondence should be addressed.

E-mail: yadavdk072@gmail.com, shalikaa12@gmail.com and gck223@gmail.com**Keywords:** semi-Heusler alloys, half-metals, ferromagnets, modified Becke-Johnson method, elastic constants, semi-Heusler

Original content from this work may be used under the terms of the [Creative Commons Attribution 4.0 licence](https://creativecommons.org/licenses/by/4.0/).

Any further distribution of this work must maintain attribution to the author(s) and the title of the work, journal citation and DOI.

**Abstract**

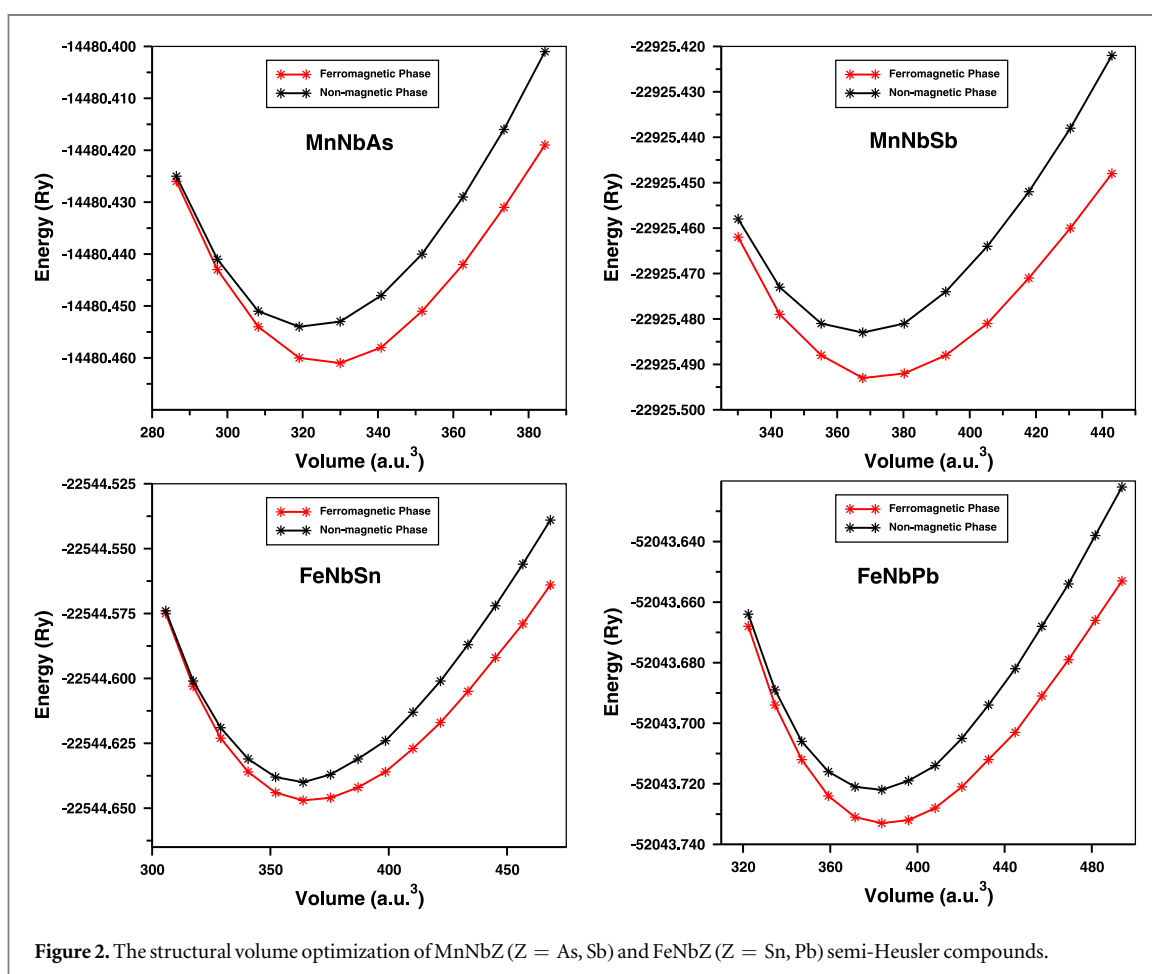
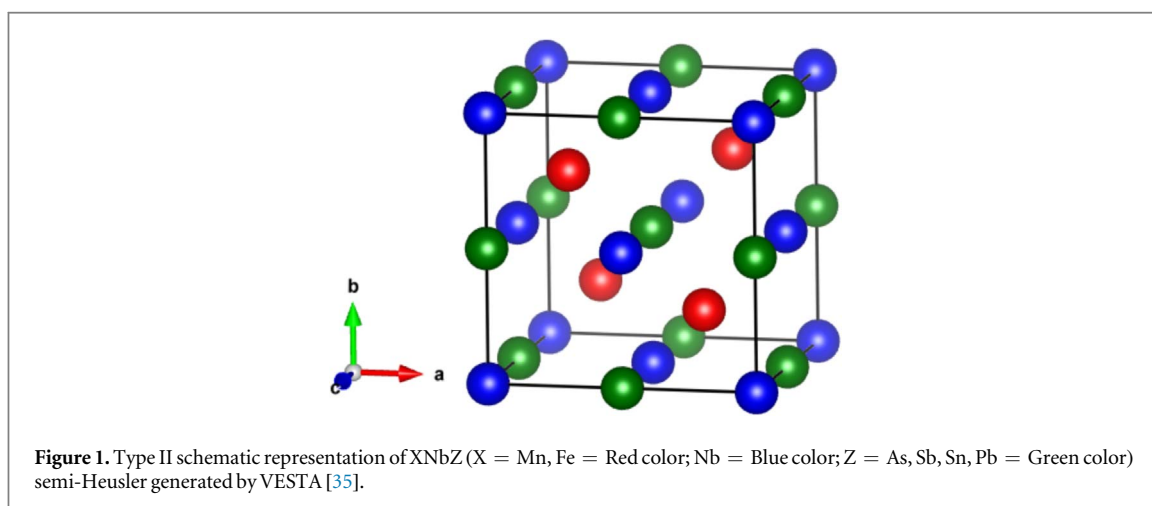
The study of structural, electronic, magnetic, and elastic properties of a new series of semi-Heusler alloys MnNbZ (Z = As, Sb) and FeNbZ (Z = Sn, Pb) has been performed by density functional theory. The magnetic phase and hence the structural stability of the alloys were considered wherein the ferromagnetic state is found to be stable. The half-metallic states are observed from the density of states and band structure calculations. The total magnetic moments found for all studied compounds are $1 \mu_B/\text{f.u.}$, which obey the Slater-Pauling rule for semi-Heusler with ferromagnetic behavior. The calculated cohesive and formation energies confirmed the thermodynamical stability and elastic constant C_{ij} confirmed the mechanical stability. Among the four systems, MnNbAs is found to have the highest ductility (i.e., non-directional metallic bonding) while the remaining systems are found to be brittle in nature (i.e., directional covalent bonding). These properties confirmed that among others, MnNbAs is one of the novel candidate for spintronic device applications.

1. Introduction

The development of new half-metallic ferromagnets is a great interest due to their potential for technological applications in electronic devices [1, 2]. Half-metallic means one of the channel is semiconducting or insulating in nature and other channel is metallic character around the Fermi level, which means 100% polarization at the Fermi level. Many half-metallic materials have been investigated theoretically with high spin polarization [3–6]. The different types of materials have been studied, like transition metal pnictides [7], perovskites and double perovskite [8–12], oxides [13, 14], and Heusler alloys [15, 16]. These magnetic materials are very important in terms of spintronics applications [17, 18]. Among these structures, Heusler alloys are the best candidate for electronic devices because of their high Curie temperature, which is used for industrial applications.

Heusler alloys are classified into three categories; full-Heusler alloys such as Co_2CrSi , Fe_2TaGe [19, 20] quaternary Heusler alloys such as CoFeHfGe , CoFeZrZ (Z = Ge, Sb, Si), FeVRuSi , ZrRhHfZ (Z = Al, Ga, In) [21–24], and semi-Heusler alloys such as NiXSb (X = Ti, V, Cr, Mn), CrZrZ (Z = In, Sn, Sb, Te) [25, 26]. The semi-Heusler alloys show more interesting features as compare to other types of Heusler. These materials show high efficiency thermoelectric properties [27], topological insulator [28], piezoelectric [29], and optoelectronic semiconductors [30]. The semi-Heusler alloys with half-metallic ferromagnet (HMF) are the commonly used materials for spintronic devices. The first half-metal ferromagnetic material was discovered in 1983 by de Groot *et al* in the NiMnSb semi-Heusler compound [31]. After that, researchers were focused on many half-metallic Heusler compounds by experimental synthesis and computational investigations. Semi-Heusler with half metals have attracted for ideal electrode materials for magnetic tunneling junctions (MTJs) [32], giant magnetoresistance devices (GMRs) [33], and for injecting spin polarized currents into semiconductors [34].

The semi-Heusler alloys with the stoichiometric composition XYZ with the ratio of each element are equal in the C1_b structure, while the full Heusler alloys with the stoichiometric form X_2YZ with a ratio of each element is 2:1:1 in the L2_1 structure. Where, X and Y are transition elements such as 3d, 4d, and 5d elements and Z is s and



p-block elements of the periodic table. The cubic full-Heusler compounds have four inter-penetrating positions, while the semi-Heusler structure is obtained by removing (0.75, 0.75, 0.75) position is vacant. The three possible conventional cubic cell of semi-Heusler compounds are X-type1: $4a(0, 0, 0)$, $4b(1/2, 1/2, 1/2)$, $4c(1/4, 1/4, 1/4)$; X-type2: $4c(1/4, 1/4, 1/4)$, $4a(0, 0, 0)$, $4b(1/2, 1/2, 1/2)$, and X-type3: $4b(1/2, 1/2, 1/2)$, $4c(1/4, 1/4, 1/4)$, $4a(0, 0, 0)$ [36]. The structural properties were examined in space group number-216. There are many semi-Heusler compounds predict computationally started using all these three types of structures with varying different parameters on the basis of previously studied isoelectronic compounds.

The aim of the study to investigate the theoretical calculations of structural, electronic, magnetic, and elastic properties of Nb-based compounds. These are computationally investigated compounds so their thermodynamical and mechanical stabilities were checked through cohesive and formation energies and elastic constants. In this study, it has been shown that MnNbAs, MnNbSb, FeNbSn, and FeNbPb compounds are promising candidates for spintronic device fabrications and seeking for future experiment.

Table 1. The lattice parameter, the bulk modulus and its first derivative, equilibrium volume and energies, formation energies (eV/atom), cohesive energy (eV/atom), and energy differences between ferromagnetic and non-magnetic phases.

Compound	a(Angstrom)	B(GPa)	B ¹	V ₀ (a.u. ³)	E ₀ (Ry)	E _{for}	E _{coh}	ΔE _{o(FM-NM)} (Ry/meV)
MnNbAs	5.7769	164.4593	6.0071	325.2488	-14480.460638	-0.38	-7.89	-0.0061/-83.5400
MnNbSb	6.0353	147.9024	7.0661	370.8716	-22925.492987	-0.35	-7.62	-0.0099/-135.2928
FeNbSn	6.0140	139.3926	5.1715	366.9658	-22544.646741	-0.40	-3.87	-0.0076/-103.6456
FeNbPb	6.1091	126.0180	5.5185	384.6463	-52043.732634	-0.05	-3.46	-0.0105/-142.3648

2. Method of calculations

We performed the density functional theory (DFT) calculations to investigate new semi-Heusler compounds using the full-potential linearized augmented plane wave (FP-LAPW) method as implemented in the WIEN2k code [37]. The standard generalized gradient approximation (PBE-GGA) [38] and Tran-Blaha modified Becke-Johnson (TB-mBJ) potential [39, 40] were used for the exchange correlation correction. For mechanical stability, the elastic results were studied using the ElaStic-1.0 package [41].

For the calculation, each atom has a specific muffin-tin radius (R_{MT}) in the range of 2.29 to 2.50. Different atom has different R_{MT} values depending upon the size of the atoms. The initial values of the atom's positions and lattice parameters were the same in both GGA and mBJ calculations. The expansion in spherical harmonics was taken up to $l = 10$ for the radial wave function and charge densities and potentials were represented up to $l = 6$. The commonly used convergence criterion was chosen to be 7.0 of basis set $K_{max} \times R_{MT}$, where R_{MT} and K_{max} are the smallest atomic sphere radius and plane wave cutoff respectively. The G_{max} and cut off energy values used for all these calculations were 10 and -6 respectively in order to get stability in calculations. For the convergence test, the energy criterion and charge criterion were 10^{-6} Ry and 10^{-4} electron respectively, which gives reliable results for the semi-Heusler compounds. Using the tetrahedron method, full Brillouin Zone was sample by 5000 kpoints ($17 \times 17 \times 17$ k-mesh) for self consistent field (SCF) calculations.

3. Results and discussion

3.1. Structural optimization and elastic properties

We begin our calculation by optimizing three possible structures for magnetic and nonmagnetic (NM) phases and found type-2 structure has the lowest energy. We used this type of structure for further calculations of electronic, magnetic, and elastic properties. For the prediction of MnNbZ ($Z = \text{As, Sb}$) and FeNbZ ($Z = \text{Sn, Pb}$) four new cubic semi-Heusler alloys are based on isoelectronic compounds of recently investigated compounds [42]. By optimization for the non-magnetic and ferromagnetic (FM) phases, we got the ferromagnetic state is more stable for all alloys mentioned here, which are clear from energy versus volume optimization for the type-2 structures in figure 2. The energy differences are very small, which is also listed in table 1. From the figure and table, it is clear that all the compounds show the ferromagnetic state is energetically stable. The highest energy difference in FeNbPb is 142.36 meV and the lowest energy difference in MnNbAs is 83.54 meV from FM to NM. The Murnaghan's equation of states (EOS) is given by [43],

$$E = E_0(V) + \frac{BV}{B'(B' - 1)} \left[B \left(1 - \frac{V_0}{V} \right) + \left(\frac{V_0}{V} \right)^{B'} - 1 \right] \quad (1)$$

Where, E_0 and V_0 are the minimum equilibrium energy and volume, B is the bulk modulus, B' is the derivative of the bulk modulus. The first compound MnNbAs is stable at ferromagnetic (red color line) state as compared to nonmagnetic (blue color line) state shown in figure 2. The negative side from the minimum value of the lattice parameter at one point both phases have same energy but on the right side, energy differences are increased from FM to NM. The optimized value of volume is 325.25 a.u.³ and the respective lattice parameter is 5.78 Å. The equilibrium lattice constants for ferromagnetic phase are obtained by minimizing the total energy. The bulk modulus and its first derivative of this compound are 164.46 GPa and 6.01 respectively, which are tabulated in the table 1. Similarly, for remaining three MnNbSb, FeNbSn, and FeNbPb semi-Heusler optimization plots are shown in the same figure 2 and all parameters are tabulated in the same table 1.

The cohesive and formation energies for all these compounds are calculated by using the formula given below to check the investigated compounds are thermodynamically stable or not.

$$E_{coh} = E_{XNbZ}^{tot} - [E_X^{iso} + E_{Nb}^{iso} + E_Z^{iso}] \quad (2)$$

$$E_{for} = E_{XNbZ}^{tot} - [E_X^{bulk} + E_{Nb}^{bulk} + E_Z^{bulk}] \quad (3)$$

Table 2. The calculated elastic constants C_{ij} , bulk modulus B (GPa), shear modulus G (GPa), Young modulus E (GPa), B/G ratio, Cauchy pressure C^μ and Poisson's ratio ν . All units are in GPa except ν and B/G.

Compounds	C_{11}	C_{12}	C_{44}	B	G	E	B/G	C^μ	ν
MnNbAs	224.8	150	57.7	174.92	48.49	133.17	3.61	92.3	0.37
MnNbSb	245.4	91.0	135.9	142.46	108.36	259.33	1.31	-44.9	0.20
FeNbSn	260.6	92.8	143.9	148.74	115.87	275.95	1.28	-51.1	0.19
FeNbPb	202.5	94.1	137.9	130.19	94.84	228.93	1.37	-43.8	0.21

Where as, X = Mn, Fe; Z = As, Sb, Sn, Pb, E_{XNbZ}^{tot} is the total energy and E_X^{bulk} , E_{Nb}^{bulk} , and E_Z^{bulk} are energies of the bulk of X, Nb, and Z-sites elements respectively. In equation (3) E_X^{iso} , E_{Nb}^{iso} , and E_Z^{iso} are the total energies of isolated X, Nb, and Z-sites elements respectively. The obtained cohesive and formation energies are tabulated in the table 1. The negative values for both cohesive and formation energies confirmed the thermodynamical or chemical stability of all four semi-Heusler compounds. Thus, these hypothetical compounds are stable and their experimental synthesis is also possible.

Elastic properties calculation gives the mechanical stability of a solid structure against the arbitrary deformation and the physical properties by using elastic constants (C_{ij}). The strain was used to determine these elastic constants in such a way that the total volume of the system remains constant. Due to the symmetry of the cubic system reduces the total number of three independent elastic parameters, i.e. C_{11} , C_{12} , and C_{44} . These are the elements of elastic stiffness matrix of order 6×6 , with 6 eigen values. On the basis of these parameters, the mechanical stability of crystals has been studied. The Born and Huang mechanical stability conditions for cubical materials are given by the following equations [44, 45]:

$$C_{11} > 0, C_{44} > 0, C_{11} - C_{12} > 0, C_{11} + 2C_{12} > 0, C_{12} < B < C_{11} \quad (4)$$

From the above equation if these criterion are not satisfied by elastic constants, then cubic crystals become unstable. The C_{11} , C_{12} and C_{44} elastic constants were obtained by calculation, which are depicted in the table 2. By analyzing these calculated elastic constants, all these compounds satisfying the stability conditions. Therefore, MnNbAs, MnNbSb, FeNbSn and FeNbPb compounds are mechanically stable against deformation.

The bulk modulus is a measure of resistance to volume change and the shear modulus can be explained as reversible deformations on shear stress. The bulk modulus (B) and the isotropic shear modulus (G) have been calculated using the Voigt-Reuss and Hill approximation [46]. Using C_{ij} elastic constants, they can be calculated as:

$$B = \frac{1}{3}(C_{11} + 2C_{12}) \quad (5)$$

$$G = \frac{1}{2}(G_V + G_R) \quad (6)$$

where,

$$G_V = \frac{1}{5}(C_{11} - C_{12} + 3C_{44}) \quad (7)$$

$$G_R = \frac{5}{3} \frac{(C_{11} - C_{12})C_{44}}{(C_{11} - C_{12}) + 4C_{44}} \quad (8)$$

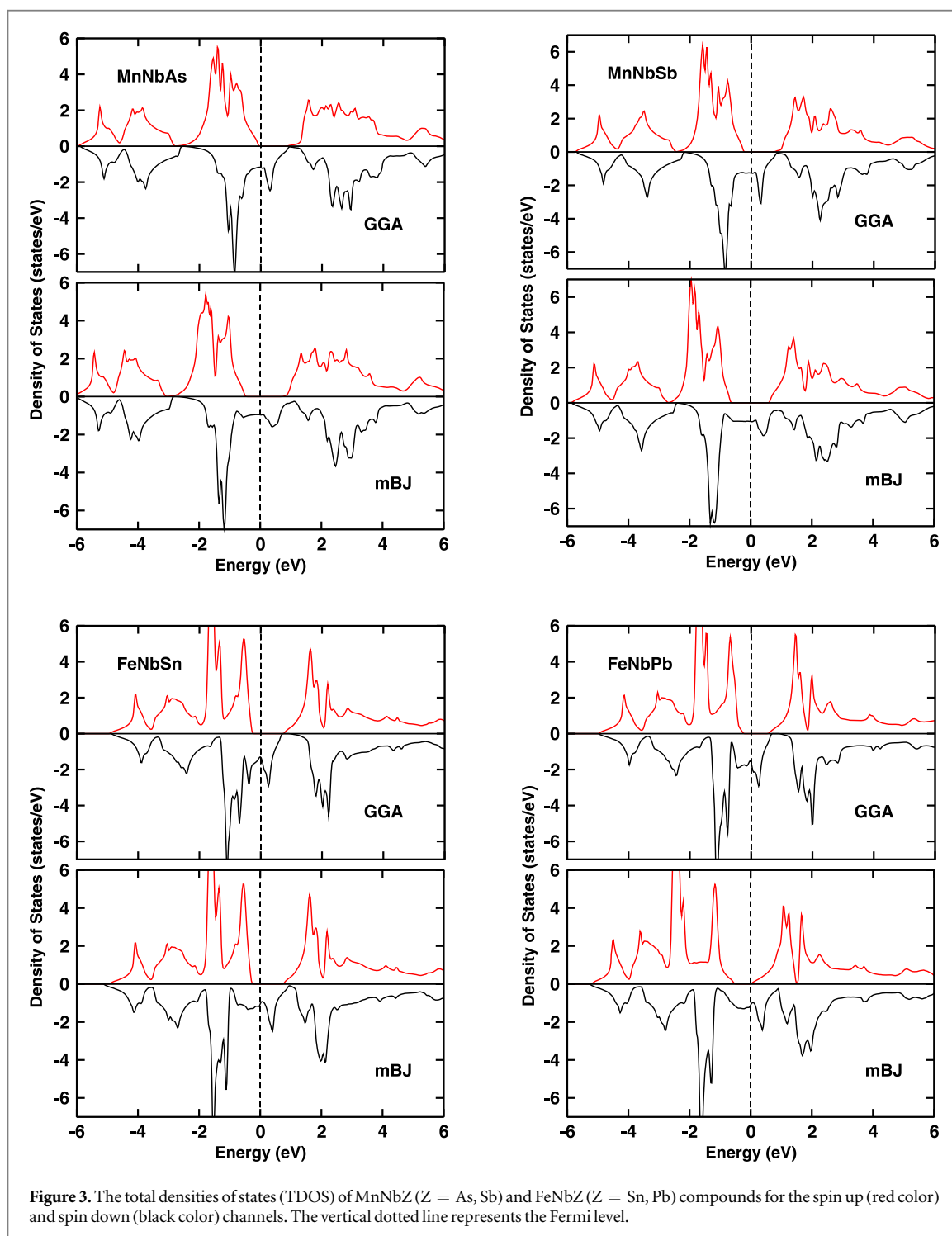
The fact that the bulk modulus calculated from the optimization and the elastic properties give very close results to each other indicate that the calculations are correct, which are clearly shown in tables 1 and 2.

The Young's modulus and Poisson's ratio used to investigate the hardness of polycrystalline materials were calculated using the following formulas,

$$E = \frac{9BG}{3B + G} \quad (9)$$

$$\nu = \frac{3B - 2G}{2(3B + G)} \quad (10)$$

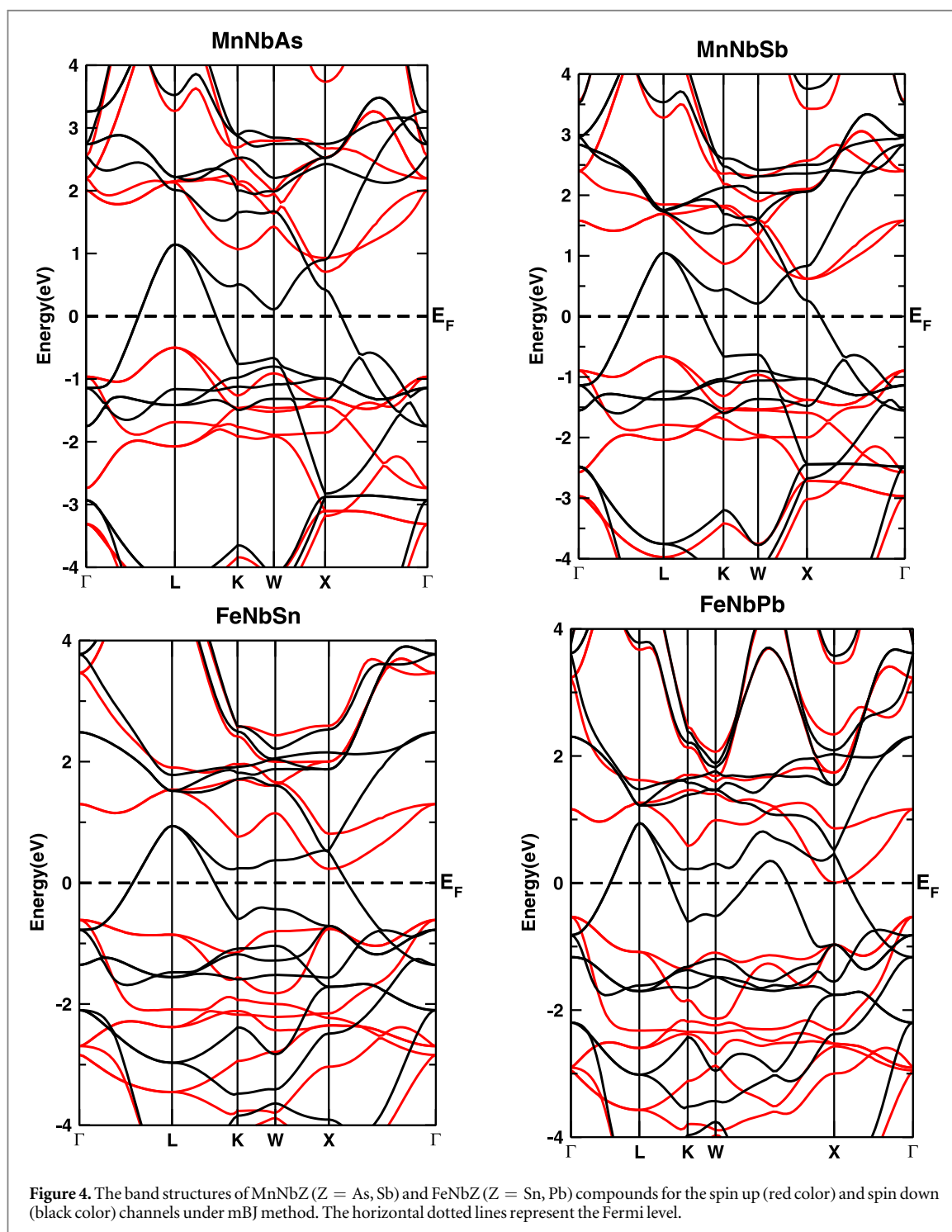
E is the ratio of tensile stress to tensile strain that measures the stiffness of the material and ν determines the nature of atomic bonding present in the materials. Among these four compounds FeNbSn is the stiffest materials and MnNbAs has the lowest stiffness. The ductility or brittleness of polycrystalline materials can be determined by B/G ratio, Cauchy pressure $C_{12} - C_{44}$ and Poisson's ratio (ν) values. The critical values of B/G and Poisson's ratio (ν) are 1.75 and 0.26, respectively [47]. If the calculated B/G and Poisson's ratio results are greater than these values, the material is ductile, otherwise, it is brittle [48]. Cauchy pressure ($C_{12}-C_{44}$) can be defined as the angular character with atomic bonding, the negative value for directional covalent bonding whereas the positive value for non-directional metallic bonding. Thus, MnNbAs has non-directional metallic bonding and MnNbSb,



FeNbSn, and FeNbPb have directional covalent bonding. Also, the negative Cauchy's pressure represents a brittle material, whereas the positive Cauchy's pressure represents a ductile material. Therefore, the obtained results show MnNbAs compound is ductile and the remaining three MnNbSb, FeNbSn, and FeNbPb compounds are brittle materials. Ductile material has the ability to receive permanent deformation without fracturing, which provides major safety for the design and manufacture of electronic devices. However, the materials that fracture by applying a small amount of deformation is called brittle materials. Due these characteristics of ductile MnNbAs material is useful for spintronic devices.

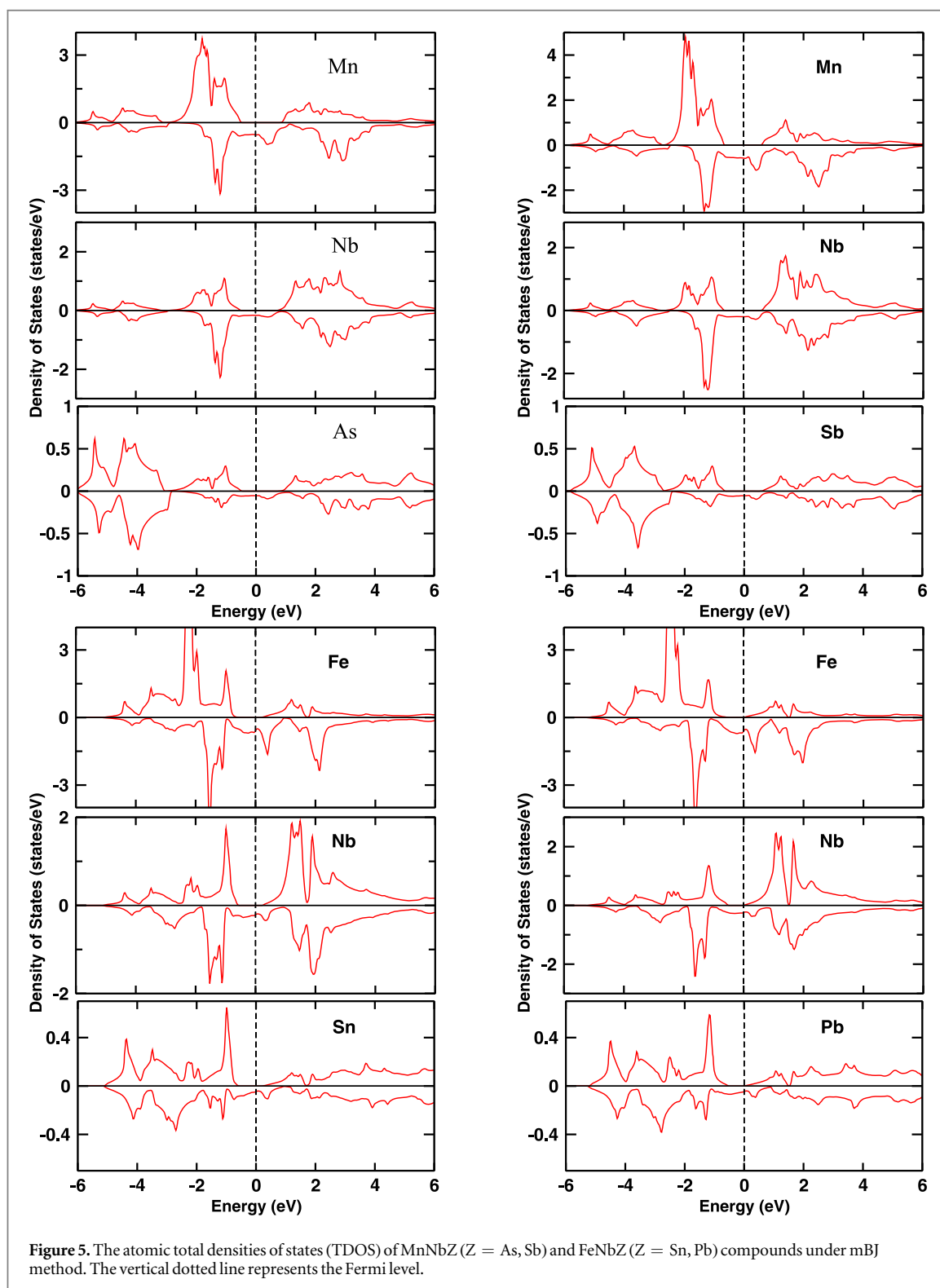
3.2. Electronic structure and magnetic properties

The study of electronic structure for ferromagnetic semi-Heusler alloys has been studied earlier in analogous compounds [42, 49, 50]. To investigate the similar nature for our system, we calculated the spin polarized calculation and understand their electronic and magnetic properties with the help of density of states (DOS)

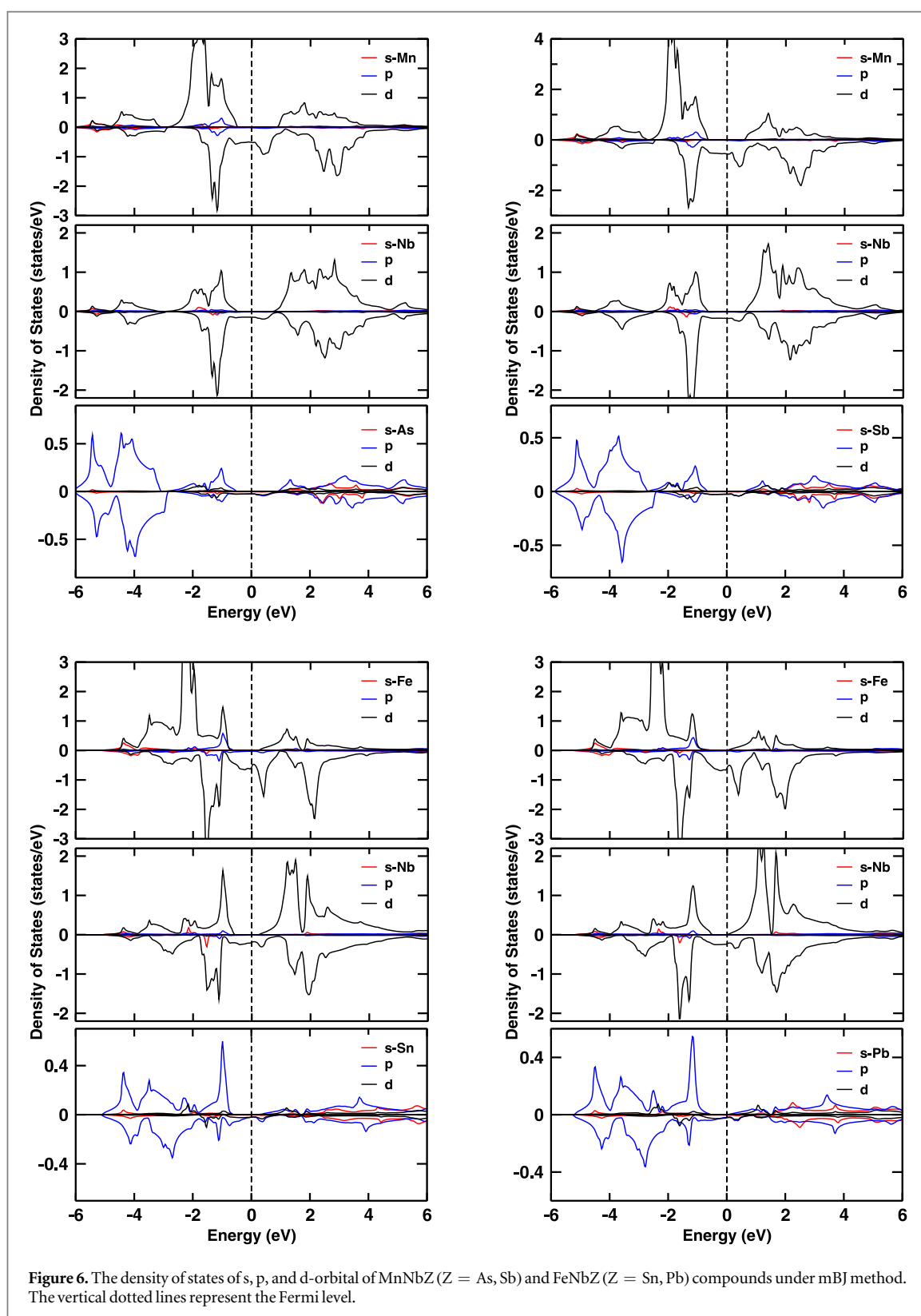


corresponding to the stable configuration. From the DOS plot as shown in figure 3, it is clear that MnNbAs, MnNbSb, FeNbSn, and FeNbPb semi-Heusler compounds are half-metallic ferromagnet under GGA and mBJ calculations. For the confirmation of the accuracy of half-metallicity, we used a second approximation called mBJ potential, which gives more accurate result for Heusler compounds [42, 49, 50] and perovskites [51, 52] and shows similar types of DOS distribution near Fermi level except for slight shifting Fermi level towards conduction and valence bands. Thus, all systems are half-metallic ferromagnetic materials, which are also clear from band structure for the families along with the high symmetry points of the first Brillouin zone of mBJ calculations. The minority spin electrons are found in the up channel and majority spin electrons in the down channel, which are semiconducting and metallic in nature respectively, as shown in DOS and band structure plots.

According to figure 5, the greatest contribution to the total density of states is due to the transition elements of Mn-3d, Fe-3d, and Nb-4d atoms. The sharp peak of MnNbAs is located in the energy range -2.0 to -1.0 eV,

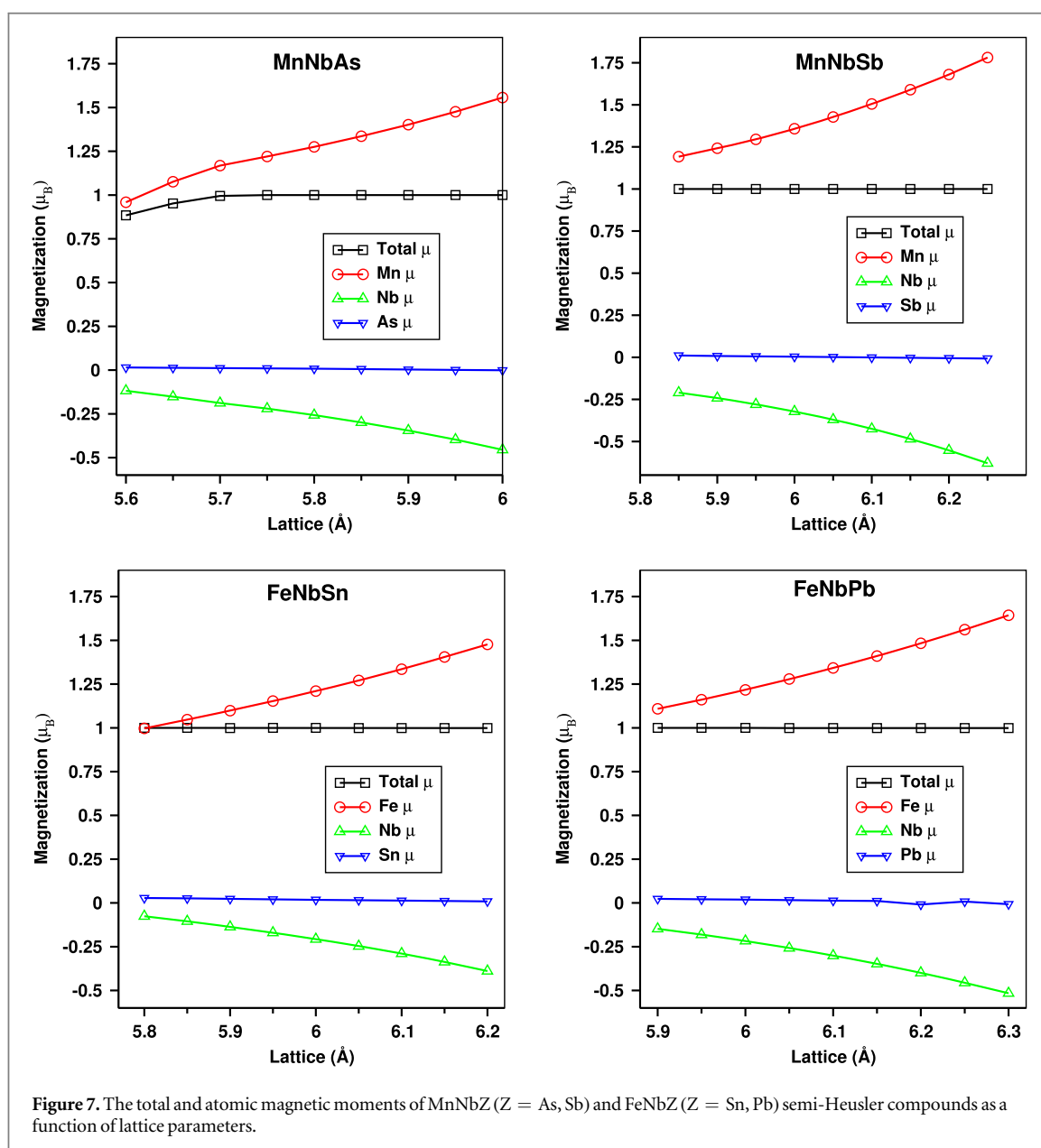


this is due to the effective hybridization between d-d orbitals of Mn-3d and Nb-4d elements, which is shown in figure 6. The d-orbital of these two elements contributed mainly to the total magnetic moment and half-metallic nature. Whereas, the contribution of s and p-orbitals are negligible as a comparison to the d-orbital. But, for As-atom p-orbital has more contribution than s and d-orbitals, whose highest peak in the range of -5.0 eV to -3.0 eV in the valence band. At the Fermi level, small contributions are found by all these elements and it varies with different energy levels in conduction and valence band. Spin up channel is semiconducting with bandgap 1.014 eV and 1.198 eV under GGA and mBJ calculations respectively, whereas the down channel is metallic. Thus, due to atomic hybridization between atomic orbitals formed metallic in spin down channel called majority channel resulting to half-metal. Similarly, for an isoelectronic compound, MnNbSb has the analogous



electronic and magnetic properties but different in band gap in spin up channel. For GGA and mBJ calculations bandgap are 0.950 eV and 1.200 eV respectively, which are tabulated in table 2.

In Fe containing compounds FeNbSn and FeNbPb, the total density of states (TDOS), band structure, and partial density of states (PDOS) are plotted in figures 3–6, which shows these are half-metal. The sharp peaks are due to the d-orbital of transition elements of Fe-3d, Nb-4d elements and p-orbital of Sn and Pb elements. The Sn and Pb atoms have two fulfilled s-orbital and only three electrons are occupied by p-orbital. This s-orbital contribution is far from the Fermi level but in p-orbital has small energy at Fermi level and high at far from the



Fermi level in both conduction and valence bands as comparison to the transition elements. The band gap in the upper channel for FeNbSn is increased by applying mBJ but in FeNbPb band gap decreases as shown in table 3.

From figures 3 and 4, the spin up and spin down channels are represented by the red and black colors respectively, which were calculated under mBJ method. The semiconducting nature of the spin-up channel and metallic in the spin-down channel are shown from the DOS and band structure plots. Thus, the gap found on these semiconducting sides at the Fermi level is called band gap. The half-metallic or spin-flip gap is defined as the absolute value of maximum energy in valence band relative to the Fermi level, which are depicted in the table 3. The band located on occupied region (valence region) at maximum energy level is called valence band maximum (VBM), while the band located on unoccupied region (conduction region) at minimum energy level is called conduction band minimum (CBM). Hence, energy difference between VBM and CBM at Fermi level is called band gap. Thus, by analyzing VBM and CBM at different symmetry points shows, all these compounds have indirect band gap for spin-up channel with different band gap, while down channels are metallic. As a result by combining both semiconducting and metallic states, these compounds show half-metal ferromagnetic materials under GGA and mBJ approach. In addition to this, from plots of GGA, we observed that except MnNbAs remaining three compounds show 100% polarization but for mBJ calculations except FeNbPb remaining three compounds have 100% polarization, due to this nature these semi-Heusler compounds are very important for spintronic applications.

The Slater-Pauling (SP) rule is one of the methods to determine the total magnetic moment in Heusler compounds. This method can be used by subtracting 24 of the total valence electrons in full-Heusler compounds

Table 3. Valence band maximum (VBM), conduction band minimum (CBM), band gap (E_{bg}), Half-metallic/spin-flip gap (E_{HM}), total and atomic magnetic moments of MnNbZ ($Z = \text{As, Sb}$) and FeNbZ ($Z = \text{Sn, Pb}$) compounds.

Compound	VBM (eV)	CBM (eV)	E_{bg} (eV)	E_{HM} (eV)	$M_{Tot}(\mu_B/\text{f.u.})$	$M_X(\mu_B)$	$M_{Nb}(\mu_B)$	$M_Z(\mu_B)$
MnNbAs ^{GGA}	-0.037	0.864	0.901	0.037	1.00	1.26	-0.24	0.0086
MnNbAs ^{mBJ}	-0.454	0.711	1.165	0.454	1.00	1.47	-0.39	0.0022
MnNbSb ^{GGA}	-0.207	0.753	0.960	0.207	1.00	1.40	-0.35	0.0025
MnNbSb ^{mBJ}	-0.598	0.548	1.146	0.598	1.00	1.63	-0.51	0.0075
FeNbSn ^{GGA}	-0.239	0.733	0.972	0.239	1.00	1.23	-0.22	0.0173
FeNbSn ^{mBJ}	-0.235	0.739	0.974	0.235	1.00	1.57	-0.43	0.0015
FeNbPb ^{GGA}	-0.234	0.551	0.785	0.234	1.00	1.35	-0.31	0.0132
FeNbPb ^{mBJ}	-0.446	0.000	0.446	0.446	1.00	1.78	-0.59	0.0001

and 18 of the total valence electrons in semi-Heusler compounds [53]. The electronic configurations of these atoms are Mn = $3d^5 4s^2$, Fe = $3d^6 4s^2$, Nb = $4d^4 5s^1$, As = $3d^{10} 4s^2 4p^3$, Sb = $4d^{10} 5s^2 5p^3$, Sn = $4d^{10} 5s^2 5p^2$, and Pb = $4f^{14} 5d^{10} 6s^2 6p^2$.

The total number of valence electrons Z_t of MnNbAs compound is 17. According to SP rule ($M_t = Z_t - 18$), therefore the total magnetic moment of MnNbAs compound is $1.00 \mu_B/\text{f.u.}$ Similarly, other remaining three compounds have also 17 valence electrons, so their magnetic moments are the same, i.e., $1.00 \mu_B/\text{f.u.}$, as shown in table 3. To check the magnetic stability of these compounds on the basis of SP rule and by applying strains with changing the lattice parameters but total magnetic moment remains same for all these compounds. Thus, our results are compatible with the SP rule. The total and atomic moments are plotted as a function of lattice parameters as shown in figure 7.

From table 3, the total magnetic moment obtained by using GGA and mBJ methods are $1.00 \mu_B/\text{f.u.}$ for all compounds, which comes from Slater-Pauling and confirmed these are ferromagnetic analogous to the previously reported compounds [42, 49]. The spin magnetic moment of transition elements Mn-3d, Fe-3d, and Nb-4d atoms have increased after applying mBJ over GGA but total magnetic moments remain the same. This is because, 3d-elements show positive spin magnetic moment and 4d-element has a negative spin magnetic moment, which cancels each other and finally shows total magnetic remains the same under both approximations. While other p-orbital elements As, Sb, Sn, and Pb have very small magnetic moments, which is clear from table 3 and as shown in figures 5 and 7.

4. Conclusions

The ground state electronic and magnetic properties of newsemi-Heusler compounds MnNbZ ($Z = \text{As, Sb}$) and FeNbZ ($Z = \text{Sn, Pb}$) were investigated using the density functional theory under generalized gradient approximation (GGA) and modified Becke-Johnson (mBJ) potential. By analyzing volume optimization plots, density of states, and band structure, these are ferromagnetic with half-metallic character. The cohesive energy, formation energy and calculated independent elastic constants C_{ij} confirmed these are thermodynamically and mechanically stable and possible to synthesized experimentally. In addition, the total magnetic moments per formula unit for all half-metallic compounds were found to be $1.00 \mu_B$ which comes from Slater-Pauling rule for semi-Heusler. MnNbAs shows ductile and remaining three MnNbSb, FeNbSn, and FeNbPb compounds are brittle materials. Since there are no experimental studies of these compounds and their related properties. Thus, these studies are interesting in the future for an experimental researcher to synthesize and utilize for spintronic applications.

Acknowledgments

DKY thanks Condensed Matter Physics Research Center, Nepal for the technical support.

Declaration of competing interest

There is no conflict of interest.

References

- [1] Zutic I, Fabian J and Sharma S D 2004 *Rev. Mod. Phys.* **76** 323
- [2] Wolf S A, Awschalom D D, Buhrman R A, Daughton J M, Molnar S V, Roukes M L, Chtchelkanova A Y and Treger D M 2001 *Science* **294** 1488

- [3] Roy T, Pandey D and Chakrabarti A 2016 *Phys. Rev. B* **93** 184102
- [4] Roy T and Chakrabarti A 2017 *J. Magn. Magn. Mater.* **423** 395
- [5] Ma J, Hegde V I, Munira K, Xie Y, Keshavarz S, Mildebrath D T, Wolverton C, Ghosh A W and Butler W H 2017 *Phys. Rev. B* **95** 024411
- [6] Ram M, Saxena A, Aly A E and Shankar A 2020 *RSC Adv.* **10** 7661
- [7] Galanakis I and Mavropoulos P 2003 *Phys. Rev. B* **67** 104417
- [8] Zhu Z H and Yan X H 2009 *J. Appl. Phys.* **106** 023713
- [9] Kobayashi K I, Kimura T, Sawada H, Terakura K and Tokura Y 1998 *Nature* **95** 677
- [10] Ghimire M P and Hu X 2016 *Mater. Res. Express* **3** 106107
- [11] Ghimire M P, Wu L H and Hu X 2016 *Phys. Rev. B* **93** 134421
- [12] Bhandari S R, Yadav D K, Belbase B P, Zeeshan M, Sadhukhan B, Rai D P, Thapa R K, Kaphle G C and Ghimire M P 2020 *RSC Adv.* **10** 16179
- [13] Soeya S, Hayakawa J, Takahashi H and Ito K 2002 *Appl. Phys. Lett.* **80** 823
- [14] Dho J, Ki S, Gubkin A F, Park J M S and Sherstobitova E A 2010 *Solid State Commun.* **150** 86
- [15] Nourmohammadi A and Abolhasani M R 2010 *Solid State Commun.* **150** 1501
- [16] Wang W Z and Wei X P 2011 *Comput. Mater. Sci.* **50** 2253
- [17] Ohno H 1998 *Science* **281** 951
- [18] Jimbo M, Hirano S, Meguro K, Tsunashima S and Uchiyama S 1994 *Jpn. J. Appl. Phys.* **33** 850
- [19] Rai D P, Ghimire M P and Thapa R K 2011 *Bull. Mater. Sci.* **34** 1219
- [20] Khandy S A and Chai J D 2019 *J. Magn. Magn. Mater.* **487** 165289
- [21] Paudel R, Zhou F, Liao M and Zhu J 2020 *J. Phys. Chem. Solids* **136** 109190
- [22] Paudel R and Zhu J 2018 *J. Magn. Magn. Mater.* **453** 10
- [23] Khandy S A 2018 *Mater. Res. Express* **5** 056516
- [24] Wang X, Cheng Z, Guo R, Wang J, Rozale H, Wang L, Yu Z and Liu G 2017 *Mater. Chem. Phys.* **193** 99
- [25] Ghimire M P, Sinha T P and Thapa R K 2011 *J. Alloys Compd.* **509** 9742
- [26] Kervan S and Kervan N 2017 *J. Supercond. Nov. Magn.* **30** 657
- [27] Graf T, Klaer P, Barth J, Balke B, Elmers H J and Felser C 2010 *Scr. Mater.* **63** 1216
- [28] Chadov S, Qi X, Kübler J, Fecher G H, Felser C and Zhang S C 2010 *Nat. Mater.* **9** 541
- [29] Roy A, Bennett J W, Rabe K M and Vanderbilt D 2012 *Phys. Rev. Lett.* **109** 037602
- [30] Kieven D, Klenk R, Naghavi S, Felser C and Gruhn T 2010 *Phys. Rev. B* **81** 075208
- [31] De Groot R A, Mueller F M, Van Engen P G and Buschow K H J 1983 *Phys. Rev. Lett.* **50** 2014
- [32] Tanaka C T, Nowak J and Moodera J S 1999 *J. Appl. Phys.* **86** 6239
- [33] Hordequin C, Nozieres J and Pierre J 1998 *J. Magn. Magn. Mater.* **183** 225
- [34] Roy W V, Boeck J D, Brijs B and Borghs G 2000 *Appl. Phys. Lett.* **77** 4190
- [35] Momma K and Izumi F 2011 *J. Appl. Crystallogr.* **44** 1272
- [36] Graf T, Felser C and Parkin S S P 2011 *Prog. Solid State Ch.* **39** 1
- [37] Blaha P, Schwarz K, Madsen G K H, Kvasnicka D and Luitz J 2001 *WIEN2k, An Augmented Plane Wave+Local Orbitals Program for Calculating Crystal Properties* Technische Universität Wien, Vienna, Austria
- [38] Perdew J P, Burke K and Ernzerhof M 1996 *Phys. Rev. Lett.* **77** 3865
- [39] Tran F and Blaha P 2009 *Phys. Rev. Lett.* **102** 226401
- [40] Becke A D and Johnson E R 2006 *J. Chem. Phys.* **124** 221101
- [41] Golesorkhtabar R, Pavone P, Spitaler J, Puschnig P and Draxl C 2013 *Comput. Phys. Commun.* **184** 1861
- [42] Özdemir E G and Merdan Z 2019 *J. Magn. Magn. Mater.* **491** 165567
- [43] Murnaghan F D 1944 *The Compressibility of Media Under Extreme Pressures (Proc. of the National Academy of Sciences of the United States of America)* (<https://doi.org/10.1073/pnas.30.9.244>)
- [44] Born M and Huang K 1954 *Dynamical Theory of Crystal Lattices* (UK: Oxford; Clarendon press) 9780198503699
- [45] Wu Z J, Zhao E J, Xiang H P, Hao X F, Liu X J and Meng J 2007 *Phys. Rev. B* **76** 054115
- [46] Zuo L, Humbert M and Esling C 1992 *J. Appl. Crystallogr.* **25** 751
- [47] Frantsevich I N, Voronov F F and Bakuta S A 1982 *Elastic Constants and Elastic Moduli of Metals and Nonmetals* (Kiev: Naukova Dnmka)
- [48] Perdew J P, Chevary J A, Vosko S H, Jackson K A, Pederson M R, Singh D J and Fiolhais C 1992 *Phys. Rev. B* **46** 6671
- [49] Özdemir E G and Merdan Z 2019 *Mater. Res. Express* **6** 116124
- [50] Joshi H, Rai D P, Laref A and Thapa R K 2019 *Mater. Res. Express* **6** 066307
- [51] Rai D P, Shankar A, Ghimire M P, Khenata R, Omran S B, Syrotyuk S V and Thapa R K 2017 *Mater. Chem. Phys.* **192** 282
- [52] Yadav D K, Bhandari S R, Belbase B P, Kaphle G C, Rai D P and Ghimire M P 2019 *Comput. Mater. Sci.* **170** 109168
- [53] Luo H, Liu G, Meng F, Wang L, Liu E, Wu G, Zhu X and Jiang C 2011 *Comput. Mater. Sci.* **50** 3119

Comparison of energies of different magnetic configurations to find the magnetic ground state as an example for parent material: $\text{Ca}_2\text{CrOsO}_6$

GGA

Configuration	FM($\uparrow\uparrow\uparrow$)	AFM($\uparrow\downarrow\uparrow\downarrow$)	FiM1($\uparrow\uparrow\downarrow\downarrow$)	FiM2($\uparrow\downarrow\downarrow\uparrow$)
Energy (Ry)	FSM	-80582.149983	-80582.165520	-80582.146929
Net mom.	FSM	-0.000241	0.000	0.50008
Mag. mom. Cr	FSM	± 2.31	2.21	± 2.23
Mag. mom. Os	FSM	± 1.45	-1.46	± 1.22
Band Gap (eV)	FSM	0.079	1.408	metallic

FM FSM(GGA)

Mag. mom.	FSM(12)	FSM(9)	FSM(6)	FSM(4)	FSM(2)	FSM(0)
Energy(Ry)	-80582.0771	-80582.1058	-80582.1132	-80582.1326	-80582.1323	-80582.0037
Mag. mom.	12.0001	8.99	6.00004	3.99	1.99	0.00
Mag. mom. Cr	2.57	2.34	2.30	2.28	± 2.33	2.12
Mag. mom. Os	1.66	1.27	± 1.24	± 1.36	± 1.47	1.42
Band Gap(eV)	1.834	metallic	metallic	metallic	metallic	metallic

UDD(GGA+U)

U	Cr4 Os1.5	Cr4 Os2	Cr4.5 Os1.5	Cr4.5 Os2	Cr5 Os1.5	Cr5 Os2
Energy(Ry)	-80581.6039	-80581.5352	-80581.5653	-80581.4967	-80581.5275	-80581.4590
Net mom.	0.0	0.0	0.0	0.0	0.0	0.0
Mag. mom. Cr	2.52	2.52	2.54	2.54	2.55	2.56
Mag. mom. Os	-1.66	-1.68	-1.677	-1.69	-1.67	-1.69
Band gap(eV)	2.45	2.53	2.52	2.60	2.59	2.67